=========== **TOKAMAKS** ===========

# Canonical Profiles in Tokamak Plasmas with an Arbitrary Cross Section

## Yu. N. Dnestrovskij, A. Yu. Dnestrovskij, S. E. Lysenko, and S. V. Cherkasov

*Nuclear Fusion Institute, Russian Research Centre Kurchatov Institute, Moscow, 123182 Russia*
*e-mail: dnyn@nfi.kiae.ru*
Received April 18, 2002

**Abstract**—Two principles are used to determine a canonical profile: the principle of the minimum of free plasma energy with the constraint that the total current is conserved and the principle of profile consistency. A second-order differential equation for the canonical profile of the function $\mu = 1/q$ is deduced in the natural coordinate system. Soft and hard boundary conditions are proposed to find an unambiguous solution to this equation. The range of their applicability is discussed. Numerical calculations show that the half-width of the canonical profile increases with decreasing aspect ratio, increasing plasma elongation, and decreasing $q_a$ value. The canonical profiles obtained make it possible to determine the critical gradients for the heat and particle fluxes in transport models. © 2002 MAIK "Nauka/Interperiodica".

## 1. INTRODUCTION

As early as 1980, Coppi [1] pointed out that the electron temperature profiles in tokamaks tend to conserve their shape in response to an external action on the plasma. This effect, which was called "the profile consistency," was confirmed in many devices. Taylor [2] supposed that the magnetic field evolves during the discharge to a certain "relaxed" state determined by the principle of the minimum of free plasma energy with the constraint that the helicity is conserved. He successfully applied this idea to describing the plasma behavior in reversed field pinches. During the relaxation, total magnetic reconnection occurs, and the magnetic field profiles at the final (relaxed) state of the discharge are always the same.

In 1986, Kadomtsev [3] and other authors [4, 5] published papers in which they analyzed the problem of relaxed states in tokamaks. In this case, total magnetic reconnection occurs either in spatially localized regions (e.g., in the case of sawtooth oscillations) or during failures (such as major disruptions). In a usual quasi-steady state, total reconnection does not occur and the plasma is in or near a certain intermediate relaxed state. To describe this state, the principle of the minimum of free plasma energy with the constraint that the total current is conserved was proposed in [3–6]. To complete the problem, they used the effect of profile consistency. The solution to this problem is called the canonical profile. Other ideas that lead to self-consistent profiles were discussed in [7, 8].

The canonical profile model defines an ultimate state to which the plasma relaxes. However, it does not propose the possible physical mechanisms and ways to achieve this state. The creators of the canonical profile theory (CPT) were aware of this gap and tried to fill it.

Kadomtsev [6] proposed that the relaxation to the minimum of free plasma energy is the result of the excitation of potential and magnetic fluctuations in the plasma; the generation of chains of magnetic islands; a partial destruction of the magnetic surfaces in the vicinity of these chains; and, as a consequence, an increase in the effective transport coefficients. It was assumed that, if the free energy strongly deviates from a minimum, these processes are more intense. As a result, the effective transport coefficients are not only functions of the local plasma parameters, but also depend on the profiles of parameters as a whole.

Later, independently of the CPT, numerous theoretical and experimental papers were published in which the origins of anomalous transport in the plasma were analyzed [9–11]. These origins were associated with the development of some types of drift instabilities. They include instabilities induced by the ion temperature gradient (ITG mode), electron temperature gradient (ETG mode), trapped electrons (TEM mode), and others. The solution of multidimensional gyro kinetic and gyro fluid equations allowed the study of the plasma behavior during the linear and nonlinear phases of instability together with the features of the resulting turbulence and the mechanisms of anomalous transport.

From the viewpoint of the CPT, the investigations performed partially filled the aforementioned gap between the initial and relaxed plasma states. As a result, the understanding of mechanisms for plasma relaxation was improved. Now it is possible to compare the profiles of the plasma parameters and the critical gradients in both transient relaxation states (defined by gyro equations) and the relaxed state (defined by the CPT).

In [3], the problem of a canonical profile in a circular plasma cylinder was considered. Some partial solutions in the form of rational functions were found, which is equivalent to the condition that the solution tends to zero at infinity. This boundary condition for the canonical profile corresponds to the assumption that the processes at the edge only slightly influence the relaxed state. We will refer to such boundary conditions as "soft" ones. The solution obtained in [3] for the canonical profile of $\mu_c = 1/q_c$ (i.e., for the poloidal magnetic field) with soft boundary conditions has the form

$$\mu_c = \mu_c^K = \mu_0/(1 + \rho^2/a_j^2), \quad a_j^2 = a^2 q_0/(q_a - q_0), \quad (1)$$

where $\rho$ is the radial coordinate, $a$ is the radius of the cylinder, and $a_j$ is the current radius. We will refer to this solution as the Kadomtsev canonical profile and will denote it by the superscript $K$.

As early as in the mid 1990s, however, experiments with a strong impact on the plasma boundary were performed [12]. At a certain instant, various impurities were injected into the plasma. The response of the plasma core was unexpected: after some delay $\tau_d$, which is much less than the energy confinement time $\tau_E$, the temperature of the plasma core begins to rise. Such plasma behavior may naturally be associated with a change of the relaxed state due to the change of the boundary conditions. New "stiff" boundary conditions for the canonical profiles, more strongly related to physical conditions at the edge, were introduced in [13].

The aim of this paper is to formulate and solve the problem of the relaxed states (canonical profiles) for a toroidal plasma with an arbitrary cross section. In this way, we need to overcome some difficulties. First, it is desirable to retain the one-dimensional character of the canonical profile problem, as was done in the case with a circular cylinder. This means that we should choose as an independent variable a certain variable related to the magnetic surfaces. However, after such a choice, if we want to find an analogue of Kadomtsev solution (1), another difficulty associated with the definition of the boundary condition at infinity arises. For a toroidal plasma with an elongated cross section, the magnetic surfaces are always surrounded by a separatrix, beyond which these surfaces are not closed and a unified radial coordinate does not exist. Therefore, the boundary conditions, which in the cylindrical case were defined at infinity, should be reformulated at the last closed magnetic surface (for a limiter plasma) or at the separatrix.

In [14–17], a transport model with critical gradients determined by canonical profile (1) was developed. We applied this model to the analysis of the energy balance in various tokamaks with circular and noncircular cross sections. Reasonable agreement between the calculated and experimental profiles of the temperature and pressure leads to the conclusion that the canonical profiles for a noncircular toroidal plasma only slightly differ from the profiles used in Eq. (1). However, as a rule, the calculated electron and ion temperature profiles were slightly more peaked than the experimental ones. This was pointed out in [15], where "corrected," slightly broader canonical profiles were introduced into the model and a better agreement between calculations and experiment was obtained. Such a correction was usually justified because the $Z_{eff}$ profile was unknown, the boundary conditions at infinity were formulated inadequately, and toroidal effects might be significant. Of course, such an intuitive correction of the model always raises a number of questions. Thus, the solution of the problem of canonical profiles for a toroidal plasma is of significant interest both from the standpoint of the generalization of the problem and as a tool for the verification of the canonical profile transport model (CPTM), which uses the corrected canonical profiles for a circular cylinder. In particular, in this paper, we will show that the canonical profiles for a toroidal plasma are slightly broader than the canonical profiles for a circular cylinder. Thereby, we justify the use of corrected canonical profiles in [15–17].

The paper is organized as follows. In Section 2, using natural coordinates related to the calculated equilibrium, we deduce a second-order equation for the canonical profile; this equation is the Euler equation for the free energy functional with the constraint of current conservation. Section 3 is devoted to the formulation of the boundary conditions for the canonical profiles. Here, we construct the soft and stiff boundary conditions and discuss the range of their applicability. The canonical profile evolution caused by the change of the boundary conditions is discussed in Section 4. In Section 5, we discuss the results of the calculations. Here, we show the dependences of the canonical profile half-width on the aspect ratio and other parameters. In Section 6, the relation between the canonical profiles and transport models is considered. In the Conclusion, we summarize the results obtained.

## 2. EQUATION FOR A CANONICAL PROFILE

Let us suppose that, for given pressure and current distributions in a toroidal plasma with an arbitrary cross section, we have solved the equilibrium problem (the Grad–Shafranov equation with respect to the magnetic flux $\psi$) with some boundary conditions. Then, the equation $\psi = $ const defines the magnetic surfaces.

We denote the polar coordinates by $r$, $z$, and $\varphi$ with the main axis coinciding with the axis of symmetry of the torus. We also consider the natural coordinates $\rho$, $\theta$, and $\zeta$, where $\rho$ is the coordinate of the magnetic surface defined by the toroidal magnetic field flux $\Phi$:

$$\pi \rho^2 B_0 = \Phi, \quad \Phi = \int_S \mathbf{B} \cdot d\mathbf{S}. \quad (2)$$

Here, $B_0$ is the vacuum toroidal field in the chamber center, $\theta$ is the poloidal angle, and $\zeta = r\varphi$. At the plasma edge, we have $\rho = \rho_{max} = a$, where $a$ is the effective plasma radius. At a low plasma pressure and large

aspect ratio, we can write $a = \sqrt{k}\,a_m$, where $a_m$ is the minor plasma radius and $k$ is the elongation of the plasma cross section. We also denote by the angular brackets $\langle\dots\rangle$ the operation of averaging along the magnetic surface:

$$\langle f \rangle = 2\pi/V' \int_0^{2\pi} \sqrt{g}\,f\,d\theta, \tag{3}$$

where $g$ is the determinant of the metric tensor of the assumed coordinate system, and

$$\sqrt{g} = r\frac{D(r,z)}{D(\rho,\vartheta)}. \tag{4}$$

As in [3–5], we also assume that the canonical profiles of the tokamak plasma are determined by the minimum of the free energy functional

$$F = \int_V (B_{\text{pol}}^2/8\pi + p/(\gamma-1))d^3x + \lambda_1 \int_S j_\varphi dS. \tag{5}$$

Here, $B_{\text{pol}} = (|\nabla\rho|/2\pi)\partial\psi/\partial\rho$ is the poloidal magnetic field, $p$ is the plasma pressure, and $\lambda_1$ is a Lagrangian multiplier. The last term in functional (5) describes the constraint that the total plasma current $\int_S j_\varphi dS = I_p$ is conserved.

To reduce the problem of the minimum of functional (5) to a one-dimensional problem, we will use, as in [3], self-consistency conditions for a circular cylinder, assuming that they should also be satisfied for a toroidal plasma:

$$p = p(\mu), \quad j_\varphi = j_\varphi(\mu), \quad j_\varphi(\mu) = Ap(\mu), \tag{6}$$

where

$$\mu = \partial\psi/\partial\Phi = 1/(2\pi B_0\rho)\partial\psi/\partial\rho, \tag{7}$$

$j_\varphi$ is the averaged plasma current density, and $A$ is a proportionality coefficient. The equation $\mu = \text{const}$ also defines the magnetic surfaces. Conditions (6) are to be satisfied for the total class of functions in which the minimum of functional (5) is sought; of course, they are not obligatory for real current and pressure profiles. The relation between canonical and real profiles is discussed in Section 6.

Let us represent functional (5) as a sum of one-dimensional integrals

$$F = F_B + F_p + F_j, \tag{8}$$

where [14]

$$F_B = \int_V (B_{\text{pol}}^2/8\pi d^3x$$
$$= \frac{1}{8\pi}\int_0^a V'(\partial\psi/\partial\rho)^2 G/(4\pi^2 R^2)d\rho, \tag{9}$$

$$F_p = \int_0^a V'p/(\gamma-1)d\rho, \tag{10}$$

$$F_j = \lambda_{11}\int_0^a V'j_\varphi d\rho, \quad \lambda_{11} = \lambda_1/(2\pi R_0). \tag{11}$$

Here,

$$V'(\rho) \equiv dV/d\rho = 2\pi\int_0^{2\pi} \sqrt{g}\,d\theta, \tag{12}$$

$V$ is the plasma volume, $V'$ and

$$G = R^2\langle(\nabla\rho)^2/r^2\rangle \tag{13}$$

are the metric coefficients (the coefficient $G$ is dimensionless), and $R$ is the plasma major radius. From Maxwell's equation, we obtain

$$j_\varphi = (B_0/(\mu_{00}V'R)\partial/\partial\rho(V'G\rho\mu), \tag{14}$$

where $\mu_{00}$ is the vacuum magnetic permeability. For a plasma with a circular cross section and large aspect ratio [the so called circular cylinder approximation (CCA)], we have $V \longrightarrow 2\pi^2 R\rho^2$, $V' \longrightarrow 4\pi^2 R\rho$, $G \longrightarrow 1$, and $G_2 = GV' \longrightarrow 4\pi^2 R\rho$.

Let us treat the potential $\Psi$ as an independent argument in the functional $F$ and carry out the variation of $F$ over this argument. By virtue of conditions (6) and (7), we have

$$\delta p = \partial p/\partial\mu\,\delta\mu, \quad \delta j_\varphi = \partial j_\varphi/\partial\mu\,\delta\mu,$$
$$\delta\mu = 1/(2\pi B_0\rho)\partial/\partial\rho\,\delta\psi. \tag{15}$$

Integrating $\delta F$ by parts, we obtain

$$\delta F = -\int_0^{\rho_{\max}} \delta\psi\partial/\partial\rho\{V'/\rho(B_0^2\rho^2/(4\pi R^2)G\mu$$
$$+ \partial p/\partial\mu/(\gamma-1) + \lambda_{11}\partial j_\varphi/\partial\mu)\}d\rho = 0. \tag{16}$$

Using Eq. (6), we find the Euler equation for functional (16)

$$\partial/\partial\rho\{V'/\rho(B_0^2\rho^2/(4\pi R^2)G\mu + \lambda_{12}\partial j_\varphi/\partial\mu)\} = 0,$$
$$\lambda_{12} = \lambda_{11} + \frac{1}{A(\gamma-1)}. \tag{17}$$

Using expression (14) and again renormalizing $\lambda$, we obtain the third-order equation with respect to $\mu$

$$\partial/\partial\rho\{V'/(\rho\mu')[\rho^2 G\partial\mu^2/\partial\rho$$
$$+ (\lambda_2/2)\partial/\partial\rho((1/V')\partial/\partial\rho(G_2\rho\mu))]\} = 0; \tag{18}$$

Here, $\mu' = \partial\mu/\partial\rho$. The parameter $\lambda_2$ corresponds to the notation of [13]. It will be defined below by using the boundary conditions.

Note that in the CCA, Eq. (18) takes the form

$$\partial/\partial\rho\{1/(\mu')[\rho^2\partial\mu^2/\partial\rho$$
$$+ (\lambda_2/2)\partial/\partial\rho((1/\rho)\partial(\rho^2\mu)/\partial\rho)]\} = 0. \tag{19}$$

After integrating Eq. (18), we obtain the Euler equation in the form of a second-order equation with an arbitrary constant $C$:

$$\rho^2 G\partial\mu^2/\partial\rho + (\lambda_2/2)\partial/\partial\rho((1/V')\partial/\partial\rho(G_2\rho\mu))$$
$$= C\rho\mu'/V', \tag{20}$$

or

$$L_1[\mu] + (\lambda_2/2)L_2[\mu] = (\lambda_2/2)L_3[\mu], \tag{21}$$

where

$$L_1[\mu] = \rho^2 G\partial\mu^2/\partial\rho,$$
$$L_2[\mu] = \partial/\partial\rho((1/V')\partial/\partial\rho(G_2\rho\mu)), \tag{22}$$
$$L_3[\mu] = (C/(\lambda_2/2))\rho\mu'/V'.$$

The constant of integration $C$ should be defined so that, at the point $\rho = 0$ (on the axis), the derivative $\partial\mu/\partial\rho$ vanishes.

Assuming that the solution to Eq. (20) at $\rho = 0$ is limited ($\mu(0) = \mu_0$ and $\mu'(0) = \partial\mu/\partial\rho(\rho = 0) = 0$), we expand it in the vicinity of this point in powers of $\rho$:

$$\mu/\mu_0 = 1 + \alpha_2\rho^2,$$
$$\mu'/\mu_0 = 2\alpha_2\rho, \tag{23}$$
$$\mu''/\mu_0 = 2\alpha_2.$$

Moreover, we have

$$V' = V''(0)\rho(1 + O(\rho^2)). \tag{24}$$

The first term, $L_1$, in Eq. (21) has a higher order of smallness over $\rho$ near $\rho = 0$; therefore, we can neglect it when choosing the constant of integration. The second term, $L_2$, in Eq. (21) can be presented as a sum of three terms:

$$L_2[\mu] = \mu\partial/\partial\rho[(1/V')\partial/\partial\rho(G_2\rho)]$$
$$+ \mu'[\partial/\partial\rho(G\rho) + (1/V')\partial/\partial\rho(G_2\rho)] + \mu''G\rho. \tag{25}$$

Substituting expressions (23) and (24) into formula (21), omitting $L_1$, and taking account expression (25), we obtain

$$(\lambda_2/2)\{\partial/\partial\rho[(1/V')\partial/\partial\rho(G_2\rho)]$$
$$+ 2\alpha_2\rho[\partial/\partial\rho(G\rho) + (1/V')\partial/\partial\rho(G_2\rho)] \tag{26}$$
$$+ 2\alpha_2 G\rho\} = C\rho \cdot 2\alpha_2/V'.$$

For $\rho \longrightarrow 0$, we have

$$\partial/\partial\rho[(1/V')\partial/\partial\rho(G_2\rho)] \longrightarrow 3G'(0) + \rho G''(0),$$
$$\partial/\partial\rho(G\rho) + (1/V')\partial/\partial\rho(G_2\rho) \longrightarrow 3G(0) + 2\rho G'(0),$$
$$\rho/V' \longrightarrow 1/V''(0). \tag{27}$$

Equating coefficients by the same powers of $\rho$, we obtain

$$3G'(0) = 0 \quad (\rho^0), \tag{28}$$

$$(\lambda_2/2)(8\alpha_2 G(0) + G''(0)) = 2\alpha_2 C/V''(0) \quad (\rho^1). \tag{29}$$

In the CCA, we have $G = \text{const}$; therefore, $G'(0) = 0$ and $G''(0) = 0$. Numerical calculations show that these equalities are valid in the general case of a toroidal plasma. As a result, Eq. (28) is satisfied automatically and Eq. (29) becomes homogenous in $\alpha_2$. The value of $C$ should be chosen from the condition $\alpha_2 \neq 0$. It is satisfied when

$$C = 4(\lambda_2/2)G(0)V''(0). \tag{30}$$

Substituting expression (30) into formulas (22) and (23), we obtain the final equation for a canonical profile:

$$L[\mu] \equiv \rho^2 G\partial\mu^2/\partial\rho$$
$$+ (\lambda_2/2)\partial/\partial\rho((1/V')\partial/\partial\rho(V'G\rho\mu)) \tag{31}$$
$$- 4(\lambda_2/2)G(0)V''(0)\rho\mu'/V' = 0.$$

In the CCA, Eq. (31) takes the form

$$\rho^2\partial\mu^2/\partial\rho + (\lambda_2/2)(-\partial\mu/\partial\rho + \rho\partial^2\mu/\partial\rho^2) = 0 \tag{32}$$

or

$$\rho^2\partial/\partial\rho(\mu^2 + \lambda_2\partial\mu/\partial\rho^2) = 0 \tag{33}$$

and can be integrated analytically.

## 3. BOUNDARY AND MATCHING CONDITIONS FOR CANONICAL PROFILES

We will distinguish two types of $\mu(\rho)$ functions. The canonical profiles, which are the solutions to Eqs. (31) or (32), will be denoted as $\mu_c(\rho)$. The "real" profiles of these functions, which are the solutions to the set of transport equations, we will denote as $\mu(\rho)$ without indices. When formulating the problem in [3], besides Eq. (32), the following boundary conditions were implicitly used

$$\mu_c(0) = \mu_0,$$
$$\mu_c(a) = \mu(a) \equiv \mu_a, \tag{34}$$
$$\lim\mu_c(\rho \longrightarrow \infty) = 0.$$

Here, $\mu_0 \sim 1$ and $\mu_a$ is the boundary condition for $\mu(\rho)$. In the CCA, we have $\mu_a = RB_\theta/aB_0 = 0.2RI_p/a^2B_0$. The last of boundary condition (34) assumes that the real

boundary conditions at the plasma edge do not influence the choice of the canonical profile. Such a type of boundary conditions is naturally called "soft." In the Introduction, we called problem (32) with boundary conditions (34) the Kadomtsev problem [3] and denoted its solution by the superscript $K$. The solution to the Kadomtsev problem has form (1).

In the general case of a toroidal plasma with a noncircular cross section, the region with closed magnetic surfaces is localized and the "radial" coordinate $\rho$ cannot be defined over a half-infinite interval. So, the third Kadomtsev boundary condition (34) should be reformulated for the plasma surface. This is convenient to do using the impedance of solution (1). For a toroidal plasma, the first-order impedance can be written in the following form:

$$X = i_a/(2G_a\mu_a), \qquad (35)$$

where $i = i(\rho)$ is the dimensionless current,

$$i = (\mu_{00}R/B_0)j_\varphi = (1/V')\partial/\partial\rho(V'G\rho\mu),$$
$$i_a = i(\rho = a). \qquad (36)$$

Note that, in the CCA, we have $G_a = 1$ and, for the Kadomtsev problem, we obtain

$$X^K = \mu_a/\mu_0. \qquad (37)$$

In the CCA, instead of conditions (34), the following equivalent boundary conditions can be used:

$$\mu_c(0) = \mu_0,$$
$$\mu_c(a) = \mu(a) \equiv \mu_a, \qquad (38)$$
$$X_c = X^K = \mu_a/\mu_0.$$

Here, we have no condition at infinity. We will also assume that, in the general case of a toroidal plasma, the special Kadomtsev-type solutions to Eq. (31) are defined by soft boundary conditions (38) at the plasma edge or at the separatrix.

To determine the Lagrange factor $\lambda_2$, we rewrite Eq. (31) using expression (36):

$$\rho^2 G\partial\mu^2/\partial\rho + (\lambda_2/2)i'$$
$$- 4(\lambda_2/2)G(0)V''(0)\rho\mu'/V' = 0, \qquad (39)$$

where $i' = \partial i/\partial\rho$. Turning $\rho$ to $a$ in Eq. (39), we find the formal relation between $\lambda_2$ and the boundary values of $\mu$, $i$, and their derivatives:

$$\lambda = \lambda_2/(a^2\mu_a) = \frac{G(a)}{\xi(1 - Y)}, \qquad (40)$$

where

$$Y = i_a'/(4\xi\mu_a') \qquad (41)$$

is the second-order impedance and $\xi = aV''(0)/V_a'$ ($\xi \geq 1$).

For boundary conditions (38), the derivative $\mu_c'(a)$ is

defined by the boundary condition $X_c = X^K$. Therefore, to solve the boundary problem for Eq. (31), we can use the shooting method, by fitting the parameter $\lambda = \lambda_2/a^2\mu_a$. Note that, in the CCA, Eq. (40) takes the form [13]

$$\lambda = 4/(1 - a\mu_a''/\mu_a'), \qquad (42)$$

and, for solution to Kadomtsev problem (1), we have

$$\lambda^K = 1/(1 - \mu_a/\mu_0). \qquad (43)$$

Let us now consider a plasma that undergoes a strong external action that leads to a change of the plasma boundary temperature and density and the intensity of periphery radiation. Examples of such an action are pulsed gas puffing, impurity injection, periphery injection of hydrogen pellets, and surface current drive. It is obvious that boundary conditions (38) do not reflect such processes. On the other hand, many experiments show a fast plasma reaction over the entire plasma cross section as a response to the periphery action. Apparently, the boundary conditions for the canonical profiles should be related to the boundary conditions for the other plasma parameters. An example of such a relation that does not contradict CPTMs is presented in [13], where the following "stiff" boundary conditions for the CCA were proposed:

$$\mu_c(a) = \mu(a),$$
$$\mu_c'(a) = \mu'(a), \qquad (44)$$
$$\mu_c''(a) = \mu''(a).$$

In contrast to conditions (38), all boundary conditions (44) are defined at the plasma surface. Usually, such a problem is referred to as the Cauchy problem.

We assume that conditions (44) are also suitable for a toroidal plasma with an arbitrary cross section. The physical sense of conditions (44) is as follows. It is implicitly supposed that, in a thin periphery layer, the canonical profiles $\mu_c(\rho)$ satisfy not only Maxwell equation (14), but also Ohm's law, because the function $\mu(\rho)$ satisfies these equations over the entire cross section and, at the boundary, the first and second derivatives of $\mu_c(\rho)$ and $\mu(\rho)$ are the same.

Boundary conditions (44) can be written in terms of the surface impedances similarly to conditions (38):

$$\mu_c(a) = \mu_a,$$
$$X_c = X, \qquad (45)$$
$$Y_c = Y.$$

Here, $X$ and $Y$ are defined by formulas (35) and (41) and can be calculated through derivatives of $\mu(\rho)$, and $\lambda$ is defined by Eq. (40).

The third of boundary conditions (45) contains the second spatial derivative of $\mu(\rho)$, i.e. the third derivative of $\psi(\rho)$ at the edge. In transport codes, a parabolic

equation of the second order with respect to $\psi$ is typically used. Hence, the computation of the third derivative is an ill-posed problem. To regularize this process, it is possible to use Ohm's law

$$j = \sigma E, \tag{46}$$

where $\sigma$ is the plasma conductivity, and the assumption of a quasi-steady character of current diffusion near the edge,

$$\partial E/\partial \rho(a) = 0, \tag{47}$$

where $E$ is the toroidal electric field. This assumption is true when the electron temperature in the vicinity of the edge is small and the rate at which the total plasma current changes is not large. From Eqs. (46) and (47), we have

$$j'_a/j_a = i'_a/i_a \approx \sigma'_a/\sigma_a. \tag{48}$$

Hence, we obtain an approximate expression for the second-order impedance,

$$Y = i'_a/(4\gamma\mu'_a) \approx (\sigma'_a/\sigma_a)(i_a/4\xi\mu'_a). \tag{49}$$

This expression does not contain third-order derivatives and can be used in boundary conditions (45).

In [15], the following criterion for the transition from soft boundary conditions (34) to stiff conditions (45) in the CCA was proposed:

$$Y < Y^K = \mu_a/\mu_0. \tag{50}$$

This criterion was used in the CPTM to describe the L−RI mode transition in TEXTOR with a circular cross section [18]. In the general case of a toroidal plasma, criterion (50) needs experimental verification. In view of expression (49), this criterion can be written in the form

$$(\sigma'_a/\sigma_a)i_a/(4\xi\mu'_a) < \mu_a/\mu_0. \tag{51}$$

Let us now discuss in more detail the plasma evolution to the relaxed state in the core and the behavior of the canonical profile in this region. If the peakedness of the current profile is high enough, then a region where $\mu(\rho) > 1$ appears. A magnetic surface with the coordinate $\rho = \rho_S$, where $\mu(\rho_S) = 1$, is usually called the resonant surface. Sawtooth oscillations with a total magnetic reconnection usually arise inside the resonant surface. The total reconnection means that the magnetic shear is absent and $\mu = $ const in this region. The value of current inside the resonant surface $\rho < \rho_S$ is not conserved (a part of this current is thrown out from this region); hence, the minimum of functional (5) in this region does not correspond to a more deeply relaxed state $\mu(\rho) = $ const. The effective canonical profile of the $\mu(\rho)$ function, which corresponds to the total relaxation in the region $\rho < \rho_S$ and the limited relaxation [defined

by the minimum of functional (5)] in the region $\rho > \rho_S$, can be described as follows:

$$\mu_c^{\text{eff}} = \begin{cases} \text{const} = \mu_c(\rho_S) & \text{for} \quad \rho < \rho_S, \\ \mu_c(\rho) & \text{for} \quad \rho > \rho_S. \end{cases} \tag{52}$$

Here, the first condition is the matching condition. At the point $\rho = \rho_S$, function (52) is continuous but undergoes a jump of the derivative due to a partial ejection of the current from the region $\rho < \rho_S$. The value of the total current does not depend on the position of the point $\rho_S$, because it is determined by the boundary condition $\mu_c(a) = \mu_a$. We emphasize that the profile $\mu_c^{\text{eff}}(\rho)$ exactly defines the possible relaxed plasma state. During the plasma evolution, the possible relaxed state also changes.

## 4. EVOLUTION OF CANONICAL PROFILES

Boundary conditions (38) and (45) and matching conditions (52) are not stationary. Moreover, a transition from soft conditions to stiff ones, and vice versa, is possible. Therefore, the canonical profiles are evolving in time. Since Eq. (31) is of an elliptical type, the evolution may be described by the diffusion equation

$$\tau_c \partial \mu_c/\partial t = L[\mu_c], \tag{53}$$

where the operator $L[\mu_c]$ is defined by Eq. (31) and $\tau_c$ is the characteristic time of the canonical profile evolution. Apparently, $\tau_c \sim \tau_d$, where $\tau_d$ is the characteristic time delay of the plasma core response from the edge action. Experiments [12, 19, 20] show that $\tau_c \sim 1$–5 ms, which is considerably (by 1–2 orders) less than the energy confinement time $\tau_E$.

## 5. RESULTS OF THE CANONICAL PROFILE CALCULATIONS

To find a canonical profile, we should carry out a series of calculations. First, we should establish the current and pressure distributions and solve the Grad–Shafranov equation with respect to the magnetic flux function $\psi$ for chosen boundary conditions. Next, using the solution obtained, we should find the metric coefficients $V'(\rho)$ and $G(\rho)$; the boundary values of $\mu$; and, if necessary, its derivatives. After this, we can determine the boundary conditions and the coefficients entering into the equation for the canonical profile.

As an example, we consider a plasma with the following parameters:

$$R = 3 \text{ m}, \quad a_m = 1 \text{ m}, \quad A = R/a_m = 3,$$
$$B_0 = 2.8 \text{ T}, \quad I_p = 2 \text{ MA}, \quad k = 1.7, \quad \delta = 0.3. \tag{54}$$

Here, $R$ and $a_m$ are the major and minor plasma radii, $B_0$ is the toroidal magnetic field, $I_p$ is the plasma current, and $k$ and $\delta$ are the elongation and triangularity of the
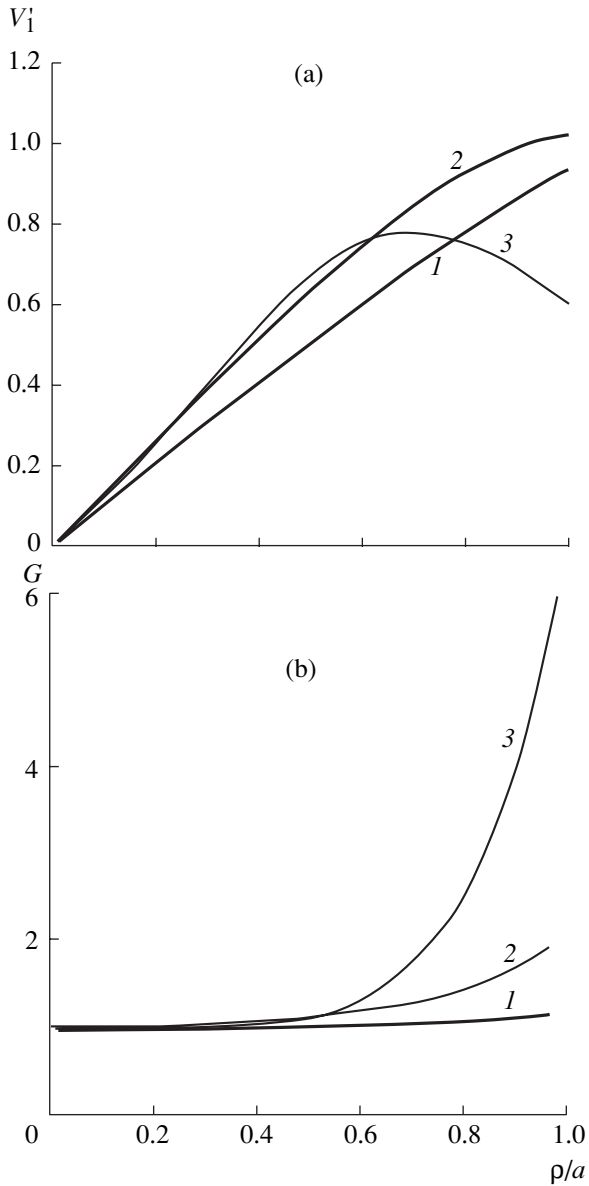
**Fig. 1.** Profiles of the metric coefficients (a) $V_1' = V'/4\pi^2 Ra$ and (b) $G$ for $q_a = 7$ and different aspect ratios $A = R/a =$ (*1*) 5, (*2*) 3, and (*3*) 1.5.

cross section. The calculations were performed with the ASTRA code [21].

We take reasonable (close to parabolic) profiles of the electron and ion temperatures and the plasma density. Using Ohm's law, we calculate the current density. Then, these data are used in the equilibrium block to calculate the positions of the magnetic surfaces and the function $\psi$. Figure 1 shows the results of calculations of the normalized metric coefficients $V_1' = V'(\rho)/(4\pi^2 Ra)$ and $G(\rho)$ for different aspect ratios. Here, $q_a = 7$. It can be seen that, in the central zone, $G \approx \text{const} = 1$ and
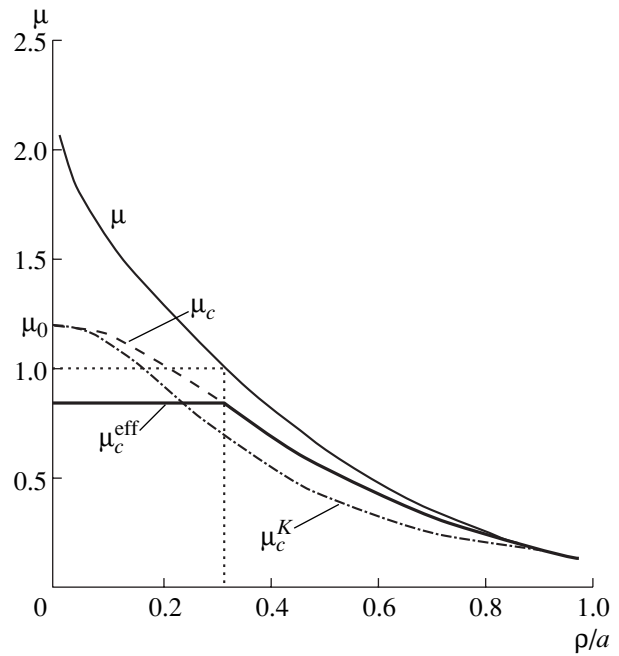


**Fig. 2.** Canonical profile $\mu_c$ determined from Eq. (31), Kadomtsev canonical profile $\mu_c^K$, and the effective canonical profile $\mu_c^{\text{eff}}$ with allowance for sawtooth oscillations for $R = 3$ m, $a = 1$ m, $B_0 = 2.8$ T, $I_p = 2$ MA, $k = 1.6$, $\delta = 0.3$, and $q_a = 7$. The $\mu$ profile shows the initial profile, determining the plasma geometry and the position of the resonant surface $q = 1/\mu = 1$.

$V_1'(\rho) \approx \rho$. At the edge, $G(\rho)$ increases by several times and the function $V_1'(\rho)$ deviates from a straight line.

If we know the metric coefficients, we can move to the solution of the boundary problem for Eq. (31). Let us first consider soft boundary conditions (38), assuming $\mu_0 = 1.2$. Figure 2 shows the results of the calculations for the canonical profile of $\mu_c(\rho)$ for a plasma with parameters (54). For comparison, the Kadomtsev canonical profile $\mu_c^K(\rho)$ and the $\mu(\rho)$ profile of the initial transport problem are also shown. We note two main features of the resulting profiles:

(i) The canonical profile $\mu_c(\rho)$ for a toroidal plasma is broader than the Kadomtsev canonical profile derived for a circular cylindrical plasma.

(ii) In the initial transport problem, $\mu(\rho) > 1$ at the center; this should lead to sawtooth oscillations inside the resonant surface. This means that the resulting canonical profile $\mu_c(\rho)$ should be corrected to the effective canonical profile defined by Eq. (51). The corrected profile is shown by the heavy line in Fig. 2.

When the plasma geometry and the parameter $q_a$ are varied, the first feature is retained. To quantitatively estimate the difference between $\mu_c(\rho)$ and $\mu_c^K(\rho)$ pro-
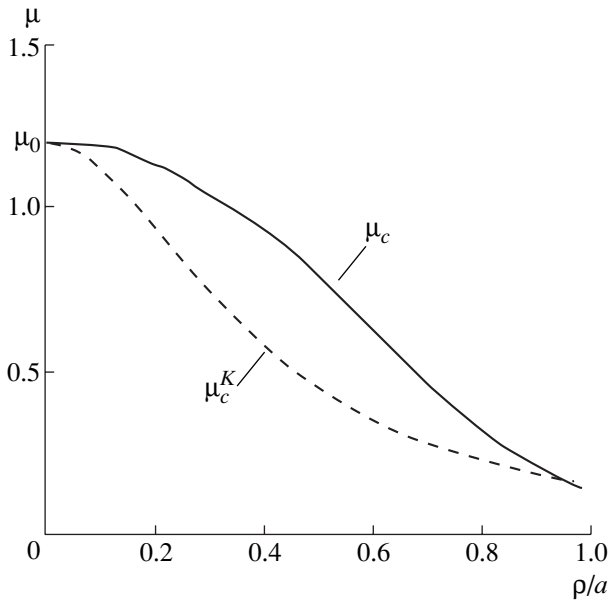
**Fig. 3.** Canonical profiles $\mu_c$ and $\mu_c^K$ for the same parameters as in Fig. 2, but for $R = 1.5$ m ($A = 1.5$).
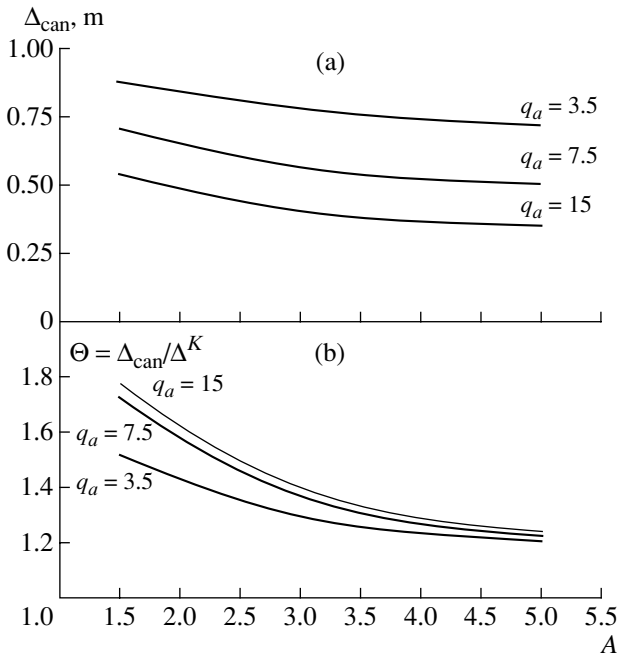


**Fig. 4.** (a) Half-width $\Delta_{can}$ of the canonical profile and (b) the ratio of this half-width to the half-width of the Kadomtsev canonical profile, $\Theta = \Delta_{can}/\Delta^K$, as functions of the aspect ratio $A = R/a$ for $k = 1.6$, $\delta = 0.3$, and different values of $q_a$.

files, we denote by $\Delta_{can}$ and $\Delta^K$ the half-widths of these profiles, which are determined by the relationships $\mu_c(\Delta_{can}) = 0.5\mu_0$ and $\mu_c^K(\Delta^K) = 0.5\mu_0$. For Kadomtsev

profile (1), the half-width is equal to the current radius: $\Delta^K = a_j$.

We choose parameters (54) as initial ones and vary the major radius $R$ in the range $R = 1.5$–5, so that the aspect ratio is varied in the range $A = 1.5$–5. Also, in order to keep a constant value of $q_a$, we simultaneously vary the current $I_p$.

Figure 3 shows the profiles $\mu_c(\rho)$ and $\mu_c^K(\rho)$ for the aspect ratio $A = 1.5$. We can see that the profile $\mu_c(\rho)$ is appreciably broader than the profile $\mu_c^K(\rho)$. Figure 4a shows the dependences of the half-width $\Delta_{can}$ on the aspect ratio $A$ for $q_a = 15, 7.5$, and 3.8. It is seen that the half-width $\Delta_{can}$ slowly increases with decreasing $A$. At $q_a \sim 4$, the value of $\Delta_{can}$ attains a value of $(0.85$–$0.9)a$; i.e., the canonical profiles for spherical tokamaks are very flat. Figure 4b shows the half-widths ratio $\Theta = \Delta_{can}/\Delta^K$ as a function of the aspect ratio $A$ for the same values of $q_a$. Since $\mu_c^K$ defined by expression (1) is independent of the aspect ratio, the value of $\Delta^K$ is also independent of this ratio. For moderate and high aspect ratios ($A \sim 3$–5), the ratio $\Theta$ varies slowly in the range $\Theta = 1.2$–1.3. For small $A \sim 1.5$ (for spherical tokamaks), this ratio increases to $\Theta = 1.5$–1.8.

Now we discuss the behavior of $\Delta_{can}$ and $\Theta$ when other geometrical factors are varied. Figure 5 shows the dependences of these quantities on the elongation $k$ at $A = 3$ and different values of $q_a$. As $k$ increases, the canonical profiles becomes flatter as compared to the Kadomtsev profiles. Figure 6 shows the dependences of the same quantities on the triangularity $\delta$ for $k = 1.6$ and $A = 3$, keeping other parameters of set (54) fixed. We can see that the canonical profiles weakly depend on the triangularity.

Next, we consider stiff boundary conditions. This type of boundary conditions corresponds to a strong cooling of the edge plasma, when the current density and the radial derivative of the current density near the boundary are small and condition (49) or the equivalent condition (50) is satisfied. To describe this process, we consider reasonable parabolic profiles of the ion temperature $T_i(\rho)$ and plasma density $n(\rho)$ and the following model profile of the electron temperature:

$$T_e(\rho) = T_{ea} + T_0(1 - \rho^2/a^2)^\alpha.$$

The current profile does not depend explicitly on the profiles of $T_i(\rho)$ and $n(\rho)$; therefore, the details of these profiles are inessential. As an example, we choose the following plasma parameters: $R = 5$ m, $a_m = 1$ m, $A = R/a_m = 5$, $B_0 = 2.8$ T, $k = 1$, and $\delta = 0$.

Solving the Grad–Shafranov equation, we find the equilibrium, the function $\mu(\rho)$, and the impedances $X$ and $Y$ [see expressions (35) and (41)]. The dependence of the impedance $Y$ on the power exponent $\alpha$ for $T_{ea} =$
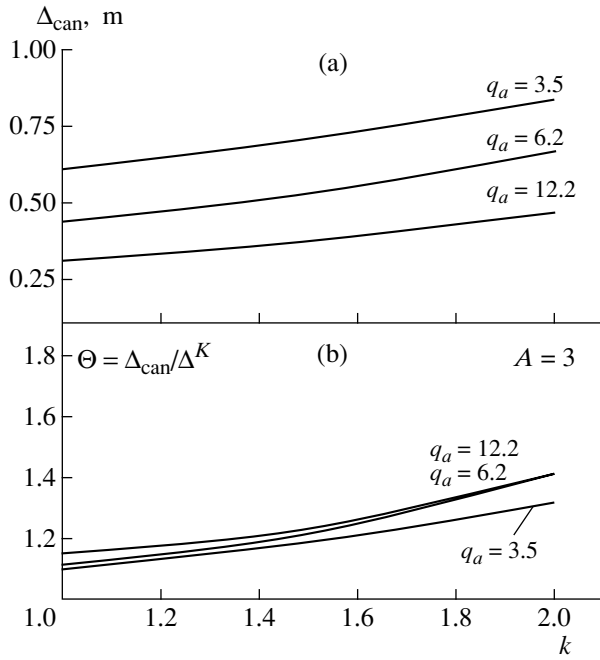
**Fig. 5.** Same as in Fig. 4, but as functions of the elongation $k$ for $A = 3$, $\delta = 0.3$, and different values of $q_a$.
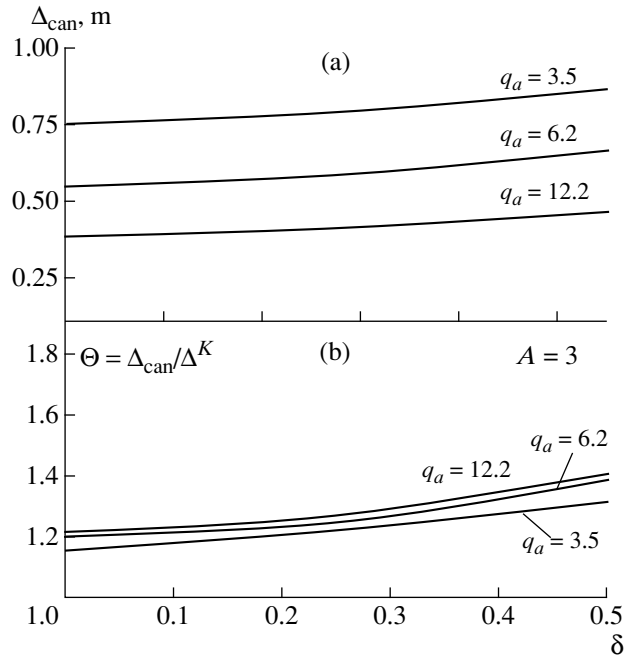


**Fig. 6.** Same as in Fig. 4, but as functions of the triangularity $\delta$ for $A = 3$, $k = 1.6$, and different values of $q_a$.

40 eV is shown in Fig. 7. The value of this impedance for the Kadomtsev profile ($Y^K = \mu_a/\mu_0 = 0.26$) is also shown. We can see that, for $\alpha > 1.45$, inequality (50) is satisfied; hence, in the transport model with canonical profiles, we should change soft boundary conditions to stiff ones.

Figure 8 shows the transformation of the shape of the canonical profiles. We can see here the canonical profile $\mu_c(\rho)$ for stiff boundary conditions (44) with $\alpha = 1.25$, 1.5, 1.75, and 2.0, keeping other plasma parameters fixed. For comparison, we show here the canonical profile $\mu_c^{soft}(\rho)$ obtained with soft boundary conditions (38) (this profile is almost independent of $\alpha$) and the profile $\mu(\rho)$ of the initial transport problem. We can see that, as $\alpha$ increases and the impedance $Y$ approaches the critical value $Y^K$, the profile $\mu_c(\rho)$ begins to peak. However, if we take into account sawtooth oscillations, the $\mu_c^{eff}(\rho)$ profile for $\alpha < 1.25$ remains close to the $\mu_c^{soft}(\rho)$ profile. As $\alpha$ increases further and $Y$ decreases, condition (50) is satisfied and the $\mu_c(\rho)$ profile peaks dramatically. In this case, even a flatter $\mu_c^{eff}(\rho)$ profile (with a plateau at $\rho < \rho_s$) becomes more peaked than $\mu_c^{soft}(\rho)$. In transport models with canonical profiles, such a change leads to a substantial decrease in the effective transport coefficients and an increase in the temperature in the region where $\mu_c^{eff}(\rho) > \mu_c^{soft}(\rho)$.

## 6. CANONICAL PROFILES AND TRANSPORT MODELS

In transport models, the canonical profiles determine the critical gradients above which the heat and particle fluxes substantially increase; however, expres-
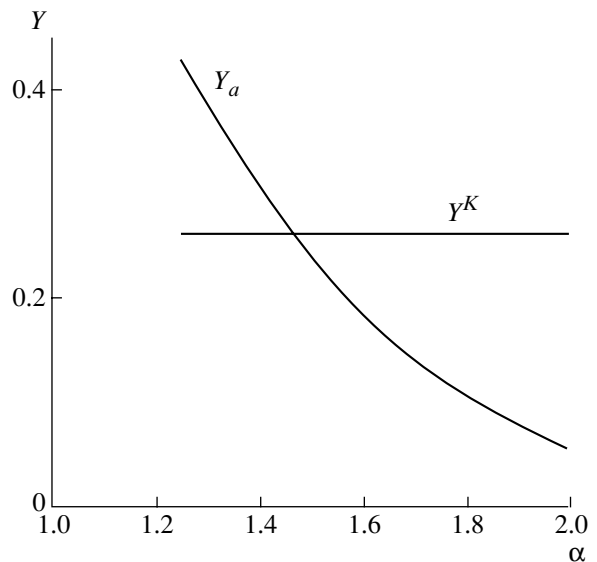


**Fig. 7.** Second-order impedance $Y_a$ as a function of the power exponent $\alpha$ of the model temperature profile $T_e(\rho) = T_{ea} + T_0(1 - \rho^2/a^2)^{\alpha}$ for $A = 5$, $k = 1$, $\delta = 0$, $T_{ea} = 40$ eV, and $T_0 = 1$ keV. The horizontal line shows the impedance for the Kadomtsev canonical profile, $Y^K = \mu_a/\mu_0$.
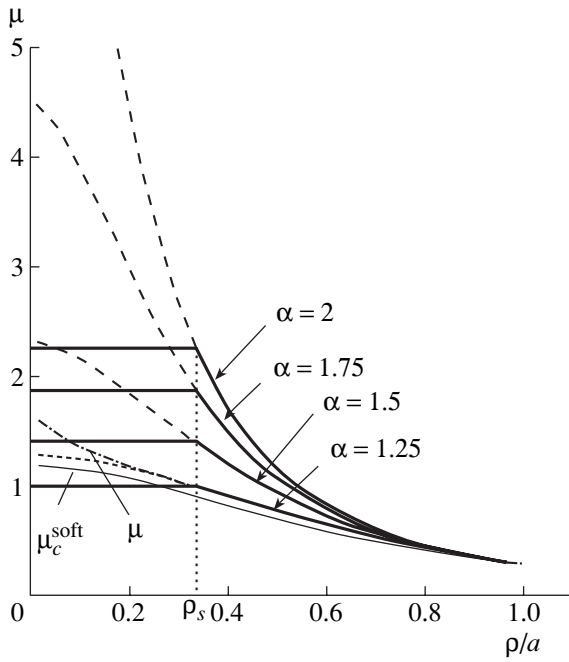
**Fig. 8.** Canonical profiles for different power exponents of the model temperature profile $\alpha$ (the other parameters are the same as in Fig. 7). For comparison, the canonical profile $\mu_c^{\text{soft}}$ for soft boundary condition and the initial $\mu$ profile, determining the plasma geometry and the position of the resonant surface $\mu = 1$, are also shown.
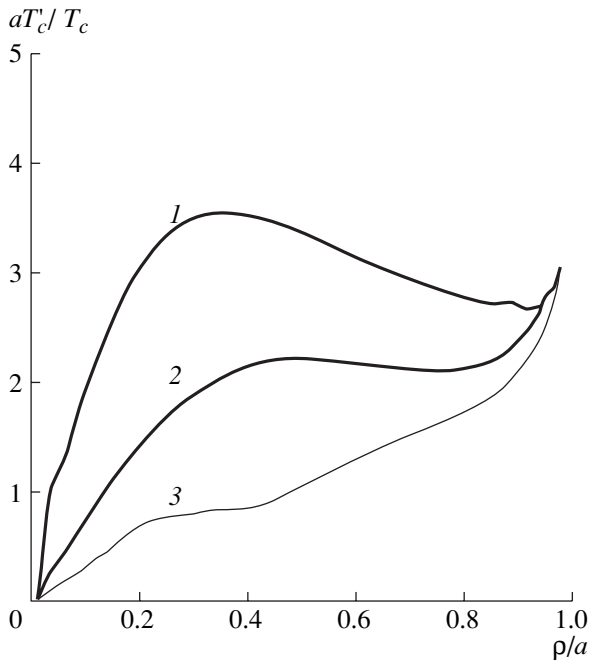


**Fig. 9.** Profiles of the critical dimensionless temperature gradient $aT_c'/T_c$ for $q_a = 7$ and three sets of the plasma parameters: (*1*) $A = 5$, $k = 1$, and $\delta = 0$; (*2*) $A = 3$, $k = 1.6$, and $\delta = 0.3$; and (*3*) $A = 1.5$, $k = 1.6$, and $\delta = 0.3$.

sions for these fluxes are not defined unambiguously. In [14–17], the simplest linear model was considered. For example, the heat flux was described as

$$Q = -n\kappa T(T'/T - T_c'/T_c) + Q_1, \qquad (55)$$

where $T_c$ is the canonical profile for the temperature, $Q_1$ is the heat flux that is not related to the canonical profile, the prime stands for the derivative with respect to $\rho$, $\kappa$ is the stiffness of the profile (which is proportional to $T^{1/2}$), $n$ is the plasma density, and the logarithmic derivative of the canonical temperature profile plays the role of a critical gradient. Flux (55) explicitly contains the thermal pinch effect. To avoid this pinch, many authors [9–11] use the following strongly nonlinear expression for the heat flux:

$$Q = -n\chi T' + Q_1, \qquad (56)$$

where

$$\chi = \zeta\kappa T^{\alpha}(-(T'/T - T_c'/T_c))^{\alpha} \\ \times H(-(T'/T - T_c'/T_c)), \qquad (57)$$

$\zeta$ is a dimensional factor, $\alpha \sim 1$, and $H(x)$ is the Heaviside step function ($H(x) = 1$ for $x > 0$ and $H(x) = 0$ for $x < 0$). There are still no reliable experimental data allowing us to choose between models (55) and (56).

If we know the canonical profile $\mu(\rho)$, we can create the canonical profile for the temperature $T_c(\rho)$ using the following arguments. In a relaxed quasi-steady state, the profiles of the current and electron temperature are close to the canonical profiles

$$j_\varphi(\rho) \approx j_c(\rho), \quad T_e(\rho) \approx T_c(\rho). \qquad (58)$$

At the same time, the $j_\varphi(\rho)$ and $T_e(\rho)$ profiles are related to each other by Ohm's law:

$$j_\varphi(\rho) \sim T_e^{3/2}(\rho). \qquad (59)$$

By virtue of the consistency of profile (6) and profiles (58) and (59), we have

$$p_c(\rho) = n_c(\rho)T_c(\rho) \sim j_c(\rho) \sim T_e^{3/2} \sim T_c^{3/2}; \qquad (60)$$

hence,

$$T_c \sim j_c^{2/3}, \quad n_c \sim T_c^{1/2} \sim j_c^{1/3}, \qquad (61)$$

and the dimensionless relative critical gradients of the temperature and density are determined by the following expressions:

$$aT_c'/T_c = 2/3\Omega_j, \quad an_c'/n_c = 1/3\Omega_j, \qquad (62)$$

where

$$\Omega_j = aj_c'/j_c, \quad \Omega_\mu = a\mu_c'/\mu_c \qquad (63)$$

are the dimensionless logarithmic derivatives of the canonical profiles. Later, we will refer to expressions (62) and (63) as basic formulas.

The profiles of the critical temperature gradient $aT_c'/T_c$ calculated from basic formulas (62) and (63) for three sets of plasma parameters ($A = 1.5$, $k = 1.6$, and $\delta = 0.3$; $A = 3$, $k = 1.6$, and $\delta = 0.3$; and $A = 5$, $k = 1$, and $\delta = 0$ at $q_a = 7$) are shown in Fig. 9. It is seen that inside the gradient region ($0.3 < \rho/a < 0.7$) the value of $aT_c'/T_c$ changes only slightly. The experimental gradients of the electron temperature in several tokamaks show a similar behavior [11]. However, the absolute values of $aT_c'/T_c$ depend on the plasma parameters.

Figure 10 shows the dependence of the $aT_c'/T_c$ value at the point $\rho/a = 0.5$ on the parameters $q_a$ for $k = 1.6$, $\delta = 0.3$, and two values of the aspect ratio ($A = 1.5$ and 3). It is seen that the critical gradient increases with increasing $q_a$ and $A$. This leads to an increase in the peakedness of the temperature profiles calculated by the transport model.

The structure of the full model describing the transport processes in tokamaks is shown in Fig. 11. The model consists of three parts. The first part is a proper transport model determining the electron and ion temperatures $T_e$ and $T_i$, the plasma density $n$, the function $\mu$, and the current density $j$. These data are used in the second part to solve the Grad–Shafranov equation and to find the magnetic surface geometry, the natural coordinate $\rho$, and the metric coefficients $V'$ and $G$. Finally, in the third part, the functions $\mu_c$ and $j_c$ and the critical gradients $T_c'/T_c$ are found by solving Eq. (31). In our previous papers, it was assumed that the critical gradients were the same for the electrons and ions.

Besides formulas (62), other forms of critical gradients are possible. For example, for the Kadomtsev problem [3], we have

$$j_c^K \sim (\mu_c^K)^2, \tag{64}$$

therefore,

$$\Omega_j^K \equiv a(j_c^K)'/j_c^K = 2a(\mu_c^K)'/\mu_c^K \equiv 2\Omega_\mu^K, \tag{65}$$

and, in the right-hand side of Eq. (62) we can use $2\Omega_\mu^K$ instead of $\Omega_j^K$. In the general case of a toroidal plasma, equality (64) is not strictly satisfied. Figure 12a shows the profiles of $(j_c/j_c(0))^{2/3}$ and $(\mu_c/\mu_0)^{4/3}$ for the parameters $A = 3$, $k = 1.6$, and $\delta = 0.3$ at $q_a \sim 7$. Here, the exponential power for the current is chosen in accordance with expressions (61). It is seen that the $j_c^{2/3}$ profile is slightly broader than the $\mu_c^{4/3}$ profile. Figure 12b shows the profiles of $\Omega_j$ and $2\Omega_\mu$ for the same geometric factors. We see that almost over the entire radius, the values of $\Omega_j$ and $2\Omega_\mu$ are close to each other. Substituting $2\Omega_\mu$ instead of $\Omega_j$ in formulas (62), we obtain

$$aT_c'/T_c = 4/3\Omega_\mu, \quad an_c'/n_c = 2/3\Omega_\mu \quad (A > 2.5). \tag{66}$$
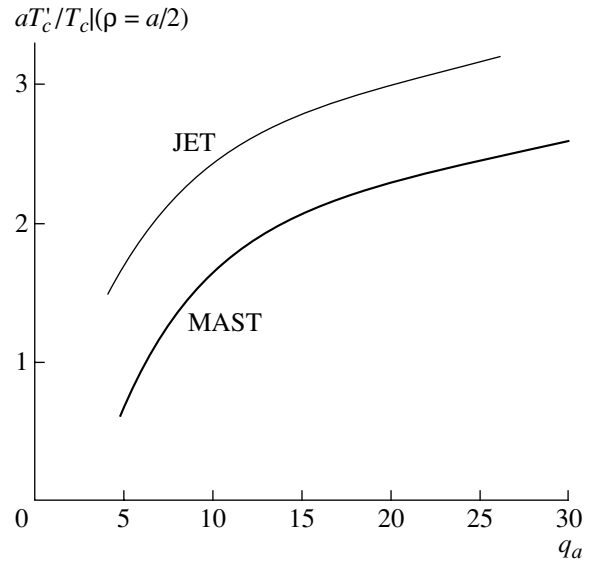
$aT_c'/T_c|(\rho = a/2)$

**Fig. 10.** The critical gradient $aT_c'/T_c$ at $\rho = a/2$ as a function of the edge safety factor $q_a$ for $k = 1.6$, $\delta = 0.3$, and two aspect ratios $A = 3$ (JET) and $A = 1.5$ (MAST).
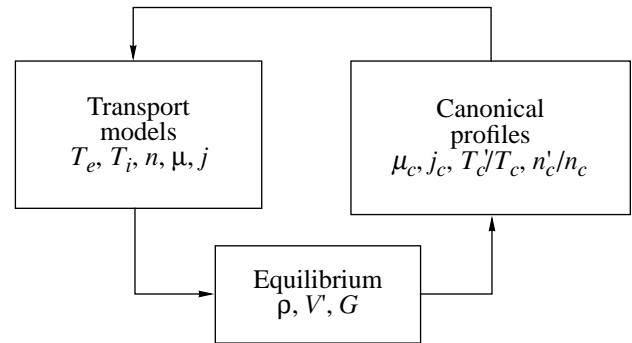
**Fig. 11.** The flow chart of the CPTM.

At smaller values of $A$, the difference between $\Omega_j$ and $2\Omega_\mu$ rapidly increases; therefore, formulas (66) are valid only for $A > 2.5$. For smaller aspect ratios, we should use basic formulas (62).

In [14], it was supposed that the Kadomtsev canonical profiles $\mu_c^K(\rho)$ can be used in Eq. (66) because the canonical profiles for toroidal plasmas were unknown. However, this supposition resulted in the calculated temperature profiles that were more peaked than the experimental ones [15]. Therefore, in [15–17], it was proposed to use, instead of Eq. (66), a slightly corrected formula for the critical gradients

$$aT_c'/T_c = \Omega_\mu^K, \quad an_c'/n_c = 1/2\Omega_\mu^K. \tag{67}$$
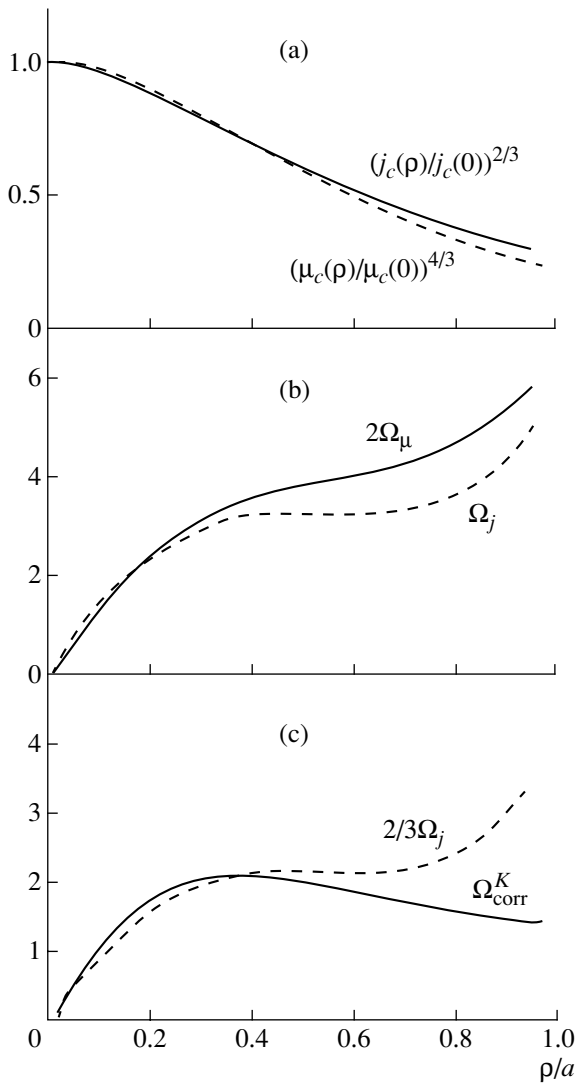
**Fig. 12.** Profiles of (a) $(j_c/j_c(0))^{2/3}$ and $(\mu_c/\mu_0)^{4/3}$, (b) the gradients $\Omega_j$ and $2\Omega_\mu$, and (c) the "true" critical temperature gradient $2/3\Omega_j$ and the "corrected" Kadomtsev critical temperature gradient $\Omega_\mu^K$ from our previous transport models for $A = 3$, $k = 1.6$, $\delta = 0.3$, and $q_a \sim 7$.

Now, knowing the canonical profiles for toroidal plasmas, we may estimate the validity of expressions (67) by comparing them with basic formulas (62). Figure 12c shows the profiles of the parameters $(2/3)\Omega_j$ and $\Omega_\mu^K$ entering into the right-hand sides of Eqs. (62) and (67). They are rather close to each other in the gradient zone ($\rho/a < 0.7$). Note that the difference at the edge has a weak effect on fluxes (55) and (56). Hence, an intuitive-empirical choice of Eqs. (67) for the temperature in [15] is confirmed by the theoretical account of the toroidal effects investigated in the presented paper. Apparently, an inverse statement is also valid. As far as the transport model with Eqs. (67) reasonably describes the

experimental temperature profiles [15–17], the model with basic formulas (62) should give the same results. However, one needs to verify this conclusion by comparing the calculated results with the experiments in tokamaks with different aspect ratios.

Now we discuss when the conditions of the profile consistency (6) may be violated. The last of conditions (6) does not take into account that the boundary values of functions $p(\mu)$ and $j_\varphi(\mu)$ are not self-consistent. Therefore, it would be more logical to use the conditions of profile consistency in the form proposed in [8]:

$$(j_\varphi(\mu)/j_\varphi(\mu_0))' = (p(\mu)/p(\mu_0))'. \tag{68}$$

The profiles of $j_\varphi(\mu)$ and $p(\mu)$ defined by Eqs. (6) and (68) differ by a constant that is important only near the plasma boundary. Therefore, the critical gradients calculated by Eq. (6) or (68) will be different only in this region. As was mentioned above, transport fluxes (55) or (56) change slightly in this case.

Finally, we will comments the application of the canonical profiles theory to spherical tokamaks. In modern spherical tokamaks, the discharge duration is not long and the steady state is not established. Moreover, the current profile is distorted by sawtooth oscillations. As a result, the validity of profile consistency conditions (6) for spherical tokamaks is not yet confirmed. It is not clear whether Ohm's law can be used to separate out the canonical profiles of the temperature and density when the canonical profile for the pressure is determined. The point is that, at $A \sim 1.5$–2, the fraction of trapped particles dramatically increases. It is widely assumed that the trapped particles do not contribute to the current and, thus, to the plasma conductivity. In this case, Ohm's law has the form

$$j = \sigma^{\text{neo}}E, \quad \sigma^{\text{neo}} = \sigma^{\text{Sp}}f, \tag{69}$$

where $\sigma^{\text{Sp}}$ is the Spitzer conductivity, which is proportional to $T_e^{3/2}/Z_{\text{eff}}$, and $f = f(\varepsilon, \nu_e^*, Z_{\text{eff}})$ is a rapidly decreasing function of the radius $\rho$, which is equal to unity at $\rho = 0$ and has a minimum at $\rho \sim 0.85a$. For typical experiments in START [17], the minimum value of $f$ is about 1/6. Hence, the current density should be strongly peaked in the steady state. As a result, formulas (59)–(61), which relate the steady-state current density and the electron temperature, may fail. Our experience of the transport model application to spherical tokamaks [17] shows that the canonical pressure profile determined by Eq. (31) is apparently rather reliable. However, one should take care when using Ohm's law to separate the canonical profiles of the temperature and pressure. Moreover, such a separation may be nonunique and may depend on some discharge parameters that are still unknown.

## 7. CONCLUSION

In this paper, we have solved the problem of the canonical profiles for a tokamak plasma with an arbitrary cross section. The canonical profiles are treated as an ultimate state to which the plasma relaxes. The solution is based on the principle of the free energy minimum with the constraint that the total current is conserved and the relaxed profiles of the pressure and current density are self-similar (the profile self-consistency). We have constructed a differential Euler equation for the canonical profile of the $\mu$ function and have discussed the possible boundary conditions. Two types of boundary conditions (soft and stiff conditions) have been discussed. The soft conditions correspond to the absence of strong action on the plasma boundary. They are analogous to the Kadomtsev conditions stated at infinity for a circular cylindrical plasma. Under strong action on the plasma boundary, we should use stiff conditions describing the close relation between the real and canonical profiles in the edge region.

The obtained canonical profiles allow us to calculate the critical temperature and pressure gradients and to construct a transport model. Calculations have shown that, as the aspect ratio decreases, the canonical profiles become flatter. The same effect takes place when the elongation of the cross section increases. The canonical profiles become more peaked with increasing parameter $q_a$. Similar tendencies for the real profiles of the electron temperature were pointed out in our previous papers where we analyzed experiments in JET and START.

Note that our interpretation of the profile consistency assumes that the real profiles of the ion and electron temperatures differ from their canonical profiles. The heat fluxes are proportional to the distances between the real and canonical profiles in a certain metrics defined through the critical gradients. In this sense, our approach is equivalent to a traditional approach in which the fluxes are described through the critical gradients. The difference is that the CPTM proposes an algorithm for finding the critical gradients, whereas in traditional models, the critical gradients should be found by independent methods based on additional assumptions.

## ACKNOWLEDGMENTS

## REFERENCES

1. B. Coppi, Comm. Plasma Phys. Control. Fusion **5**, 261 (1980).

2. J. B. Taylor, Phys. Rev. Lett. **33**, 1139 (1974).

3. B. B. Kadomtsev, Fiz. Plazmy **13**, 443 (1987) [Sov. J. Plasma Phys. **13**, 443 (1987)].

4. D. Biskamp, Comm. Plasma Phys. Control. Fusion **10**, 165 (1986).

5. J. Y. Hsu and M. S. Chu, Phys. Fluids **30**, 1221 (1987).

6. B. B. Kadomtsev, Plasma Phys. Controlled Fusion **34**, 1931 (1992).

7. J. B. Taylor, Phys. Fluids B **5**, 4378 (1993).

8. E. Minardi, Phys. Lett. A **240**, 70 (1998).

9. M. Kotschenreuther, W. Dorland, G. W. Hammet, and M. A. Beer, Phys. Plasmas **2**, 2381 (1995).

10. F. Jenko, W. Dorland, M. Kotschenreuther, and B. N. Rogers, Phys. Plasmas **7**, 1904 (2000).

11. F. Ryter, C. Angioni, M. Beurskens, *et al.*, in *Proceedings of the 28th EPS Conference on Controlled Fusion and Plasma Physics, Madeira, 2001*, Plasma Phys. Controlled Fusion **43**, A323 (2001).

12. K. W. Gentle, W. L. Rowan, R. V. Bravenec, *et al.*, Phys. Rev. Lett. **74**, 3620 (1995).

13. Yu. N. Dnestrovskij, S. V. Cherkasov, S. E. Lysenko, *et al.*, Nucl. Fusion **38**, 373 (1998).

14. Yu. N. Dnestrovskij and G. V. Pereverzev, Plasma Phys. Controlled Fusion **30**, 47 (1988).

15. Yu. N. Dnestrovskij, E. L. Berezovskij, S. E. Lysenko, *et al.*, Nucl. Fusion **31**, 1877 (1991).

16. Yu. N. Dnestrovskiĭ, Yu. V. Esipchuk, N. A. Kirneva, *et al.*, Fiz. Plazmy **23**, 614 (1997) [Plasma Phys. Rep. **23**, 566 (1997)].

17. Yu. N. Dnestrovskiĭ, M. P. Gryaznevich, A. Yu. Dnestrovskiĭ, *et al.*, Fiz. Plazmy **26**, 579 (2000) [Plasma Phys. Rep. **26**, 539 (2000)].

18. Yu. N. Dnestrovskij, S. V. Cherkasov, S. E. Lysenko, *et al.*, in *Proceedings of the 26th EPS Conference on Controlled Fusion and Plasma Physics, Maastricht, 1999*, Rep. P2.065.

19. M. W. Kissik, J. D. Callen, E. D. Fredrickson, *et al.*, Nucl. Fusion **36**, 1691 (1996).

20. R. De Angelis, N. Deliyanakis, F. De Luca, *et al.*, in *Proceedings of the 22nd EPS Conference on Controlled Fusion and Plasma Physics, Bournemouth, 1995*, ECA, Vol. 19C, Part I, p. 53.

21. G. V. Pereverzev and P. N. Yushmanov, *ASTRA: an Automatic System for Transport Analysis in a Tokamak* (Max-Planck Institute, Garching, 2002), IPP 5/98.

*Translated by the authors*

## PLASMA
## DIAGNOSTICS

# Two-Wire Microwave Resonator Probe

## I. G. Kondrat'ev, A. V. Kostrov, A. I. Smirnov, A. V. Strikovskiĭ, and A. V. Shashurin

*Institute of Applied Physics, Russian Academy of Sciences, ul. Ul'yanova 46, Nizhni Novgorod, 603600 Russia*

Received April 17, 2002

**Abstract**—Results are presented from theoretical and experimental studies of the influence of ponderomotive effects on the operation of a two-wire plasma microwave resonator probe. It is shown that the nonlinear regime of probe operation can be used to measure not only the plasma density, but also the plasma temperature. © 2002 MAIK "Nauka/Interperiodica".

## 1. INTRODUCTION

Highly sensitive resonator probes are successfully used to diagnose various natural and artificial media, including plasma. In such measurements, most of the information is derived from the modification of the probe resonance curve, first of all, its displacement and broadening. It is usually required that the probe introduce minimal perturbations into the ambient medium; however, an analysis of these perturbations can also provide additional information about the properties of an object under study.

In this paper, we consider a two-wire plasma microwave resonator probe.[1] Such probes are frequently used to measure the charged particle density in both isotropic and magnetoactive plasmas [2, 3]. The probe operation is based on the dependence of the resonance frequency on the permittivity of a medium filling the space between the wires of a double line. The probe is usually employed in a transparent plasma at frequencies substantially exceeding the critical frequency for a given plasma density. For simplicity, in calculations, it is usually assumed that the plasma is uniform over the resonator segment of the double line.

A characteristic feature of the microwave probe under consideration is a relatively low threshold for nonlinear effects. In a weakly collisional plasma, these effects are mainly of a ponderomotive nature. Under the action of the electromagnetic field, the plasma is pushed away from the resonator wires, thereby substantially affecting the resonance characteristics of the probe [4]. In the present paper, it is shown that the nonlinear regime of probe operation can be successfully used to diagnose plasmas, in particular, to measure the electron temperature. The paper is organized as follows. In Section 2, a theory of a nonlinear two-wire microwave probe is developed, and, in Section 3, we discuss the experimental results and compare them with the results of theoretical calculations.

---

[1] Note that the resonant properties of this probe are not related to the plasma resonance [1].

## 2. THEORY OF A MICROWAVE RESONATOR PROBE

Figure 1 shows a schematic of the microwave resonator probe used in [2, 3] and in the experiments described below. Two identical coaxial cables are ended with magnetic-coupling loops; the shorted end of the double line of length $\ell$ is placed symmetrically between the loops. On the other side, the line is open. The distance $d$ between the wires substantially exceeds the wire radius $a$ ($a/d \ll 1$) and coincides with the diameter of the coupling loops.

The inductive reactance of the coupling loops, $\omega L_c/c^2$, is negligibly small as compared to the impedance of the coaxial cables, $\rho_c$. The coefficients of mutual induction between the coupling loops ($M_{2,3}$) and between the coupling loops and the double line ($M_{2,1}$ and $M_{3,1}$) are close to $L_c$. It is assumed that $M_{2,1} = M_{3,1} = M$ and that the impedance $\rho$ of the double line is on the order of $\rho_c$. It follows from here that

$$\frac{1}{c^2}\omega L_c \ll \rho_c, \quad \frac{1}{c^2}\omega M \ll \rho. \qquad (1)$$

If a probing wave with the current amplitude $I_0$ and voltage $U_0 = \rho_c I_0$ is excited in cable *2*, then, in the nonresonant regime, this wave reflects from the cable end as from a load with an almost zero resistance. In this case, the current $I_2$ in coupling loop *2* is close to $2I_0$, whereas the current $I_3$ in loop *3* and the current $I_1$ in the
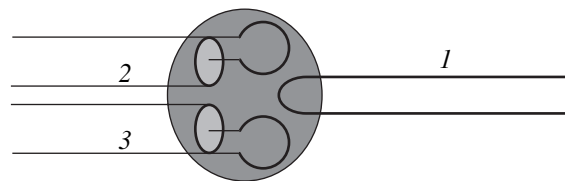


**Fig. 1.** (*1*) Quarter-wave resonator and (*2*) exciting and (*3*) receiving lines.

shorted double-line segment are negligibly low ($|I_1|$, $|I_3| \ll |I_0|$). On the other hand, under resonance conditions, when the segment $\ell$ matches a quarter of the wave propagating through a long line, the current $I_1$ can attain a fairly high value and its influence on the currents $I_2$ and $I_3$ cannot be ignored. Writing the emf induced in cables *2* and *3* as $-\dfrac{i}{c^2}\omega M I_1$, we obtain the following expressions for $I_2$ and $I_3$:

$$I_2 = 2I_0 - \frac{i}{c^2 \rho_c}\omega M I_1, \quad I_3 = -\frac{i}{c^2 \rho_c}\omega M I_1. \quad (2)$$

The current $I(z)$ and the voltage $U(z)$ in long line *1* (the $z$ coordinate is counted from the shorted end) satisfy the telegraph equations

$$\frac{dU}{dz} = -\frac{i}{c^2}\omega \tilde{L}I + E\delta(z+0),$$

$$\frac{dI}{dz} = -i\omega \tilde{C}U \quad (3)$$

with the boundary conditions

$$U(0) = 0, \quad I(z = \ell) = 0, \quad (4)$$

where $\tilde{L}$ and $\tilde{C}$ are the inductance and capacitance per unit length of line *1*, $E = -\dfrac{i}{c^2}\omega M(I_2 + I_3)$ is the mutual-induction emf at the shorted end ($z = 0$), $\delta(z+0)$ is the delta function ($\int_0^\ell \delta(z+0)dz = 1$), and $I_1 = I(0)$.

Plasma diagnostics commonly use frequencies $\omega$ substantially exceeding the electron plasma frequency $\omega_{pe}$ and the electron gyrofrequency $\omega_{He}$. In this case, the electrodynamic characteristics of the plasma differ only slightly from those in a vacuum. As a result, it may be assumed that $\tilde{L} = \tilde{L}_0 \approx 4\ln(d/a)$, and $\tilde{C} = \tilde{C}_0(1 + \delta C)$, where $\tilde{C}_0 \approx \dfrac{1}{4\ln(d/a)}$, $|\delta C| \ll 1$, and $\tilde{L}_0$ and $\tilde{C}_0$ are the inductance and capacitance per unit length of line *1* in a vacuum ($\tilde{L}_0 \tilde{C}_0 = 1$). In nonlinear media, $\delta C$ is determined by the field in the line and smoothly (on the length $d$) varies with the $z$ coordinate.

At frequencies $\omega$ close to the vacuum resonance frequency $\omega_0 = \dfrac{\pi c}{2\ell}$ ($\omega = \omega_0 + \Delta\omega$, $\omega_0 \gg |\Delta\omega|$), the solution to problem (3) and (4) can be sought as an asymptotic expansion in a small parameter

$$\nu \sim \max\left\{\frac{|\Delta\omega|}{\omega_0}, |\delta C|, \left(\frac{\omega M}{c^2 \rho}\right)^2, \left(\frac{\omega M}{c^2 \rho_c}\right)^2, \left|\frac{I_0}{I_1}\right|\right\} \ll 1. \quad (5)$$

We can write

$$I = I^{(0)} + I^{(1)} + \dots, \quad U = U^{(0)} + U^{(1)} + \dots, \quad (6)$$

where $I^{(j)}$ and $U^{(j)}$ are the $\nu^j$ terms of the asymptotic expansions for the current and voltage in powers of $\nu$. Substituting expressions (6) into Eqs. (3) and taking into account boundary conditions (4), in the zeroth order of $\nu$, we have

$$I^{(0)} = \bar{I}\cos\left(\frac{\pi z}{2\ell}\right), \quad U^{(0)} = \bar{U}\sin\left(\frac{\pi z}{2\ell}\right),$$

$$\left(\bar{U} = -i\rho\bar{I}, \rho = \frac{1}{c}\sqrt{\frac{\tilde{L}_0}{\tilde{C}_0}}\right). \quad (7)$$

In the first order of $\nu$, we obtain the following equation for $I^{(1)}$:

$$\frac{d^2}{dz^2}I^{(1)} + \left(\frac{\omega_0}{c}\right)^2 I^{(1)} = F_1(z), \quad (8)$$

where

$$F_1 = -\bar{I}\left[2\frac{\omega_0^2}{c^2}\delta\omega\cos\left(\frac{\pi z}{2\ell}\right) + \frac{\omega_0}{c}\frac{d}{dz}\left(\delta C \sin\left(\frac{\pi z}{2\ell}\right)\right)\right.$$

$$\left. - 2i\frac{\omega_0}{c}\alpha\alpha_c\delta(z)\right] - 2\frac{\omega_0}{c}\alpha I_0\delta(z)$$

with the boundary conditions

$$\frac{d}{dz}I^{(1)}(z = 0) = 0, \quad I^{(1)}(z = \ell) = 0.$$

Here, $\delta\omega = \dfrac{\Delta\omega}{\omega_0}$, $\alpha = \dfrac{\omega_0 M}{c^2 \rho}$, and $\alpha_c = \dfrac{\omega_0 M}{c^2 \rho_c}$ are the small parameters of the problem.

According to the Fredholm theorem of an alternative, boundary problem (8) has a solution if the right-hand side of $F_1(z)$ is "orthogonal" to the eigensolution of the homogeneous equation, i.e., when

$$\int_0^\ell F_1(z)\cos\left(\frac{\pi z}{2\ell}\right)dz = 0. \quad (9)$$

Substituting $F_1(z)$ into Eq. (9) and integrating over $z$, we obtain

$$\frac{\bar{I}}{I_0} = \frac{\frac{4}{\pi}a}{-\delta\omega - q + i\frac{4}{\pi}\alpha\alpha_c}, \quad (10a)$$

with the parameter

$$q = \frac{1}{\ell}\int_0^\ell \delta C \sin^2\left(\frac{\pi z}{2\ell}\right)dz. \quad (10b)$$

If the microwave probe is in a vacuum and $\delta C = 0$, then, at the frequency $\omega = \omega_0$ ($\delta\omega = 0$), coaxial cable *2*

is matched with coaxial cable *3*, accurate to terms on the order of $\nu$. In this case, the current amplitudes in coupling loops *2* and *3* are equal to the current $I_0$ ($I_2 = -I_3 = I_0$), the microwave power from coaxial cable *2* is completely transmitted into coaxial *3*, and the quantity $|\bar{I}|^2$ reaches its maximum:

$$\max\left|\frac{\bar{I}}{I_0}\right|^2 = \frac{1}{\alpha_c^2} = \frac{8}{\pi}\frac{\rho_c}{\rho}Q_0, \quad Q_0 = \frac{\pi}{8}\frac{1}{\alpha\alpha_c}, \qquad (11)$$

where $Q_0$ is the vacuum resonance Q-factor, which is almost completely determined by the coupling between the resonator and coaxial cables *2* and *3* (the label "0" stands for $\delta C = 0$).

In the presence of a plasma, the current amplitude in the line [see formula (10)] depends not only on $Q_0$, but also on the parameter $q$. We introduce a transmission factor $\beta = \dfrac{|I_3|^2}{|I_0|^2}$; then, using relationships (2), (7), (10), and (11), it is easy to find that

$$\beta = \frac{1}{\frac{1}{4}Q_0^2(\delta\omega + \mathrm{Re}\,q)^2 + \left(1 + \frac{1}{2}Q_0\,\mathrm{Im}\,q\right)^2}. \qquad (12)$$

It can be seen from expression (12) that the real part of the parameter $q$ determines the frequency shift $\delta\omega_m$ of the maximum of the resonance curve $\beta(\delta\omega)$, whereas the imaginary part of $q$ gives the value of this maximum:

$$\delta\omega_m = -\mathrm{Re}\,q, \quad \max\beta = \frac{1}{\left(1 + \frac{1}{2}Q_0\,\mathrm{Im}\,q\right)^2}. \qquad (13)$$

As an example, we consider the case of a collisionless plasma, assuming its permittivity to be

$$\varepsilon = 1 - \frac{N}{N_c}, \quad N_c = \frac{\omega^2 m_e}{4\pi e^2}, \qquad (14)$$

where $N$ is the plasma density, $m_e$ is the electron mass, and $e$ is the electron charge.

Under steady-state conditions, the ponderomotive effect can be described by the following dependence of the plasma density on the electric field strength $\mathbf{E}\exp(i\omega t)$ [5]:

$$N = N_0\exp\left(-\frac{|\mathbf{E}|^2}{E_c^2}\right), \qquad (15)$$

where $E_c = \left(\dfrac{4(T_e + T_i)m_e\omega^2}{e^2}\right)^{1/2}$ is the characteristic ponderomotive field and $T_e$ and $T_i$ are the electron and ion temperatures, respectively.

We have chosen the probing frequency such that the inequality $N/N_c \ll 1$ holds. Hence, when calculating the perturbation of the capacitance per unit length $\delta C$ in expression (15) accurate to terms linear in $N/N_c$, we can assume that the spatial distribution of the field $\mathbf{E}$ is the same as in a vacuum. As a result, we find

$$\delta C \approx -\frac{1}{\ln(d/a)}\frac{N_0}{N_c}\int_1^{d/a}\frac{1}{s}\exp\left(-\frac{g}{s}\sin^2\frac{\pi}{2}\frac{z}{\ell}\right)ds, \qquad (16)$$

where $g = \dfrac{E_a^2}{E_c^2} = \dfrac{|\bar{I}|^2}{I_c^2}$, $E_a\left|\sin\dfrac{\pi}{2}\dfrac{z}{\ell}\right|$ is the magnitude of the electric field strength on the wire surfaces in line *1*, $\bar{I}$ is the amplitude of the microwave current in resonator *1*, and $I_c = \dfrac{ca}{2}E_c$ is the critical value of $\bar{I}$ at which the ponderomotive effects come into play. The parameter $g$ can be expressed through the transmission factor $\beta(\delta\omega)$:

$$g = g_m\beta(\delta\omega), \quad g_m = \frac{I_0^2}{\alpha_c^2 I_c^2}. \qquad (17)$$

In this case, according to (10b), we have

$$q \approx -\frac{1}{\ln(d/a)}\frac{N_0}{N_c}\frac{1}{\ell}\int_0^{\ell}\sin^2\left(\frac{\pi}{2}\frac{z}{\ell}\right)dz$$
$$\times \int_1^{d/a}\frac{1}{s}\exp\left(-\frac{g_m}{s}\beta(\delta\omega)\sin^2\frac{\pi}{2}\frac{z}{\ell}\right)ds. \qquad (18)$$

In the linear regime, which is characterized by a small value of the parameter $g_m$ ($g_m \ll 1$), we have $N \approx N_0$ and expression (18) takes the form $q \approx -\dfrac{1}{2}\dfrac{N_0}{N_c}$. In this case, the resonance curve $\beta(\omega)$ is the same as in a vacuum, but the curve itself shifts as a whole along the frequency axis by the value

$$\Delta\omega_m \approx \frac{1}{2}\frac{N_0}{N_c}\omega_0. \qquad (19)$$

Relationship (19) relates the value of the unperturbed plasma density $N_0$ and $\Delta\omega_m$.

Nonlinear properties of the microwave resonator, including hysteresis effects, manifest themselves when $g_m > 1$. Figure 2 shows the resonance curves $\beta(\delta\omega)$ calculated for a line with $d/a = 20$ in a plasma with a density satisfying the values (a) $n = \dfrac{Q_0}{4}\dfrac{N_0}{N_c} = 50$ and (b) $n = 100$ for different values of the parameter $g_m = 0.1, 1, 10, 50,$ and $400$ (curves *1–5*, respectively). For $g_m = 0.1$, we have the linear regime. For $g_m \geq 1$, the resonance curve is substantially modified. At the segments of the resonance curve between the "jump" points (at which
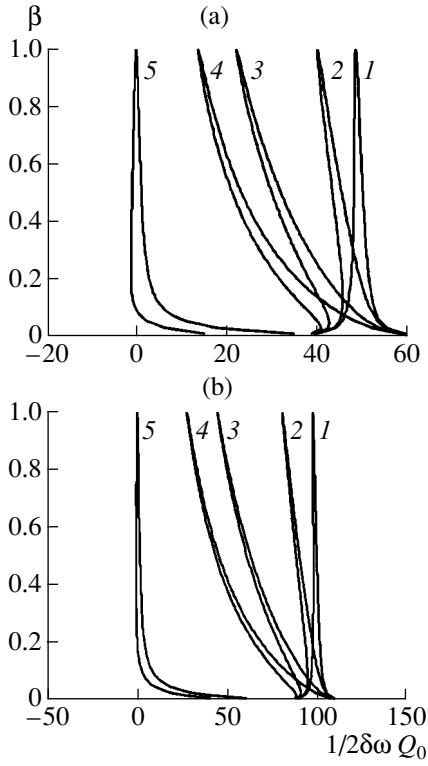
**Fig. 2.** Resonance curves $\beta(\delta\omega)$ calculated for a line with $d/a = 20$ in a plasma with (a) $n = \dfrac{Q_0 N_0}{4 \, N_c} = 50$ and (b) $n = 100$ for different values of $g_m = $ (*1*) 0.1, (*2*) 1, (*3*) 10, (*4*) 50, and (*5*) 400.
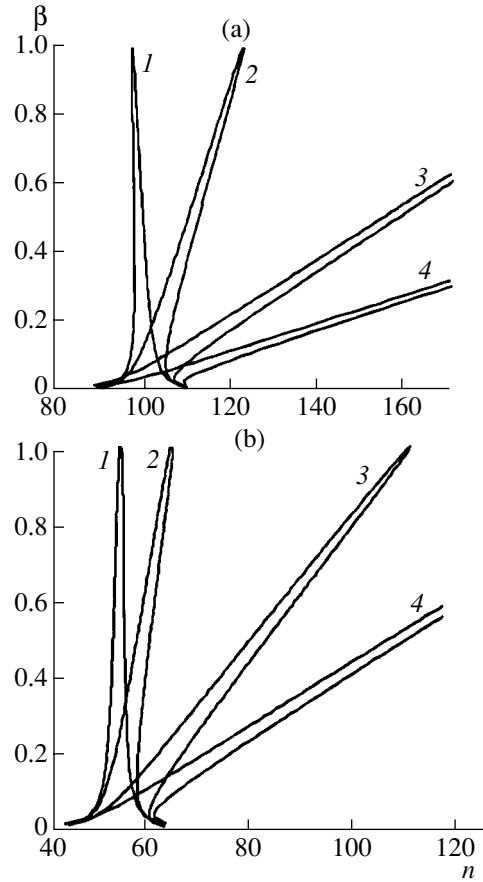


**Fig. 3.** Resonance curves $\beta(n)$ (where $n = \dfrac{Q_0 N_0}{4 \, N_c}$) calculated for a line with $d/a = 20$ at fixed values of (a) $\Omega = \dfrac{Q_0}{2}\delta\omega = 50$ and (b) $\Omega = 100$ for different values of the parameter $g_m = $ (*1*) 0.1, (*2*) 1, (*3*) 10, and (*4*) 50.

$\dfrac{d\beta}{d\delta\omega} = \infty$), there are three values of the transmission factor $\beta$ corresponding to the same frequency shift $\delta\omega$ (the central value corresponds to an unstable solution). Such a system possesses a hysteresis effect. If the frequency is decreased after reaching the upper jump point lying near the maximum of the resonance curve, then $\beta(\delta\omega)$ decreases stepwise. In contrast, if $\delta\omega$ is increased, then, at the lower jump point, $\beta$ jumps from the lower to upper branch of the resonance curve. At sufficiently high values of $g_m$ ($g_m > d^2/a^2$), the plasma is entirely displaced by a strong microwave field from the region between the resonator wires ($q \longrightarrow 0$) and the resonance curve $\beta(\delta\omega)$ in the vicinity of its maximum, positioned near $\delta\omega = 0$, becomes independent of the plasma density and almost coincides with the resonance curve in a vacuum ($N/N_c = 0$).

In experiments, the situation is often met where the frequency $\delta\omega$ is fixed, whereas the plasma density varies with time (e.g., it falls after the plasma source is switched off). In this case, instead of the resonance curves $\beta(\delta\omega)|_{N = \text{const}}$, it is more convenient to analyze the dependences $\beta(N)|_{\delta\omega = \text{const}}$. These dependences for

(a) $\Omega = \dfrac{Q_0}{2}\delta\omega = 50$ and (b) $\Omega = 100$ are presented in Fig. 3.

It can be easily seen that, when $g_m$ lies within the range $1 < g_m < \left(\dfrac{3\Omega}{2\ln d/a}\right)^{1/2}$, the value of $g = g_m\beta$ at the lower jump point $n = n_b$ is below unity ($g < 1$). In this case, we obtain the following formula relating the bifurcation value $n = n_b$ to $g_m$ (and, consequently, to the plasma temperature):

$$n_b - \Omega \approx \left(\dfrac{3\Omega g_m}{2\ln d/a}\right)^{1/3}. \tag{20}$$

This formula makes it possible to use the above probe to measure the plasma temperature.
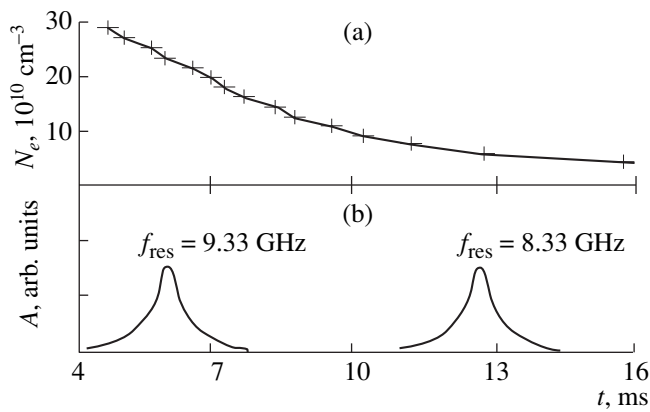
**Fig. 4.** (a) Time behavior of the plasma density and (b) typical waveforms obtained from a microwave probe for two resonance frequencies.
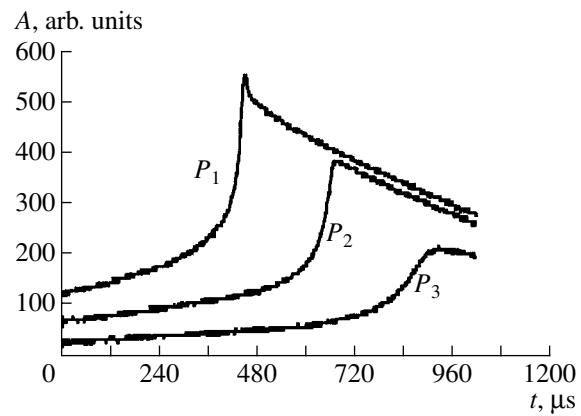


**Fig. 5.** Waveforms of the output signal from a microwave probe in a decaying plasma at a fixed frequency for three values of the input power ($P_1 > P_2 > P_3$).

## 3. MEASUREMENTS OF THE PLASMA PARAMETERS WITH A MICROWAVE RESONATOR PROBE

The above two-wire microwave resonator probe was used to measure the plasma parameters in the KROT experimental device. The vacuum chamber of the device is 3 m in diameter and 10 m long. The plasma is produced by an inductive RF breakdown ($f = 5$ MHz, $\tau_{pulse} \approx 1.6$ ms, and $H \approx 200$ Oe) in argon at a pressure of $5 \times 10^{-4}$ torr. The experiments were carried out in the decaying plasma; i.e., after the RF source was switched off. Figure 4a shows the time behavior of the density; the characteristic plasma decay time is about 10 ms.

The microwave resonator (a quarter-wave segment of a double line shorted on one side and open on the other) was made from a silvered copper wire 8 mm long and 0.2 mm in diameter. The distance between the resonator wires was 2 mm. For exciting the resonator and receiving its response, we used magnetic-coupling loops 2 mm in diameter (Fig. 1). In the absence of a plasma, the minimum eigenfrequency of the resonator was $f_0 = 8$ GHz and its Q-factor was $Q_0 \approx 100$. Estimates showed that the Q-factor was determined by the coupling with the exciting and receiving lines.

Figure 4b shows a response signal from the microwave resonator probe in a decaying plasma at a low level of the input microwave power. The higher the signal frequency, the higher the plasma density for which the resonance occurs. By varying $\delta\omega$ and using relationship (19), we could reconstruct the time dependence of the density.

An increase in the microwave power input to the probe results in the deformation of the shape of the response signal. Figure 5 shows the waveforms of the output signals for three values of the microwave power. It is seen that, when the plasma density reaches a certain critical value (which depends on the input power), the output signal increases sharply and then falls smoothly. As the input power increases, the position of

the jump $N = N_b$ (in accordance with the nonlinear theory considered in Section 2) shifts toward the higher plasma densities (see Fig. 3 and the comment on it in the text), or, in other words, the jump is observed at earlier times after the plasma source is switched off.

From the dependence of $N_b$ on $P$ and relationship (20), we can determine the electron temperature $T_e$ ($T_e \gg T_i$) with good accuracy. Figure 6 shows the results of the electron temperature measurements with a microwave probe and with a double probe. It is seen that the results are in good agreement.

To directly observe the hysteresis effects in the microwave resonator probe, we performed an experiment under conditions such that the plasma density varied nonmonotonically over a certain time interval: first, it grew and, then, fell. In this case, with a properly chosen $\delta\omega$, resonance condition (19) can be satisfied twice (when the plasma density increases, and when it decreases).

Figure 7a shows the time dependence of the plasma density measured with a microwave probe operating in the nonlinear regime. Figure 7b shows the waveforms of the output signals for different input powers ($P_1 < P_2 < P_3 < P_4$). The behavior of these signals can be explained based on the nonlinear resonance curves given in Fig. 3. First, the density increases and the operating point moves along the resonance curve to the upper jump point. After a certain period of time, the plasma density begins to fall and reaches the value corresponding to the lower jump point. By comparing curves *1* and *2*, we can see that, in accordance with theoretical predictions, the hysteresis jumps shift toward the higher plasma densities as the input power increases. However, at a sufficiently high power, the upper jump point may be unattainable even at the maximum density. This case corresponds to curves *3* and *4*.

The characteristic times over which nonlinear effects in the plasma develop were measured with the
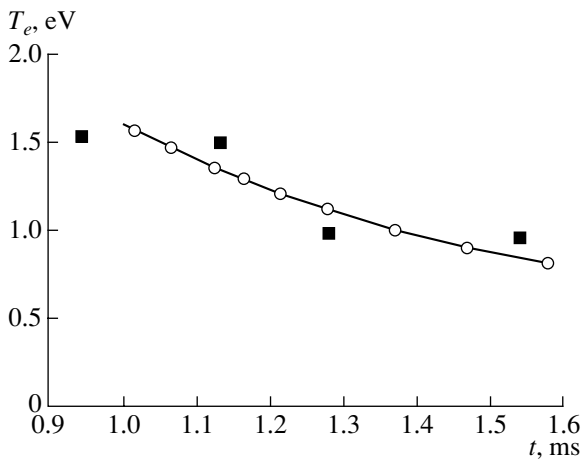
**Fig. 6.** Measurements of the time behavior of the electron temperature with the help of a double probe (squares) and a microwave probe (circles).
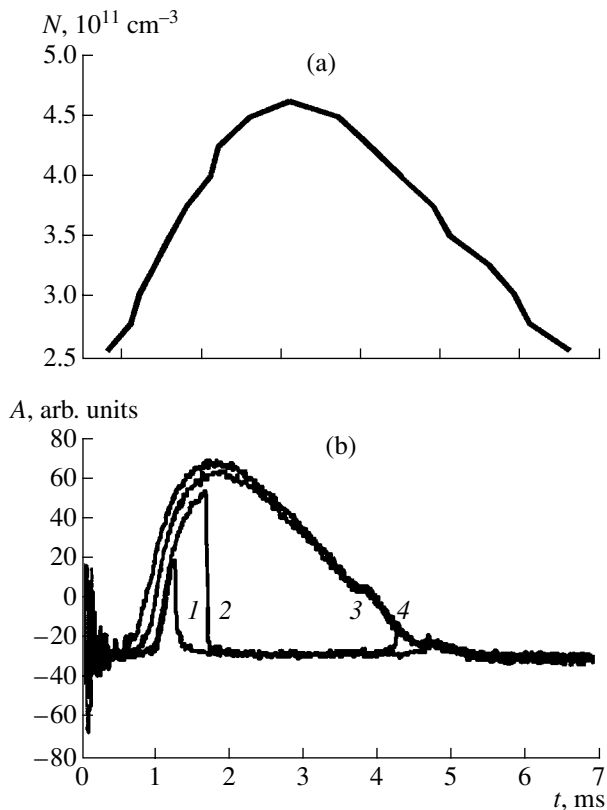


**Fig. 7.** (a) Nonmonotonic time behavior of the plasma density and (b) typical waveforms of the output signal from a microwave probe for four values of the input power: $P_1 < P_2 < P_3 < P_4$.

help of the amplitude modulation of the input microwave signal applied to the resonator probe. 100% modulation was achieved by applying rectangular pulses with a repetition period of $T = 30$ μs and rise and fall times of $\sim10^{-5}$ s. In the course of the experiment, it was revealed that the plasma density inside the microwave resonator was redistributed during a time interval

shorter than 10 μs. Estimates of the time of the ponderomotive displacement of the plasma from the resonator show that this time is no longer than $\tau_s \le d/V_s = 1$ μs, where $d$ is the distance between the double-line wires and $V_s$ is the ion acoustic velocity. The characteristic times over which other nonlinear (heating and ionization) processes develop are substantially longer than 10 μs.

## 4. CONCLUSION

We have shown that theoretical calculations of the nonlinear regime of a two-wire microwave resonator probe adequately describe the experimental data. This allows us to conclude that the nonlinear effects observed are ponderomotive in nature and can be used to measure the plasma electron temperature. The plasma density and temperature determined with the microwave detector under study agree well with the results of measurements by means of conventional single and double probes.

Of course, the theory developed does not pretend to completely describe all of the effects occurring in the plasma surrounding the microwave probe. In particular, the double-line segment itself, even in the absence of a microwave field, perturbs the plasma density because of the appearance of charged-particle fluxes onto the wire surface. The calculations (or at least estimates) of these perturbations will make it possible to improve the accuracy of determining the plasma parameters. Note, however, that the higher the microwave field, the more strongly the plasma is pushed away from the wires and the less important are the flux effects.

## REFERENCES

1. M. A. Heald and C. B. Wharton, *Plasma Diagnostics with Microwaves* (Wiley, New York, 1965; Atomizdat, Moscow, 1968).

2. R. L. Stenzel, Rev. Sci. Instrum. **47**, 603 (1976).

3. A. V. Kostrov, A. V. Strikovskiĭ, Yu. V. Chugunov, *et al.*, Preprint No. 510 (Inst. of Applied Physics, Russ. Acad. Sci., Nizhni Novgorod, 1999).

4. V. G. Denisov, V. A. Isaev, and A. I. Smirnov, Fiz. Plazmy **13**, 229 (1987) [Sov. J. Plasma Phys. **13**, 130 (1987)].

5. A. V. Gaponov and M. A. Miller, Zh. Éksp. Teor. Fiz. **34**, 242 (1958) [Sov. Phys. JETP **7**, 168 (1958)].

*Translated by N. F. Larionova*

# ECR Heating of a Dense Plasma by Helicon Waves

## A. V. Timofeev

*Russian Research Centre Kurchatov Institute, pl. Kurchatova 1, Moscow, 123182 Russia*
Received May 23, 2002

**Abstract**—Eigenmodes of an axisymmetric plasma column that is uniform along the magnetic field are investigated. It is shown that, as the plasma density increases, eigenmodes with frequencies close to the electron gyrofrequency tend to localize at the plasma periphery. This effect is likely to restrict the electron density at which the plasma can be heated by means of such modes. A theory is developed for the excitation of the eigenmodes of a plasma column in a weakly nonuniform magnetic field by an external antenna. © *2002 MAIK "Nauka/Interperiodica"*.

## 1. INTRODUCTION

The distinguishing feature of helicon waves (helicons) is their ability to propagate in a plasma whose density exceeds the critical density, which is defined by the relationship $\omega_{pe} = \omega$ (where $\omega_{pe}$ is the electron plasma frequency). This effect makes it possible to create and heat plasmas with comparatively high densities (see, e.g., [1–5]). Since the frequency range of the helicons is broad ($\omega_i \ll \omega < \omega_e$, where $\omega_j$ is the gyrofrequency of the particles of species $j = i, e$), they can be used for electron-cyclotron-resonance (ECR) plasma heating by the "magnetic beach" method. In this method, the eigenmodes of the plasma column are excited at a certain distance from the ECR region and then approach it along the magnetic field. As the ECR region is approached, the longitudinal component $N_\parallel$ of the refractive index for the helicons increases sharply. Oscillations with $|N_\parallel| \gg 1$ are difficult to excite by an antenna positioned in vacuum, because their transverse refractive index is imaginary and is large in absolute value: $\mathrm{Im} N_\perp \approx N_\parallel \gg 1$. Consequently, the electromagnetic field of the antenna should be the strongest in its vicinity and should fall off exponentially toward the plasma column. The necessity of placing the antenna at a large distance from the ECR region leads automatically to a magnetic beach configuration.

Although the magnetic field variations can substantially change the eigenvalues of $N_\parallel$, they have an insignificant impact on the spatial structure of the eigenmodes. The plasma density variations affect the oscillations in a different way. In this paper, it is shown that, as the plasma density increases, the lowest radial modes with comparatively small eigenvalues of $N_\parallel$ tend to localize near the boundary of the plasma column, while the central (highest density) region of the column becomes opaque to eigenmodes. Presumably, this effect is a manifestation of a general feature peculiar to helicons with frequencies close to the electron gyrofrequency. This feature was pointed out in my earlier paper [6], which was aimed at investigating the ray trajectories of helicons in an inhomogeneous plasma in an open confinement system. It was found that, as a result of refraction, the ray trajectories escape from the central region of the plasma to the plasma periphery.

As the plasma density increases, the tendency for the helicons to localize near the plasma boundary becomes more pronounced. Presumably, it is this effect that will impose a limit on the electron density at which the plasma can be heated by helicons. However, it should be noted that the effect is weaker for a plasma in which the radial density profile is flat in the central region and decreases abruptly near the boundary.

Microwave discharges (especially those used in technological applications) are often initiated in comparatively weak magnetic fields (with strengths of about 100 G). In this case, the vacuum wavelength of electromagnetic oscillations with $\omega \approx \omega_e$ is much larger than the length of the system. Such oscillations can be excited by antennas of the same type as ion-cyclotron-resonance (ICR) heating antennas (see, e.g., [5]). Note that, although the magnetic fields required for fusion experiments are much stronger than those indicated above, they can weaken substantially at high plasma pressures.

The objective of this paper is to analyze the excitation of the eigenmodes of a plasma column in a nonuniform magnetic field by an antenna placed outside the plasma (in a vacuum). The distribution of the antenna electric current over the longitudinal coordinate is expanded in a Fourier integral over $N_\parallel$. An individual Fourier harmonic of the antenna current with a certain value of $N_\parallel$ resonantly transfers its energy to the eigenmodes in the vicinity of the point at which the eigenvalue of the longitudinal wavenumber is exactly equal to $N_\parallel$. The power expended by the antenna to excite the eigenmodes of the plasma column is calculated.

## 2. EIGENMODES OF THE PLASMA COLUMN

We assume that the parameters of the system vary in the longitudinal direction over distances much larger than the radius of the plasma column. In this case, the eigenmode parameters can be determined in the uniform plasma column approximation, and the longitudinal nonuniformity of the column can be taken into account by varying the parameters of the problem. In this model, we consider a one-dimensional problem, assuming that the axisymmetric plasma column is infinitely long and is uniform along the magnetic field. In accordance with the symmetry of the problem, the perturbed quantities can be described by the spatiotemporal dependence $\propto f(r)\exp(-i(\omega t + m\theta + N_\| z))$ in cylindrical coordinates consistent with the geometry of the column.

The set of Maxwell's equations for the oscillations in question has the form

$$N_\| B_\theta - \frac{m}{r} B_z = \varepsilon E_r + ig E_\theta,$$

$$N_\| B_r + i\frac{dB_z}{dr} = ig E_r - \varepsilon E_\theta,$$

$$\frac{i}{r}\frac{d}{dr} r B_\theta + \frac{m}{r} B_r = \varepsilon_\| E_z,$$

$$\frac{m}{r} E_z - N_\| E_\theta = B_r, \qquad (1)$$

$$N_\| E_r + i\frac{dE_z}{dr} = B_\theta,$$

$$\frac{i}{r}\frac{d}{dr} r E_\theta + \frac{m}{r} E_r = -B_z,$$

where $\varepsilon = 1 - \dfrac{\omega_{pe}^2}{\omega^2 - \omega_e^2}$, $g = \dfrac{\omega_e}{\omega}\dfrac{\omega_{pe}^2}{\omega^2 - \omega_e^2}$, $\varepsilon_\| = 1 - \dfrac{\omega_{pe}^2}{\omega^2}$, $\omega_{pe}$ is the electron plasma frequency, and $\omega_e$ is the electron gyrofrequency. The plasma is assumed to be cold, and the ion contribution to the plasma dielectric response is neglected. Equations (1) are written in terms of the dimensionless length $r\omega/c \longrightarrow r$. The radial plasma density profile is chosen to be $n_0(r) = n_0(r_0)\left(1 - \tanh\left(\dfrac{r^2 - r_0^2}{2r_0\Delta}\right)\right)$, which is close to a Gaussian profile when $\Delta \gg r_0$ and to a smeared step function when $\Delta \ll r_0$. It is also assumed that, at $r = r_B$, the plasma is bounded by a perfectly conducting wall.

When integrating Eqs. (1), the value $B_z(0)$ at the axis of the plasma column was specified; the value $E_z(0)$ and the eigenvalue of $N_\|$ were adjusted by a shooting method so as to satisfy the condition that the tangential components $E_\theta$ and $E_z$ of the electric field vanish at $r = r_B$. Equations (1) imply that, in the vicinity of the
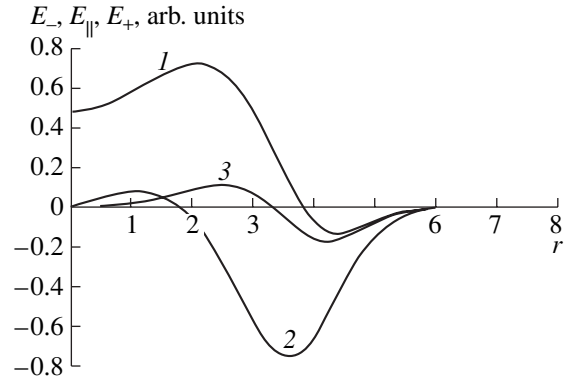


**Fig. 1.** Radial profiles of the electric field components (*1*) $E_-$, (*2*) $E_\|$, and (*3*) $E_+$ of the ($n = 1$, $m = 1$) eigenmode of the plasma column. The computation parameters are $(\omega_{pe}/\omega)^2 = 3$, $\omega_e/\omega = 1.5$, $r_0 = 3$, $\Delta = 2$, and $r_B = 7$, the eigenvalue being $N_\| = 3.2$.

origin of the coordinate system, the electromagnetic field components depend on the radius according to the laws $E_r, E_\theta, B_r, B_\theta \propto r^{|m|-1}$ and $E_z, B_z \propto r^{|m|}$. We introduce the quantities $e_\theta(0)$, $b_\theta(0)$, $b_z(0)$, and $e_z(0)$ through the relationships $E_\theta \xrightarrow[r \to 0]{} r^{|m|-1} e_\theta(0)$, $B_\theta \xrightarrow[r \to 0]{} r^{|m|-1} b_\theta(0)$, $E_z \xrightarrow[r \to 0]{} r^{|m|} e_z(0)$, and $B_z \xrightarrow[r \to 0]{} r^{|m|} b_z(0)$. In order to integrate Eqs. (1), it is necessary to express the quantities $e_\theta(0)$ and $b_\theta(0)$ in terms of $e_z(0)$ and $b_z(0)$, which can also be done by means of Eqs. (1):

$$
\begin{aligned}
e_\theta(0) &= -|m|(i(\mathscr{E}(0) + s\mathscr{G}(0))b_z(0) \\
&\quad + N_\|(\mathscr{G}(0) + s\mathscr{E}(0))e_z(0)), \\
b_\theta(0) &= |m|N_\|(-(\mathscr{G}(0) + s\mathscr{E}(0))b_z(0) \\
&\quad + iN_\|(\mathscr{E}(0) + s\mathscr{G}(0))e_z(0)) + i|m|e_z(0),
\end{aligned} \qquad (2)
$$

where we have introduced the notation

$$\mathscr{E}(r) = \frac{\varepsilon(r) - N_\|^2}{(\varepsilon(r) - N_\|^2)^2 - g^2(r)},$$

$$\mathscr{G}(r) = \frac{g(r)}{(\varepsilon(r) - N_\|^2)^2 - g^2(r)}, \quad s = m/|m|.$$

The results of integrating Eqs. (1) are illustrated in the figures presented below. Figure 1 shows the radial profiles of the electric field components of the first radial mode of the oscillations ($n = 1$), whose spatial scale in the case at hand is the longest. Note that the mode that can be regarded as the zeroth one is a surface mode (see below). We consider oscillations rotating azimuthally in the same direction as the electrons and having the smallest azimuthal wavenumber $m = 1$. We also assume that the plasma density is only several times higher than the critical density, $(\omega_{pe}/\omega)^2 = 3$. In
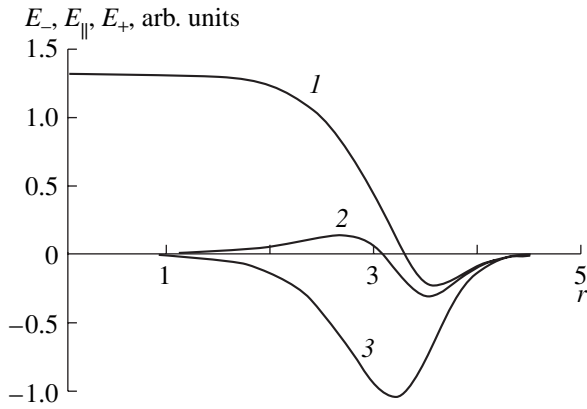
**Fig. 2.** Same as in Fig. 1, but for $(\omega_{pe}/\omega)^2 = 5$, $\omega_e/\omega = 1.5$, $r_0 = 3$, $\Delta = 0.5$, and $r_B = 6$ and for the eigenvalue $N_{\parallel} = 4.6$.
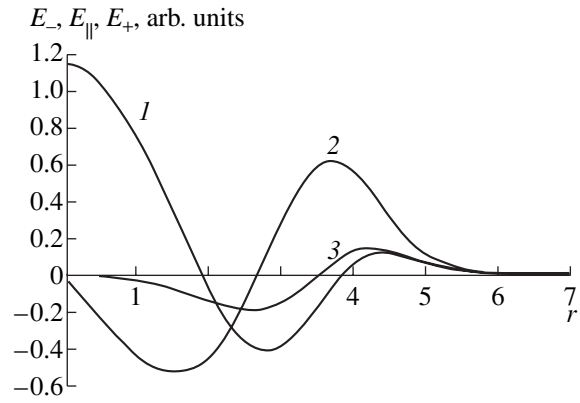


**Fig. 3.** Same as in Fig. 1, but for the ($n = 2$, $m = 1$) eigenmode and for the eigenvalue $N_{\parallel} = 3.88$.

the central region of the plasma column, the electric field is right-polarized, is perpendicular to the main magnetic field, and rotates in the same direction as the electrons: $E \approx E_-$, where $E_- = (E_r - iE_\theta)/\sqrt{2}$. In the peripheral plasma region in which $\omega_{pe} \approx \omega$, the electric field has a significant longitudinal component. The electromagnetic oscillations are coupled with the potential plasma electron oscillations. The conversion of electromagnetic oscillations into plasma electron oscillations propagating along the magnetic field is most efficient for short-wavelength oscillations, which can be described in the quasiclassical approximation [7].

The larger the ratio $r_0/\Delta$ (which corresponds to the transition from a Gaussian profile to a smeared step function), the greater the tendency for the longitudinal and left-polarized components of the electric field, $E_{\parallel}$ and $E_+ = (E_r + iE_\theta)/\sqrt{2}$, to localize near the plasma boundary. In the main part of the plasma column, where the plasma density is approximately constant, there remains only the right-polarized electric field component (Fig. 2). Of course, the refractive index for such oscillations can be described with good accuracy by the familiar expression

$$N^2 \approx N_{\parallel}^2 \approx 1 - \frac{\omega_{pe}^2}{\omega(\omega - \omega_e)}. \tag{3}$$

Thus, for the plasma parameters of Fig. 2, the eigenvalues of $N_{\parallel}$ differ by no more than 15% from those described by expression (3) when the ratio $\omega_e/\omega$ changes in the range from 1.5 to 1.15. Note that, although the eigenvalues of $N_{\parallel}$ change sharply as $\omega_e$ approaches $\omega$, the shape of the eigenfunctions changes only slightly. This conclusion can also be derived on the basis of expression (8) for $N_{\perp}^2$ (see below).

The amplitudes of the right-polarized and longitudinal electric fields of the higher radial modes are approximately the same regardless of the shape of the radial profile of the plasma density; moreover, the longitudinal electric field is strong in the regions where the right-polarized electric field is weak, and vice versa (Fig. 3).

It should be noted that, in the cold plasma approximation, the number of radial eigenmodes is infinitely large. In spatially bounded systems, the wavelength of the oscillations decreases to zero as the radial wavenumber increases; hence, an infinitely high "confining" potential is required to localize such oscillations. In the case under consideration, an infinitely high potential is provided by a singularity that arises in the wave equation because of the coupling of the oscillations in question to the potential oscillations, which are also called the Trivelpiece–Gould (TG) modes. Because of the singularity in the wave equation, the characteristic wavelength of the TG modes in a cold plasma tends to zero. The coupling of the helicon waves to the TG modes was pointed out, in particular, in [1, 4, 5]. The above plasma electron oscillations can be regarded as a particular case of the TG modes (namely, those with $N_{\perp} = 0$). In a homogeneous plasma, the TG modes propagate at a certain angle $\theta = \theta_{\text{res}}$ (the angle at the vertex of the so-called resonant cone) to the magnetic field:

$$\tan\theta_{\text{res}} = \left(-\frac{\varepsilon_{\parallel}}{\varepsilon}\right)^{1/2}. \tag{4}$$

For a high-density ($\omega_{pe} \gg \omega$) plasma, expression (4) yields

$$\theta_{\text{res}} \approx \arccos(\omega/\omega_e). \tag{5}$$

The problem under discussion differs substantially from those of the eigenmodes of the plasma in a rectangular waveguide. However, if we set $N_r \approx n\pi/r_0$ and $N_\theta = m/r_0$, then we can see that the dependence of

the eigenvalues of the longitudinal wavenumber on $n$ and $m$,

$$N_\parallel^{(n,m)} \approx \frac{1}{r_0} \sqrt{\frac{(n\pi)^2 + m^2}{(\omega_e/\omega)^2 - 1}}, \qquad (6)$$

which follows from relationship (5), agrees in general with the dependence obtained by solving the wave equation (Fig. 4). The agreement is better for the highest radial modes, which convert into the potential TG modes.

As the plasma density decreases, the lowest radial modes also convert into potential modes. In fact, as was noted above, the electromagnetic oscillations convert into plasma electron oscillations in the vicinity of the critical surface, at which $\omega_{pe} = \omega$. The lower the plasma density, the smaller the transparency region ($\omega_{pe}(r) > \omega$) and, consequently, the larger the effective transverse wavenumber. As a result, the boundary region where $\omega_{pe} \approx \omega$ plays an increasingly important role, and the oscillations convert into TG modes. Relationship (3) implies that, as $\varepsilon_\parallel \longrightarrow 0$, the longitudinal wavenumber of these modes should increase sharply. This conclusion is confirmed by the results of calculations (Fig. 5).

Note that, in the opposite case of a high-density plasma ($\omega_{pe} \gg \omega$), the lowest radial modes also acquire the nature of TG modes and simultaneously tend to localize near the boundary of the plasma column. In order to analyze these phenomena at a qualitative level, we use the following familiar dispersion relation for helicons (see, e.g., [2]):

$$N^2 \approx \frac{\omega_{pe}^2}{\omega(\omega_e \cos\theta - \omega)}. \qquad (7)$$

The refractive index of a high-density plasma for electromagnetic oscillations propagating in it is large, $N \geq \omega_{pe}/\omega \gg 1$. On the other hand, the transverse component of the refractive index for the lowest radial modes is comparatively small, $N_\perp \approx \pi/r_0 \leq 1$. These lowest modes satisfy the condition $\theta \ll 1$, which puts dispersion relation (7) in the form

$$N_\perp^2 \approx \frac{(\omega_e/\omega - 1)}{(1 - \omega_e/2\omega)}\left(N_\parallel^2 - \frac{\omega_{pe}^2}{\omega(\omega_e - \omega)}\right). \qquad (8)$$

Here, as in numerical analysis, we assume that the condition $2 > \omega_e/\omega > 1$ holds.

Dispersion relation (8) implies that, for an inhomogeneous plasma, the condition $N_\perp \ll N_\parallel$ can be satisfied only in a small region where $N_\parallel^2 \approx \dfrac{\omega_{pe}^2}{\omega(\omega_e - \omega)}$. This region should lie at the edge of the plasma column, while the inner plasma region where $N_\perp \approx N_\parallel$ is opaque to the oscillations under consideration ($N_\perp^2 < 0$). In the boundary region, we have $\varepsilon_\parallel \longrightarrow 0$, which makes it pos-
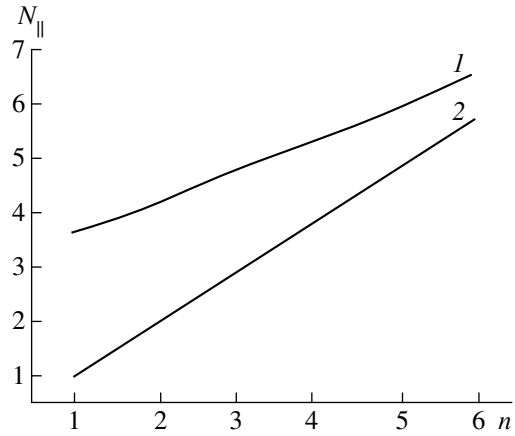


**Fig. 4.** Eigenvalues of the longitudinal refractive index vs. radial mode number: (*1*) calculations from Eqs. (1) and (*2*) calculations from expression (6). The only physically meaningful values are the integer values of the mode number. The computation parameters are $(\omega_{pe}/\omega)^2 = 5$, $\omega_e/\omega = 1.5$, $r_0 = 3$, $\Delta = 2$, and $r_B = 5.5$.
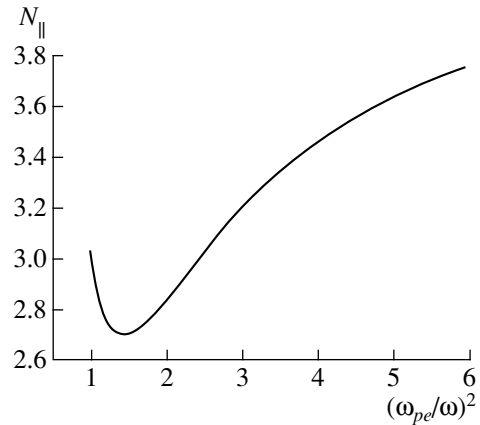


**Fig. 5.** Eigenvalues of the longitudinal refractive index vs. plasma density for $\omega_e/\omega = 1.5$, $r_0 = 3$, $\Delta = 2$, $r_B = 7$, and $n = m = 1$.

sible to satisfy condition (4) for the lowest radial modes.

The above conclusions are confirmed by numerical calculations (see Figs. 1, 2, 6, 7). The numerical results show that, in a plasma with a sufficiently high density, the lowest radial modes are actually expelled to the plasma periphery, where they acquire the nature of surface modes. In the case of short-wavelength oscillations whose propagation can be described in the ray approximation, this effect corresponds to the escape of the ray trajectories of helicons to the peripheral plasma region. This latter effect was pointed out in my earlier paper [6], in which the approximate analysis of the ray trajec-

$E_-$, $E_\parallel$, $E_+$, arb. units
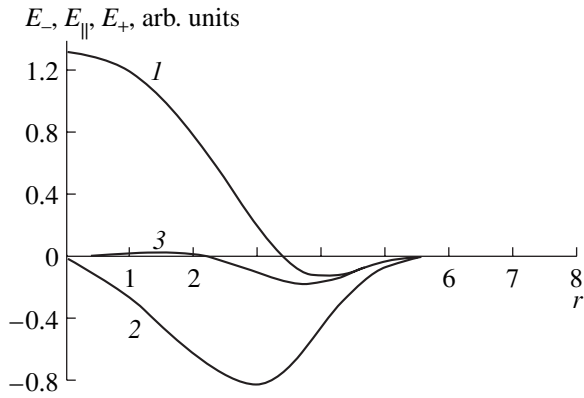


**Fig. 6.** Same as in Fig. 1, but for $(\omega_{pe}/\omega)^2 = 2$ and for the eigenvalue $N_\parallel = 2.84$.

$E_-$, $E_\parallel$, $E_+$, arb. units
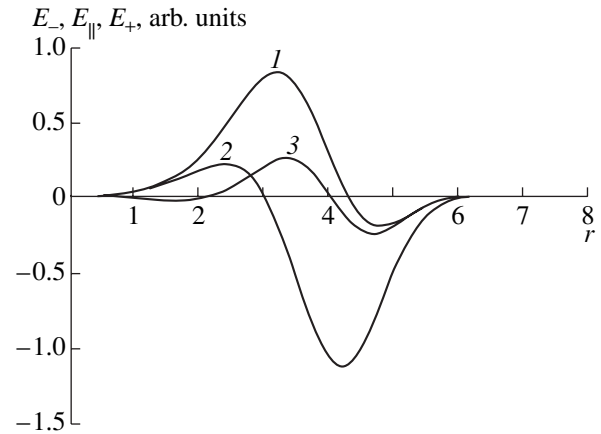


**Fig. 7.** Same as in Fig. 6, but for $(\omega_{pe}/\omega)^2 = 5$ and for the eigenvalue $N_\parallel = 3.62$.

$E_-$, $E_\parallel$, $E_+$, arb. units
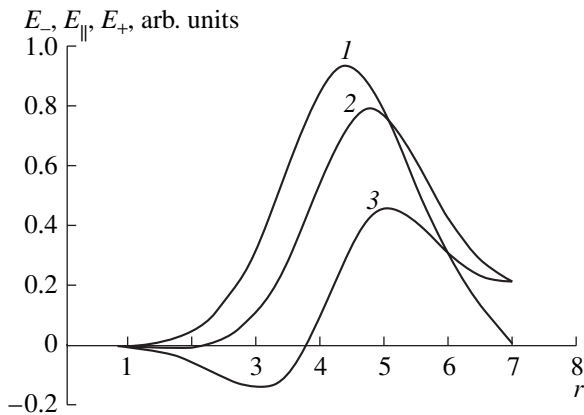


**Fig. 8.** Same as in Fig. 1, but for the $(n = 0, m = 1)$ surface mode and for the eigenvalue $N_\parallel = 1.47$.

$E_-$, $E_\parallel$, $E_+$, arb. units



**Fig. 9.** Same as in Fig. 1, but for the $(n = 1, m = 0)$ mode and for the eigenvalue $N_\parallel = 3.64$.

tories was carried by means of a dispersion relation analogous to relation (8).

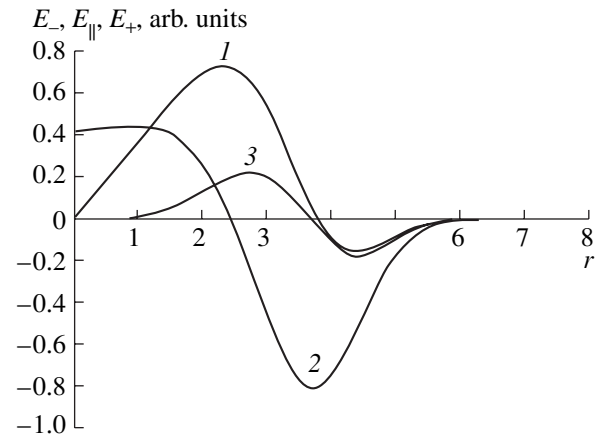In addition to the internal modes considered above, there also exists a mode that can be referred to as the surface mode of the plasma column or the fundamental mode of the entire radial interval $0 < r < r_B$ in question. This mode is localized in the boundary region where $\omega_{pe} \approx \omega$. The refractive index of the plasma for this mode is substantially smaller than that for the internal modes (cf. the captions in Figs. 1, 3, 8). As a result, the electromagnetic field of the surface mode penetrates deeper into vacuum in comparison with the fields of the internal modes (Fig. 8). Note that, in contrast to the internal modes, the longitudinal refractive index for the surface mode changes slightly with increasing plasma density.

If the plasma column is separated from the chamber wall by a vacuum gap, then there exist higher order modes of the gap. Thus, for the above radial profile of the plasma density, the next mode arises when the radius of the perfectly conducting wall is about $r_B \approx 9.5$. Note that, at this radius, the longitudinal wavenumber of the mode is zero.

We have thoroughly discussed oscillations that rotate in the same direction as the electrons ($m > 0$). The general features of oscillations with $m \le 0$ are essentially the same. The most profound difference between these types of oscillations is in their polarization at $r \longrightarrow 0$. At the axis of the plasma column, only the left-polarized electric-field component of the modes rotating in the same direction as the ions is nonzero, while

the only nonzero electric-field component of the modes with $m = 0$ is the longitudinal one (Figs. 9, 10).

## 3. EXCITATION OF EIGENMODES

In order for plasma heating by means of helicons to hold promise for practical applications, the helicons should be efficiently excited by an antenna placed outside the plasma. Let us analyze this heating process.

We consider an axisymmetric magnetic field and assume that (as is commonly the case) the plasma column lies entirely in the axial region of the device. In this situation, the radial nonuniformity of the magnetic field across the column is of little importance, whereas the longitudinal magnetic-field nonuniformity can play a significant role. The nonzero longitudinal gradient of the magnetic field is characteristic of open magnetic confinement systems and also of a broad variety of gas-discharge devices in which plasma is used for technological applications.

The eigenvalues of the longitudinal refractive index for helicons depend on $\omega_e$ (see above). Consequently, as the helicons propagate along a nonuniform magnetic field, the longitudinal refractive index for them changes. As a function of the longitudinal coordinate, the electric current flowing in an antenna can be expanded in a Fourier integral. Each individual Fourier harmonic of the antenna current interacts efficiently with the eigenmode only in the vicinity of the resonant point $z_s$, at which the equality $N_\parallel = N_\parallel^{(n, m)}(z_s)$ is satisfied. As will be shown below, the length of the interaction interval along the plasma axis ($l \approx \sqrt{L_\parallel}$) is short in comparison with the characteristic length scale $L_\parallel$ on which the magnetic field varies in the longitudinal direction. (Recall that all of the quantities having the dimension of length are nondimensionalized by multiplying by $c/\omega$.) Calculations show that the radial dependence of the electromagnetic fields remains essentially unchanged even when the longitudinal variations in the magnetic field are substantial. This fact, together with the short length of the region where the antenna field interacts efficiently with the plasma, allows us to assume that the radial profile of the eigenmodes remains unchanged and to represent their spatially varying complex amplitude in the form $E_i(\mathbf{r}) = \exp(im\theta + iN_\parallel z)E_i^{(1)}(r)E_i^{(2)}(z)$ and $B_i(\mathbf{r}) = \exp(im\theta + iN_\parallel z)B_i^{(1)}(r)B_i^{(2)}(z)$. We also assume that the characteristic length scale $L_\parallel$ on which the magnetic field varies is much larger than the plasma radius. In this case, in calculating the eigenmodes of the plasma column (i.e., in determining the radial dependences $E_i^{(1)}(r)$ and $B_i^{(1)}(r)$), the magnetic field can be treated as a slowly varying parameter.
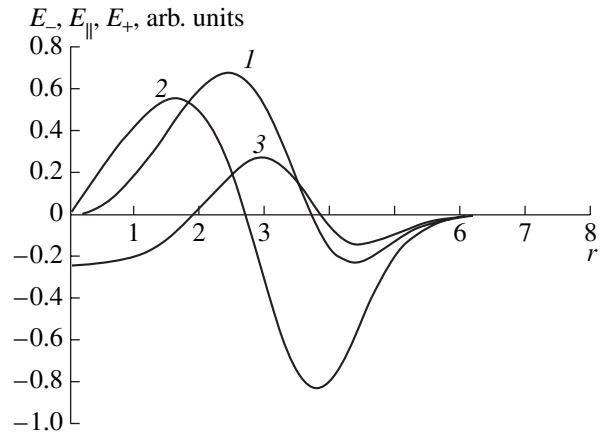
$E_-$, $E_\parallel$, $E_+$, arb. units

**Fig. 10.** Same as in Fig. 1, but for the ($n = 1$, $m = -1$) mode and for the eigenvalue $N_\parallel = 4.36$.

Outside the plasma, as the ECR region is approached, the electromagnetic fields tend to localize in the vicinity of the antenna. This effect is associated with an increase in $N_\parallel$ and is described by the approximate equality $\mathrm{Im} N_r \approx N_\parallel$, which is valid for $N_\parallel \gg 1$. Consequently, during ECR plasma heating in devices with a longitudinally nonuniform magnetic field (such as open magnetic systems), the eigenmodes should be excited far from the ECR region, specifically, in the region where they can efficiently interact with the field of the antenna located outside the plasma. It is precisely in this way that electromagnetic oscillations are generated during ICR plasma heating by the magnetic beach method. Note that, in contrast to the case under discussion, the transparency region for the eigenmodes shrinks toward the axis of the plasma column as the ICR region is approached [8].

We assume that the electric current generating helicons flows along a cylindrical surface of radius $r_A$ ($r_A < r_B$). In order to describe the dependence of the current on the spatial coordinates, we expand it in a Fourier integral in the longitudinal coordinate $z$ and in a Fourier series in the azimuthal coordinate $\theta$.

The electric field excited by an individual Fourier harmonic of the current can be described by the following set of equations derived in [8]:

$$L_1 B_z - L_2 F + B_z = \frac{4\pi}{\omega}\frac{1}{N_\parallel^2 - 1}(\boldsymbol{\nabla} \times \mathbf{j})_z,$$

$$L_1 F - L_2 B_z + \frac{1}{N_\parallel^2}L_3 F = \frac{4\pi}{\omega N_\parallel}\frac{1}{N_\parallel^2 - 1}j_z, \qquad (9)$$

where

$$F = iN_\parallel E_z, \quad L_1 = \frac{1}{r}\frac{d}{dr}r\mathscr{E}\frac{d}{dr} - \left(\frac{m}{r}\right)^2\mathscr{E} + \frac{m}{r}\frac{d\mathscr{G}}{dr},$$

$$L_2 = \frac{1}{r}\frac{d}{dr}r\mathcal{G}\frac{d}{dr} - \left(\frac{m}{r}\right)^2\mathcal{G} + \frac{m}{r}\frac{d\mathcal{E}}{dr},$$

$$L_3 = \frac{1}{r}\frac{d}{dr}r\frac{d}{dr} - \left(\frac{m}{r}\right)^2 + \varepsilon_\parallel,$$

and $\mathbf{j}$ is the Fourier harmonic of the current. The subscripts $m$ and $N_\parallel$ in the Fourier harmonics of the current and the electromagnetic field are omitted.

Note that the set of homogeneous equations (9) is equivalent the set of Maxwell's equations (1). However, Eqs. (9) cannot be used in numerical calculations because the coefficient in front of the second derivative vanishes at the points at which the equalities $\varepsilon - N_\parallel^2 = \pm g$ hold. In numerical integration, these points manifest themselves as singular points. Meanwhile, the analysis carried out in [9] shows that, because of some special relationships between the coefficients in Eqs. (9), the solution at these points is regular (in the terminology of [9], these points are fictitious singular points).

We multiply the first and second of Eqs. (2) by $B_z^{(1)}(r)$ and $F^{(1)}(r)$, respectively, and integrate the resulting equations over the radius. As a result, we arrive at the following algebraic equations

$$\begin{aligned} a_{11}B_z^{(2)} + a_{12}F^{(2)} &= h_1 I_\theta, \\ a_{12}B_z^{(2)} + a_{22}F^{(2)} &= h_2 I_\theta, \end{aligned} \tag{10}$$

where

$$a_{11} = -\left\langle r\mathcal{E}\left(\left(\frac{dB_z^{(1)}}{dr}\right)^2 + \left(\frac{m}{r}\right)^2 (B_z^{(1)})^2\right)\right\rangle$$

$$+ m\left\langle \frac{d\mathcal{G}}{dr}(B_z^{(1)})^2\right\rangle + \left\langle r(B_z^{(1)})^2\right\rangle,$$

$$a_{12} = -\left\langle r\mathcal{G}\left(\left(\frac{dB_z^{(1)}}{dr}\right)\left(\frac{dF^{(1)}}{dr}\right) + \left(\frac{m}{r}\right)^2 B_z^{(1)}F^{(1)}\right)\right\rangle$$

$$+ m\left\langle \frac{d\mathcal{E}}{dr}B_z^{(1)}F^{(1)}\right\rangle,$$

$$a_{22} = -\left\langle r\mathcal{E}\left(\left(\frac{dF^{(1)}}{dr}\right)^2 + \left(\frac{m}{r}\right)^2 (F^{(1)})^2\right)\right\rangle$$

$$+ m\left\langle \frac{d\mathcal{G}}{dr}(F^{(1)})^2\right\rangle - \frac{1}{N_\parallel^2}\left\langle r\left(\left(\frac{dF^{(1)}}{dr}\right)^2 + \left(\frac{m}{r}\right)^2 (F^{(1)})^2\right)\right\rangle$$

$$+ \frac{1}{N_\parallel^2}\left\langle r\varepsilon_\parallel (F^{(1)})^2\right\rangle,$$

the angular brackets denote averaging over the radial coordinate, $I_\theta$ is the $\theta$-component of the surface current density, $h_1 = \dfrac{4\pi}{\omega}\dfrac{1}{1 - N_\parallel^2} r_A (B_z^{(1)}(r_A))'_{r_A}$, and $h_2 = -\dfrac{4\pi}{\omega}\dfrac{m}{(1 - N_\parallel^2)N_\parallel^2} F^{(1)}(r_A)$. When deriving Eqs. (10), we took into account the current continuity equation $\dfrac{m}{r_A} I_\theta + N_\parallel I_\parallel = 0$.

Equations (10) are equivalent to the equalities

$$\begin{aligned} DB_z^{(2)} &= (h_1 a_{22} - h_2 a_{12})I_\theta, \\ DF^{(2)} &= (h_2 a_{11} - h_1 a_{12})I_\theta, \end{aligned} \tag{11}$$

where $D = a_{11}a_{22} - a_{12}^2$.

For the eigenvalues $N_\parallel = N_\parallel^{(n,m)}$, the quantity $D$ vanishes, which indicates that the plasma is in resonance with the antenna current. If the magnetic field varies in the longitudinal direction, then the eigenvalues $N_\parallel^{(n,m)}$ are functions of the $z$ coordinate. Therefore, the eigenmode is in resonance with the Fourier harmonic of the antenna current only in a neighborhood of a certain point $z_s$, at which $N_\parallel = N_\parallel^{(n,m)}(z_s)$. In order to analyze the process of the excitation of eigenmodes by an external current, we turn to the general method for deriving equations for the envelopes $E_i^{(2)}(z)$ and $B_i^{(2)}(z)$. Specifically, we consider the quantity $D$ on the left-hand sides of relationships (11) as the operator

$$D \approx - iD'_{N_\parallel}(N_\parallel, z_s)\frac{d}{dz} + (z - z_s)D'_z(N_\parallel, z_s).$$

In this way, the first of Eqs. (11) becomes

$$\frac{dB_z^{(2)}}{dz} + iP(z - z_s)B_z^{(2)} = iQ_1 I_\theta, \tag{12}$$

where $P = D'_z/D'_{N_\parallel}$ and $Q_1 = (h_1 a_{22} - h_2 a_{12})/D'_{N_\parallel}$. The second of Eqs. (11) can be reduced to a form similar to Eq. (12) with the replacement of $Q_1$ by $Q_2 = (h_2 a_{11} - h_1 a_{12})/D'_{N_\parallel}$.

Equation (12) has the solution

$$B_z^{(2)}(z) = iQ_1 J(z), \tag{13}$$

where $J(z) = \exp(-iP(z - z_s)^2/2)\int_{-\infty}^{z} dz' \exp(iP(z' - z_s)^2/2)$.

Using expression (13) and an analogous expressions for $F^{(2)}(z)$, we can determine the power expended by the antenna current to excite the eigenmode. To do this, we

turn to the following relationships, which are valid in the vacuum region:

$$E_\theta = \frac{i}{1 - N_\parallel^2}\left(\frac{dB_z}{dr} + \frac{m}{r}F\right),$$

$$E_z = -\frac{i}{N_\parallel}F,$$

in which case we have

$$\mathbf{E} \cdot \mathbf{I}^* = \frac{i}{1 - N_\parallel^2}\left(-\frac{dB_z}{dr} + \frac{m}{rN_\parallel^2}F\right)_{r = r_A} \frac{4\pi}{\omega}I_\theta^*. \quad (14)$$

We also exploit the condition $D = a_{11}a_{22} - a_{12}^2 = 0$, which is valid for eigenmodes. As a result, we obtain the following spatial distribution of the work done by the current on exciting an individual eigenmode:

$$W^{(n, m)}(z, N_\parallel) = -\mathrm{Re}(\mathbf{E} \cdot \mathbf{I}^*) = -\frac{8\pi^2}{\omega^2}\frac{s_1 r_A|I_\theta|^2}{|D_z'|(1 - N_\parallel^2)^2}$$

$$\times\left(r_A(B_z^{(1)}(r_A))_{r_A}'|a_{22}|^{1/2} + \frac{ms_2}{N_\parallel^2}F^{(1)}(r_A)|a_{11}|^{1/2}\right)^2 \mathrm{Re}\, J(z),$$

where $s_1 = \mathrm{sgn}(a_{11}D_{N_\parallel}')$ and $s_2 = \mathrm{sgn}(a_{11}a_{12})$.

The total power lost by a Fourier harmonic of the current is equal to

$$W^{(n, m)}(N_\parallel) = \int_{-\infty}^{\infty} dz W^{(n, m)}(z, N_\parallel).$$

Integrating by parts readily yields

$$J = \mathrm{Re}\int_{-\infty}^{\infty} dz J(z) = \frac{\pi}{|P|}.$$

Then, we obtain

$$W^{(n, m)}(N_\parallel) = -\frac{8\pi^3 c}{\omega^2}\frac{s_1 r_A|I_\theta|^2|D_{N_\parallel}'|}{(D_z')^2(1 - N_\parallel^2)^2}$$

$$\times\left(r_A(B_z^{(1)}(r_A))_{r_A}'|a_{22}|^{1/2} + \frac{ms_2}{N_\parallel^2}F^{(1)}(r_A)|a_{11}|^{1/2}\right)^2. \quad (15)$$

The same result can also be derived in a simpler ("heuristic") way. From the first of Eqs. (11), we find

$$B_z^{(2)} = \frac{Q_1 D_{N_\parallel}'}{D}I_\theta. \quad (16)$$

The second of Eqs. (11) gives a similar expression for $F^{(2)}$.

The work done by the current on exciting the eigenmode is proportional to the imaginary parts of the inte-

grals $\int_{-\infty}^{\infty} dz B_z^{(2)}$ and $\int_{-\infty}^{\infty} dz F^{(2)}$, which in turn are proportional to $\mathrm{Im}\int_{-\infty}^{\infty} dz \frac{1}{D}$. The last expression is satisfied in the vicinity of the resonant point $z_s$, at which $N_\parallel$ is equal to the eigenvalue $N_\parallel^{(n, m)}$. Following the Landau circumvention rule, we represent the quantity $D$ in this vicinity in the form $D \approx i\nu D_\omega' + (z - z_s)D_z'$, where $\nu \longrightarrow 0$. Using this representation, we obtain

$$\mathrm{Im}\int_{-\infty}^{\infty} dz \frac{1}{D} = -\frac{\pi}{|D_z'|}\mathrm{sgn}\, D_\omega'. \quad (17)$$

From the relationship $\frac{d\omega}{dN_\parallel} = -\frac{\partial D/\partial N_\parallel}{\partial D/\partial \omega}$, we can see that, for the oscillations propagating in the positive direction along the z-axis, the quantities $D_{N_\parallel}'$ and $D_\omega'$ have opposite signs. Taking into account this circumstance and using expressions (14), (16), and (17), we again arrive at expression (15) for $W^{(n, m)}(N_\parallel)$.

The quantity $W^{(n, m)}(N_\parallel)$ should be positive. I failed to prove this assertion in the general case. However, in the Appendix, this assertion is proved for oscillations whose electric field is dominated by the right-polarized circular component and which offer the greatest promise for ECR plasma heating.

In the case of propagation along a nonuniform magnetic fields, the eigenvalue $N_\parallel^{(n, m)}$ changes and eigenmodes come into resonance with different Fourier harmonics of the antenna current. The total power expended by the antenna to excite the $(n, m)$ mode is equal to

$$W^{(n, m)} = \int dN_\parallel W^{(n, m)}(N_\parallel).$$

In order of magnitude, this power is

$$W^{(n, m)} \approx \frac{8\pi^3 c}{\omega^2}\frac{L_\parallel^2 r_A}{(N_{\parallel, \min}^{(n, m)})^3}e^{-2N_{\parallel, \min}^{(n, m)}\Delta_A}|I_\theta|^2, \quad (18)$$

where $N_{\parallel, \min}^{(n, m)}$ is the minimum value of $N_\parallel^{(n, m)}$ over the interval between the antenna and the ECR region, $\Delta_A$ is the distance from the antenna to the plasma boundary (to the critical surface), and all of the quantities having the dimension of length are again nondimensionalized by multiplying by $c/\omega$.

According to estimate (18), the power expended on the excitation of eigenmodes falls off sharply with increasing $N_\parallel^{(n, m)}$. Since the eigenvalues increase with $n$ and $m$, most of the antenna power should be spent on the excitation of the lowest mode (or several lowest modes).

Since the power expended on the excitation of eigenmodes depends nonmonotonically on the plasma density, it is expected that plasmas with densities far above the critical density will be difficult to maintain. The fact that the central part of a high-density plasma column is opaque to eigenmodes is also unfavorable for the maintenance of such plasmas.

## 4. CONCLUSION

Hence, in this paper, the suitability of helicon waves for ECR plasma heating in a magnetic beach configuration has been analyzed. The results of the analysis make it possible to conclude that this method can be used to heat plasmas with densities that are several times higher than the critical density. The heating of higher-density plasmas is hindered by the tendency of the eigenmodes of the plasma column to localize near the plasma boundary. The power expended by the antenna on exciting the eigenmodes of the plasma column in a longitudinally nonuniform magnetic field has been calculated.

*APPENDIX*

For ECR plasma heating, it is expedient to use oscillations whose electric fields are dominated by the right-polarized circular component. These are oscillations rotating azimuthally in the same direction as the electrons and having the azimuthal wavenumber $m = 1$. The left-polarized circular component of the electric field of such oscillations is small over the entire radial interval under consideration. Their longitudinal electric-field component is also small in the central part of the plasma column but becomes comparable to the right-polarized circular component in the peripheral region, where the plasma density passes through the critical value. An approximate analysis of these oscillations can be carried out by assuming that $E_+ = (E_r + iE_\theta)/\sqrt{2} = 0$, in which case the set of Maxwell's equations (1) can be reduced to the following two second-order equations, whose general structure is similar to that of Eqs. (11):

$$L_{11}E_\theta - L_{12}E_z = -\frac{4\pi i}{\omega} j_\theta,$$

$$L_{21}E_\theta - L_{22}E_z = -\frac{4\pi i}{\omega} j_z,$$

(A.1)

where $L_{11} = \frac{1}{r}\frac{d}{dr}r\frac{d}{dr} - \frac{(m-1)^2}{r^2} + 2(\varepsilon - g - N_\parallel^2)$, $L_{12} = N_\parallel\left(\frac{d}{dr} + \frac{m}{r}\right)$, $L_{21} = -N_\parallel\left(\frac{d}{dr} - \frac{m-1}{r}\right)$, and $L_{22} = \frac{1}{r}\frac{d}{dr}r\frac{d}{dr} - \frac{m^2}{r^2} + \varepsilon_\parallel$.

As in Section 3, we represent the components $E_\theta$ and $E_z$ in the form $E_\theta(\mathbf{r}) = E_\theta^{(1)}(r)E_\theta^{(2)}(z)$ and $E_z(\mathbf{r}) = E_z^{(1)}(r)E_z^{(2)}(z)$. We multiply the first and second of Eqs. (A.1) by $rE_\theta^{(1)}(r)$ and $rE_z^{(1)}(r)$, respectively, and integrate over the radius. As a result, we obtain

$$a_{11}E_\theta^{(2)} + a_{12}E_z^{(2)} = -\frac{4\pi i}{\omega} r_A E_\theta^{(1)}(r_A) I_\theta,$$

$$a_{12}E_\theta^{(2)} + a_{22}E_z^{(2)} = -\frac{4\pi i}{\omega} r_A E_z^{(1)}(r_A) I_z,$$

where a $a_{11} = -\left\langle r\left(\left(\frac{dE_\theta^{(1)}}{dr}\right)^2 + \left(\frac{m-1}{r}\right)^2(E_\theta^{(1)})^2\right)\right\rangle + 2\langle r(\varepsilon - g - N_\parallel^2)(E_\theta^{(1)})^2\rangle$, $a_{12} = \left\langle rE_\theta^{(1)}\left(\frac{dE_z^{(1)}}{dr} + \frac{m}{r}E_z^{(1)}\right)\right\rangle$, and $a_{22} = -\left\langle r\left(\left(\frac{dE_z^{(1)}}{dr}\right)^2 + \left(\frac{m}{r}\right)^2(E_z^{(1)})^2\right)\right\rangle + \langle r\varepsilon_\parallel(E_z^{(1)})^2\rangle$.

Using the same method as in Section 3, we arrive at the following expression for the work done by the antenna current on exciting an eigenmode of the plasma column in a nonuniform magnetic field:

$$W^{(n,m)}(N_\parallel) = -\langle \mathbf{j} \cdot \mathbf{E}^* \rangle$$

$$= -\frac{8\pi^3 c s_1 r_A}{\omega^2 |D_z'|}(I_z E_z^{(1)}(r_A)|a_{11}|^{1/2} + s_2 I_\theta E_\theta^{(1)}(r_A)|a_{22}|^{1/2})^2.$$

The quantity $Q = a_{11}\frac{\partial D}{\partial N_\parallel}$, which determines the sign of $W^{(n,m)}(N_\parallel)$, can be represented as

$$Q = -2\frac{a_{12}^2}{N_\parallel}\left(N_\parallel^2\langle r(E_\theta^{(1)})^2\rangle + \frac{a_{12}^2}{a_{22}}\right).$$

The first term in parentheses is positive, while the sign of the second term remains undetermined.

For a radial plasma density profile in the form of a smeared step function with $r_0 \gg \Delta$ (see Section 2), the longitudinal electric field is localized at the plasma–vacuum interface and varies radially on a characteristic scale of about $\approx \Delta$. Hence, we arrive at the following order-of-magnitude estimates: $a_{11} \approx r_0^2$, $a_{12} \approx N_\parallel r_0$, and $a_{22} \approx r_0$. If $r_0 \gg 1$, then the first term in parentheses is

larger in absolute value than the second term; as a result, we have $Q < 0$ and, accordingly, $W^{(n, m)}(N_{\parallel}) > 0$.

## REFERENCES

1. F. F. Chen, Phys. Plasmas **3**, 1783 (1996).

2. B. M. Harvey and C. N. Lashmore-Davis, Phys. Fluids B **5**, 3864 (1993).

3. A. Ganguli, M. K. Akhtar, and R. D. Tarey, Phys. Plasmas **5**, 1178 (1998).

4. S. Shinohara and K. P. Shamrai, Plasma Phys. Controlled Fusion **42**, 865 (2000).

5. V. F. Virko, G. S. Kirichenko, and K. P. Shamrai, Plasma Sources Sci. Technol. **11**, 10 (2002).

6. A. V. Timofeev, Fiz. Plazmy **27**, 131 (2001) [Plasma Phys. Rep. **27**, 119 (2001)].

7. A. V. Timofeev, Fiz. Plazmy **26**, 874 (2000) [Plasma Phys. Rep. **26**, 820 (2000)].

8. A. V. Zvonkov and A. V. Timofeev, Fiz. Plazmy **13**, 282 (1987) [Sov. J. Plasma Phys. **13**, 158 (1987)].

9. A. V. Timofeev and K. Yu. Kharitonov, Fiz. Plazmy **15**, 674 (1989) [Sov. J. Plasma Phys. **15**, 389 (1989)].

*Translated by O. E. Khadin*

<div align="center">

**PLASMA OSCILLATIONS
AND WAVES**

</div>

# Asymmetric Long-Wavelength Surface Waves in Magnetized Plasma Waveguides Entirely Filled with Plasma

## V. O. Girka and I. O. Girka

*Karazin National University, pl. Svobody 4, Kharkiv, 61077 Ukraine*
*e-mail: girkai@pht.univer.kharkov.ua*
Received April 3, 2002

**Abstract**—A theoretical study is made of the dispersion properties of electromagnetic surface waves with arbitrary azimuthal mode numbers and with a small axial wavenumber in cylindrical metal waveguides entirely filled with a radially inhomogeneous, cold, magnetized plasma. The frequency ranges in which the extraordinary polarized waves under analysis can exist are found, and the conditions for their resonant interaction with an ordinary bulk wave are determined. The eigenfrequency of these surface waves is investigated as a function of the plasma parameters, the axial wavenumber, and the azimuthal mode number. Simple analytic expressions are derived for the eigenfrequencies of the surface waves under study propagating in a homogeneous plasma waveguide. © 2002 MAIK "Nauka/Interperiodica".

## 1. INTRODUCTION

In order to choose optimum conditions for the generation of oscillations in plasma-filled waveguides, it is necessary to know the waveguide eigenfrequencies, because it is precisely at frequencies close to them that the plasma interaction with charged particle beams [1] or with an external alternating electric field [2] is most efficient. Filling a waveguide with plasma expands the range of the waveguide eigenfrequencies. The dispersion properties of plasma waveguides began to be investigated using the simplest models [3] and are still being studied for the cases of gaseous [4–10] and solid-state [11–13] plasmas.

The dispersion properties of electromagnetic waves propagating strictly in the azimuthal direction in cylindrical metal waveguides entirely filled with a homogeneous plasma—the so-called azimuthal surface waves (ASWs)—were investigated in [14] and, in the potential approximation, in [15]. In [16, 17], it was shown that ASWs can be generated as a result of beam–plasma instability or dissipative instability. One of the main advantages of the oscillators based on ASWs is their relative compactness in the axial direction. A useful property of ASWs is that they propagate in only one direction along the plasma–metal boundaries. This phenomenon is well known for surface waves propagating across the external magnetic field in waveguide structures with the Voight geometry [15]. During the excitation of such waves, the reflected signal in the system is absent, which may turn out to be very helpful in some cases.

Over the past decade, interest in the eigenmodes of plasma waveguides has increased in connection with their use in sustaining gas discharges [10, 18–21]. Plasma sources that are based on surface waves (SWs)

find wide application in plasma technology; e.g., they are used to process solid-state plates with large working surfaces [20, 21].

In [19], it was shown that ASWs can be employed to sustain low-pressure gas discharges that are used in modern-day plasma microtechnologies. The properties of gas discharges sustained by axisymmetric ($m = 0$) and dipole ($m = \pm 1$) SWs propagating along the axis of a cylindrical chamber were investigated experimentally in [18, 22, 23]. The possibility of sustaining gas discharges in a magnetized plasma column by quadrupole ($m = \pm 2$) and octopole ($m = \pm 3$) SWs was studied numerically in [10, 24].

The dispersion properties of electromagnetic SWs with small axial wavenumbers at cylindrical plasma–metal boundaries have not yet been studied. For arbitrary values of the parameters of a magnetized plasma system, the azimuthal mode number $m$, and the axial wavenumber $k_z$, the dispersion properties of SWs can be investigated only numerically. For long axial wavelengths, the problem can be solved by means of perturbation theory, in which case ASWs are used as a zeroth approximation [14]. The objective of our work is to investigate the dispersion properties of long-wavelength SWs.

Our paper is organized as follows. In Section 2, we describe the waveguide model and write out the basic equations. In Section 3, we derive a second-order dispersion relation for long-wavelength magnetoplasma SWs in a cylindrical metal waveguide entirely filled with a plasma with a radially nonuniform density profile. We also investigate the limiting case of a plasma with a radially uniform density profile. In Section 4, we solve the dispersion relation for SWs with positive azimuthal mode numbers, and, in Section 5, we solve the

same relation for SWs with negative azimuthal mode numbers. In Section 6, we show that the dispersion properties of long-wavelength, high-frequency SWs can be affected in a resonant fashion by the value of $k_z$. In the Conclusion, we summarize the main results of our study.

## 2. FORMULATION OF THE PROBLEM

We consider a perfectly conducting, circular cylindrical metal waveguide of radius $a$ filled entirely with a plasma that is assumed to be homogeneous in the cylindrical coordinates $z$ and $\vartheta$. The external magnetic field is directed along the waveguide axis ($\mathbf{H}_0 \parallel \mathbf{z}$).

The electrodynamic properties of a cold, weakly collisional, magnetized plasma are described by the dielectric tensor (see, e.g., [3–5])

$$\varepsilon_{ik}(r) = \begin{pmatrix} \varepsilon_1 & i\varepsilon_2 & 0 \\ -i\varepsilon_2 & \varepsilon_1 & 0 \\ 0 & 0 & \varepsilon_3 \end{pmatrix}. \quad (1)$$

In this case, the components of the wave electromagnetic field, which are assumed to be proportional to $\propto \exp i(k_z z + m\vartheta - \omega t)$, are described by the following Maxwell's equations:

$$\varepsilon_1 E_r + i\varepsilon_2 E_\vartheta = -N_\vartheta B_z + N_z B_\vartheta, \quad (2)$$

$$-i\varepsilon_2 E_r + \varepsilon_1 E_\vartheta = -N_z B_r + \frac{c}{i\omega}\frac{\partial B_z}{\partial r}, \quad (3)$$

$$\varepsilon_3 E_z = \frac{ic}{\omega r}\frac{\partial}{\partial r}(rB_\vartheta) + N_\vartheta B_r, \quad (4)$$

$$B_r = N_\vartheta E_z - N_z E_\vartheta, \quad (5)$$

$$B_\vartheta = N_z E_r - \frac{c}{i\omega}\frac{\partial E_z}{\partial r}, \quad (6)$$

$$B_z = \frac{c}{i\omega r}\frac{\partial}{\partial r}(rE_\vartheta) - N_\vartheta E_r. \quad (7)$$

Here and below, $N_z = ck_z/\omega$ is the axial refractive index and $N_\vartheta = cm/(\omega r)$ is the azimuthal refractive index.

For ASWs propagating strictly in the azimuthal direction ($k_z = 0$), the set of Maxwell's equations (2)–(7) splits into two independent subsets of equations. The subset consisting of Eqs. (4)–(6) describes an H-wave, having the field components $E_z$, $B_r$, and $B_\vartheta$. The subset consisting of Eqs. (2), (3), and (7) describes an E-wave, having the field components $E_r$, $E_\vartheta$, and $B_z$. Hence, ASWs of the E- and H-types propagate independently of one another. For long-wavelength SWs with a small but finite axial wavenumber $k_z$, the coupling between the E- and H-waves is weak. The dispersion properties of such waves can be studied by means of

perturbation theory and by using the theory of ASWs as a zeroth approximation [14].

We restrict ourselves to considering a high-density plasma such that $\omega_{pe}^2 \gg \omega_{ce}^2$ (where $\omega_{pe}$ is the electron plasma frequency and $\omega_{ce}$ is the electron cyclotron frequency). This inequality always holds for an $n$-semiconductor plasma and can be satisfied for a gas plasma in a weak magnetic field under laboratory conditions. It is precisely the limiting case of a high-density plasma that is most interesting for plasma technologies [18]. Note also that the dispersion properties of ASWs in cylindrical, strongly magnetized ($\omega_{pe}^2 < \omega_{ce}^2$) plasma waveguides were investigated in [25].

The fields of an SW satisfy the following boundary conditions: the wave field amplitudes are finite over the waveguide volume and the tangential component of the electric field vanishes at the inner surface of the metal chamber.

## 3. LONG-WAVELENGTH SURFACE WAVES IN A RADIALLY INHOMOGENEOUS PLASMA

If we neglect the terms of second order and higher, we can reduce Eqs. (2)–(7) to the following two second-order differential equations for the axial components of the electric and magnetic fields in a radially inhomogeneous plasma:

$$\frac{1}{r}\frac{\partial}{\partial r}\frac{r}{k_H^2}\frac{\partial B_z}{\partial r} - \left[1 + \frac{m^2}{r^2 k_H^2} - \frac{m}{r}\frac{\partial}{\partial r}\left(\frac{\mu}{k_H^2}\right)\right]B_z = \hat{K}E_z, \quad (8)$$

$$\frac{1}{r}\frac{\partial}{\partial r}r\frac{\partial E_z}{\partial r} - \left(k_0^2 + \frac{m^2}{r^2}\right)E_z = \hat{M}B_z. \quad (9)$$

The small right-hand sides of Eqs. (8) and (9) have the form

$$\hat{K}E_z = iN_z\left\{\frac{m}{r}E_z\frac{\partial}{\partial r}\left(\frac{1}{k_H^2}\right) + \frac{\mu k_0^2}{k_H^2}E_z + \frac{\partial}{\partial r}\left(\frac{\mu}{k_H^2}\right)\frac{\partial E_z}{\partial r}\right\}, \quad (10)$$

$$\hat{M}B_z = iN_z\left\{\frac{1}{N_H^2}\frac{\partial \mu}{\partial r}\frac{\partial B_z}{\partial r}\right.$$

$$\left. + \left[\frac{\omega^2}{c^2}\mu + \frac{m}{r}\frac{\partial}{\partial r}\left(\frac{1}{N_H^2}\right) - \frac{\mu m}{r}\frac{\partial}{\partial r}\left(\frac{\mu}{N_H^2}\right)\right]B_z\right\}. \quad (11)$$

The penetration depth $k_0^{-1}$ for an H-wave field (with ordinary polarization) and the penetration depth $k_H^{-1}$ for

an E-wave (with extraordinary polarization) are defined in terms of the tensor elements $\varepsilon_{ik}$ as follows:

$$k_0^2 = -(\omega/c)^2 \varepsilon_3, \quad k_H^2 = (\omega/c)^2 N_H^2,$$

$$N_H^2 = (\varepsilon_1 - N_z^2)(\mu^2 - 1), \quad \mu = \varepsilon_2/(\varepsilon_1 - N_z^2). \tag{12}$$

In [26], the set of coupled equations for the longitudinal components $E_z$ and $B_z$ of the wave electromagnetic field was derived for arbitrary values of $k_z$ and for a radially homogeneous plasma in an axial magnetic field.

Equations (8) and (9) can be solved by the method of varying a constant:

$$B_z = \left(A_2 - A_1 \int_a^r \frac{\tilde{\psi} k_H^2 \hat{K} \varphi dr}{W(\psi, \tilde{\psi})}\right)\psi + A_1\tilde{\psi}\int_0^r \frac{\psi k_H^2 \hat{K}\varphi dr}{W(\psi, \tilde{\psi})}, \tag{13}$$

$$E_z = \left(A_1 - A_2 \int_a^r \frac{\tilde{\varphi}\hat{M}\psi dr}{W(\varphi, \tilde{\varphi})}\right)\varphi + A_2\tilde{\varphi}\int_0^r \frac{\varphi\hat{M}\psi dr}{W(\varphi, \tilde{\varphi})}. \tag{14}$$

Here, $\psi(r)$ and $\varphi(r)$ are such solutions to Eqs. (8) and (9) with zero on the right-hand sides that are finite at the waveguide axis (at $r = 0$) and the functions $\tilde{\psi}(r)$ and $\tilde{\varphi}(r)$ are solutions to the same equations that are linearly independent of $\psi$ and $\varphi$. Solutions (13) and (14) contain two integration constants $A_1$ and $A_2$. The remaining two integration constants have already been determined from the condition that the field components $E_z$ and $B_z$ are finite at the waveguide axis, where the functions $\tilde{\varphi}$ and $\tilde{\psi}$ have singularities. The Wronskian of the functions $\psi(r)$ and $\tilde{\psi}(r)$ is equal to

$$W(\psi, \tilde{\psi}) = \psi\frac{\partial\tilde{\psi}}{\partial r} - \tilde{\psi}\frac{\partial\psi}{\partial r} \propto \frac{k_H^2}{r}, \tag{15}$$

and the Wronskian of the functions $\varphi(r)$ and $\tilde{\varphi}(r)$ is inversely proportional to the radial coordinate $r$:

$$W(\varphi, \tilde{\varphi}) = \varphi\frac{\partial\tilde{\varphi}}{\partial r} - \tilde{\varphi}\frac{\partial\varphi}{\partial r} \propto \frac{1}{r}. \tag{16}$$

According to Eqs. (2)–(7), the azimuthal component of the electric field is expressed in terms of $E_z$ and $B_z$ as follows (see, e.g., [4]):

$$E_\vartheta = \frac{ic}{\omega N_H^2}\frac{\partial B_z}{\partial r} + \frac{i\mu N_\vartheta}{N_H^2}B_z + \frac{N_z N_\vartheta}{N_H^2}E_z + \frac{\mu N_z c}{\omega N_H^2}\frac{\partial E_z}{\partial r}. \tag{17}$$

The above boundary conditions for $E_\vartheta$ and $E_z$ at the inner surface of a metal waveguide make it possible to write the dispersion relation for long-wavelength SWs in the form

$$A_{12}A_{21} = A_{11}A_{22}, \tag{18}$$

where

$$A_{11} = \left\{\frac{ic}{\omega N_H^2}\frac{\partial\tilde{\psi}}{\partial r}\int_0^a \frac{\psi k_H^2 \hat{K}\varphi dr}{W(\psi, \tilde{\psi})}\right.$$

$$\left. + \frac{i\mu N_\vartheta}{N_H^2}\tilde{\psi}\int_0^a \frac{\psi k_H^2 \hat{K}\varphi dr}{W(\psi, \hat{\psi})} + \frac{N_z N_\vartheta}{N_H^2}\varphi + \frac{\mu N_z c}{\omega N_H^2}\frac{\partial\varphi}{\partial r}\right\}\Bigg|_{r=a}, \tag{19}$$

$$A_{12} = \left\{\frac{ic}{\omega N_H^2}\frac{\partial\psi}{\partial r} + \frac{\mu N_\vartheta}{N_H^2}\psi\right\}\Bigg|_{r=a}, \tag{20}$$

$$A_{21} = \varphi(a), \tag{21}$$

$$A_{22} = \tilde{\varphi}(a)\int_0^a \frac{\varphi\hat{M}\psi dr}{W(\varphi, \tilde{\varphi})}. \tag{22}$$

It should be noted that dispersion relation (18) is, on the one hand, a generalization of the dispersion relation obtained in [14] to small values of $k_z$, and, on the other, a particular case of the general dispersion relation that was derived in [8] in order to determine the spectra of the eigenfrequencies of a coaxial plasma waveguide in a finite magnetic field. Let us discuss the structure of dispersion relation (18), which is similar to the structure of the dispersion relations for weakly coupled oscillations. In such an approach, the condition $A_{12} = 0$ plays the role of the dispersion relation for extraordinary ASWs (an E-wave), and the solution $\omega_0$ to the dispersion relation is assumed to be known. The variable sign of this coefficient in the frequency ranges where the waves under consideration can exist (in [14], these ranges were determined for the case of an ASW) ensures that Eq. (18) has solutions. The condition $A_{21} = 0$ could be the dispersion relation for ASWs (H-waves); however, under the given conditions, its solutions describe only bulk waves. The right-hand side of dispersion relation (18) is quadratic in the small axial wavenumber $k_z$, which serves as the parameter of the weak coupling between E- and H-waves. These circumstances allow us to conclude that the correction $\Delta\omega$ to the eigenfrequency of the long-wavelength SWs is quadratic in the axial wavenumber, $\Delta\omega \propto k_z^2$. We stress that the axial wavenumber also enters the left-hand side of dispersion relation (18) through the penetration depth $k_H^{-1}$ of the SWs into the plasma.

## 4. LONG-WAVELENGTH, LOW-FREQUENCY SURFACE WAVES IN A HOMOGENEOUS PLASMA WAVEGUIDE

In what follows, we restrict ourselves to analyzing the model with a uniform radial plasma density profile. The reasons for this are twofold. First, this model provides a good description of solid-state plasmas. Sec-

ond, the radial density variations can be neglected when the plasma density changes insignificantly over distances on the order of the penetration depth of the wave into the plasma; for a gas discharge sustained by an SW, it is precisely at these distances that the plasma density is maintained at a constant level.

For a radially homogeneous plasma, Eqs. (8) and (9) for $E_z$ and $B_z$ are inhomogeneous Bessel equations. The solutions to the corresponding homogeneous equations that are finite at the waveguide axis are modified Bessel functions of the first kind:

$$\psi = I_m(k_H r), \quad \varphi = I_m(k_0 r). \tag{23}$$

The solutions to Eqs. (8) and (9) that are linearly independent of solutions (23) are modified Bessel functions of the second kind:

$$\tilde{\psi} = K_m(k_H r), \quad \tilde{\varphi} = K_m(k_0 r). \tag{24}$$

Solutions (23) and (24) are valid for $k_0^2 > 0$ and $k_H^2 > 0$. It is the latter condition, $k_H^2 > 0$, that determines the frequency ranges in which SWs can exist and which, in the limit $k_z = 0$, coincide with the ranges where ASWs exist [14]: SWs with positive azimuthal mode numbers $m$ exist in the low-frequency (LF) range

$$|\omega_{ce}|\sqrt{\frac{\omega_{pi}^2 + c^2 k_z^2}{\omega_{pe}^2 + \omega_{ce}^2}} < \omega < |\omega_{ce}|, \tag{25}$$

and SWs with negative azimuthal mode numbers $m$ exist in the high-frequency (HF) range

$$\sqrt{\omega_{ce}^2 + \omega_{pe}^2 + c^2 k_z^2} < \omega < \frac{1}{2}|\omega_{ce}|$$
$$+ \sqrt{\frac{1}{4}\omega_{ce}^2 + \omega_{pe}^2 + c^2 k_z^2}. \tag{26}$$

The property of SWs to propagate in only one direction across the external magnetic field is well known for waveguides in which the plasma is in contact with the metal wall [3, 15]. This property, which is called "unidirectionality," can be especially useful in various radio engineering devices in which it is necessary to ensure that the reflected signal be absent.

In frequency ranges (25) and (26), the quantity $k_0^2$ has different signs, namely $k_0^2 > 0$ in the LF range and $k_0^2 < 0$ in the HF range.

For a uniform density profile, expressions (10) and (11) for the right-hand sides of Eqs. (8) and (9) can be significantly simplified:

$$\hat{K}E_z = -iN_z\frac{\mu\varepsilon_3}{N_H^2}E_z, \quad \hat{M}B_z = iN_z\mu\frac{\omega^2}{c^2}B_z, \tag{27}$$
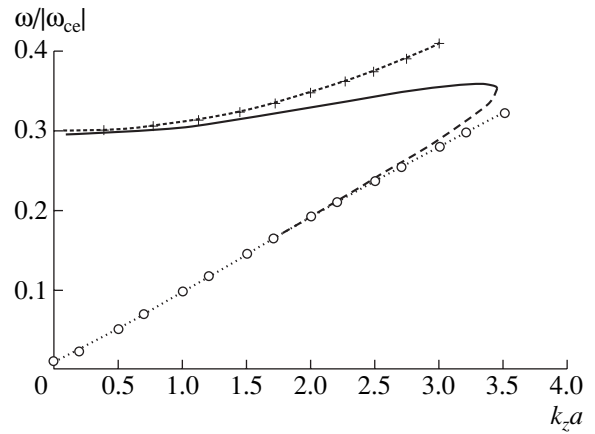
**Fig. 1.** Frequency of an LF SW with extraordinary polarization, normalized to the absolute value of the electron cyclotron frequency, as a function of the product of the axial wavenumber and the waveguide radius. The calculations were carried out for the azimuthal mode number $m = 3$, $\omega_{pe} = 5|\omega_{ce}|$, and $a = 10\delta$.

in which case dispersion relation (18) can be written in a fairly simple explicit form:

$$A_{11} = N_z\mu k_0^2 aQ\left[\frac{1}{N_H}K_m'(k_H a) + \frac{\mu N_\vartheta}{N_H^2}K_m(k_H a)\right]$$
$$+ \frac{N_z N_\vartheta}{N_H^2}I_m(k_0 a) + \frac{\mu k_z k_0}{k_H^2}I_m'(k_0 a), \tag{28}$$

$$A_{12} = \frac{i}{N_H^2}[N_H I_m'(k_H a) + \mu N_\vartheta I_m(k_H a)], \tag{29}$$

$$A_{21} = I_m(k_0 a), \tag{30}$$

$$A_{22} = -i\frac{\omega^2}{c^2}N_z\mu a K_m(k_0 a)Q, \tag{31}$$

$$Q = (k_0^2 - k_H^2)[k_0 I_m(k_H a)I_m'(k_0 a)$$
$$- k_H I_m(k_0 a)I_m'(k_H a)]. \tag{32}$$

Taking into account the small axial wavenumber $k_z$ leads to an additional (in comparison with the case of ASWs) solution to the dispersion relation. This additional solution describes the wave that will be referred to as a slow mode. In the LF range, the frequency $\omega_-$ of the slow mode is approximately proportional to $k_z$; i.e., the frequency $\omega_-$ approaches the cutoff frequency as $k_z \longrightarrow 0$ (Fig. 1). The group velocity of the slow mode is always positive, $\partial\omega_-/\partial k_z > 0$, and in absolute value exceeds the group velocity of the fast mode.

The fast mode can be described as follows. In the limit $k_z \longrightarrow 0$, its frequency $\omega_+$ approaches the frequency of the ASW. For very small $k_z$ values, there exists a portion of the dispersion curve of the fast mode

**Table**

| Quantity | Limit $a \ll |m|\delta$ | | Limit $a \gg |m|\delta$ | |
|---|---|---|---|---|
| $\omega_0 \approx$ | $\|\omega_{ce}\|\left(1 - \dfrac{a^2}{2m^2\delta^2}\right)$ | (34) | $\|\omega_{ce}\|m\delta/a$ | (36) |
| $\Delta\omega \approx$ | $\dfrac{1}{2}\left(\dfrac{a}{2\delta(m+1)}\right)^2\left(\dfrac{k_z a}{m}\right)^2\omega_0$ | (35) | $(3/8)(k_z a/m)^2\omega_0$ | (37) |

over which the dispersion is normal, $\partial\omega_+/\partial k_z > 0$. When the small value of the axial wavenumber is taken into account, the frequency of the SW is slightly higher than the frequency of the ASW. This allows us to calculate the frequency of the fast mode of the SW by the method of successive approximations, i.e., by representing it in the form $\omega_+ = \omega_0 + \Delta\omega$, and by using the theory of ASWs as a zeroth approximation [14], according to which $\omega_0$ is the frequency of the ASW in the waveguide under consideration. In this way, the small correction $\Delta\omega$ to the frequency is quadratic in $k_z$:

$$\Delta\omega = \left(\frac{A_{11}A_{22}}{A_{21}} - \frac{\partial A_{12}}{\partial k_z^2}\bigg|_{\omega=\omega_0} k_z^2\right)\left[\frac{\partial A_{12}}{\partial\omega}\bigg|_{\omega=\omega_0}\right]^{-1} \propto k_z^2. \quad (33)$$

Simple analytic solutions to dispersion relation (18) can be obtained only in the two limiting cases of a wide ($a \gg |m|\delta$) and a narrow ($a \ll |m|\delta$) waveguide for an SW with the given azimuthal mode number $m$ (here and below, $\delta = c/\Omega_e$ is the skin depth).

For the benefit of our readers, the results of our analytic investigation are summarized in the table (for expressions 34–37, see the table).

An analysis of expressions (35) and (37) shows that the method of successive approximations can be used to study the dispersion properties of the fast mode of a long-wavelength low-frequency SW in a fairly wide range of axial wavenumbers. For wide waveguides, this range is determined by the inequality

$$k_z^2 \ll 8(m/a)^2. \quad (38)$$

For narrow waveguides, the analytic solution is valid over a wider range:

$$k_z^2 \ll 8(m(m+1)\delta/a^2)^2. \quad (39)$$

For larger values of $k_z$, the frequency $\omega_+$ increases to its maximum value; then, the dispersion becomes anomalous, $\partial\omega_+/\partial k_z < 0$, over a certain portion of the dispersion curve (Fig. 1). As the axial wavenumber $k_z$ further increases, the frequencies of the fast and slow modes approach one another and, at a certain value $k_z = k_m$, the modes have the same frequency $\omega_m$. It turns out that the group velocity $\partial\omega/\partial k_z$ of the SWs increases without bound as their frequencies approach $\omega_m$; as a result, the notion of group velocity becomes meaningless.

This circumstance can be interpreted as follows. For an SW whose frequency and axial wavenumber are close to $\omega_m$ and $k_m$, respectively, the above representation of the electromagnetic perturbation in the form of a single harmonic, $\propto \exp[i(k_z z + m\vartheta - \omega t)]$, is incorrect. Near the point in question, the dispersion curve $k_z(\omega)$ can be approximately described by the squared parabola

$$k_z(\omega) = k_m - (\omega - \omega_m)^2/\alpha, \quad (40)$$

where $k_m = k_z(\omega_m)$ and $\alpha$ is a constant having the dimension of acceleration (m/s$^2$). In this case, an electromagnetic pulse with the field $\propto \exp(-t^2/(2\tau^2))\cos(k_m z - \omega_m t)$ (where $\tau$ is the pulse duration) spreads out from the point at which it was originally formed in the axial direction over a distance of about $\alpha\tau^2/2$.

Now we compare the results of an analytic investigation of dispersion relation (18) with the results of its numerical solution. Figure 1 illustrates the dependence $\omega(k_z)$ for an SW in the LF range (25). The abscissa is the product $k_z a$ of the axial wavenumber times the waveguide radius, and the ordinate is the frequency normalized to the absolute value of the electron cyclotron frequency. The parameters of the wave and of the plasma column were chosen to be $m = 3$, $\omega_{pe} = 5|\omega_{ce}|$, and $a = 10\delta$. Recall that, in the case at hand, the applicability of our approach is restricted to the values of the product $k_z a$ that satisfy the inequality $k_z a < m$. The solid line is the dispersion curve of the fast mode, and the dashed line is for the slow mode. The dotted line with open circles indicates the boundary of the LH range (25). The dotted line with crosses was calculated from asymptotic formulas (36) and (37).

In Fig. 1, we do not plot the dispersion curve for a narrow waveguide, because, in the case at hand, the dependence $\Delta\omega(k_z)$ is very weak [see expression (35)].

## 5. LONG-WAVELENGTH, HIGH-FREQUENCY SURFACE WAVES IN A HOMOGENEOUS PLASMA WAVEGUIDE

It is known that bulk H-waves exist under conditions corresponding to the HF range (26). In this case, the

solutions to Eq. (9) with zero on the right-hand side can be represented as

$$\varphi = J_m(k_1 r), \quad \tilde{\varphi} = N_m(k_1 r), \quad k_1^2 = -k_0^2 > 0, \quad (41)$$

where $J_m$ is the Bessel function and $N_m$ is the Neumann function [27]. In dispersion relation (18) for HF SWs with negative azimuthal mode numbers, the coefficient $A_{12}$ is, as before, described by expression (29) and the other coefficients $A_{ij}$ are given by

$$A_{11} = -N_z \mu k_1^2 Q_1 \left[ \frac{K_m'(k_H a)}{N_H} + \mu \frac{N_\vartheta}{N_H^2} K_m(k_H a) \right]$$
$$+ \frac{N_z N_\vartheta}{N_H^2} J_m(k_1 a) + \frac{\mu k_z k_1}{k_H^2} J_m'(k_1 a), \quad (42)$$

$$A_{21} = J_m(k_1 a), \quad (43)$$

$$A_{22} = \frac{i\pi}{2} \frac{\omega^2}{c^2} N_z \mu N_m(k_1 a) Q_1,$$
$$Q_1 = \int_0^a r J_m(k_1 r) I_m(k_H r) dr. \quad (44)$$

An analysis of dispersion relation (18) shows that HF ASWs cannot propagate in narrow waveguides. The radius of the waveguide in which HF ASWs exist can be estimated analytically from the inequality $a/\delta > \omega_{pe}|m/\omega_{ce}|$. For $\omega_{pe} = 3|\omega_{ce}|$, the analytic estimate shows that HF ASWs with the azimuthal mode number $m = -2$ can propagate only in waveguides whose radius is larger than the skin depth by a factor of six or more. Numerical analysis also shows that the dispersion relation $A_{12} = 0$ for ASWs has a solution when $a > 5\delta$, which justifies the validity of analytic calculations.

For wide waveguides, the eigenfrequency of HF ASWs can be roughly estimated as

$$\omega_0 = \sqrt{\omega_{pe}^2 + \omega_{ce}^2 + (m^2 c^2/a^2)}, \quad (45)$$

which leads to the following estimate for the argument $k_1 a$ of the Bessel function in the coefficient $A_{21}$:

$$k_1 a \approx (m^2 + \omega_{ce}^2 a^2/c^2)^{\frac{1}{2}}. \quad (46)$$

If the applied magnetic field is not too strong and the waveguide dimensions are not too large,

$$a^2 \omega_{ce}^2/c^2 < j_{|m|, s}^2 - m^2, \quad (47)$$

then the azimuthal ordinary bulk eigenmodes cannot exist in such a waveguide. Here, $j_{|m|, s}$ is the $s$th root of the $|m|$th order Bessel function and $J_{|m|}(j_{|m|, s}) = 0$. In this
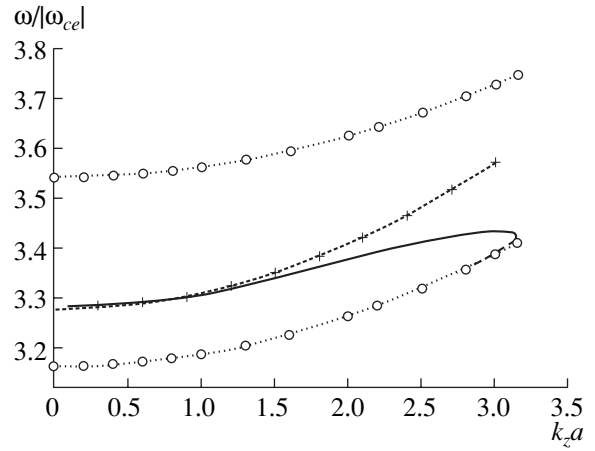


**Fig. 2.** Same as in Fig. 1, but for the HF SW; the azimuthal mode number is $m = -2$, $\omega_{pe} = 3|\omega_{ce}|$, and $a = 7\delta$.

case, the finite axial wavenumber gives rise to a positive correction to the frequency of HF SWs:

$$\Delta\omega = \frac{1}{2} N_z^2 \omega_0 + \frac{\pi}{2} |m| N_z^2 J_{|m|}'(\sqrt{m^2 + a^2 \omega_{ce}^2/c^2})$$
$$\times N_{|m|}(\sqrt{m^2 + a^2 \omega_{ce}^2/c^2}) \omega_0. \quad (48)$$

The results of a numerical solution of dispersion relation (18) for SWs with the azimuthal mode number $m = -2$ are illustrated in Fig. 2. The abscissa and ordinate are the same as in Fig. 1. The computations were carried out for the waveguide parameters $\omega_{pe} = 3|\omega_{ce}|$ and $a = 7\delta$. The boundaries of the HF range (26) are indicated by the dotted line with open circles. The dotted line with crosses was calculated from asymptotic formulas (45) and (48). Note that, for the chosen parameters of the wave and the plasma, all of the eigenfrequencies of an ordinary bulk mode, which are determined from the condition

$$k_1 a = j_{|m|, s}, \quad (49)$$

lie above the HF range (26).

It seems worthwhile to try to compare our results with the results obtained in other papers (e.g., in papers by Azarenkov *et al.* [10, 24]) in which a thorough numerical analysis of the dispersion properties of the quadrupole and octopole modes of SWs was carried out. The dispersion curves presented in [24] contain an error: there are points at which the wave group velocity is infinite. Although our analysis is restricted to small values of the axial wavenumber, the interval of $k_z$ values in Figs. 1 and 2 is more than half of the interval considered in [24]. Unfortunately, our results cannot be compared with the results of [24] even at a qualitative level, because, in that paper, a study was made of a plasma cylinder in an infinite empty space.

The objective of [10] was to numerically investigate the dispersion properties of SWs, in particular, of the
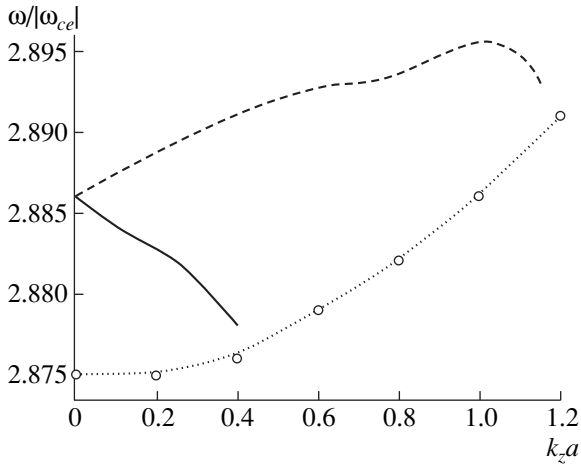
**Fig. 3.** Frequency of an HF SW with extraordinary polarization, normalized to the absolute value of the electron cyclotron frequency, as a function of the product of the axial wavenumber and the waveguide radius under the conditions of resonant interaction with an ordinary bulk wave. The calculations were carried out for the azimuthal mode number $m = -1$, $\omega_{pe} = 2.695|\omega_{ce}|$, and $a = 10\delta$.
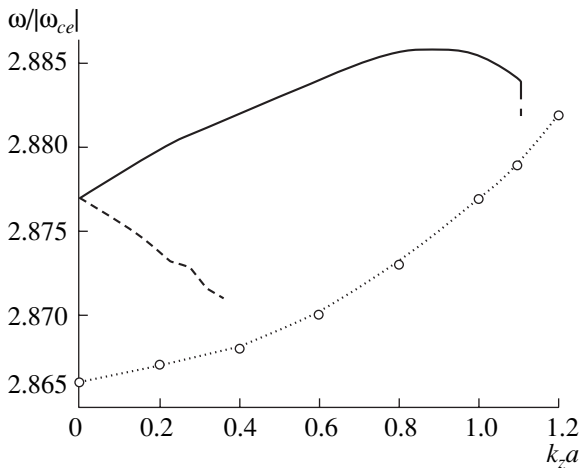


**Fig. 4.** Same as in Fig. 3, but for the azimuthal mode number $m = -1$, $\omega_{pe} = 2.686|\omega_{ce}|$, and $a = 10\delta$.

waves with a small axial wavenumber (up to $k_z a = 0.1$), in waveguides, including those with a narrow vacuum gap (up to $(a - a_{pl}) = 0.1a$, where $a_{pl}$ is the radius of the plasma cylinder). At first glance, it might be expected that the dispersion properties of the SWs described in [10] would be very similar to those of ASWs at the plasma–metal boundary. However, in [28], it was shown that, in order for a vacuum gap between the metal waveguide wall and the plasma to be ignored in the investigation of the dispersion properties of ASWs, the gap width should be small enough to satisfy the inequality

$$\sqrt{a - a_{pl}} \ll |\omega_{ce}| \sqrt{a}/(2\sqrt{|m|}\omega_{pe}). \tag{50}$$

In [10], the computations were carried out for a wide range of waveguides (with vacuum gaps of different widths), but in all cases condition (50) was not satisfied. Consequently, none of the plots presented in [10] are suitable for comparison with the results of our study. On the other hand, the results obtained in [10] from a numerical solution of the dispersion relation in the long-wavelength limit agree well with the results of [28], where the dispersion properties of ASWs were investigated in a waveguide with a vacuum gap between the plasma cylinder and the metal wall. Judging from the description of the plots in [10], it appears that the radius of the plasma column exceeds the radius of the metal chamber, while the formulation of the problem implies that the column is inside the chamber. However, it seems that the source of this mistake lies not in computational errors but rather in inaccurate description of the plots.

## 6. RESONANT EFFECT OF THE AXIAL WAVENUMBER ON THE DISPERSION PROPERTIES OF SURFACE WAVES

The eigenfrequencies of an extraordinary ASW and an ordinary azimuthal bulk wave can be brought into coincidence by increasing the waveguide radius $a$ and/or the magnetic field. The conditions under which this can be done may be estimated from formula (47) with the equality sign in place of the relation "less than." Under these conditions, dispersion relation (18) reduces to a quadratic equation for the correction $\Delta\omega$:

$$\left(\frac{\partial A_{12}}{\partial k_z^2}\bigg|_{\omega = \omega_0} k_z^2 + \frac{\partial A_{12}}{\partial \omega}\bigg|_{\omega = \omega_0} \Delta\omega\right)\frac{\partial A_{21}}{\partial \omega}\bigg|_{\omega = \omega_0} \Delta\omega$$
$$= A_{11}A_{22}. \tag{51}$$

In solving Eq. (51), we can neglect the first term in parentheses on the left-hand side, because this term is quadratic in the axial wavenumber, while the second term is linear in $k_z$. In this case, the solution to Eq. (51) has the form $\omega = \omega_0 + \Delta\omega$, where

$$\omega_0 = \sqrt{\omega_{pe}^2 + j_{|m|, s}^2 c^2/a^2}, \tag{52}$$

$$\Delta\omega = \pm\omega_0 N_z N_\vartheta \left(\frac{\pi}{2|m|} j_{|m|, s} N_{|m|}(j_{|m|, s})\bar{J}_{|m|}\right)^{\frac{1}{2}}, \tag{53}$$

with the mean value $\bar{J}_{|m|} = Q_1 k_H/(aI_m(k_H a))$.

Under the above conditions, the small axial wavenumber has a stronger effect on the eigenfrequency of an SW: the correction $\Delta\omega$ (52) introduced by the small axial wavenumber $k_z$ is directly proportional to it, $\Delta\omega \propto k_z^1$. For this reason, it is natural to call these conditions the resonance conditions. The magnetic field sat-

isfying the resonance conditions is minimum for a wave with the azimuthal mode number $m = -1$. For this wave, condition (47) becomes $a^2 \omega_{ce}^2/c^2 = j_{1,1}^2 - 1 \approx 13.68$. The magnetic field $H_0$ and the waveguide radius $a$ with which to satisfy this relationship can be estimated as $aH_0 \approx 6000$ G cm. Consequently, for a waveguide of radius $a \approx 20$ cm, the magnetic field satisfying the resonance condition is not too strong, $H_0 \approx 300$ G. For wide waveguides of radius $a = 10\delta$, the resonance condition is satisfied with $\omega_{pe} = 2.7|\omega_{ce}|$. Numerical analysis of dispersion relation (18) confirms that this estimate is very accurate: the solutions to the equations $A_{12}|_{k_z = 0} = 0$ and $A_{21} = 0$ for the frequency coincide with good accuracy (to within three significant decimal digits) in the range $\omega_{pe} = (2.686–2.695)|\omega_{ce}|$.

Figure 3 illustrates the results of a numerical analysis of dispersion relation (18) for waves with the azimuthal mode number $m = -1$ under the resonance conditions $a = 10\delta$ and $\omega_{pe} = 2.695|\omega_{ce}|$. The solid line indicates the dispersion curve of an SW, and the dotted line is for the dispersion curve of an ordinary bulk wave. For magnetic fields slightly stronger than the resonant field and for small axial wavenumbers, the dispersion curves of an SW and an ordinary bulk wave trade places with one another in comparison with the case shown in Fig. 3. Figure 4 illustrates a numerical solution to dispersion relation (18) for a waveguide with $\omega_{pe} = 2.686|\omega_{ce}|$, the other parameters of the waveguide and the wave being the same as those in Fig. 3.

For stronger magnetic fields, the dependence of the wave frequency on the small axial wavenumber begins to deviate from being linear (Fig. 5). The magnetic field for which the dispersion curves in Fig. 5 were calculated was chosen to be stronger than that in Fig. 4 by 2% ($\omega_{pe} = 2.636|\omega_{ce}|$) and the other parameters of the waveguide and wave were the same as in Fig. 3.

For magnetic fields slightly weaker than the resonant field, the frequency dependence of the axial wavenumber is also seen to be nonlinear. This is illustrated in Fig. 6, in which the dispersion curves were calculated for $\omega_{pe} = 2.754|\omega_{ce}|$, all other parameters of the waveguide and wave being the same as in Fig. 3.

Since the roots $j_{|m|,s}$ of the Bessel functions are irrational, the resonant values of the parameters of a plasma waveguide with the SWs in question are related by irrational numbers. That is why, in order to capture all possible physical solutions and to not obtain physically meaningless ones, we investigated the resonant effect of the axial wavenumber on the dispersion properties of SWs by carrying out preliminary numerical estimates before solving dispersion relation (18) numerically. From a methodological point of view, this approach seems to be more appropriate than that in which a
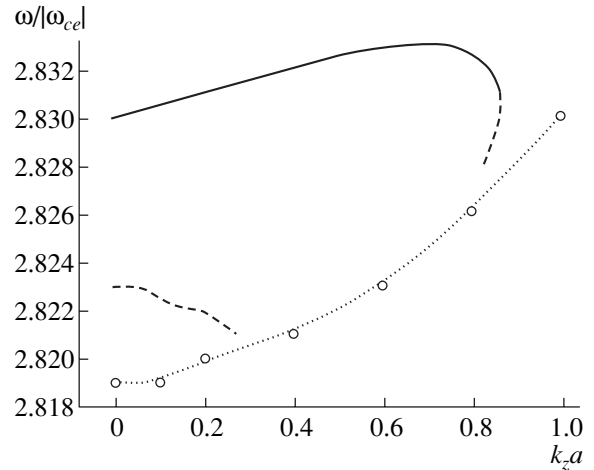
**Fig. 5.** Frequency of an HF SW with extraordinary polarization, normalized to the absolute value of the electron cyclotron frequency, as a function of the product of the axial wavenumber and the waveguide radius under conditions such that the constant magnetic field is slightly stronger than the resonant field. The calculations were carried out for the azimuthal mode number $m = -1$, $\omega_{pe} = 2.636|\omega_{ce}|$, and $a = 10\delta$.
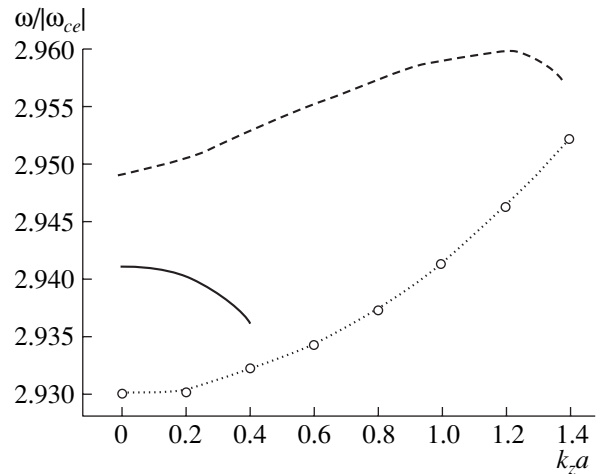


**Fig. 6.** Same as in Fig. 5, but for conditions such that the constant magnetic field is slightly weaker than the resonant field; the azimuthal mode number is $m = -1$, $\omega_{pe} = 2.754|\omega_{ce}|$, and $a = 10\delta$.

"detailed" numerical analysis is performed without any preliminary analytic investigation.

## 7. CONCLUSION

We have shown theoretically that SWs with an arbitrary azimuthal mode number $m$ and a small axial wavenumber $k_z$ can propagate along the boundary between a cold, magnetized plasma and a metal wall with a finite radius of curvature $a$. We have derived dispersion relation (18) for such waves propagating in a waveguide entirely filled with a plasma with a radially nonuniform density profile. For a radially uniform

plasma density profile, this dispersion relation has been investigated analytically in the two frequency ranges (25) and (26) by the method of successive approximations, in which the theory of ASWs is used as a zeroth approximation. In the general case, the correction to the eigenfrequency of SWs introduced by the small axial wavenumber is quadratic in $k_z$, $\Delta\omega \propto k_z^2$. The results of a numerical solution of the dispersion relation agree well with the analytic expressions for the eigenfrequency. We have also determined the resonance conditions under which the correction to the eigenfrequency of SWs introduced by the small axial wavenumber is linear in $k_z$: $\Delta\omega \propto k_z^1$.

In conclusion, we point out a difference between our work and the studies by Azarenkov *et al.* [10, 24], who investigated the propagation of SWs in waveguides in which the magnetized plasma column is separated from the metal chamber by a vacuum gap of finite [10] and infinite [24] width. In those papers, the dispersion properties of SWs were studied only numerically and the analysis was carried out only for some values of the azimuthal mode number. In contrast, in our paper, simple analytic expressions were obtained for the eigenfrequencies of SWs with arbitrary azimuthal mode numbers. Simple analytic solutions (34)–(37), (45) and (48) make it possible to significantly simplify the search for a numerical solution to dispersion relation (18). With these analytic solutions, the dispersion relation can be numerically analyzed on conventional personal computers with the help of standard software packages. The analytic solutions have been obtained in the following limiting cases. First, we have investigated the case of SWs with positive azimuthal mode numbers *m* and with long axial wavelengths restricted by conditions (38) and (39). Second, we have derived asymptotic expressions (34)–(37), (45) and (48) for the frequencies of SWs in a narrow and a wide waveguide.

## ACKNOWLEDGMENTS

## REFERENCES

1. M. V. Kuzelev and A. A. Rukhadze, *Electrodynamics of Dense Electron Beams in Plasma* (Nauka, Moscow, 1990).
2. V. P. Silin, *Parametric Action of High-Power Radiation on a Plasma* (Nauka, Moscow, 1973).
3. A. N. Kondratenko, *Surface and Bulk Waves in a Bounded Plasma* (Énergoatomizdat, Moscow, 1985).
4. A. F. Alexandrov, L. S. Bogdankevich, and A. A. Rukhadze, *Principles of Plasma Electrocdynamics* (Vysshaya Shkola, Moscow, 1988; Springer-Verlag, Berlin, 1984).
5. A. F. Aleksandrov, L. S. Bogdankevich, and A. A. Rukhadze, *Oscillations and Waves in Plasma Media* (Mosk. Gos. Univ., Moscow, 1990).
6. M. J. Ballico and R. C. Gross, Fusion Eng. Des. **12**, 197 (1990).
7. P. I. Markov, I. N. Onishchenko, G. V. Sotnikov, and Ya. B. Faĭnberg, Fiz. Plazmy **19**, 3 (1993) [Plasma Phys. Rep. **19**, 7 (1993)].
8. M. V. Kuzelev, R. V. Romanov, I. A. Selivanov, *et al.*, Tr. Inst. Obshch. Fiz. Ross. Akad. Nauk **45**, 17 (1994).
9. J. Bernd, D. Grozevand, and H. Schluter, J. Phys. D **33**, 877 (2000).
10. N. A. Azarenkov, V. F. Klepikov, V. P. Olefir, and A. E. Sporov, Vestn. Khar'k. Univ., Ser. Fiz.: Yadra, Chastitsy, Polya, No. 1, 41 (2000).
11. E. P. Kurushin and E. I. Nefedov, *Electrodynamics of Anisotropic Waveguide Structures* (Nauka, Moscow, 1983).
12. N. N. Beletskiĭ, A. A. Bulgakov, S. I. Khankina, and V. M. Yakovenko, *Plasma Instabilities and Nonlinear Phenomena in Semiconductors* (Naukova Dumka, Kiev, 1984).
13. *Surface Waves in Plasmas and Solids*, Ed. by S. Vukovic (World Scientific, Singapore, 1986).
14. V. A. Girka, I. A. Girka, A. N. Kondratenko, and V. I. Tkachenko, Radiotekh. Élektron. (Moscow) **34** (2), 296 (1989) [Sov. J. Commun. Technol. Electron. **34** (4), 96 (1989)].
15. N. A. Azarenkov, A. N. Kondratenko, and K. N. Ostrikov, Izv. Vyssh. Uchebn. Zaved., Radiofiz. **36** (5), 335 (1993).
16. V. A. Girka, I. A. Girka, V. P. Olefir, and V. I. Tkachenko, Pis'ma Zh. Tekh. Fiz. **17**, 87 (1991) [Sov. Tech. Phys. Lett. **17**, 35 (1991)].
17. V. A. Girka, I. A. Girka, and V. I. Tkachenko, Zh. Tekh. Fiz. **66** (4), 114 (1996) [Tech. Phys. **41**, 357 (1996)].
18. *Microwave Discharges: Fundamentals and Applications*, Ed. by C. M. Ferreira and M. Moisan (Plenum, New York, 1993), NATO ASI Ser., Ser. B: Phys., Vol. 302.
19. V. O. Girka, I. O. Girka, and I. V. Pavlenko, Contrib. Plasma Phys. **41** (4), 393 (2001).
20. S. Nonaka, Jpn. J. Appl. Phys. **33**, 4226 (1994).
21. M. Nagatsu, I. Ghanashev, and H. Sugai, Plasma Sources Sci. Technol. **7**, 230 (1998).
22. J. Margot-Chaker, M. Moisan, M. Chaker, *et al.*, J. Appl. Phys. **66**, 4134 (1989).
23. I. Zhelyazkov and V. Atanassov, Phys. Rep. **255**, 79 (1995).
24. N. A. Azarenkov, V. P. Olefir, and A. E. Sporov, Phys. Scr. **63**, 36 (2001).
25. I. A. Girka and P. K. Kovtun, Zh. Tekh. Fiz. **68** (12), 25 (1998) [Tech. Phys. **43** (12), 1424 (1998)].
26. B. A. Aronov, L. S. Bogdankevich, and A. A. Rukhadze, Zh. Tekh. Fiz. **43**, 2493 (1973) [Sov. Phys. Tech. Phys. **18**, 1569 (1973)].
27. E. Jahnke, F. Emde, and F. Losch, *Tables of Higher Functions* (McGraw-Hill, New York, 1960; Nauka, Moscow, 1977).
28. V. A. Girka, I. A, Girka, A. N. Kondratenko, and V. I. Tkachenko, Radiotekh. Élektron. (Moscow) **33** (5), 1031 (1988) [Sov. J. Commun. Technol. Electron. **33** (8), 37 (1988)].

*Translated by I. A. Kalabalyk*

======= PLASMA =======
DYNAMICS

# Modeling of Electron Heating and the Spatiotemporal Evolution of Emission in a Current-Sheet Plasma

## G. S. Voronov, N. P. Kyrie, and A. G. Frank

*Institute of General Physics, Russian Academy of Sciences, ul. Vavilova 38, Moscow, 119991 Russia*
Received December 27, 2001; in final form, April 18, 2002

**Abstract**—Results are presented from a detailed study of the behavior of the electron temperature during the evolution of a current sheet by comparing the data from spectral measurements with the spatiotemporal evolution of the emission intensities of the atomic and ionic lines of the working gas (He) and impurities (C, O) calculated in the collisional–radiative model. It is shown that the electron temperature in the center of the sheet attains a value of $T_e = 110 \pm 40$ eV; under these conditions, taking into account metastable states affects the calculated results only slightly. The spatial profiles of the electron temperature and the plasma emission in the spectral lines of various atoms and ions across the plasma sheet are calculated as functions of time. It is shown that as the electron temperature grows most of the spectral lines of atoms and ions of the working gas and impurities are depleted in the center of the sheet and the emission region shifts toward the periphery of the sheet. The results obtained confirm the previous conclusion that, in this regime, a hot plasma is formed in the center of the sheet. © 2002 MAIK "Nauka/Interperiodica".

## 1. INTRODUCTION

Studies of the heating processes in current sheets occupy an important place in research of the problem of magnetic reconnection in plasma [1]. For this reason, in recent years, spectroscopic measurements of the electron temperature have been conducted in current sheet devices at the Institute of General Physics of the Russian Academy of Sciences under various operating conditions. In experiments carried out in the CS-3 device, successive emission bursts in helium, carbon, nitrogen, and oxygen lines were observed during the current sheet evolution [2]. A hydrodynamic interpretation of these observations [3] led to the conclusion that a high-temperature region was produced in current sheets formed in the nonlinear regimes and that the electron temperature in this region reached a value of $T_e \approx$ 100 eV by the beginning of the impulsive phase of magnetic reconnection [1, 4, 5].

Similar methods for measuring the plasma electron temperature from the observed emission in the spectral lines of impurity ions are widely used in controlled fusion experiments [6–9], in particular, in experiments conducted in the L-2M stellarator [10]. Numerical codes developed for interpreting these observations made it possible to reconstruct in detail the spatiotemporal evolution of the electron temperature $T_e$ by using a collisional–radiative model incorporating the processes of ionization, excitation, and transport of ions, as well as the metastable states of some ions.

In this paper, we study the behavior of the electron temperature during the evolution of a current sheet by comparing the data from spectral measurements [2, 4] with the spatiotemporal evolution of the emission

intensities of the atomic and ionic lines of the working gas (He) and impurities (C, O) calculated in the collisional–radiative model.

## 2. EXPERIMENTAL DEVICE AND THE SCHEME OF SPECTRAL MEASUREMENTS

The measurements were conducted in the CS-3 experimental device (Fig. 1), which included a system
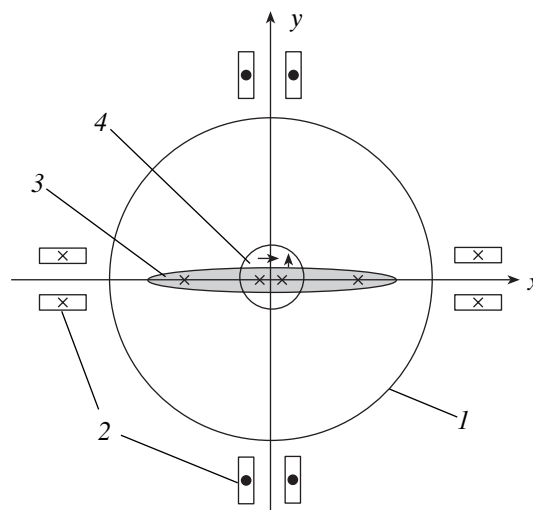


**Fig. 1.** CS-3 device (end view): (*1*) vacuum chamber, (*2*) conductors for creating a quadrupole magnetic field with a null line, (*3*) current sheet (the arrows near the sheet surface indicate the positions and orientations of magnetic probes), and (*4*) central region from which plasma emission is collected.

for creating a quasi-steady magnetic field with a null line, a system for producing a plasma in this field, and a system for exciting an electric current and a plasma flow to form a current sheet (*3*). A two-dimensional quadrupole field with a null line ($x = 0$, $y = 0$) was produced by eight straight conductors (*2*), the magnetic-field gradient being 0.54 kG/cm. The null line coincided with the axis of a 10-cm-diameter cylindrical vacuum chamber (*1*). A plasma was produced in the vacuum chamber by the breakdown of helium at a pressure of $p_0 = 50$ mtorr; the initial electron density was $(1–2) \times 10^{15}$ cm$^{-3}$. The plasma electron current directed along the null line of the magnetic field (the *z*-axis) was generated by a pulsed voltage applied between two electrodes inserted into the chamber from both ends; the distance between the electrodes was 40 cm. A maximum current of 60 kA was reached by the time $t = 1.4$ µs; the half-period of the current pulse was $T/2 = 4.4$ µs.

Time-resolved spectral measurements of emission from the current-sheet plasma were performed by using a two-channel optical scheme that allowed simultaneous observations of two different spectral lines. The plasma emission was divided into two identical channels with the help of a semitransparent mirror placed behind one of the device ends. In each channel, the same region near the center of the vacuum chamber, 2–2.5 cm in diameter and 40 cm long (*4*), was imaged with the help of an objective onto a bundle of quartz fibers 0.3 mm in diameter and 10 m long. Then, the plasma emission was transmitted onto the entrance slits of a DFS-24 and an MDR-3 monochromators. Signals from the exit slits of the monochromators were detected by low-noise FEU-79 photomultipliers in combination with an oscillograph (see [5] for details).

## 3. DETERMINATION OF THE ELECTRON TEMPERATURE OF THE CURRENT-SHEET PLASMA BY MEANS OF A COLLISIONAL–RADIATIVE MODEL

In calculations, we used a 1.5-dimensional model of a planar current sheet. The electron density and temperature were assumed to be nonuniform across the sheet (in the *y*-direction), whereas all the plasma parameters were assumed to be uniform over the sheet width (in the *x*-direction). The distribution of the plasma parameters and impurity ions across the sheet were computed on a 47-cell mesh. The heat and particle losses along the sheet were simulated by limiting the particle lifetime within 1–2 µs. In calculations, we specified the time behavior of the electron temperature and calculated the evolutions of the intensities of the chosen spectral lines and the electron density with allowance for both the ionization of the working gas and the plasma transport due to constant-velocity MHD flows in the current sheet. Then, the results of calculations were compared with the data from spectral measurements and the results of electron-density measurements by holo-

graphic interferometry [5, 11]. The profile of $T_e$ across the sheet was specified to be Gaussian with a characteristic length $\Delta y \sim 0.6$ cm fitted from the two-dimensional electron-density distributions in the sheet [5, 11].

The current-sheet plasma formed in the nonlinear regime [5] is characterized by the following parameters. The maximum electron density in the sheet is $n_e = (1–2) \times 10^{16}$ cm$^{-3}$, the maximum electron temperature is $T_e \approx 100$ eV, and the characteristic time of variations in the plasma parameters in the sheet is $t_c \approx 10^{-6}$ s. Under these conditions, the emission of atoms and ions in the current-sheet plasma, (as well as in the L-2M stellarator) is most adequately described by the collisional–radiative model. Note that, for current-sheet and stellarator plasmas, the dimensionless parameters characterizing the problem under study, namely, $n_e St_c$, $At_c$, and $\nu t_c$ (where $n_e$ is the electron density, $S$ is the ionization or excitation rate, $A$ are the probabilities of optical transitions, $\nu$ is the ion collision rate, and $t_c$ is the characteristic duration of the process), either have the same order of magnitude or satisfy the same inequalities. Indeed, in the current sheet, the plasma density ($n_e \sim 10^{16}$ cm$^{-3}$) is three orders higher than in the stellarator ($n_e \sim 10^{13}$ cm$^{-3}$), while the characteristic process duration ($t_c \sim 10^{-6}$ s) is three orders lower; hence, the quantity $n_e St_c$ for the current-sheet plasma is of the same order of magnitude as that for the stellarator. Two other parameters for the current-sheet plasma are estimated at $At \sim 10^8 \times 10^{-6} \sim 10^2$ and $\nu t \sim 3 \times 10^8 \times 10^{-6} \sim 3 \times 10^2$; i.e., as for the stellarator, these parameters are much greater than unity.

In calculations, we took into account the following main processes: electron-impact ionization and excitation of atoms and ions, emission, and diffusive and convective transport. The characteristic recombination time for light ions (He, C, O) is $t_r \approx 10^{-4}$ s $\gg t_c$; hence, recombination can be neglected. Then, the equations for the ion densities of the working gas and impurities can be written in the form

$$\frac{\partial N_{KZ}}{\partial t} = \frac{\partial}{\partial y}\left( D\frac{\partial N_{KZ}}{\partial y} - V_y N_{KZ} \right)$$
$$- n_e N_{KZ} S_{KZ} + n_e N_{Z-1} S_{KZ-1} - \frac{N_{KZ}}{\tau}, \tag{1}$$

where $N_{KZ}$ is the density of the ions of species $K$ in the ionization state $Z$; $Z$ is the ion spectroscopic symbol ($Z = 1$ for neutral atoms); $S_{KZ}$ is the ionization rate for the corresponding atoms and ions (for fully ionized atoms, e.g., HeIII, the ionization rate is taken to be $S_{KZ} = 0$); $D$ is the diffusion coefficient; $V_y$ is the convective transport rate along the *y*-axis (across the sheet); and $\tau$ is the particle lifetime in the sheet, which is limited by the particle loss along the *x*-axis toward the wall of the vacuum chamber.

The initial conditions of the problem are

**Table 1**

| Ion | $\Delta E$, eV | $A$ | $p$ | $X$ | $k_1$ | $k_2$ |
|---|---|---|---|---|---|---|
| HeI | 19.82 | $2.44 \times 10^{-8}$ | 0 | 0.544 | 0.1 | 1 |
| HeII | 54.418 | $2.05 \times 10^{-9}$ | 1 | 0.265 | 0.25 | 1 |
| CI | 11.3 | $6.85 \times 10^{-8}$ | 0 | 0.193 | 0.25 | 1 |
| CII | 24.4 | $1.86 \times 10^{-8}$ | 1 | 0.286 | 0.24 | 1 |
| CIII | 47.9 | $1.41 \times 10^{-8}$ | 0 | 0.427 | 0.30 | 0.8 |
| CIV | 64.5 | $1.50 \times 10^{-9}$ | 1 | 0.416 | 0.13 | 1 |
| CV | 392.1 | $6.26 \times 10^{-10}$ | 0 | 0.604 | 0.25 | 0.95 |
| CVI | 490 | $1.23 \times 10^{-10}$ | 1 | 0.620 | 0.16 | 1 |
| OI | 13.6 | $3.65 \times 10^{-8}$ | 0 | 0.128 | 0.26 | 1.05 |
| OII | 35.1 | $3.01 \times 10^{-8}$ | 0 | 0.232 | 0.35 | 0.92 |
| OIII | 54.9 | $1.71 \times 10^{-8}$ | 0 | 0.112 | 0.51 | 0.75 |
| OIV | 77.4 | $6.94 \times 10^{-9}$ | 0 | 0.079 | 0.54 | 0.75 |
| OV | 113.9 | $4.30 \times 10^{-9}$ | 0 | 0.659 | 0.28 | 0.75 |
| OVI | 138.1 | $1.58 \times 10^{-9}$ | 0 | 0.636 | 0.24 | 0.90 |
| OVII | 739.3 | $2.48 \times 10^{-10}$ | 0 | 0.641 | 0.24 | 0.95 |

$$N_{\text{HeI}}(y, 0) = 10^{16} \text{ cm}^{-3}, \quad N_{\text{CI}}(y, 0) = 0.02 \times N_{\text{HeI}}(0),$$

$$N_{\text{OI}}(y, 0) = 0.02 \times N_{\text{HeI}}(y, 0), \quad N_{KZ>1}(Y, 0) = 0, \quad (2)$$

$$N_e(0) = 10^{16} \text{ cm}^{-3},$$

and the boundary conditions are

$$N_{\text{HeI}}(a, t) = N_{\text{HeI}}(y, 0), N_{\text{HeII}}(a, t) = N_e(0),$$

where $a = 1.4$ cm is the coordinate of the boundary of the calculation region.

The He neutral flux is $F_{\text{HeI}} = N_{\text{HeI}}(a, t) \times V_y$, and the impurity neutral flux is $F_{KI} = 0.02 \times F_{\text{HeI}}$.

In the center of the sheet ($y = 0$), we set

$$\frac{\partial N_{KZ}(0, t)}{\partial y} = 0. \quad (3)$$

The ionization and excitation rates were calculated using the data of [12, 13]. The ionization rates of atoms and ions were calculated by the formula [12]

$$S_{KZ} = \frac{A(1 + p\sqrt{\beta})\beta^{k_1}}{(X + \beta^{k_2})} e^{-\beta} \quad [\text{cm}^2/\text{s}],$$

$$\beta = \frac{\Delta E}{T_e}, \quad (4)$$

where $\Delta E$ is the ionization energy, and $T_e$ is the electron temperature.

Table 1 shows the values of $\Delta E$, $A$, $p$, $X$, $k_1$, and $k_2$ for helium, carbon, and oxygen calculated in [12] for the plasma density $n_e = 10^{16}$ cm$^{-3}$ taking into account the contribution from metastable states.

The radiation characteristics of the levels corresponding to the given emission lines were taken from the NIST database [14] (see Table 2, where $\Delta E^*$ is the excitation energy).

The diffusion coefficients in a dense current-sheet plasma, in which ions are weakly magnetized and the collision frequencies are high [1], were estimated in the gas-kinetic approximation: $D = 1/3\lambda_i v_i = v_i^2/3\nu_i$. In this approximation, the diffusion coefficient of helium ions is equal to $4 \times 10^3$ cm$^2$/s at a characteristic temperature of $T_i = 10$ eV; in calculations, the maximum estimate $D = 3 \times 10^4$ cm$^2$/s was used for all of the ions. In this case, the characteristic diffusion length falls in the

**Table 2**

| Ion | $\lambda$, nm | Transition | $\Delta E^*$, eV |
|---|---|---|---|
| HeI | 587.6 | $2p^3P - 3d^3D$ | 20.29 |
| HeII | 468.6 | $3 - 4$ | 51.02 |
| CII | 392.0 | $3p^2{}^2P^0 - 4s^2S$ | 19.49 |
| CIII | 464.7 | $3s^3S - 3p^3P$ | 32.2 |
| OII | 464.9 | $3s^4P - 3p^4D$ | 25.66 |
| OIII | 559.2 | $3s^1P - 3p^1P$ | 36.074 |
| OIV | 479.8 | $2p^2P - 3d^4D$ | 61.98 |
| OV | 493.1 | $6 - 7$ | 106.95 |
| OVI | 529.0 | $7 - 8$ | 130.46 |
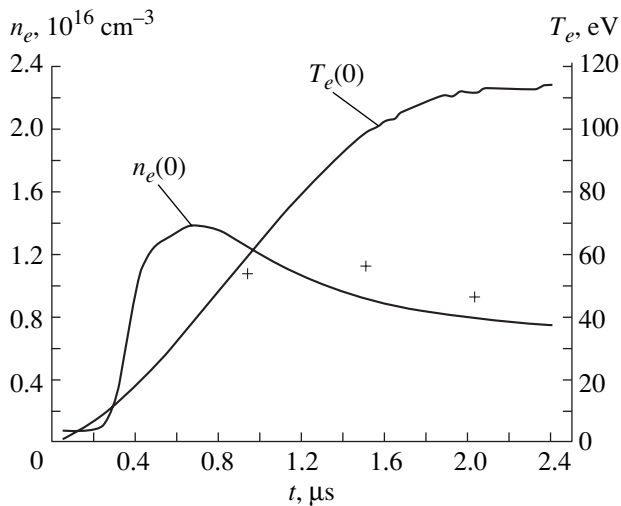
**Fig. 2.** Calculated evolution of the electron density $n_e(0)$ and electron temperature $T_e(0)$ in the center of the current sheet in the nonlinear regime; the crosses indicate the measured values of $n_e(0)$ [5, 11].

range $\delta = \sqrt{Dt_c} \approx 0.06–0.16$ cm, which is much shorter than the sheet thickness $2\Delta y = 1.2$ cm. Consequently, the $D$ value in the current-sheet plasma is very low and cannot substantially affect the results of calculations. However, for the sake of generality (for the purpose of refining the model in further experiments), we retained the diffusion term in the numerical code.

The convective transport velocity along the $y$-axis (across the sheet) and the particle lifetime in the sheet were taken as $V_y = 10^6$ cm/s and $\tau = 1$ μs, respectively; both these estimates are based on the results of previous spectroscopic measurements [5].

Equations (1) with the initial and boundary conditions (2) and (3) were integrated numerically by an implicit difference scheme with an appropriate choice of the time step $\Delta t$. The profiles of the plasma emission intensity along the $y$-axis in various spectral lines were computed within the limits of 1.4 cm about the central plane of the current sheet. This distance was divided into 47 cells, each having the width $\Delta y = 0.03$ cm. The program allowed us to trace the evolution of the temperatures and densities of the electrons and the working-gas and impurity ions, as well as their emission intensities up to the time $t = 2.4$ μs with a time step of 0.001 s.

**Table 3**

| $k$ | 0 | 1 | 2 | 3 | 4 | 5 |
|-----|---|----|----|------|------|-----|
| $A_k$ | 0 | 22 | 68 | −18.5 | −9.7 | 3.1 |

## 4. CALCULATIONS OF THE SPATIOTEMPORAL EVOLUTION OF PLASMA EMISSION FROM THE CURRENT SHEET

Figure 2 shows the results of calculations of the time evolution of the electron density and temperature along with the data from independent measurements of the electron density in the center of the sheet [5, 11]. The best agreement between the calculations and the experiment was achieved by fitting the coefficients of a fifth-degree polynomial describing the time dependence of the electron temperature $T_{e0}$ in the center of the sheet:

$$T_{e0}(t) = \sum_{k=0}^{5} A_k t^k. \tag{5}$$

The polynomial coefficients $A_k$ are listed in Table 3.

The electron temperature profile across the sheet, $T_e(y, t)$, was given in the form

$$T_e(y, t) = T_{e0}(t)\exp\left(-\frac{y^2}{\Delta y^2}\right), \tag{6}$$

where the characteristic length determining the rate at which $T_e$ decreased along the $y$-axis was assumed to be equal to the half-width of the current sheet $\Delta y = 0.6$ cm [5, 11]. When solving Eqs. (1), the electron density $n_e(y, t)$ was calculated from the quasineutrality condition:

$$n_e = N_{\text{HeII}} + 2N_{\text{HeIII}} \tag{7}$$

and, consequently, was self-consistent with the behavior of $T_e(y, t)$ given by Eqs. (4) and (5).

It is seen in Fig. 2 that the calculated values of the electron density almost coincide with the measured ones [5, 11] at $t \geq 0.9$ μs. The electron temperature in the center of the current sheet reaches the value $T_e \approx 110$ eV at $t \approx 1.8–2.0$ μs (at the end of the metastable stage). The calculated evolution of the electron temperature is determined by the intensities of the working-gas and impurity spectral lines. The time behavior of the normalized (to the maximum values) intensities of helium, carbon, and oxygen lines is shown in Figs. 3 and 4. When calculating the intensity, the location and size of the observation region were taken into consideration. The instants corresponding to the maximum measured intensities are indicated by closed circles. The ionization energies of the CII (24 eV), CIII (49 eV), OII (35 eV), and OIII (55 eV) ions are less than or comparable with the ionization energy of the HeII ion (54 eV); however, the maximum intensities of these ions were observed at later times than that for the helium line. In view of this fact, it is clear that, in addition to the initial impurity concentration in the sheet, it is necessary to take into account the carbon and oxygen impurities coming in the plasma in the course of the sheet formation. In the calculations, the velocity of incoming impurities was assumed to be equal to the thermal ion velocity at a temperature of 10 eV, which

Intensity, rel. units
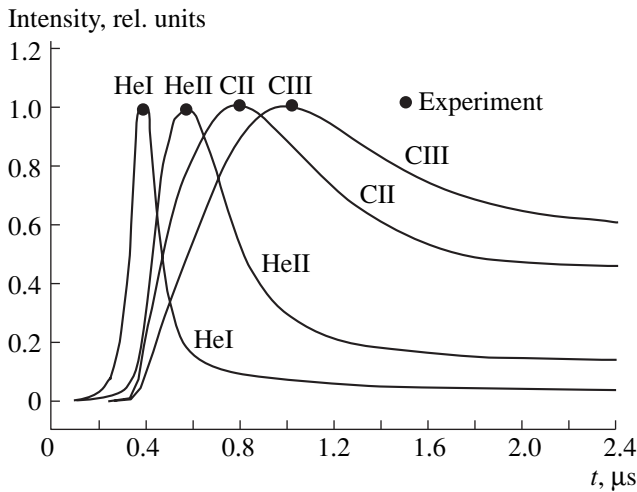


**Fig. 3.** Calculated time evolution of the plasma emission intensities in the HeI 667.8-nm, HeII 468.6-nm, CII 426.7-nm, and CIII 464.7-nm spectral lines; the closed circles indicate the times corresponding to the maximum measured intensities of the given lines.

Intensity, rel. units
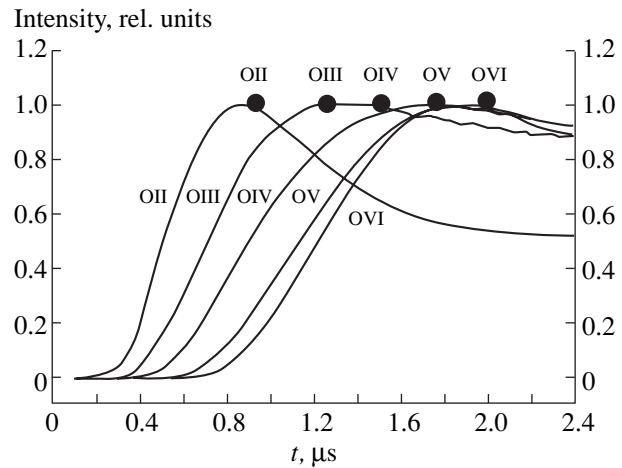


**Fig. 4.** Calculated time evolution of the plasma emission intensities in the OII 464.9-nm, OIII 59.2-nm, OIV 479.8-nm, OV 559.8-nm, and OVI 529.1-nm spectral lines; the closed circles indicate the times corresponding to the maximum measured intensities of the given lines.

follows from the time delay in the appearance of impurity emission in the center of the sheet.

Note that the behavior of the line intensities of weakly ionized CII, CIII, OII, and OIII ions is determined by sequential ionization. Experiments show that the lines of highly ionized oxygen atoms OV and OVI reach their maximum intensities at nearly the same time $t \approx 1.8–2$ μs. To simulate such a behavior, we had to substantially decrease the growth rate of $T_e$ after the time $t \approx 2$ μs. This can be explained by the fact that the plasma motion in the sheet changes abruptly at this time because the sheet becomes unstable.

To find out to which extent metastable levels affect the results, we performed calculations in which only the ground levels of CIII and CIV ions were taken into account in the excitation and ionization processes. Figure 5 shows the time dependence of the line intensity of carbon ions calculated with and without taking into account the contribution from metastable levels. It is seen that the difference does not exceed 20–30% and the time at which the intensity is maximum varies only slightly.

Figures 6–8 show the calculated profiles of the electron density and the emission intensities of helium atoms and helium and oxygen ions in different ionization states. It is seen that, as the electron temperature increases, the regions where each spectral line is the most intense are displaced from the sheet center toward the periphery, following the regions where the electron temperatures characteristic of these lines are localized. The values of these characteristic temperatures depend on the ion ionization energy and the excitation energy of the corresponding line. Figure 9 shows the electron temperature profile across the sheet (along the $y$-axis). The figure also shows the measured positions of the

maximums of the helium, carbon, and oxygen spectral line intensities at $t = 2$ μs. It is from these positions that the localization regions of the corresponding characteristic temperatures were determined for this instant. It is seen that, even for an oxygen ion with the charge number equal to 5 (the ionization energy is ~138 eV), the localization region of its characteristic temperature is shifted from the midplane toward the periphery of the current sheet. At the same time, an appreciable fraction of plasma emission in the OVI 529.1-nm line is radiated from the central region of the sheet (Fig. 8e). This feature distinguishes the OVI ion from the other oxygen ions, which have lower ionization energies and whose

Intensity, rel. units
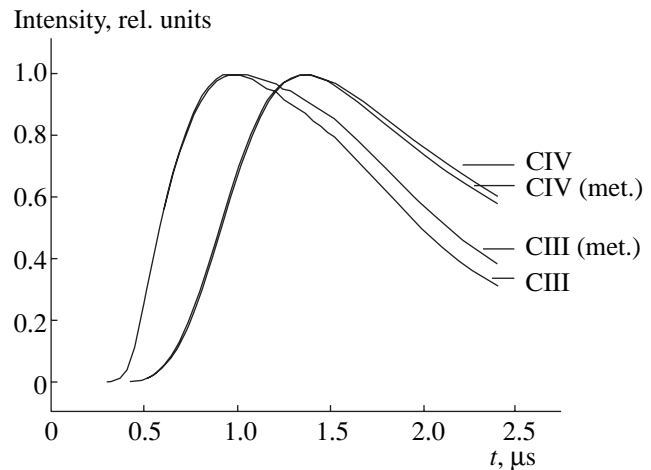


**Fig. 5.** Calculated time evolution of the intensities of the CIII 464.7-nm and CIV 580.1-nm carbon ion lines with and without allowance for the contribution from metastable levels.
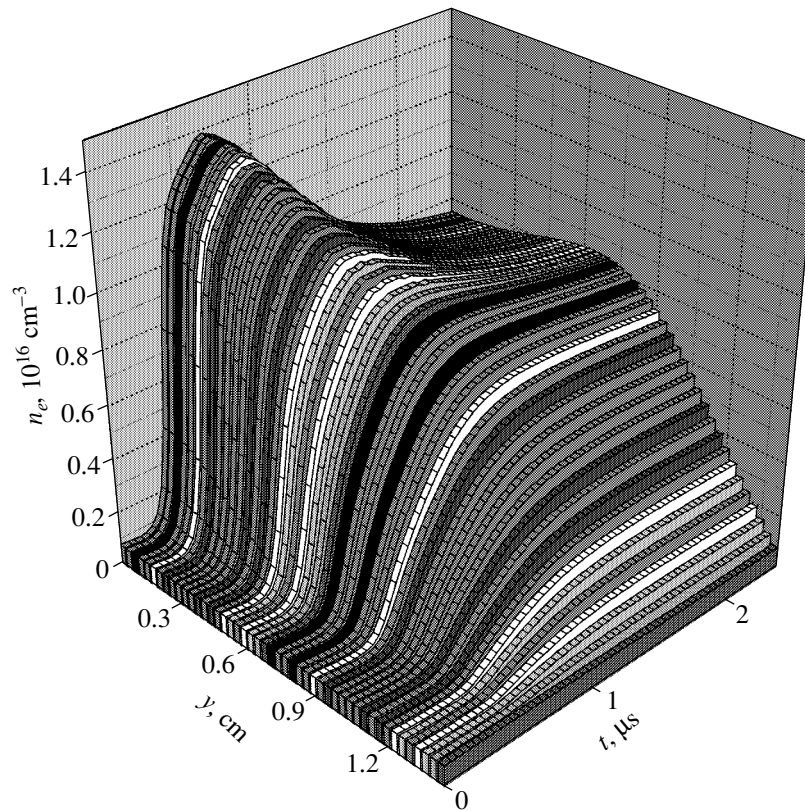
**Fig. 6.** Time evolution of the electron density profile across the current sheet.

## 5. DISCUSSION OF RESULTS

The technique used in this study to estimate the electron temperature from time-resolved measurements of the emission lines of the working-gas and impurity ions is based on the strong dependence of the ionization and excitation cross sections on $T_e$: $S \sim S_0 \exp(-\Delta E/T_e)$. The energy $\Delta E$ is usually known with a high accuracy, and the preexponential factor $S_0$ is usually known within 20–30%. When deducing the electron temperature from this relation, the dependence of $T_e$ on the value of the cross section appears to be rather weak (logarithmic). For this reason, an errors of 20–30% in the cross-section value insignificantly affect the accuracy in determining $T_e$.

Besides the ionization and excitation cross sections, the problem contains some additional parameters that are known with insufficient accuracy. These are the diffusion coefficients, the plasma convection velocity, the sheet thickness $2\Delta y$, and the particle lifetime $\tau$ determined by the loss of particles from the sheet along the magnetic field lines (along the $x$-axis). To estimate how the uncertainty in these parameters affects the accuracy

in determining $T_e$, we varied these parameters in calculations. As a result, it was shown that, when diffusion was ignored (see Section 3), an uncertainty in the listed parameters led to a total error of ~40% in determining $T_e$. Hence, the electron temperature in the center of the sheet at the end of the metastable stage ($t = 1.8–2$ μs) is $T_e = 110 \pm 40$ eV.

We emphasize that the correct modeling of the metastable stage of the current-sheet evolution is impossible if the convection is ignored. This was revealed already at the initial stage of calculations of $T_e$, when it became clear that it was impossible to achieve an agreement between the solution to Eqs. (1) and the experimental results if convection was ignored. Indeed, since the convection velocity under our experimental conditions amounts to $V_y = 10^6$ cm/s, the size of the region involved in convection, $Vt_c \sim 10^6 \times 10^{-6} \sim 1$ cm, is comparable with the sheet thickness $2\Delta y = 1.2$ cm.

Calculations show that a transition from the metastable stage of the sheet evolution to the impulsive phase of magnetic reconnection can be traced in the behavior of the OVI 529.1-nm line. Indeed, if we assume that $T_e$ continues to grow after the time $t = 2$ μs, then the intensity of the OVI line will grow as well, which contradicts to the experiment. To describe the observed decrease in the intensity of the OVI 529.1-nm
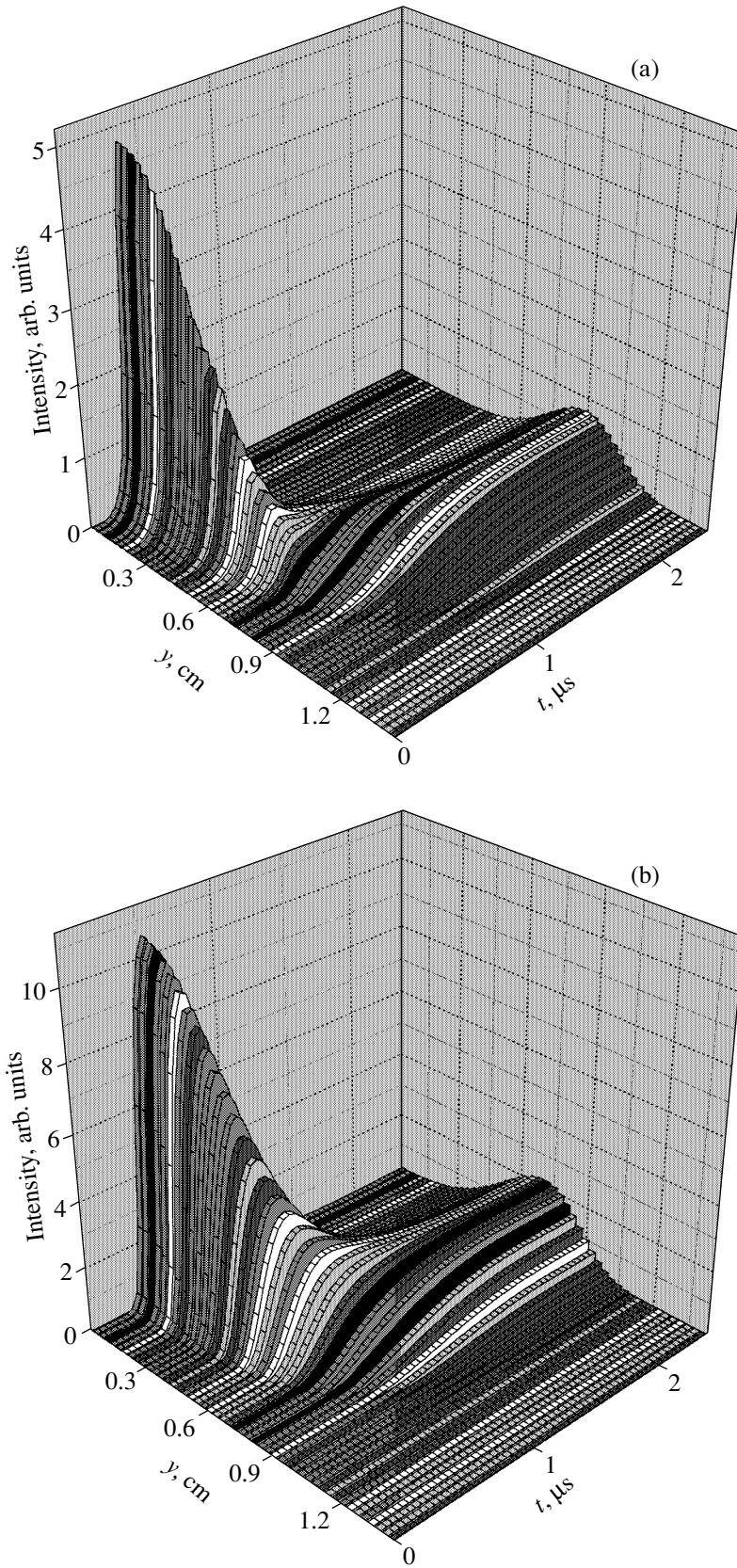
**Fig. 7.** Time evolution of the transverse (along the *y*-axis) profiles of the plasma emission intensity in the (a) HeI 587.6-nm and (b) HeII 468.6-nm helium spectral lines.
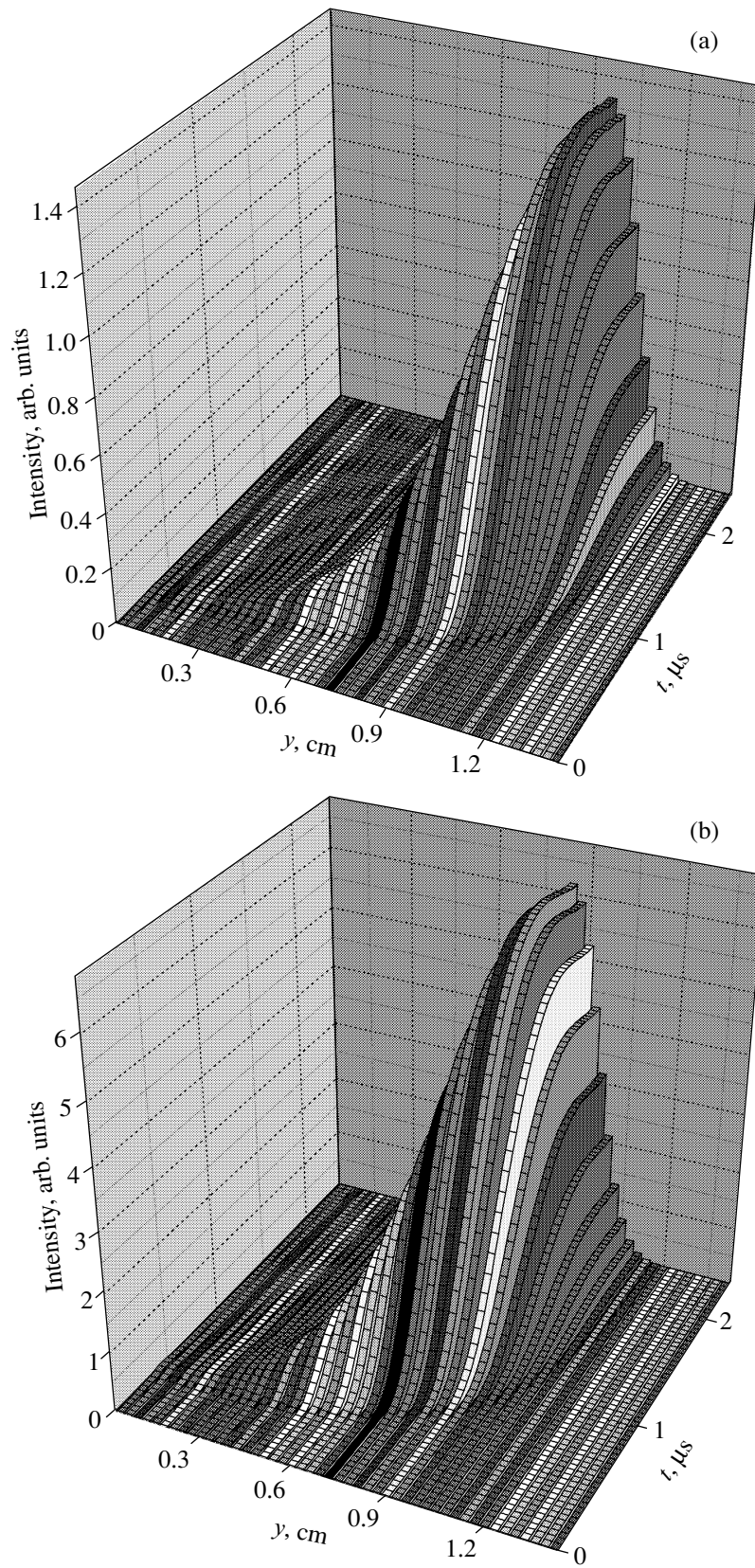
**Fig. 8.** Time evolution of the transverse (along the *y*-axis) profiles of the plasma emission intensity in the (a) OII 464.9-nm, (b) OIII 559.2-nm, (c) OIV 479.8-nm, (d) OV 493.1-nm, and (e) OVI 529.0-nm oxygen spectral lines.
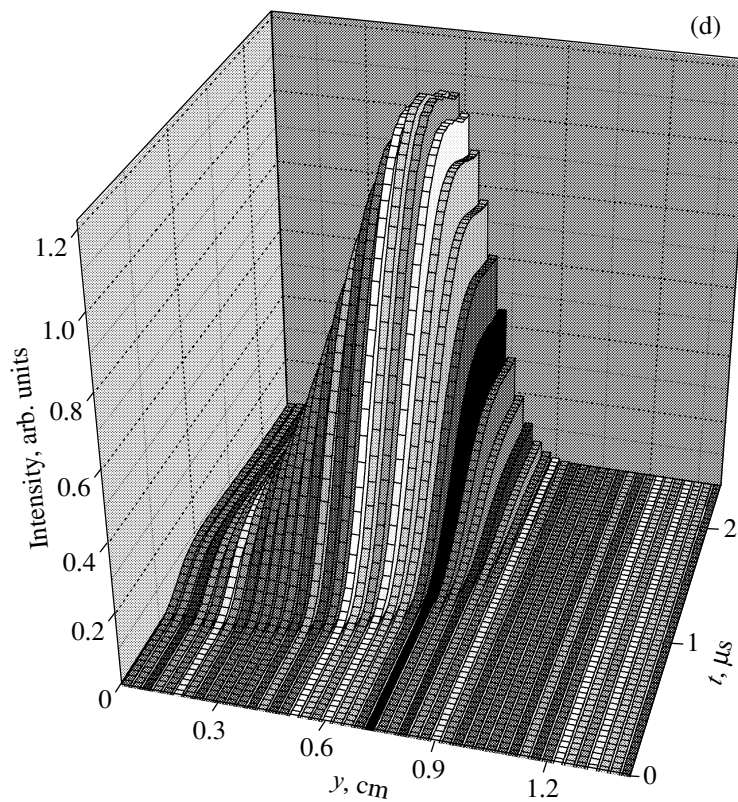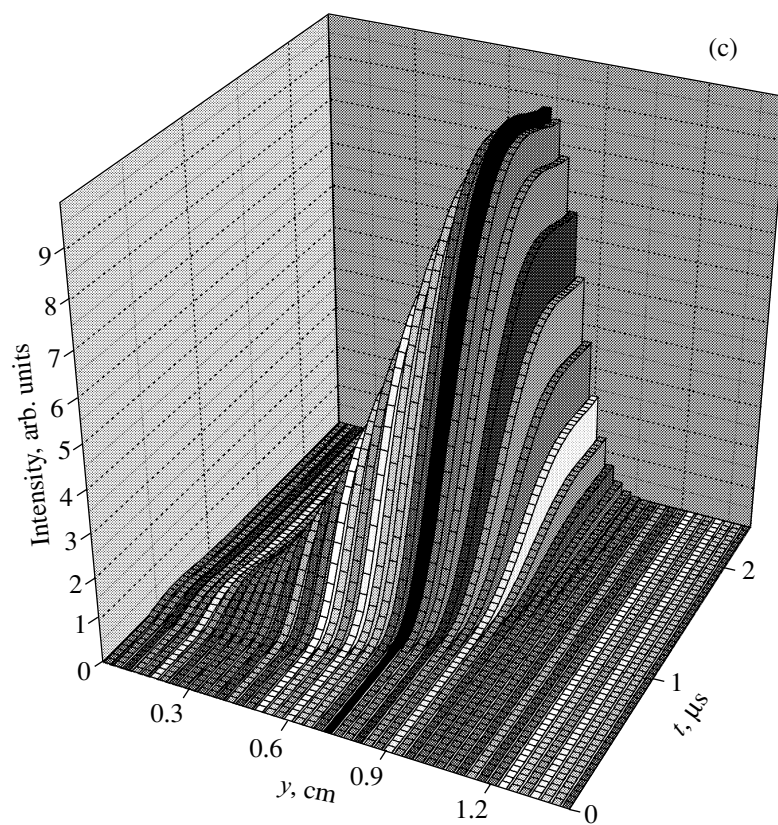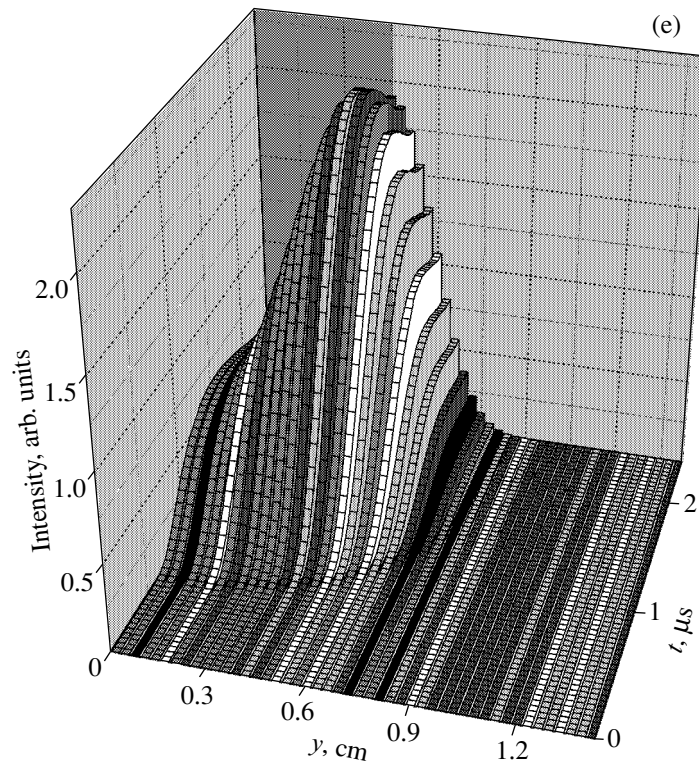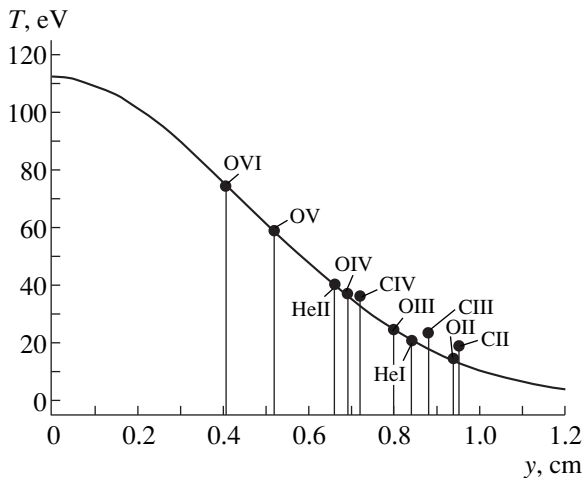
(c)



(d)

**Fig. 8.** (Contd.)

**Fig. 8.** (Contd.)

line after $t \sim 2.0$ μs, we artificially introduced either a substantially lower growth rate or even a decrease in $T_e$ after this moment. On the other hand, as follows from magnetic probe measurements (Fig. 1) conducted simultaneously with spectroscopic measurements (see [4, 5] for details), the impulsive phase of magnetic reconnection in this regime began at $t \geq 1.8$–$2$ μs, when the transverse plasma equilibrium in the magnetic field was disturbed and the sheet began to expand [4, 5]. This process should apparently be accompanied by a decrease in $T_e$; we used this fact to describe the observed decrease in the intensity of the OVI 529.1-nm line at $t \sim 2.0$ μs.

## 6. CONCLUSION

The evolution of the plasma electron temperature in a current sheet formed in the nonlinear regime has been calculated by using the collisional–radiative model. It is shown that the electron temperature in the center of the sheet reaches a value of $T_e = 110 \pm 40$ eV by the time $t \approx 1.8$–$2.0$ μs, i.e., by the end of the metastable stage of the current-sheet evolution, just before the disruption of the sheet and the transition to the impulsive phase of magnetic reconnection. The results obtained confirm the previous conclusion that, in this regime, a hot plasma is formed in the center of the sheet.

A specific feature of the code used in this study is that it takes into account the metastable states of some emitting carbon and oxygen ions. It is shown that, under these conditions, metastable states only slightly affect the dynamics of the electron temperature in the sheet.



**Fig. 9.** Electron-temperature distribution across the sheet (along the $y$-axis) at $t = 2$ μs. The closed circles indicate the positions of the maximum intensities of the OVI 529.1-nm, OV 559.8-nm, OIV 479.8-nm, OIII 559.2-nm, OII 464.9-nm, CIV 580.1-nm, CIII 464.7-nm, and CII 426.7-nm spectral lines.

The spatial profiles of the electron temperature and plasma emission in the spectral lines of various atoms and ions across the plasma sheet have been calculated as functions of time. It is shown that, as the electron temperature grows, most of the spectral lines of the atoms and ions of the working gas and impurities are depleted in the center of the sheet and the emission region shifts toward the periphery of the sheet. This conclusion agrees qualitatively with the results of measurements of the spatial profiles of the emission in the spectral lines of helium and impurities in the vicinity of the current sheet [4, 5, 15].

## ACKNOWLEDGMENTS

## REFERENCES

1. A. G. Frank, Tr. Fiz. Inst. Akad. Nauk SSSR **160**, 93 (1985).

2. N. P. Kiriĭ, V. S. Markov, and A. G. Frank, Pis'ma Zh. Éksp. Teor. Fiz. **48**, 419 (1988) [JETP Lett. **48**, 459 (1988)].

3. I. L. Beĭgman, V. P. Gavrilenko, N. P. Kirye, and A. G. Frank, Zh. Prikl. Spektrosk. **54**, 1021 (1991).

4. N. P. Kirye, V. S. Markov, and A. G. Frank, Pis'ma Zh. Éksp. Teor. Fiz. **56**, 82 (1992) [JETP Lett. **56**, 82 (1992)].

5. S. Yu. Bogdanov, N. P. Kirye, and A. G. Frank, Tr. Inst. Obshch. Fiz. Ross. Akad. Nauk **51**, 3 (1996).

6. M. G. Kaganskiĭ, S. G. Kalmykov, S. V. Lebedev, and K. G. Shakhovets, Fiz. Plazmy **3**, 674 (1977) [Sov. J. Plasma Phys. **3**, 382 (1977)].

7. M. G. Kaganskiĭ, *Adiabatic Compression of Tokamak Plasma* (Nauka, Leningrad, 1976).

8. Yu. N. Dnestrovskij and D. P. Kostomarov, *Mathematical Simulation of Plasmas* (Fizmatgiz, Moscow, 1993).

9. M. Keilhacker, R. Simonini, A. Taroni, and M. L. Watkins, Nucl. Fusion **31**, 535 (1991).

10. G. S. Voronov and V. I. Roshchin, Tr. Inst. Obshch. Fiz. Akad. Nauk SSSR **31**, 165 (1991).

11. S. Yu. Bogdanov, G. V. Dreĭden, N. P. Kirye, *et al.*, Fiz. Plazmy **18**, 1283 (1992) [Sov. J. Plasma Phys. **18**, 661 (1992)].

12. G. S. Voronov, At. Data Nucl. Data Tables **65**, 1 (1997).

13. I. I. Sobelman, L. A. Vainshtein, and E. A. Yukov, *Excitation of Atoms and Broadening of Spectral Lines* (Nauka, Moscow, 1979; Springer-Verlag, Berlin, 1981).

14. NIST Atomic Spectra Database Lines Form, http://physics.nist.gov/cgi-bin/AtData/lines_form.

15. S. Yu. Bogdanov, Yu. F. Bondar', V. B. Burilina, *et al.*, Zh. Tekh. Fiz. **64** (9), 30 (1994) [Tech. Phys. **39**, 877 (1994)].

*Translated by N. F. Larionova*

# Nonlinear Inverse Bremsstrahlung Absorption in a Photoionized Plasma

## V. P. Silin and P. V. Silin

*Lebedev Institute of Physics, Russian Academy of Sciences, Leninskiĭ pr. 53, Moscow, 117924 Russia*

Received April 15, 2002

**Abstract**—Nonlinear inverse bremsstrahlung absorption is investigated for a plasma photoionized in the Bethe regime of suppression of the ionization barrier, in which case the electron velocity distribution coincides with the distribution of atomic electrons. A comparison is made between the characteristic features of absorption in the cases where atomic electrons before ionization are in the *ns* and *np* states. It is established that, in the case of *np* states, the effective high-frequency conductivity is always nonlinear; in particular, for weak pump fields, it is proportional to the square of the pump field strength. The maximum plasma conductivity associated with *p* electrons is one order of magnitude lower than the maximum effective conductivity associated with *s* electrons, which creates conditions for less efficient plasma heating through inverse bremsstrahlung absorption. © 2002 MAIK "Nauka/Interperiodica".

**1.** Nonlinear inverse bremsstrahlung absorption in a plasma began to be theoretically studied in [1]. The approach developed in that paper provides a more exact description of electron–ion collisions than those involving the Boltzmann collision integral or the approximate Landau collision integral, which is derived from the Boltzmann collision integral. The approach of [1], which is based on the classical mechanics of the motion of interacting plasma particles in an alternating electric field, was then generalized in [2] to include quantum-mechanical effects. The results obtained in [2] demonstrate that nonlinear inverse bremsstrahlung absorption has a rich variety of properties. However, all this variety shows up in various logarithmic dependences, differing from the Coulomb logarithm in the Landau collision integral. Recall that the Coulomb logarithm is defined as the logarithm of the ratio of the maximum and minimum impact parameters, which characterize the region of efficient collisions (see, e.g., [3]). In particular, this indicates that the main dependence (except for the logarithmic corrections) of the inverse bremsstrahlung absorption can be obtained using the Landau collision integral. Moreover, in describing inverse bremsstrahlung absorption, small quantities on the order of the electron-to-ion mass ratio can be neglected because they are significant for energy transfer from electrons to heavy particles but are unimportant for the momentum transfer, which governs inverse bremsstrahlung absorption. Hence, the Landau collision integral required for further analysis can be written in the form

$$J_{ei}[f] = \frac{2\pi e^2 e_i^2 N_i \Lambda}{m^2} \frac{\partial}{\partial V_k} \frac{V^2 \delta_{kj} - V_k V_j}{V^3} \frac{\partial f}{\partial V_j}, \quad (1.1)$$

where *f* is the electron distribution function, *e* and *m* are the charge and mass of an electron, $e_i$ is the charge of an ion, and $N_i$ is the ion density.

In this paper, expression (1.1) serves as the basis for analyzing inverse bremsstrahlung absorption in a photoionized plasma of hydrogen-like atoms. We consider photoionization in the Bethe regime of suppression of the photoionization barrier, i.e., under the Bethe condition [4–6]

$$E \geq \frac{I_Z^2}{4Z}, \quad (1.2)$$

where the electric field of radiation *E*, the ionization energy $I_Z$, and the charge number *Z* of the nucleus of a hydrogen-like atom are all expressed in atomic units. The ionization energy is described by the expression $I_Z = Z^2/(2n^2)$, where the principal quantum number *n* determines the energy of an electronic state of a hydrogen-like atom. This expression makes it possible to write the Bethe condition for the intensity of the pump field in the form

$$q\left[\frac{W}{cm^2}\right] \geq 1.37 \times 10^{14} \frac{Z^6}{n^8}. \quad (1.3)$$

Our interest in inverse bremsstrahlung absorption in a plasma that is produced under the Bethe condition and is characterized by different values of the principal quantum number stems from the fact that such a plasma is a convenient object for studying the generation of harmonics of the pump field. Thus, in 2000, it was shown theoretically that, in a plasma produced through the photoionization of a gas of hydrogen-like atoms whose electrons are in the *ns* states, the efficiency of the higher harmonic generation increases by several orders

of magnitude with increasing principal quantum number [7]. In the same year, the generation of the third harmonic of laser radiation in a gas preionized by a single laser pulse was studied experimentally [8]. The plasma produced during the prepulse recombined, and then the generation of the third harmonic of the laser frequency during the next laser pulse was observed. As was shown in [8], the preionization of a gas followed by the recombination of the plasma produced increases the efficiency of the third-harmonic generation by orders of magnitude. This phenomenon was interpreted on the basis of the hypothesis that, after the recombination, the gas atoms are in excited states. A theoretical analysis carried out in [9] for the particular case of the third-harmonic generation showed that, in a plasma produced by the photoionization of a gas with atoms in the excited electronic $ns$ states with the principal quantum number $n$, the third-harmonic generation efficiency increases in proportion to the tenth power of the principal quantum number. In [10], it was shown that the efficiency of the fifth-harmonic generation obeys a similar dependence.

The regular features established in [7, 9, 10] are closely associated with the fact that the electrons for which the Bethe condition is satisfied are almost freely ejected from the atoms. In this case, the electron velocity spread is determined by the electron wave function of the hydrogen-like atom under consideration [11, 12]:

$$\psi_{nlm}(\mathbf{r}) = Y_{lm}(\theta, \varphi) F_{nl}(r). \tag{1.4}$$

Here, the eigenfunctions $Y_{lm}(\theta, \varphi)$ of the angular momentum are normalized to unity and

$$F_{nl}(r) = N_{nl}\left(\frac{2Zr}{na_B}\right)^l F\left(-n + l + 1, 2l + 2; \frac{2Zr}{na_B}\right)$$
$$\times \exp\left(-\frac{Zr}{na_B}\right), \tag{1.5}$$

$$N_{nl} = \frac{1}{(2l+1)!}\left[\frac{(n+l)!}{2n(n-l-1)!}\right]^{1/2}\left(\frac{2Z}{na_B}\right)^{3/2}, \tag{1.6}$$

where $a_B = (\hbar^2/me^2)$ is the Bohr radius and $F(\alpha, \beta; x)$ is a degenerate hypergeometric function.

According to [13, 14], the probability distribution of electrons over momenta in a spatially homogeneous plasma is determined by the square of the electron wave function, $a_{nlm}(\mathbf{p})$, in momentum space,

$$f_{nlm}(\mathbf{p}) = |a_{nlm}(\mathbf{p})|^2 N_e, \tag{1.7}$$

which "remembers" the distribution of electrons in an atom before its photoionization. However, this distribution of atomic electrons is violated by electron–electron collisions; as a result, the electrons evolve from distribution (1.7) to a Maxwellian distribution. The charac-

teristic time scale of such Maxwellianization of the electron distribution is

$$t_{ee} = \frac{3m^{1/2}(\kappa_B T_e)^{3/2}}{4\sqrt{2\pi}e^4 N_e \Lambda}, \tag{1.8}$$

where $N_e$ and $T_e$ are the electron density and electron temperature in a photoionized plasma. When the relaxation time of electron distribution (1.7) is short enough for the electrons to be heated to any significant extent, we obtain the following relationship for a photoionized plasma [7]:

$$\kappa_B T_e = \frac{mV_Z^2}{3n^2}, \tag{1.9}$$

where $V_Z = Ze^2/\hbar \equiv ZV_a$ is the Coulomb velocity unit [11]. In [9], it was shown that, after the relaxation to a Maxwellian distribution with temperature (1.9), the harmonic generation efficiency in a plasma produced by the photoionization of a gas with atoms in the $ns$ states is proportional to the sixth (rather than tenth) power of the principal quantum number. In other words, the harmonic generation efficiency decreases. According to relationships (1.8) and (1.9), this occurs on the time scale

$$t_{ee} \approx \frac{1}{n^3}\left(\frac{10}{\Lambda}\right)\frac{Z^3}{Z_i}\frac{10^{-13}\ \text{s}}{(N_i/10^{18}\ \text{cm}^{-3})}, \tag{1.10}$$

where $Z_i$ is the ion charge number and $N_i$ is the ion density. However, the harmonic generation efficiency decreases in this manner only when the generation time is too short for the plasma electrons to be heated by inverse bremsstrahlung absorption. The fact that an increase in the electron temperature lowers the harmonic generation efficiency makes it necessary to study inverse bremsstrahlung absorption in a plasma photoionized in the Bethe regime of suppression of the ionization barrier.

Preliminary results of the investigation of inverse bremsstrahlung absorption in a plasma produced through the photoionization of excited atoms in the $ns$ states were published in [9]. In the present paper, we are going to deepen the understanding developed in [9]. However, our main objective here is to consider the absorption in a plasma produced by the photoionization of atoms in excited states with a nonzero orbital quantum number. We thoroughly examine the case of $np$ states. First, we show that inverse bremsstrahlung absorption is always nonlinear. Second, we demonstrate the possibility of a substantial nonlinear reduction in the intensity of inverse bremsstrahlung absorption and obtain the scaling of the absorption intensity with the principal quantum number. We also point out that an analogous nonlinear effect can take place for states with large orbital quantum numbers and show that the larger the orbital quantum number, the more pronounced the effect.

**2.** For a pump electric field of the form

$$\mathbf{E}(t) = \mathbf{E}\cos\omega t, \tag{2.1}$$

the Boltzmann kinetic equation, which is the basic equation for our analysis, can be written as

$$\frac{\partial f}{\partial t} + \mathbf{V}\frac{\partial F}{\partial \mathbf{r}} + \frac{e}{m}\mathbf{E}\cos\omega t\frac{\partial f}{\partial \mathbf{V}} = J_{ee}[f, f] + J_{ei}[f]. \tag{2.2}$$

The particular form of the electron–electron collision integral $J_{ee}[f, f]$ is unimportant for further analysis. We only need the relationship

$$\int d\mathbf{V}\mathbf{V}J_{ee}[f, f] = 0, \tag{2.3}$$

which stems from the electron momentum conservation in electron–electron collisions. In the dipole approximation, we can neglect the dependence of the electric field on the coordinates. We can also neglect the corresponding coordinate-dependence of the distribution function. Then, from Eq. (2.2), we obtain the equation

$$\frac{d\mathbf{j}}{dt} = \frac{e^2 N_e}{m}\mathbf{E}\cos\omega t + \int d\mathbf{V}e\mathbf{V}J_{ei}[f(\mathbf{V}, t), \mathbf{V}], \tag{2.4}$$

where

$$\mathbf{j} = \int d\mathbf{V}e\mathbf{V}f(\mathbf{V}, t) \equiv \frac{e^2 N_e}{m\omega}\mathbf{E}\sin\omega t + \delta\mathbf{j} \tag{2.5}$$

is the electric current density and $\delta\mathbf{j}$ is the contribution of collisions to the current density. In order to determine this contribution, we assume that it is small (which corresponds to a pump field with a frequency much higher than the collision frequency) and turn to the approximate distribution function $f_0(\mathbf{V}, t)$ for which the collisions are ignored:

$$f_0(\mathbf{V}, t) = F(\mathbf{V} - \mathbf{u}_E(t)), \tag{2.6}$$

where

$$\mathbf{u}_E(t) = \frac{e\mathbf{E}}{m\omega}\sin\omega t \tag{2.7}$$

is the electron velocity in an alternating electric field and, in the case at hand, $F(\mathbf{V})$ is the velocity distribution (1.7) of atomic electrons. As a result, using formulas (2.4)–(2.7), we can write

$$\frac{d\delta\mathbf{j}}{dt} = \int d\mathbf{V}e\mathbf{V}J_{ei}[F(\mathbf{V} - \mathbf{u}_E(t), \mathbf{V}]. \tag{2.8}$$

With the electron–ion collision integral of the form (1.1), Eq. (2.8) becomes

$$\frac{d\delta\mathbf{j}}{dt} = -\frac{4\pi e^2 e_i^2 N_i\Lambda}{m^2}\int d\mathbf{V}\frac{e\mathbf{V}}{V^3}F(\mathbf{V} - \mathbf{u}_E(t)). \tag{2.9}$$

Using the relationship

$$\frac{\mathbf{V}}{V^3} = -\frac{\partial}{\partial \mathbf{V}}\frac{1}{V} = -\int\frac{d\mathbf{q}}{(2\pi)^3}\frac{4\pi}{q^2}\exp(i\mathbf{q}\cdot\mathbf{V}), \tag{2.10}$$

we can represent Eq. (2.9) as

$$\frac{d\delta\mathbf{j}}{dt} = i\frac{2e^3 e_i^2 N_i\Lambda N_e}{\pi m^2}\int d\mathbf{q}\frac{\mathbf{q}}{q^2}\Phi(\mathbf{q})\exp(i\mathbf{q}\cdot\mathbf{u}_E(t)), \tag{2.11}$$

where

$$N_e\Phi(\mathbf{q}) = \int d\mathbf{V}F(\mathbf{V})\exp(i\mathbf{q}\cdot\mathbf{V}). \tag{2.12}$$

In what follows, we will assume that the functions $F(\mathbf{V})$ and $\Phi(q)$ depend only on the absolute values of their arguments.

We direct the $z$-axis along the vector $\mathbf{E}$, in which case Eq. (2.11) yields

$$\delta j_z = \sum_{N=0}^{\infty}\sigma^{(2N+1)}E\cos[(2N+1)\omega t], \tag{2.13}$$

where

$$\sigma^{(2N+1)} = \frac{e^2 N_e}{m\omega^2}\nu^{(2N+1)}(E) \tag{2.14}$$

are nonlinear partial conductivities.

In formula (2.14), we have introduced the following notation for the effective nonlinear collision frequencies:

$$\nu^{(2N+1)}(E)$$
$$= \frac{16e^2 e_i^2 N_i\Lambda}{mV_E(2N+1)}\int_0^{\infty}dq\Phi(q)q\int_0^1 xdxJ_{2N+1}(qxV_E), \tag{2.15}$$

where $J_n(z)$ is a Bessel function and $V_E = |eE|/m\omega$ is the amplitude of the electron oscillatory velocity in the pump field.

Inverse bremsstrahlung absorption of the pump field at the fundamental frequency is described by setting $N = 0$ in formula (2.13). So, in what follows, we will work with the expression

$$\nu^{(1)}(E) = \frac{16e^2 e_i^2 N_i\Lambda}{mV_E}\int_0^{\infty}dq\Phi(q)q\int_0^1 xdxJ_1(qxV_E). \tag{2.16}$$

**3.** Further analysis will be based on the following expressions for the electron wave function in a hydrogen-like atom in momentum space. For $ns$ states, we use a compact general formula (see Appendix 1):

$$a_{n00}(p)$$
$$= (-1)^{n-1}\frac{\sqrt{2n}\sin(2n\arctan[np/mV_Z])}{\pi(mV_Z)^{3/2}(p/mV_Z)[1 + (np/mV_Z)^2]}. \tag{3.1}$$

For *np* states, we use the following four expressions, which refer to $n = 2, 3, 4,$ and 5:

$$a_{n10}(\mathbf{p})$$
$$= \frac{\cos\theta_p}{\pi}\left(\frac{n}{2mV_Z}\right)^{5/2}\frac{pc_n(p)}{[(1/4) + (np/2mV_Z)^2]^3}, \quad (3.2)$$

where $\theta_p$ is the angle between the vector $\mathbf{p}$ and the polar axis and

$$c_2(p) = 1, \quad c_3(p) = \sqrt{6}\left(1 - \frac{1}{2[(1/4) + (3p/2mV_Z)^2]}\right),$$

$$c_4(p) = \sqrt{20}\left(1 - \frac{6}{5[(1/4) + (2p/mV_Z)]^2}\right.$$
$$\left. + \frac{3}{10[(1/4) + (2p/mV_Z)^2]^2}\right),$$
$$\quad (3.3)$$
$$c_5(p) = \sqrt{50}\left(1 - \frac{21}{10[(1/4) + (5p/2mV_Z)^2]}\right.$$
$$+ \frac{6}{5[(1/4) + (5p/2mV_Z)^2]^2}$$
$$\left. - \frac{1}{5[(1/4) + (5p/2mV_Z)^2]^3}\right).$$

Note that, in the limit $p \longrightarrow 0$, the above wave functions behave asymptotically as

$$a_{n00}(p \longrightarrow 0) = \frac{2^{3/2}n^{5/2}}{\pi(mV_Z)^{3/2}}, \quad (3.4)$$

$$a_{n10}(p \longrightarrow 0) = \frac{\cos\theta_p}{\pi}(-1)^n p\sqrt{\frac{32}{3}}\frac{(n^2 - 1)^{1/2}n^{7/2}}{(mV_Z)^{5/2}}. \quad (3.5)$$

Formula (3.2) implies that the distribution function for *np* states is proportional to $\cos^2\theta_p$. Assuming that the electrons are unpolarized, we can replace $\cos^2\theta_p$ with 1/3.

We normalize the distribution functions for *ns* and *np* states to unity;

$$f_{ns}(V) = \frac{2n\{\sin(2n\arctan[np/mV_Z])\}^2}{\pi^2 V_Z^3(V/V_Z)^2[1 + (nV/V_Z)^2]^2} \quad (3.6)$$

and

$$f_{np}(V) = \frac{1}{3\pi^2}\left(\frac{n}{2V_Z}\right)^5\frac{V^2c_n^2(mV)}{[(1/4) + (nV/2V_Z)^2]^6}. \quad (3.7)$$

For further analysis, it is expedient to present the Fourier transform of expression (2.12):

$$\Phi_{ns(p)}(q) = D_{ns(p)}\exp\{-q(V_Z/n)b\}|_{b=1}, \quad (3.8)$$

where the Fourier coefficients for *ns* states have the form

$$D_{1s} = 1 - \frac{d}{db} + \frac{1}{3}\frac{d^2}{db^2},$$

$$D_{2s} = 1 - \frac{d}{db} + \frac{1}{3}\frac{d^2}{db^2} + \frac{1}{15}\frac{d^4}{db^4},$$

$$D_{3s} = 1 - \frac{d}{db} + \frac{1}{3}\frac{d^2}{db^2} + \frac{2}{15}\frac{d^4}{db^4} + \frac{2}{45}\frac{d^5}{db^5} + \frac{2}{315}\frac{d^6}{db^6},$$

$$D_{4s} = 1 - \frac{d}{db} + \frac{1}{3}\frac{d^2}{db^2} + \frac{1}{5}\frac{d^4}{db^4} + \frac{2}{15}\frac{d^5}{db^5} + \frac{2}{45}\frac{d^6}{db^6} \quad (3.9)$$
$$+ \frac{2}{315}\frac{d^7}{db^7} + \frac{1}{2835}\frac{d^8}{db^8},$$

$$D_{5s} = 1 - \frac{d}{db} + \frac{1}{3}\frac{d^2}{db^2} + \frac{4}{15}\frac{d^4}{db^4} + \frac{4}{15}\frac{d^5}{db^5} + \frac{44}{315}\frac{d^6}{db^6}$$
$$+ \frac{4}{105}\frac{d^7}{db^7} + \frac{16}{2835}\frac{d^8}{db^8} + \frac{2}{4725}\frac{d^9}{db^9} + \frac{2}{155\,925}\frac{d^{10}}{db^{10}},$$

and, for *np* states, they are equal to

$$D_{2p} = 1 - \frac{d}{db} + \frac{1}{3}\frac{d^2}{db^2} - \frac{1}{45}\frac{d^4}{db^4},$$

$$D_{3p} = 1 - \frac{d}{db} + \frac{1}{3}\frac{d^2}{db^2} - \frac{1}{45}\frac{d^5}{db^5} - \frac{1}{315}\frac{d^6}{db^6},$$

$$D_{4p} = 1 - \frac{d}{db} + \frac{1}{3}\frac{d^2}{db^2} + \frac{1}{45}\frac{d^4}{db^4} - \frac{2}{45}\frac{d^5}{db^5}$$
$$- \frac{34}{1575}\frac{d^6}{db^6} - \frac{2}{525}\frac{d^7}{db^7} - \frac{1}{4725}\frac{d^8}{db^8}, \quad (3.10)$$

$$D_{5p} = 1 - \frac{d}{db} + \frac{1}{3}\frac{d^2}{db^2} + \frac{2}{45}\frac{d^4}{db^4} - \frac{1}{15}\frac{d^5}{db^5}$$
$$- \frac{19}{315}\frac{d^6}{db^6} - \frac{4}{189}\frac{d^7}{db^7} - \frac{2}{567}\frac{d^8}{db^8} - \frac{4}{14175}\frac{d^9}{db^9}$$
$$- \frac{4}{467\,775}\frac{d^{10}}{db^{10}}.$$

**4.** In accordance with formula (3.8), the effective collision frequency (2.16) for states with the principal
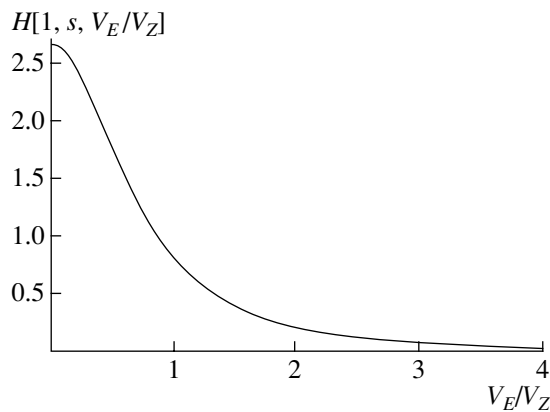
**Fig. 1.** Function $H[1, s, V_E/V_Z]$ vs. $V_E/V_Z$.

quantum number $n$ can be represented as

$$
\nu^{(1)}(n, E) = -\frac{16 e^2 e_i^2 N_i \Lambda n}{m^2 V_E V_Z} D_{ns(p)} \frac{d}{db}
$$

$$
\times \int_0^1 x\,dx \int_0^\infty dq\, J_1(xqV_E) \exp\left(-q\frac{V_Z}{n}b\right)\Bigg|_{b=1}.
$$

(4.1)

According to formula (6.611.1) in [15], we have

$$
\int_0^\infty dx \exp(-\alpha x) J_1(\beta x) = \frac{1}{\beta}\left[1 - \frac{\alpha}{\sqrt{\alpha^2 + \beta^2}}\right],
$$

which allows us to rewrite formula (4.1) as

$$
\nu^{(1)}(n, E) = \nu_Z H\left[1, ns(p), \frac{V_E}{V_Z}\right]
$$

$$
\equiv \nu_Z n^3 A\left[1, ns(p), \frac{nV_E}{V_Z}\right],
$$

(4.2)

where

$$
\nu_Z = \frac{16 e^2 e_i^2 N_i \Lambda}{m^2 V_Z^3},
$$

(4.3)

$$
A[1, ns(p), x] = \frac{1}{x^3}[D_{ns(p)}\alpha[1, b, x]]_{b=1},
$$

(4.4)

with

$$
\alpha[1, b, x] = \frac{d}{db}\left\{b\,\mathrm{arcsinh}\frac{x}{b}\right\}.
$$

Figure 1 shows the dependence that was obtained from formula (4.2) and is representative of the inverse bremsstrahlung absorption of radiation in the case of $1s$ state. In the figure, the ordinate is the function $H[1, 1s, V_E/V_Z]$ and the abscissa is the ratio $V_E/V_Z$.

In order to gain insight into the regular features described by formula (4.2), it is necessary to under-

stand the properties of the functions $H[1, ns(p), V_E/V_Z]$. First, note that formula (4.4) gives

$$
A[1, ns(p), x] = \frac{1}{x^3}\{\mathrm{arcsinh}\,x + a[1, ns(p), x]\}.
$$

(4.5)

Here,

$$
a[1, ns(p), x] = \frac{x P_{4n}[1, ns(p), x]}{(1 + x^2)^{2n + (1/2)}},
$$

(4.6)

where $P_{4n}[1, ns(p), x]$ are $4n$th-degree polynomials comprising even powers of the argument $x$. In explicit form, the polynomials for $ns$ states are presented in Appendix 2, and the polynomials for $np$ states are presented in Appendix 3. In the limit $x = \infty$, for $s$ states, we have

$$
a[1, 1s, \infty] = (1/3), \quad a[1, 2s, \infty] = (11/15),
$$

$$
a[1, 3s, \infty] = (27/35), \quad a[1, 4s, \infty] = (55/63),
$$

$$
a[1, 5s, \infty] = (89/99),
$$

and, for $p$ states, we have

$$
a[1, 2p, \infty] = (1/5), \quad a[1, 3p, \infty] = (17/35),
$$

$$
a[1, 4p, \infty] = (13/21), \quad a[1, 5p, \infty] = (23/33).
$$

In this limit, formula (4.5) becomes

$$
A[1, ns(p), z] = \frac{1}{x^3}\{\ln x + a[1, ns(p), \infty]\}.
$$

(4.7)

Consequently, since, for $x \gg 1$, the term $a[1, ns(p), \infty]$ is small as compared to the logarithmic term, we arrive at the following unified scaling:

$$
\nu^{(1)}(n, E) = \nu_Z\left(\frac{V_Z}{V_E}\right)^3 \ln\left(\frac{2nV_E}{V_Z}\right).
$$

(4.8)

This scaling applies to atoms in both $ns$ and $np$ states, which are characterized only by the principal quantum number. The dependence on the principal quantum number is seen to be weak (logarithmic).

The situation with comparatively weak pump fields is radically different. In such fields, the electron oscillatory energy is insufficiently high as compared to the electron energy at the corresponding Rydberg level of an atom:

$$
\frac{mV_E^2}{2} < \frac{mV_Z^2}{2n^2}.
$$

(4.9)

On the one hand, inequality (4.9) justifies the use of the function $A[1, ns(p), nV_E/V_Z]$. On the other hand, under this inequality, a peculiar situation exists in which the properties of the $n$ and $p$ states manifest themselves in very different ways. This can be readily seen in Figs. 2, 3, 4, and 5, which compare the functions $H[1, ns, V_E/V_Z]$ and $H[1, np, V_E/V_Z]$ for the four states with $n = 2, 3, 4$, and 5. Specifically, for high-intensity pump fields, these functions coincide, which accords with asymptotic

$H[1, 2s, V_E/V_Z], H[1, 2p, V_E/V_Z]$
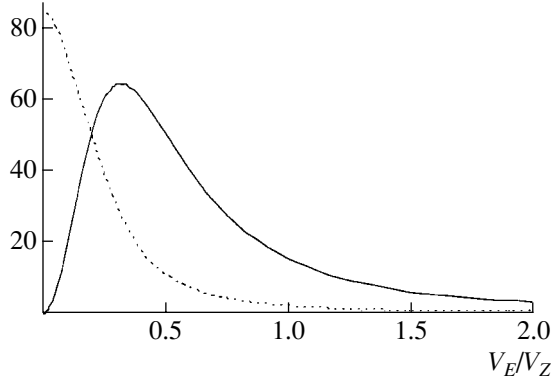


**Fig. 2.** Functions $H[1, 2s, V_E/V_Z]$ (dashed curve) and $10H[1, 2p, V_E/V_Z]$ (solid curve) vs. $V_E/V_Z$.

$H[1, 3s, V_E/V_Z], 10H[1, 3p, V_E/V_Z]$
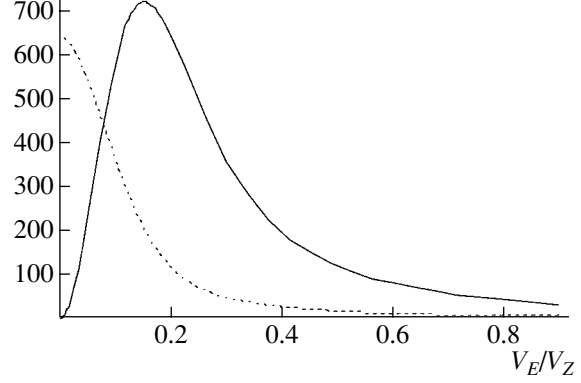


**Fig. 3.** Functions $H[1, 3s, V_E/V_Z]$ (dashed curve) and $10H[1, 3p, V_E/V_Z]$ (solid curve).

$H[1, 4s, V_E/V_Z], 10H[1, 4p, V_E/V_Z]$
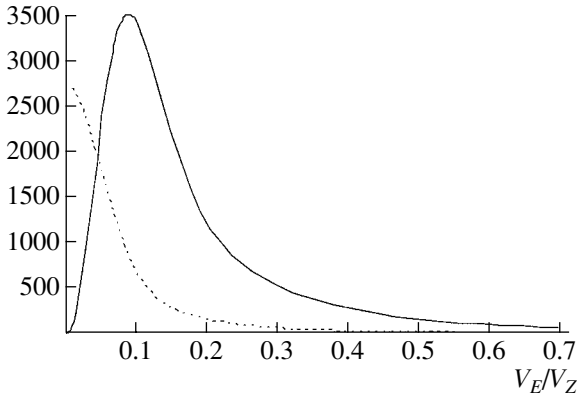


**Fig. 4.** Functions $H[1, 4s, V_E/V_Z]$ (dashed curve) and $10H[1, 4p, V_E/V_Z]$ (solid curve).

$H[1, 5s, V_E/V_Z], 10H[1, 5p, V_E/V_Z]$



**Fig. 5.** Functions $H[1, 5s, V_E/V_Z]$ (dashed curve) and $10H[1, 5p, V_E/V_Z]$ (solid curve).

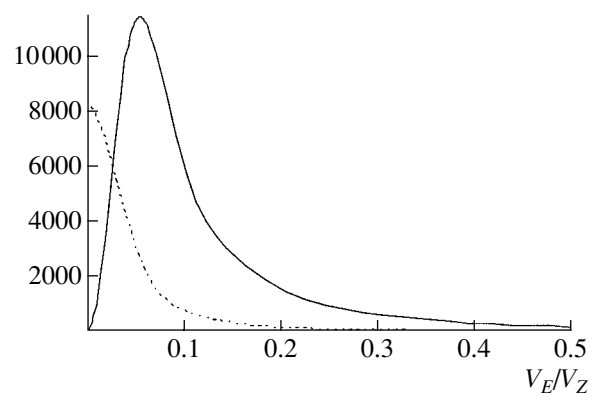scaling (4.8); in contrast, at low intensities, these functions are qualitatively different. We make the difference even more pronounced by plotting the functions in Figs. 2–5 on different scales.

In order to understand the causes for such a sharp difference, we consider the following consequence of Eq. (2.9) in the first-order approximation in the electric field strength:

$$\frac{dj_k}{dt} = \frac{4\pi e^4 e_i^2 N_i \Lambda}{m^2} u_{E,j} \int d\mathbf{V} \frac{V_k}{V^3} \frac{\partial F(V)}{\partial V_j}, \qquad (4.10)$$

which immediately yields

$$\delta\mathbf{j} = \frac{16\pi^2 e^2 e_i^2 N_i \Lambda}{3m^2} \frac{e^2 F(0)}{m\omega^2} \mathbf{E} \equiv \frac{e^2 N_e}{m\omega^2} \nu(n, 0)\mathbf{E}. \quad (4.11)$$

From the distribution function (3.6) for $ns$ states, we find

$$f_{ns}(0) = (8n^5/\pi^2 V_Z^3),$$

hence,

$$\nu(n, 0) = \nu_Z(8/3)n^5. \qquad (4.12)$$

Relationship (4.12) shows that, for small values of the argument, the functions $A[1, ns, nV_E/V_Z]$ behave asymptotically as $\sim n^2$. This asymptotic behavior partially justifies the use of the function

$$\Psi[1, ns, y] = \frac{1}{n^2}A\left[1, ns, \frac{y}{n}\right] \qquad (4.13)$$

for comparatively weak pump fields, in which case, instead of formula (4.2), we have

$$\nu^{(1)}(n, E) = \nu_Z n^5 \Psi\left[1, ns, \frac{n^2 V_E}{V_Z}\right]. \qquad (4.14)$$

That the use of the argument $y = n^2 V_E/V_Z$ is justified is clear from Fig. 6, which depicts the plots of functions

$\Psi[1, ns, n^2 V_E/V_Z]$

$\Psi[1, np, n^2 V_E/V_Z]$
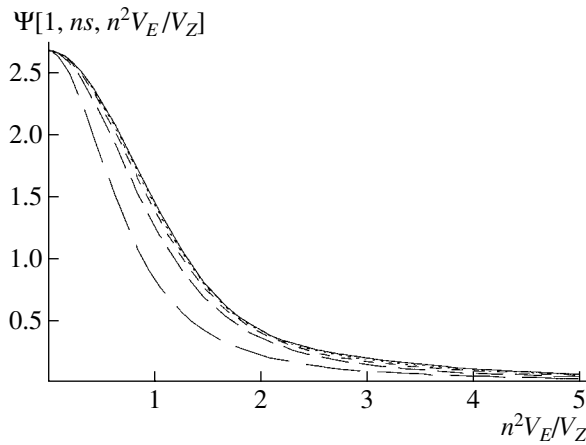
**Fig. 6.** Comparison of the functions $\Psi[1, ns, n^2 V_E/V_Z]$: the long dashes are for $n = 1$, the intermediate-length dashes are for $n = 2$, the short dashes are for $n = 3$, the dotted curve is for $n = 4$, and the solid curve is for $n = 5$.

**Fig. 7.** Comparison of the functions $\Psi[1, np, n^2 V_E/V_Z]$: the solid curve is for $n = 5$, the dotted curve is for $n = 4$, the shorter dashes are for $n = 3$, and the longer dashes are for $n = 2$.

(4.13). We can see that, for comparatively small values of the argument, functions (4.13) approach each other as the principal quantum number increases. This corresponds to the unified scaling describing inverse bremsstrahlung absorption in the case of *ns* states. Note that formula (4.13) corrects for the inaccurate formula (2.16) in [9], in which preliminary results on the subject were reported.
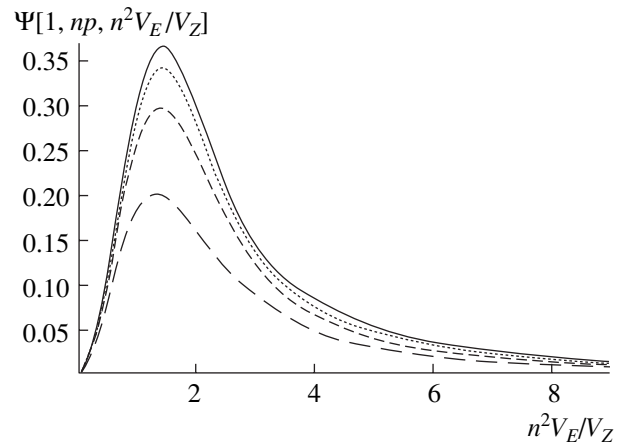
Now we again turn to the discussion of Figs. 2–5. Recall that these figures demonstrate how the properties of inverse bremsstrahlung absorption in a plasma produced through the photoionization of a gas of hydrogen-like atoms in the *np* states differ from the above-described absorption properties of the plasma in the case of *ns* states. Note that this difference can be readily understood on the basis of the equality $f_{np}(0) = 0$, which holds for *np* states and indicates that, for weak pump fields and for a plasma produced through the photoionization of a gas of hydrogen-like atoms in the *np* states, there is no linear law relating the current density to the pump field strength. In fact, for small values of *V*, we use formulas (3.7) and (3.3) to obtain from formula (3.5) the following distribution function for the first four *np* states:

$$f_{np}(V) = \frac{32}{3\pi^2} \frac{V^2}{V_Z^5} n^7 (n^2 - 1) \sim V^2. \qquad (4.15)$$

Expanding the right-hand side of Eq. (2.9) in powers of the pump field strength and retaining terms up to third order, we can write

$$\delta \mathbf{j} = \frac{e^2 N_e}{m\omega^2} \frac{8}{15} \nu_Z n^7 (n^2 - 1) \frac{V_E^2}{V_Z^2} \mathbf{E}. \qquad (4.16)$$

It is easy to guess that, for atomic states whose orbital quantum number *l* is larger than unity, the nonlinear dependence of the current density on the pump field strength is even stronger ($\sim E^{2l+1}$). This indicates that, in a plasma produced by photoionization from the excited electronic states of the gas atoms in the Bethe regime of suppression of the photoionization barrier, the high-frequency conductivity is always nonlinear.

Although the quantities given by formulas (4.10), (4.12), and (4.16) depend on the principal quantum number in different ways, we simplify a comparison between the results obtained for *ns* and *np* states by using the function

$$\Psi[1, np, y] = \frac{1}{n^2} A\left[1, np, \frac{y}{n}\right], \qquad (4.17)$$

in which case the effective nonlinear collision frequency can be described by an expression analogous to formula (4.14):

$$\nu^{(1)}(n, E) = \nu_Z n^5 \Psi\left[1, np, \frac{n^2 V_E}{V_Z}\right]. \qquad (4.18)$$

From Fig. 7, which shows the functions $\Psi[1, np, y]$ for 2*p*, 3*p*, 4*p*, and 5*p* states, we see that there is an almost direct proportionality ($\sim n$) to the principal quantum number. This stronger dependence on the principal quantum number for *p* states, as compared to the corresponding dependence for *s* states, can be understood by comparing formulas (3.4) and (3.5).

Hence, we have shown the following qualitative difference between the absorption properties of plasmas produced by the photoionization of gas atoms in the *np* states and *ns* states. In the case of *s*-states, the effective collision frequency decreases monotonically with increasing intensity of the radiation heating the plasma. In contrast, in the case of *p* states, the effective nonlinear collision frequency at low intensities of the heating

radiation increases with increasing radiation intensity; reaches its maximum value; and then decreases, approaching unified scaling (4.8).

**5.** Recall that, in order to directly compare the effective nonlinear collision frequencies that govern inverse bremsstrahlung absorption of radiation in plasmas produced by the photoionization of gas atoms in different electronic states, it is convenient to use formula (4.2). The functions $H[1, ns(p), V_E/V_Z]$ give an explicit dependence of the collision frequencies on the pump field intensity. For the $1s$ state, the corresponding function is depicted in Fig. 1. The functions corresponding to the four $ns$ and $np$ states are displayed in Figs. 2–5 (in which the ordinate is the value of the function and the abscissa is the ratio $V_E/V_Z$). When comparing the corresponding dependences for $s$ and $p$ states, it should be kept in mind that the amounts by which the functions $H[1, ns(p), V_E/V_Z]$ referring to these states vary are very different. That is why the functions in Figs. 2–5 are plotted on different vertical scales. Specifically, the ratios of the maximum values of the functions for $s$ and $p$ states are approximately equal to

$$\frac{H(1, ns, V_E/V_Z)}{H(1, ps, V_E/V_Z)} \approx \begin{cases} 13.5 & \text{for } n = 2 \\ 9.3 & \text{for } n = 3 \\ 7.9 & \text{for } n = 4 \\ 7.3 & \text{for } n = 5. \end{cases}$$

A relatively insignificant absorption in the case of $p$ states stems from the fact that the higher the velocities of the plasma particles, the lower the efficiency of the inverse bremsstrahlung effect. In the case of $s$ states, the absorption efficiency is comparatively high because electron distribution function (3.6) is maximum for $V \longrightarrow 0$. The case of $p$ states is radically different: as $V \longrightarrow 0$, distribution function (3.7) approaches zero according to law (4.15), thereby indicating that the absorption is relatively weak.

We emphasize that the pump fields of comparatively low intensities may be of particular importance. In fact, Bethe's condition (1.2) can be rewritten as

$$\frac{V_E}{V_Z} > \frac{Z^2}{n^4} \frac{I_{\mathrm{H}}}{8\hbar\omega},$$

where $I_{\mathrm{H}}$ is the ionization energy of a hydrogen atom. Accordingly, we can say that the regions of comparatively small values of the arguments of the functions shown in Figs. 1–7 (i.e., the regions for which the values of the principal quantum number are characteristically not small) are of great practical interest.

In conclusion, let us summarize the results obtained in this paper. In order to characterize nonlinear inverse bremsstrahlung absorption in a plasma produced by photoionization in the Bethe regime of suppression of the photoionization barrier, we have derived the nonlinear dependences of the high-frequency conductivity on the pump field intensity. We have established that, in the case of the photoionization of gas atoms with electrons in the $s$ states, the nonlinearity shows up in sufficiently intense pump fields (which is characteristic of a plasma with a Maxwellian electron distribution), provided that the electron oscillatory energy in the pump field is not low as compared to the energy of the atomic electrons. In contrast, in the case of atoms in electronic states with a nonzero orbital momentum, the plasma conductivity is nonlinear even in a low-intensity pump field. As a result, the plasma conductivity is reduced, indicating the possibility of the less efficient heating of plasmas produced through the photoionization of gas atoms in the excited electronic states with a nonzero orbital momentum. We have also derived the scalings characterizing inverse bremsstrahlung absorption in photoionized plasmas.

The reviewer of this paper recommended that we clarify two points. The first is associated with our choice of $np$ states in developing the theory of inverse bremsstrahlung absorption. In this context, we emphasize that this choice was dictated by the fact that these are the simplest states for which the dependence of the effective nonlinear collision frequency, governing the inverse bremsstrahlung absorption efficiency, on the intensity of the weak pump field is essentially nonlinear. This property is clearly demonstrated in Figs. 1–5 and by formula (4.16). We have mentioned that such a nonlinearity in weak pump fields is also peculiar to electronic states with large values of the orbital quantum number. Of course, the referee rightly noted that, in this case, the following circumstance should be kept in mind: the nonlinear phenomenon under discussion can occur only when the "mixing" electron–electron collisions do not cause Maxwellianization of the electron velocity distribution in velocity space. In other words, studies of the phenomenon in question should be restricted to time scales shorter than the electron collision time [see formulas (1.8) and (1.10)]. The second point to be clarified is the so-called parabolic quantization [16], which is often used to solve the Coulomb problem in the case of a nonzero electric field and to consider the corresponding radiative processes. In this connection, it should be stressed that, in the parabolic quantization description, the eigenfunctions of the discontinuous spectrum of a hydrogen-like atom can be represented as a linear superposition of the functions resulting from quantization in spherical coordinates [4]. Hence, it is evident that the approach developed here can be adapted to the parabolic quantization, with an appropriate change in the operators $D$. We are grateful to the reviewer for his suggestions.

*APPENDIX 1*

Here, we present the derivation of formula (3.6). We start by writing the wave function for *ns* states in terms of coordinates:

$$\psi_{n00}(\mathbf{r}) = \frac{1}{\sqrt{8\pi}}\left(\frac{2Z}{na_B}\right)^{3/2} F\left(-n+1.2;\frac{2Zr}{na_B}\right)$$
$$\times \exp\left(-\frac{Zr}{na_B}\right). \tag{A1.1}$$

In order to solve for the wave function

$$a_{n00}(\mathbf{p}) = \frac{1}{(2\pi\hbar)^{3/2}}\int d\mathbf{r}\exp\left(-\frac{i\mathbf{pr}}{\hbar}\right)\psi_{n00}(\mathbf{r}) \tag{A1.2}$$

in momentum space, we integrate it over the angles:

$$a_{n00}(\mathbf{p}) = \frac{\sqrt{2\pi}}{(2\pi\hbar)^{3/2}}\left(\frac{na_B}{2Z}\right)^{1/2}\frac{\hbar}{p}$$
$$\times \int_0^\infty dt\, t F(-n+1.2;\,t)\exp\left(-\frac{t}{2}\right)\sin\left(\frac{pna_B}{2Z\hbar}t\right). \tag{A1.3}$$

Then, using the relationship

$$\int_0^\infty t^{c-1} F(a,c;\,t)\exp(-st)dt = \Gamma(c)s^{-c}\left(1-\frac{1}{s}\right)^{-a}, \tag{A1.4}$$

we obtain

$$a_{n00}(\mathbf{p}) = i\frac{(-1)^{n-1}}{4\pi p}\left(\frac{na_B}{2\hbar Z}\right)^{1/2}$$
$$\times \frac{\left(\frac{1}{2}-i\frac{pna_B}{2\hbar Z}\right)^{2n}-\left(\frac{1}{2}+i\frac{pna_B}{2\hbar Z}\right)^{2n}}{\left(\frac{1}{4}+\left[\frac{pna_B}{2\hbar Z}\right]^2\right)^{n+1}}. \tag{A1.5}$$

Since

$$\left(\frac{1}{2}\pm i\frac{pna_B}{2\hbar Z}\right)^{2n}$$
$$= \left(\frac{1}{4}+\left[\frac{pna_B}{2\hbar Z}\right]^2\right)\exp\left\{\pm i\arctan\left(\frac{pna_B}{\hbar Z}\right)\right\}, \tag{A1.6}$$

the wave function (A1.5) takes the form

$$a_{n00}(\mathbf{p}) = i\frac{(-1)^{n-1}}{4\pi p}$$
$$\times \frac{\exp\left\{-in\arctan\left(\frac{pna_B}{\hbar Z}\right)\right\}-\exp\left\{in\arctan\left(\frac{pna_B}{\hbar Z}\right)\right\}}{\left(\frac{2\hbar Z}{na_B}\right)^{1/2}\left(\frac{1}{4}+\left[\frac{pna_B}{2\hbar Z}\right]^2\right)}, \tag{A1.7}$$

which immediately yields distribution function (3.6).

*APPENDIX 2*

The polynomials $P_{4n}[1, ns, x]$ for the first five *ns* states have the form

$$P_4[1, 1s, x] = \frac{-3+x^2+x^4}{3}, \tag{A2.1}$$

$$P_8[1, 2s, x] = \frac{-15+95x^2+36x^4+42x^6+11x^8}{15}, \tag{A2.2}$$

$$P_{12}[1, 3s, x] = \frac{-105+1855x^2-2023x^4+3538x^6+1017x^8+513x^{10}+87x^{12}}{105}, \tag{A2.3}$$

$$P_{16}[1, 4s, x] = \frac{1}{63}(-63+2163x^2-8106x^4+20\,628x^6-8930x^8+6094x^{10}+1320x^{12}+436x^{14}+55x^{16}), \tag{A2.4}$$

$$P_{20}[1, 5s, x] = \frac{1}{495}(-495+27\,885x^2-211\,959x^4+919\,908x^6-1\,375\,682x^8+123\,597x^{10}$$
$$-295\,050x^{12}+104\,000x^{14}+17\,925x^{16}+4425x^{18}+445x^{20}). \tag{A2.5}$$

The polynomials $P_{4n}[1, np, x]$ for the first four $np$ states ($p = 2, 3, 4, 5$) have the form

$$P_8[1, 2p, x] = \frac{-15 - 65x^2 - 12x^4 + 6x^6 + 3x^8}{15}, \tag{A3.1}$$

$$P_{12}[1, 3p, x] = \frac{-105 - 665x^2 + 2261x^4 - 341x^6 + 531x^8 + 279x^{10} + 51x^{12}}{105}, \tag{A3.2}$$

$$P_{16}[1, 4p, x]$$

$$= \frac{1}{105}(-105 - 875x^2 + 10234x^4 - 17316x^6 + 16530x^8 + 930x^{10} + 1560x^{12} + 500x^{14} + 65x^{16}), \tag{A3.3}$$

$$P_{20}[1, 5p, x] = \frac{1}{165}(-165 - 1705x^2 + 44847x^4 - 184239x^6 + 364056x^8 - 234108x^{10}$$

$$+ 97650x^{12} + 6375x^{14} + 4725x^{16} + 1125x^{18} + 115x^{20}). \tag{A3.4}$$

### REFERENCES

1. V. P. Silin, Zh. Éksp. Teor. Fiz. **47**, 2254 (1964) [Sov. Phys. JETP **20**, 1510 (1964)].

2. F. V. Bunkin, A. E. Kazakov, and M. V. Fedorov, Usp. Fiz. Nauk **107**, 559 (1972) [Sov. Phys. Usp. **15**, 416 (1973)]; V. P. Silin and S. A. Uryupin, Zh. Éksp. Teor. Fiz. **81**, 910 (1981) [Sov. Phys. JETP **54**, 485 (1981)].

3. V. P. Silin, *Introduction to the Kinetic Theory of Gases* (Nauka, Moscow, 1981; Izd. Fiz. Inst. im. P.N. Lebedeva, Moscow, 1998).

4. H. A. Bethe, *Handbuch der Physik B1, 24/1: Quantenmechanik der Ein- und Zwei-Electronenprobleme* (Springer-Verlag, Berlin, 1933; ONTI, Moscow, 1935).

5. S. August, D. D. Meyerhofer, D. Strickland, and S. I. Chin, J. Opt. Soc. Am. B **8**, 858 (1991).

6. M. V. Fedorov and J. Peatross, Phys. Rev. A **52**, 504 (1995).

7. V. P. Silin, Zh. Éksp. Teor. Fiz. **117**, 926 (2000) [JETP **90**, 805 (2000)].

8. A. B. Fedotov, A. N. Naumov, V. P. Silin, *et al.*, Phys. Lett. A **271**, 407 (2000).

9. V. P. Silin, Phys. Lett. A **286**, 190 (2001).

10. V. P. Silin, Zh. Éksp. Teor. Fiz. **121**, 291 (2002) [JETP **94**, 244 (2002)].

11. L. D. Landau and E. M. Lifshits, *Quantum Mechanics: Non-Relativisic Theory* (Fizmatgiz, Moscow, 1963; Pergamon, Oxford, 1972).

12. A. S. Davydov, *Quantum Mechanics* (Nauka, Moscow, 1973).

13. V. P. Silin, Pis'ma Zh. Éksp. Teor. Fiz. **69**, 486 (1999) [JETP Lett. **69**, 521 (1999)].

14. V. P. Silin, Kvantovaya Élektron. (Moscow) **29**, 49 (1999).

15. I. S. Gradshteyn and I. M. Ryzhik, *Table of Integrals, Series, and Products* (Fizmatgiz, Moscow, 1963; Academic, New York, 1980).

16. Y. Hahn, Rep. Prog. Phys. **60**, 69 (1997).

*Translated by O. E. Khadin*

# Calculation of the Grain Charge Fluctuations in a Dusty Plasma

## S. A. Maĭorov[1, 2], S. V. Vladimirov[2], and N. F. Cramer[2]

[1]*Prokhorov Institute of General Physics, Russian Academy of Sciences, ul. Vavilova 38, Moscow, 117942 Russia*
[2]*School of Physics, University of Sydney, NSW 2006, Sydney, Australia*
Received January 23, 2002; in final form, February 26, 2002

**Abstract**—The time characteristics of grain charging, namely, the relaxation time of the steady grain charge and the charge fluctuations of grains of different sizes, are computed from particle simulations. The results obtained are compared with some theoretical predictions (primarily those derived from the drift–diffusion model). The simulations are carried out for nonmoving and moving two-temperature argon plasmas. © *2002 MAIK "Nauka/Interperiodica".*

## 1. INTRODUCTION

In recent years, dusty plasmas have been actively studied both experimentally and theoretically (see, e.g., [1–3]). Under actual experimental conditions, the electron temperature in a collisional gas-discharge plasma is usually governed by the energy input from an external source (microwave radiation, electric current, photoionization, etc.), whereas the ions are in thermal equilibrium with the cold atoms of a buffer gas. Also, an ion flux directed toward the electrode forms in the electrode sheath. As a result, under certain conditions, the grain can be in equilibrium (or, in other words, it can levitate) because of the balance between an electric force, a gravitational force, and a frictional force in the ion flux [4]. However, experiments show that this equilibrium may be unstable [5–7] and some analytic models suggest that the instability may be driven, in particular, by fluctuations of the dust grain charge [7, 8].

In this paper, which is a continuation of [9–11], we describe the results of numerical experiments carried out to investigate different kinetic parameters of dust grains of micron size in a plasma. Numerical simulations were aimed, in particular, at calculating the dynamics of charging an initially uncharged grain (which was assumed to absorb all plasma electrons and ions striking its surface) and the kinetic parameters of the steady (established) state. We describe numerical results obtained for a nonmoving two-temperature plasma and a moving plasma and investigate the statistical properties of the grain charge fluctuations.

Most simulations were based on the particle-in-cell (PIC) method. Newton's equations of motion for a system of charged point particles (plasma electrons and ions) were solved in a cubic cell with a heavy macroparticle (grain) at its center. The reflection of electrons and ions from the cube faces was described using electron and ion velocity distribution functions at large distances from the grain. As usual, we used Maxwellian distribution functions, possibly with different electron and ion temperatures. These boundary conditions allow us to refer to the cube faces as thermostatic walls. A moving plasma was modeled by using other boundary conditions for the ions: the plasma with an ion influx was described by a shifted Maxwellian ion distribution and the cube faces were assumed to perfectly absorb the ions leaving the computation region.

Most simulations were carried out with the help of a simplified model in which the particle trajectories were computed with allowance for only the interaction of a grain with plasma particles and the screening effect. Although the model is rather crude, it provides fairly exact calculations of the kinetic parameters of a grain in a nonmoving plasma, which is confirmed by comparing its results not only with available theoretical predictions, but also with the results from more precise simulations based on the molecular dynamic (MD) method. For a moving plasma, however, the simplified model yields larger errors; in this case, it was checked only by more laborious MD simulations.

## 2. GENERAL FORMULATION OF THE PROBLEM AND SOLUTION METHODS

Computer simulations based on *ab initio* principles are widely used in solving various plasma problems [12]. The main advantage of this approach is that, in a computer model, it is necessary to specify only the shape of the potential of the interaction between particles.

The results presented here were obtained from both MD and PIC simulations of systems consisting of only several tens of thousands of particles. The plasma was assumed to consist of ions with mass $m_i$ and positive charge $e$ and electrons with mass $m_e$ and charge $-e$. We simulated the dynamics of a system of $n_e$ electrons and $n_i$ ions in a cube at the center of which there is a heavy

spherical absorbing body with radius $R$ and charge $Q = Z_0 e < 0$. The number of electrons and ions was chosen so that the entire plasma system was electrically neutral, $n_i - n_e + Z_0 = 0$. With this choice, the electron density in the cube was lower than the ion density because of the negative charge of the grain.

The particle trajectories in such a system were calculated by solving Newton's equations of motion

$$d^2\mathbf{r}_k/dt^2 = \mathbf{F}_k/m_k, \quad k = 1, 2, \ldots, n_p. \quad (1)$$

In the MD method, the force acting on any particle in the system is determined as a sum of forces from the remaining particles:

$$\mathbf{F}_k = \frac{q_k Q(\mathbf{r}_k - \mathbf{r}_g)}{|\mathbf{r}_k - \mathbf{r}_g|^3} + \sum_{l \neq k}^{n_p} \mathbf{f}_{kl}, \quad k = 1, 2, \ldots, n_p; \quad (2)$$

where $\mathbf{r}_k(t)$ is the position vector of the $k$th particle with mass $m_k$ and charge $q_k$, $\mathbf{r}_g(t)$ is the position vector of a grain with charge $Q$, and $n_p$ is the total number of particles. In order to remove singularities, the Coulomb forces of the interaction between the particles that occur at short distances from each other were modeled by the forces of the interaction between uniformly charged, completely interpenetrating spheres with a very small radius [12]. Equations (1) and (2) were solved using a fourth-order Runge–Kutta method. In contrast to [9], where the dynamics of a grain dragged by an ion flux was taken into account, we modeled an infinitely heavy (i.e., immobile) grain.

The PIC method differs from the MD method in that it uses cruder approximations for the forces acting on the particles, which clearly provides faster calculations. As in the MD method, we computed particle trajectories by solving Newton's equations of motion (1), but the force acting on plasma particles was calculated in a different way:

$$\mathbf{F}_k = \frac{q_k Q \mathbf{r}_{kg}}{|\mathbf{r}_{kg}|^3} + q_k \frac{\mathbf{r}_{kg}}{|\mathbf{r}_{kg}|^3} \sum_{\mathbf{r}_{lg} < \mathbf{r}_{kg}}^{n_p} q_l, \quad k = 1, 2, \ldots, n_p, \quad (3)$$

where $\mathbf{r}_{kg} = \mathbf{r}_k - \mathbf{r}_g$ and the summation is over all particles that are closer to the grain than the $k$th particle. This way of calculating the force acting on the particles makes it possible to take into account the screening effect of the ion–electron cloud surrounding the grain. The force acting on the grain was determined from Newton's third law. Formula (3) corresponds to an exact solution for a spherically symmetric plasma distribution, i.e., to the case in which, according to Gauss's theorem, the field on a spherical surface is determined exclusively by the total charge inside the sphere. In a spherically symmetric problem, the field is independent of the radial distribution of charges inside the sphere. An analogous method was applied by Zobnin *et al.* [13] to calculate the electric field around a charged grain.

In order to determine the extent to which the model is adequate, we compared the results of our simulations with the results obtained from Eqs. (1) and (2) in the MD method and from Eqs. (1) and (3) in the PIC method. An analysis of the results shows that it is completely justified to use formula (3) to describe a nonmoving plasma. This makes it possible to calculate the fluctuation dynamics of grain charging on a long time scale by performing computations with a large number of particles for an actual electron-to-ion mass ratio. For a moving plasma, this approach also yields fairly exact results, although it leads to somewhat larger errors.

A necessary (but not always sufficient) condition for the PIC simulation results to be adequate is that the number of particles in the volume to be modeled should be much larger than the number of particles inside the Debye sphere. In experiments on dusty plasmas, the characteristic parameter values are the following: the ion density is $N_i = 10^9$ cm$^{-3}$, the electron temperature is $T_e = 1$ eV, and the ion temperature is $T_i = 0.025$ eV. For these parameter values, there are approximately $10^6$ plasma particles inside a Debye sphere. Since the number of arithmetic operations per time step in MD simulations is proportional to the square of the particle number, even modern parallel computers are incapable of performing such an enormous amount of calculations. That is why it is necessary to refer to scalings for physical parameters and to use simplified models, which reduce the amount of computer calculations.

In dusty plasmas, an important role is played by grain charging processes and grain charge fluctuations. One of the general problems in plasma simulations is that the ion and electron masses are very different. For this reason, the slow processes associated with ion motion should be calculated on a difference grid whose time steps are determined by the fast electron time scales. A possible approach to overcoming this problem is to use models in which the electron-to-ion mass ratio is increased in order to reduce the difference between the characteristic ion and electron time scales [10, 12] or the electrons are described by a Boltzmann distribution [13]. However, these approaches are inapplicable for calculating the grain charge fluctuations.

In this paper, the main simplifying assumption that makes it possible to compute the fluctuation parameters of the grain charge is the assumption of a spherical symmetry of the charge density around the grain. This assumption, under which forces (3) were calculated, actually indicates that the plasma particles interact with each other only through the radius-averaged grain charge fluctuations and the charge acquired by the grain.

## 3. GRAIN CHARGING AND GRAIN CHARGE FLUCTUATIONS IN A PLASMA

In an ideal gas, the mean number $\Delta N$ of atoms colliding with a grain during the time interval $t$ is propor-

tional to the surface area of a grain, the atom flux density, and the time interval itself. Accordingly, for a ball in a gas with a Maxwellian distribution of atoms, the number of collisions is equal to

$$\Delta N(t) = 4\pi R^2 J_M t, \tag{4}$$

where $J_M = (T_e/2\pi m)^{1/2} n$ is the density of the atom flux onto the ball surface in a Maxwellian gas and $n$ is the atom density. Formula (4) describes the charging of an initially uncharged grain to values that are small in comparison with its mean charge.

If the mean grain charge in a steady-state plasma is equal to $\overline{Q}$, then the time dependence of the deviation $\Delta Q(t) = Q(t) - \overline{Q}$ of the grain charge from its mean value is usually described by the equation [14]

$$d\Delta Q/dt = -\Delta Q/\tau_f. \tag{5}$$

This equation is based on the assumption that the rate at which the grain charge relaxes to its mean value is proportional to the deviation from it, provided that the deviation by itself is small.

The characteristic relaxation time is usually chosen to be the characteristic time $\tau_f$ of the grain charge fluctuations. For a Maxwellian plasma, the definition of this time in the drift–diffusion approximation was given in [14]:

$$\tau_f = \left(\frac{4 r_{Di}^2}{v_i R}\right)\frac{1}{1 + T_i/T_e + \overline{\varphi}/T_e}, \tag{6}$$

where $v_i = (8T_i/\pi M)^{1/2}$ is the mean ion thermal velocity and $\overline{\varphi} = -e\overline{Q}/R$ is the height of the energy barrier. As usual, the characteristic fluctuation time is also assumed to be the characteristic time of the exponential decrease in the autocorrelation function of the grain charge fluctuations, $\langle \Delta Q(t + \tau)\Delta Q(t)\rangle = \langle \Delta Q^2\rangle \exp(-\tau/\tau_f)$.

In the Fokker–Planck approximation, the mean square of the amplitude of the grain charge fluctuations is determined by the ratio of the fluctuation time to the mean time $\tau_c$ between collisions of plasma particles with the grain:

$$\sigma^2 = \langle \Delta Q^2\rangle/e^2 = \tau_f/2\tau_c. \tag{7}$$

Cui and Goree [15] derived the following approximate dependence of the mean square deviation of the grain charge from its mean value:

$$\sigma = c_\sigma Z^{1/2}, \quad c_\sigma = 1/2, \tag{8}$$

where $Z$ is the grain charge expressed in units of the electron charge. The coefficient $c_\sigma$ was also calculated from the data obtained in our numerical experiments,

namely, from the mean grain charge and the amplitude of the grain charge fluctuations:

$$c_\sigma = \sigma/Z^{1/2}. \tag{9}$$

Another approximate dependence of the mean square deviation of the grain charge from its mean value was obtained by Matsoukas and Russel [14]:

$$\frac{\sigma^2}{e^2 R T_e} = 1 - \frac{1}{1 + T_i/T_e + \overline{\varphi}/T_e}. \tag{10}$$

When analyzing the results of numerical simulations, we described the grain charging process by the approximate function

$$Q(t) = \overline{Q} + \Delta Q(0)\exp(-t/\tau_f). \tag{11}$$

Note that we chose the time interval to be shorter than the run time of the code. Specifically, we removed a certain initial time during which Eq. (5) fails to hold from consideration because of the large deviation of the grain charge from its mean value; on the other hand, we chose the initial deviation to be much larger than the fluctuation amplitude.

## 4. RESULTS FROM SIMULATIONS OF A NONMOVING TWO-TEMPERATURE PLASMA

First, we consider the results obtained for a two-temperature argon plasma with $z = 1$ and $N_i = 2 \times 10^{12}$ cm$^{-3}$, the ion and electron temperatures being $T_i = 0.025$ eV and $T_e = 1$ eV. In terms of the characteristic distance between the ions, the electron Debye radius $r_{De} = (T_e/4\pi e^2 N_e^2)^{1/2}$ is equal to $r_{De}N_i^{1/3} = 6.6$, in which case there are 1220 electrons within the Debye sphere. We can see that the conditions for both the electron and ion plasma components to be ideal are well satisfied.

Initially, the electrons and ions were uniformly distributed inside the cube, and their velocity distributions were chosen to be Maxwellian distributions at infinity. Depending on the initial distance to the grain, the Maxwellian distribution over the absolute value of the velocity was shifted by the energy of the interaction with the grain. The initial velocity distributions of the electrons and ions were chosen to be isotropic. Hence, the initial distributions correspond to the absence of electrons and ions that are trapped by the grain and, under certain conditions, may greatly distort the grain kinetic parameters.

An initially uncharged, infinitely heavy grain with prescribed dimensions was assumed to be located at the center of the cube and to absorb all plasma electrons and ions incident on its surface. In our previous simulations, the number of electrons and ions in the cube was fixed. Consequently, because of the grain charge fluctuations, the system was, on the average, electrically neutral only on sufficiently long time intervals; this situa-

tion (at best) could be achieved by appropriately choosing the number of ions and electrons in the system on the basis of the results from preliminary computations.

We applied, for the first time, an algorithm that made it possible to strictly preserve the electrical neutrality of the entire system, specifically, the particle injection algorithm. When a plasma particle was absorbed by the grain, the neutrality of the system (of course, with allowance for the grain charge) was maintained by injecting the required number of particles into the plasma volume from a random point at the cube faces. The essence of the algorithm can be described as follows. When an electron was absorbed by the grain, the number of electrons in the system decreased; however, when an ion was absorbed, an electron–ion pair was injected into the system from a cube face. As a result, the number of ions was maintained constant, while the number of electrons was varied in time so as to ensure plasma neutrality. The reflection of electrons from the cube faces was described by the boundary conditions corresponding to thermostatic walls. This allowed us to describe the electrons by a Maxwell–Boltzmann distribution function and to model the appearance of electrons whose kinetic energy is high enough for them to overcome the potential barrier. Such a formulation of the problem provides a self-consistent description of both the charging of a grain and of the fluctuations of its charge.

Hence, our model assumes that the number of ions in the system is constant while the number of electrons may decrease because of the electron absorption by the grain. This indicates that the mean electron density in the system may become substantially lower than the ion density. The amount by which the electron density decreases can be estimated using the ratio of the grain charge to the number of ions in the system. The situation when the electron density is substantially lower than the ion density corresponds to a plasma with dust clouds or dust crystals. In our problem of the calculation of the grain charge fluctuations, a decrease in the mean electron density did not change the kinetic parameters of the entire system because it was electrically neutral. That this is the case was checked by carrying out test simulations with a much larger number of plasma particles.

Figures 1 and 2 show how the charges of spherical grains of different radii and the number of electrons and ions absorbed by them change with time. In all figures presented in this paper, the time is normalized to the ion plasma frequency $\omega_i = (4\pi e^2 N_i / M)^{1/2}$ (where $M$ is the mass of an ion), the ion plasma period being $\tau_i = \omega_i^{-1} = 3.4$ ns. The system evolution was followed over the time $t_0 = 1.7 \times 10^{-7}$ s, which was much longer than both the ion plasma period ($2.14 \times 10^{-8}$ s) and the characteristic time scale on which the grain was charged. For convenience, all figures present the results obtained for
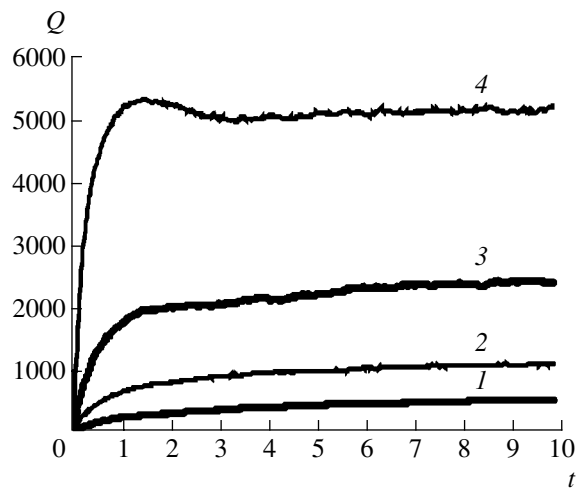


**Fig. 1.** Time evolution of the charges $Q$ of absorbing spherical grains with the radii $r = $ (*1*) 0.25, (*2*) 0.5, (*3*) 1, and (*4*) 2 µm in a nonmoving two-temperature plasma with $T_i = 1/40$ eV.
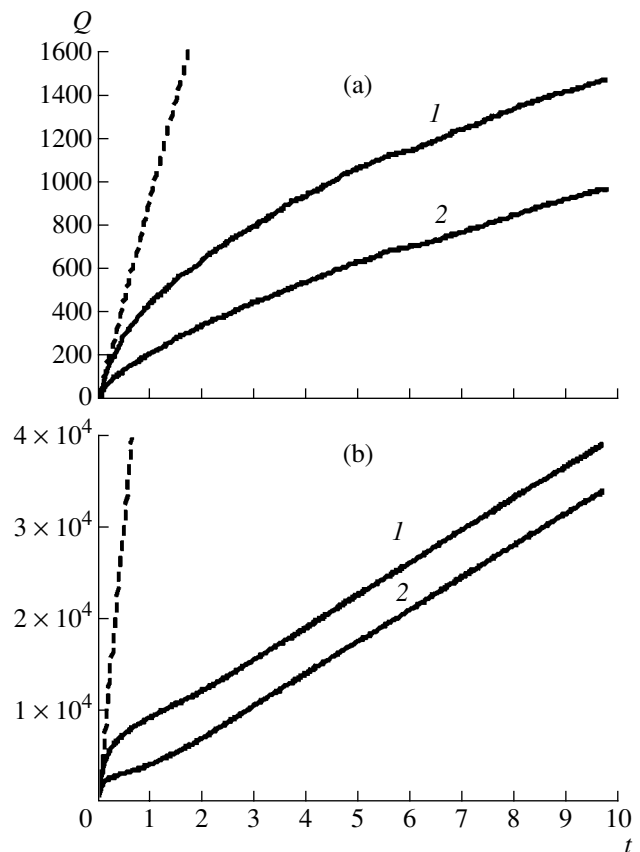


**Fig. 2.** Time evolution of the number of (*1*) electrons and (*2*) ions absorbed by spherical grains with the radii $r = $ (a) 0.25 and (b) 2 µm in a nonmoving two-temperature plasma with $T_i = 1/40$ eV. The dashed curves are calculated from the dependence $Q(t) = SJ_M(t)$.
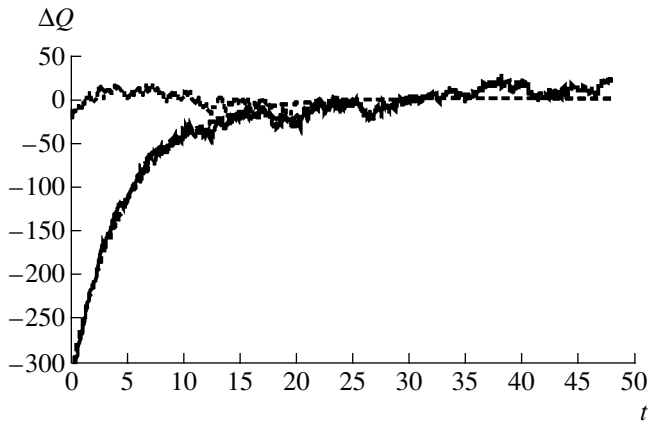
**Fig. 3.** Deviation $\Delta Q$ of the charge of an absorbing spherical grain with the radius $r = 0.25$ μm from its mean charge in a nonmoving two-temperature plasma with $T_i = 1/40$ eV. The solid curve shows the deviation of the grain charge from its mean value, the dashed curve is the approximation of this deviation by formula (11), and the dotted curve shows the deviation of the calculated grain charge from approximating dependence (11).

an initial time interval comparable with the characteristic period of the grain charge fluctuations.

Figure 1 illustrates the results of four series of computations, specifically, the time evolution of the charges of initially uncharged spherical grains with the radii $r = 0.25, 0.5, 1,$ and 2 μm (the larger the radius of the grain, the larger the charge acquired by it). The initial number of ions in the system was taken to be 15000 (this number was constant in the course of a run), and the initial number of electrons was also taken to be 15000 (this number changed in the course of a run); on the whole, the system always remained electrically neutral. The size of the computation region (the cube edge) was 19 μm.

Figure 2 shows how the number of electrons and ions absorbed by spherical grains with the radii $r = 0.25$ and 2 μm changes in time. The dashed curves were calculated from the dependence $Q(t) = SJ_M t$, following

from formula (4). The number of absorbed electrons is always larger than the number of absorbed ions.

Figure 3 illustrates the way of determining the mean grain charge, the amplitude of grain charge fluctuations, and the characteristic fluctuation time. The plots in Fig. 3 were obtained in the calculations of the evolution of the charge of a grain with the radius $r = 0.25$ μm. The solid curve shows how the grain charge deviates from its mean value as time elapses, the dashed curve is the approximation of this deviation by formula (11), and the dotted curve refers to the deviation of the calculated grain charge from approximating dependence (11).

An interesting effect revealed in simulations is that the charge of a grain with the largest radius increases nonmonotonically. An analysis of the time evolution of the ion current shows that this nonmonotonic behavior stems from the fact that the relaxation time of the screening ion cloud around the grain is longer than that of the grain charge. Accordingly, the larger the steady-state grain charge, the more pronounced this effect.

Table 1 presents the results of an analysis of the calculated data and the corresponding theoretical results. Note that the calculated fluctuation time is much longer than the theoretically predicted time (it may be even said that the calculated time is anomalously long, because it substantially exceeds the calculation error). A detailed analysis of this circumstance goes beyond the scope of our study. Note only that the fluctuation time differs, in principle, from the time during which the grain charge relaxes to its steady-state value (see also [14]); this difference was, in fact, revealed in our numerical experiments, in which the grain charge relaxation was found to be nonmonotonic.

## 5. RESULTS FROM SIMULATIONS OF A MOVING PLASMA

Here, we consider the results obtained for a moving plasma, which is most often encountered in experiments. The formulation of the problem was analogous to that described in the previous section, the only differ-

**Table 1.** Parameters of the charging of grains of different sizes in a two-temperature plasma with $T_i = 0.025$ eV: the mean grain charge and its mean square deviation from the approximating curve, the fluctuation times obtained numerically and those obtained theoretically for a Maxwellian plasma, and the height of the potential barrier

| $R$, μm | 0.25 | 0.5 | 1 | 2 |
|---|---|---|---|---|
| Mean charge $Q$ | 556 | 1172 | 2517 | 5157 |
| Charge fluctuations σ (numerical calculations) | 10.5 | 17.4 | 27.1 | 31.2 |
| Charge fluctuations σ (calculated by (10)) | 11.5 | 16.4 | 26.4 | 33.1 |
| $c_σ$ (calculated by (9)) | 0.446 | 0.507 | 0.528 | 0.434 |
| $c_σ$ (calculated by (10)) | 0.488 | 0.479 | 0.465 | 0.461 |
| Charge relaxation time $τ$, ns (calculated by (11)) | 17.6 | 17.9 | 16.8 | 11.9 |
| fluctuation time $τ$, ns (calculated by (6)) | 6.7 | 3.2 | 1.5 | 0.75 |
| Potential barrier φ, V | 3.21 | 3.38 | 3.63 | 3.72 |
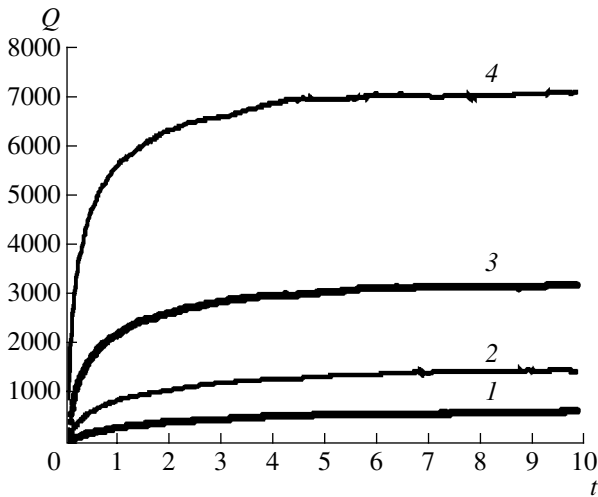
**Fig. 4.** Time evolution of the charges of absorbing spherical grains with the radii $r = (1)$ 0.25, $(2)$ 0.5, $(3)$ 1, and $(4)$ 2 μm in a moving two-temperature plasma with $T_i = 1/40$ eV; the kinetic energy of the directed ion motion is 2 eV.

ence being that each ion was assigned an initial directed velocity corresponding to the kinetic energy $K_i = 2$ eV. The remaining physical and computational parameters were the same as those in simulations of a nonmoving two-temperature plasma.

In analogy with Fig. 1, Fig. 4 illustrates the results from calculations of the time evolution of the charges of initially uncharged spherical grains with the radii $r = 0.25, 0.5, 1,$ and 2 μm.

In analogy with Fig. 2, Fig. 5 shows the time evolutions of the number of electrons and ions absorbed by spherical grains with the radii $r = 0.25$ and 2 μm, respectively. The dashed curves were calculated from the dependence $Q(t) = SJ_M t$, following from formula (4). The number of absorbed electrons is always larger than the number of absorbed ions.

Table 2 summarizes the results of an analysis of the calculated data. The fluctuation times were calculated from formula (6) for $T_i = 1$ eV, because the mean
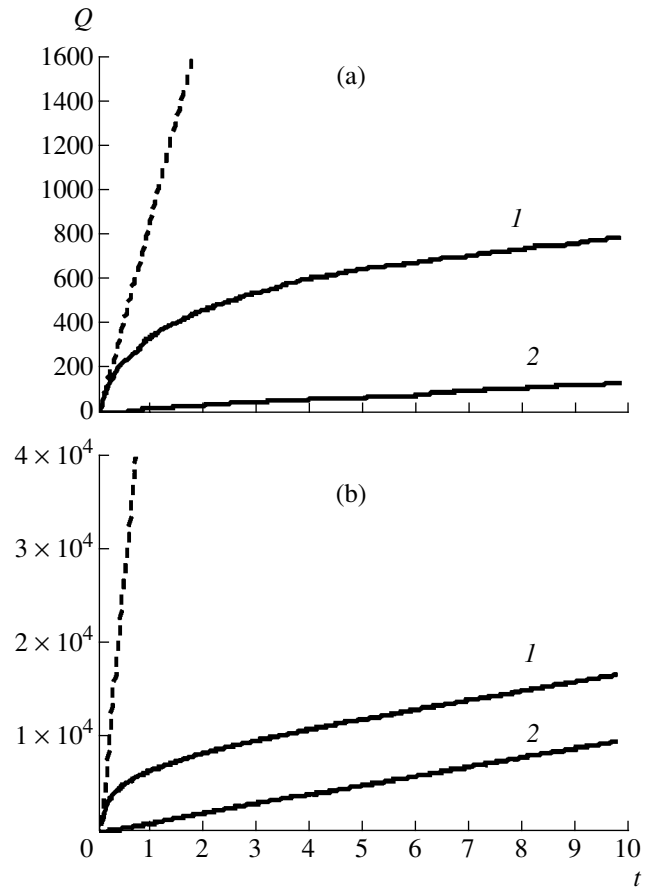


**Fig. 5.** Time evolution of the number of ($1$) electrons and ($2$) ions absorbed by spherical grains with the radii $r =$ (a) 0.25 and (b) 2 μm in a moving two-temperature plasma with $T_i = 1/40$ eV; the kinetic energy of the directed ion motion is 2 eV. The dashed curves are calculated from the dependence $Q(t) = SJ_M t$.

kinetic energy of Maxwellian ions at the grain surface is equal to

$$\langle K \rangle = \int_0^\infty v f_M(v) K dv \bigg/ \int_0^\infty v f_M(v) dv = 2T,$$

**Table 2.** Same as in Table 1, but for a moving plasma with the ion kinetic energy $K_i = 2$ eV, corresponding to argon atoms

| $R$, μm | 0.25 | 0.5 | 1 | 2 |
|---|---|---|---|---|
| Mean charge $Q$ | 751 | 1590 | 3276 | 7084 |
| Charge fluctuations σ (numerical calculations) | 9.9 | 19.7 | 23.4 | 33.4 |
| Charge fluctuations σ (calculated by (10)) | 12.1 | 17.2 | 24.3 | 34.5 |
| $c_\sigma$ (calculated by (9)) | 0.352 | 0.494 | 0.408 | 0.396 |
| $c_\sigma$ (calculated by (10)) | 0.441 | 0.430 | 0.425 | 0.410 |
| Charge relaxation time τ, ns (calculated by (11)) | 30.3 | 15.4 | 8.9 | 5.9 |
| fluctuation time τ, ns (calculated by (6)) | 28.3 | 13.6 | 6.7 | 3.2 |
| Potential barrier φ, V | 4.33 | 4.58 | 4.72 | 5.10 |

where $f_M(v) = v^2 \exp(-mv^2/2T)$ and $K(v) = mv^2/2$. Accordingly, the energy of ions with the kinetic energy $K_i = 2$ eV is equal to the mean kinetic energy of an ion flux with $T_i = 1$ eV.

Note that the computed grain-charge fluctuation times agree fairly well (within a factor of about two) with the theoretically predicted times, in contrast to the case of a nonmoving two-temperature plasma, in which the calculated fluctuation times differ from those obtained theoretically from formula (6) by more than one order of magnitude.

Since the accuracy of the calculations of the amplitude of the grain charge fluctuations depends on the ratio of the time during which the grain charging process is followed to the fluctuation time, the computational errors are the largest for small grains, for which the charge fluctuation times are the longest.

Presumably, numerical errors in determining the fluctuation times for large grains are also associated with the fact that, in the computational scheme used in our simulations, the number of electrons becomes comparable with the grain charge number; as a result, the electron density becomes substantially lower than the ion density.

## 6. CONCLUSION

The results of our numerical simulations can be used to analyze the kinetic parameters of the grain charging processes in plasmas, to check theoretical models, and to model the processes occurring in laboratory experiments. The PIC numerical method developed here makes it possible to investigate a wide scope of problems associated with the charging of dust grains and their behavior under various conditions in dusty plasmas. In particular, we have calculated the time characteristics of the relaxation of the grain charge and the amplitude of its fluctuations as functions of the grain size and the parameters of a nonmoving and moving plasma. These results are of interest for predicting the processes in experimental devices and, in particular, for analyzing the problems associated with the stability of the levitation of dust grains.

## REFERENCES

1. H. Tomas and G. Morfill, Nature (London) **379**, 806 (1996).
2. V. N. Tsytovich, Usp. Fiz. Nauk **167**, 57 (1997) [Phys. Usp. **40**, 53 (1997)].
3. A. M. Ignatov, Fiz. Plazmy **24**, 731 (1998) [Plasma Phys. Rep. **24**, 677 (1998)].
4. S. V. Vladimirov and N. F. Cramer, Phys. Rev. E **62**, 2754 (2000).
5. S. Nunomura, T. Misawa, N. Ohno, and S. Takamura, Phys. Rev. Lett. **83**, 1970 (1999).
6. A. A. Samarian, B. W. James, S. V. Vladimirov, and N. F. Cramer, Phys. Rev. E **64**, 025402(R) (2001).
7. O. S. Vaulina, A. P. Nefedov, O. F. Petrov, *et al.*, Zh. Éksp. Teor. Fiz. **120**, 1369 (2001) [JETP **93**, 1184 (2001)].
8. A. V. Ivlev, U. Konopka, and G. Morfill, Phys. Rev. E **62**, 2739 (2000).
9. S. V. Vladimirov, N. F. Cramer, and S. A. Maĭorov, Kratk. Soobshch. Fiz., No. 9, 33 (2000).
10. S. A. Maiorov, S. V. Vladimirov, and N. F. Cramer, Phys. Rev. E **63**, 17401 (2001).
11. S. V. Vladimirov, S. A. Maiorov, and N. F. Cramer, Phys. Rev. E **63**, 045401 (2001).
12. R. Hockney and J. Eastwood, *Computer Simulation Using Particles* (McGraw-Hill, New York, 1984; Mir, Moscow, 1987).
13. A. V. Zobnin, A. P. Nefedov, V. A. Sinel'shchikov, and V. E. Fortov, Zh. Éksp. Teor. Fiz. **118**, 554 (2000) [JETP **91**, 483 (2000)].
14. T. Matsoukas and M. Russel, Phys. Rev. E **55**, 991 (1997).
15. C. Cui and G. Goree, IEEE Trans. Plasma Sci. **22**, 151 (1994).

*Translated by G. V. Shepekina*

# Corona Discharge at the Tip of a Tall Object in the Electric Field of a Thundercloud

**N. L. Aleksandrov[1], E. M. Bazelyan[2], M. M. Drabkin[3],**
**R. B. Carpenter, Jr.[3], and Yu. P. Raizer[4]**

[1] *Moscow Institute of Physics and Technology, Institutskiĭ per. 9, Dolgoprudnyĭ, Moscow oblast, 141700 Russia*
[2] *Krzhizhanovsky Power Engineering Institute, Leninskiĭ pr. 19, Moscow, 117927 Russia*
[3] *LEC Inc., Boulder, Colorado, USA*
[4] *Institute for Problems in Mechanics, Russian Academy of Sciences, pr. Vernadskogo 101, Moscow, 117526 Russia*

Received April 18, 2002

**Abstract**—Characteristics of a positive transient corona discharge near the tip of a tall solitary grounded object in the electric field of a thundercloud are studied analytically and numerically. The time evolution of the discharge current and the space distribution of the total electric field are simulated for different growth rates of the external field and the dimensions and geometry of the stressed electrode. The effect of aerosol ions is shown to be negligible at a short duration of the corona. The developed simplified analytical approach agrees with numerical simulations. © 2002 MAIK "Nauka/Interperiodica".

## 1. INTRODUCTION

Both the processes in a thundercloud and those at ground level are of interest in studies of discharge phenomena in a strong atmospheric electric field. On the ground, an upward leader can initiate upward lightning or attach to downward lightning. Quasi-steady corona discharges characterized by much lower current densities are also important. Flowing through a large area and for a long time (minutes), a relatively low corona current saturates the atmosphere with electric space charge. The injected charge changes the distribution of the electric field near the ground and affects the conditions of the initiation and development of an upward leader near different tall objects, including lightning-rods and protected structures [1, 2]. In particular, this is supported by the observations [3] that it is easier to initiate triggered lightning from a high-velocity rocket lifting a grounded wire than lightning from a stationary object of the same height. In the former case, there is no shielding effect from the space charge, because, at a velocity of about 100 m/s, the rocket advances the ions injected by the corona discharge near the rocket tip. In contrast, a corona discharge near the tip of a stationary object has time to form a cloud of space charge above it. Therefore, to study corona discharge near a tall object in a strong atmospheric electric field is of fundamental and applied significance.

Studies of corona discharges in the atmosphere usually consider the formation of the total space charge over a large area of the earth surface [4, 5]. In this case, the discharge is ignited at the extremities of a great number of relatively low grounded objects (twigs of trees and bushes, grass, etc.) and is characterized by a low current (<1 μA for a solitary object). These phenomena can be simulated by using one-dimensional models in which the sources of the corona current are averaged over a large area and an effective atmospheric electric field of corona ignition is introduced.

The purpose of this work is to study the peculiarities of a positive corona discharge near the tip of tall solitary objects like towers, masts, and lightning-rods in the electric field of a thundercloud. Here, as distinct from previous works [4, 5], the system under consideration is a two-dimensional one and the discharge current can reach ~1 mA, leading to a density of injected charged particles greater than the unperturbed density of atmospheric ions by 3–5 orders of magnitude. Our work differs greatly also from laboratory studies [6] of a corona discharge in much shorter gaps, where the process reaches a steady state very quickly. In a thundercloud–ground gap, the corona discharge is a fundamentally unsteady process. First, the external electric field varies with time and a lightning stroke regains its initial value only after about 1–10 s. Second, the discharge has no time to reach a steady state because the front of the space charge does not reach the thundercloud in a typical period of time between lightning strokes during an intense thunderstorm.

Analytical and numerical methods were used in this work to study the transient regimes of a corona discharge in the electric field of a thundercloud. An analytical approach establishes the general relationships in the considered problem, which includes many parameters. However, an analytical solution can be obtained only by using significant simplifications. A numerical simulation can calculate any characteristic of the corona discharge and test the validity of the analytical theory; however, at the scale of a thundercloud–earth

gap, it needs an inappropriately long running time. Undertaking the present study, we tried to combine the advantages of analytical and numerical approaches.

## 2. SIMPLIFIED ANALYTICAL DESCRIPTION OF THE TRANSIENT CORONA DISCHARGE

A quasi-steady glow corona is ignited at a steady or slowly varying (for seconds) applied voltage. In this type of discharge, ionization occurs only in a thin layer near an electrode and the voltage drop along the ionization layer is much less that the total voltage drop along the discharge gap. In our physical model, the ionization zone is assumed to coincide with the stressed electrode surface and is considered as an ion source of unlimited productivity. As a result, the electric field $E(r_0)$ (where $r_0$ is the electrode radius) on the electrode surface is maintained at the threshold field $E_i$, which is determined from the Townsend criterion for self-sustained discharge ignition. Observations and simulations of a corona discharge confirm the stabilization of the electric field on the electrode surface with a high degree of accuracy [6, 7].

The current–voltage characteristic of a corona discharge can be obtained from the expression for the density $j$ of the discharge current,

$$j(r) = \mu E(r) e n_i, \qquad (1)$$

and Poisson's equation for electric field,

$$\operatorname{div} E(r) = \rho/\varepsilon_0. \qquad (2)$$

Here, $e$ is the charge of a singly charged ion, $n_i$ and $\mu$ are the ion density and mobility, $\rho$ is the space charge density, and $\varepsilon_0$ is the permittivity of a vacuum.

Equations (1) and (2) with the boundary condition $E(r_0) = E_i = \mathrm{const}$ can be analytically solved for a steady process, when the current and voltage are time independent. This gives the simplified Townsend formula [8, 9]

$$i = BU(U - U_c)$$

for the current–voltage characteristic of the corona discharge. Here, $U_c$ is the voltage of corona ignition and $B$ is the proportionality constant, which linearly depends on the ion mobility and changes with gap geometry.

In order to theoretically describe the transient regime of the corona discharge, it is necessary to take into account the evolution in time of the electric field due to the electric charge injected into the gap. The problem reduces to a system of integro-differential equations that cannot be solved analytically even for the simplest geometry of the gap. The sole exception is the transient corona discharge at a constant current [10]. To realize this regime, the applied voltage $U(t)$ must rise in time in a specific way. From the current stabilization and the boundary condition $E(r_0) = E_i = \mathrm{const}$, it follows that the distribution of space charge and electric field do not vary in time in the gap between the stressed electrode and the front of the space charge;

i.e., each new charge injected into the gap is spent on charging new regions during the propagation of the front of the space charge. Under these conditions, the problem was solved analytically for coaxial spheres and cylinders and for plane electrodes [10].

Interest in this abstract problem stems from the fact that a similar regime of corona discharge can occur at an arbitrary, sufficiently slow evolution in time of the applied voltage, when the relationship between $i(t)$ and $U(t)$ at any instant depends only slightly on the preceding temporal evolution of the voltage. In this case, the electric field distribution $E(r)$ and space charge distribution $\rho(r)$ follow the slowly varying current. At any instant, these magnitudes correspond to an instantaneous value of $i(t)$ as though the current were constant. This quasi-stationary model is also useful in establishing the basic relationships between the current and other parameters of the transient corona discharge. As we will see subsequently, this simplified approach agrees quantitatively with a more consistent numerical simulation under some practically important conditions. Although this model was previously described in [2, 10, 11], we will present its main points, which will facilitate the interpretation of the results obtained in this paper.

We consider a solitary spherical stressed electrode with the radius $r_0$. With the boundary condition $E(r_0) = E_i = \mathrm{const}$, the electric field at the front of the space charge with the radius $r_f$ is given by

$$E(r_f) = \frac{r_0^2}{r_f^2} E_i + \frac{q_{sp}}{4\pi\varepsilon_0 r_f^2}, \quad q_{sp} = it. \qquad (3)$$

Here, $i$ is the discharge current and $t$ is the current duration time. The first term in formula (3) is the electric field of the electrode charge and the second one is that of the space charge in the gap. Note that, if the quantity $q_{sp}(r)$ is treated as the space charge inside a sphere of radius $r$, then formula (3) also defines the distribution of the electric field in the space charge layer:

$$E(r) = \frac{r_0^2}{r^2} E_i + \frac{q_{sp}(r)}{4\pi\varepsilon_0 r^2}.$$

In the case of a corona with a constant current, the charge behind the front of space charge does not change; hence, we have $q_{sp}(r) = it(r)$, where $t(r)$ is the time during which the front propagates to the radius $r$. Since the ions at the front of space charge drift with the velocity $v = dr_f/dt = \mu E(r_f)$, where $\mu$ is the ion mobility, integration over time with allowance for formula (3) yields the following expression for the front radius:

$$r_f(t) = \sqrt[3]{r_0^3 + 3\mu\left(r_0^2 E_i t + \frac{it^2}{8\pi\varepsilon_0}\right)}. \qquad (4)$$

For a well developed discharge ($r_f(t) \gg r_0$), expression (4) reduces to

$$r_f(t) \approx \sqrt[3]{\frac{3\mu i t^2}{8\pi\varepsilon_0}}. \tag{5}$$

With allowance for the above relationships, it is easy to find the voltage across the gap as a function of the corona current $i$ and the time $t$ during which the corona exists. Indeed, for a well developed corona, we have

$$U(t) = \int_{r_0}^{\infty} E(r)dr \approx U_c + \int_{r_0}^{r_f} E_{sp}(r)dr + \frac{it}{4\pi\varepsilon_0 r_f(t)}. \tag{6}$$

Here, the first term on the right-hand side describes the contribution from the constant electrode charge ($U_c = r_0 E_i$); the second term describes the voltage drop across the space charge layer,

$$E_{sp}(r) = \frac{q_{sp}(r)}{4\pi\varepsilon_0 r^2} = \frac{it(r)}{4\pi\varepsilon_0 r^2};$$

and the third term describes the voltage drop across the region $r > r_f$, which is yet free of space charge. Substituting function $t(r)$, which can be found from formula (5) at $r_f = r$, and integrating Eq. (6) over $r$, we obtain

$$U(t) \approx U_c + \sqrt[3]{\frac{9i^2 t}{8\pi^2\varepsilon_0^2\mu}}.$$

For low, but arbitrary voltage variations, the last expression can be rewritten in the form

$$i \approx \frac{2\sqrt{2}\pi\varepsilon_0}{3}\sqrt{\frac{\mu}{t}}(U - U_c)^{3/2}. \tag{7}$$

Numerical calculations [2] with allowance for time dependence of the discharge current show that, in cases that are of interest from the practical standpoint, the inaccuracy introduced by the assumption of a constant current, used in deriving formula (7), is no higher than 30%. Note that formula (7) is applicable only to a well developed corona; however, in applied problems concerning atmospheric discharges, of most interest is just this regime of a well developed corona capable of saturating large volumes of air above the earth surface.

An analysis of formula (7) leads to the following conclusions. First, the current of the transient corona discharge depends on the ion mobility as $i \sim \mu^{1/2}$; it is a weaker dependence than that for a stationary corona, for which this dependence is close to linear [8]. This stems from the fact that the current in a transient discharge is controlled by the ion drift velocity $v = \mu E(r_f)$ in the front of space charge, which is proportional to the local electric field. The value of this field decreases with increasing $r_f$, which is longer for a higher ion mobility [see formula (5)]. The weakening of the dependence $i(\mu)$ is favorable for a numerical simulation of long transient processes in corona discharge, when ion–molecule reactions leading to a variation in the ion mobility can be important. The obtained weak dependence can allow a simplification of ion kinetics.

Second, in order to maintain a constant or rising discharge current, it is necessary to increase the applied voltage. Differentiating formula (7) with respect to $U$ gives the necessary condition for the transient corona at a nondecreasing current

$$A_U = \frac{dU}{dt} > \frac{2}{3t}(U - U_c). \tag{8}$$

The critical value of $A_U$ decreases with time tending to zero. From formula (7), it follows that, at a linearly rising voltage difference $U(t) - U_c = A_U t$, the current of a transient corona also increases linearly and that, at a fixed applied voltage $U$, the current decreases in time as $i(t) \sim t^{-1/2}$.

It also follows from formula (7) that a variation in the electrode radius affects the current of the transient discharge only through the ignition voltage $U_c$. When the values of $U$ and $U_c$ are not too different, this effect is strong because the current is proportional to $(U - U_c)^{3/2}$ (instead of $U - U_c$, as in the case with a stationary corona discharge). At a fixed voltage, the discharge current can be affected only through the variation in $U_c$. In this case, it is more reasonable to change the threshold field $E_i$, rather than the electrode radius.

It should be noted that only the simplest geometry of a solitary spherical electrode, whose field is proportional to $r^{-2}$, was analyzed analytically. In order to study the discharge for a more complex geometry, we need to use numerical simulation. A numerical approach should be used also to test the applicability of the simplified analytical method for a description of the discharge with time-dependent current.

Finally, numerical calculations would be useful in studying the differences between discharge on a laboratory scale and that in the cloud–ground gap. In the latter case, the applied voltage is generally unknown and the input parameter is the thundercloud electric field $E_0$ at the ground level. This field induces an electric charge opposite in sign to the thundercloud charge on the surface of a grounded electrode, and the corona discharge is ignited in the electric field of the induced charge. Assuming that the undisturbed value of $E_0$ does not vary noticeably over the height from the ground to the electrode tip (this is true because the distance between the earth and cloud $H_{cl}$ is much higher that the electrode height $h$), we have the potential $U_0 = E_0 h$ near the electrode tip. Inducing the charge in the grounded conductive electrode leads to zero potential of the total electric field on the electrode surface. Hence, only a small part ($U_0 = E_0 h$) of the voltage drop along the cloud–earth gap is used to maintain the electric field that initiates a corona discharge. Nevertheless, the effective voltage $U_0$ should not be directly identified with the value of $U$

in formulas (7) and (8), especially at a considerable distance from the electrode tip, where the electric field of the induced charge and that of space charge are comparable with the external electric field $E_0$. Numerical simulation will show the appropriateness of the simplified analytical approach for the description of a transient corona discharge.
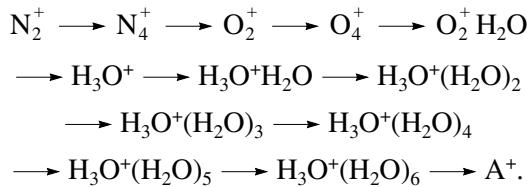
## 3. SIMULATION MODEL

The theory of transient corona discharge is based on Poisson's equation (2) and the time-dependent continuity equations

$$\frac{\partial n_j}{\partial t} + \mathrm{div}(n_j \mu_j \mathbf{E}) = S, \qquad (9)$$

where $n_j$ and $\mu_j$ are the number density and mobility of charged particles of species $j$, respectively, and $S$ is a source term describing ion–molecule reactions that affect the ion composition and, hence, the transport of charged particles. The density of space charge in Poisson's equation is $\rho = e \sum n_j$.

The ion composition in atmospheric air is a complex one [12]. Therefore, it is of importance to develop a proper model of ion kinetics which could quantitatively describe the processes in a transient corona discharge and be sufficiently simple in order to avoid time-consuming calculations.

A numerical analysis of ion–molecular reactions in humid air under standard conditions shows that the dominant species of positive ions changes in time (after producing a primary ion) in the following way [13–15]

$$N_2^+ \longrightarrow N_4^+ \longrightarrow O_2^+ \longrightarrow O_4^+ \longrightarrow O_2^+ H_2O$$
$$\longrightarrow H_3O^+ \longrightarrow H_3O^+ H_2O \longrightarrow H_3O^+(H_2O)_2$$
$$\longrightarrow H_3O^+(H_2O)_3 \longrightarrow H_3O^+(H_2O)_4$$
$$\longrightarrow H_3O^+(H_2O)_5 \longrightarrow H_3O^+(H_2O)_6 \longrightarrow A^+.$$

Here, $A^+$ denotes aerosol and $NH_4^+ \cdot X \cdot Y$ ions.

It is of interest to understand how the changes in the ion composition affect the ion mobility, which determines ion transport and electrical conductivity in a corona discharge. Reliable measured mobility data are now available for about 300 ion–gas combinations [12, 16], but there is little or no information for ion mobility measured in air. Therefore, in order to obtain the mobility data for given ion species in air, one usually uses simple models [12] that agree well with the available experimental data in pure gases.

Estimates based on the simple models show that the evolution in time of the composition of light ions in ambient air leads only to a 25% variation in the average ion mobility. Owing to a weak sensitivity of the mobility of light ions to the ion mass, it would be reasonable in a study of a corona discharge to consider only one light ion species with a mass and mobility corresponding to an $H_3O^+(H_2O)_6$ ion. In addition, this simplification is justified because all light ions, except $H_3O^+(H_2O)_6$, exist at $t < 10^{-5}$ s, when the drifting ions can cover only ~1 cm. Therefore, a good approximation to the positive-ion kinetics is to consider only $H_3O^+(H_2O)_6$ ions and aerosol ions and to take into account only the reaction
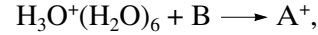
$$H_3O^+(H_2O)_6 + B \longrightarrow A^+,$$

where B is a neutral aerosol particle. This approximation will be used in our simulation.

The mobility of the $H_3O^+(H_2O)_6$ ions is assumed to be $\mu_e = 1.5$ cm$^2$ V$^{-1}$ s$^{-1}$. The kinetics, properties, and density of aerosol ions in ambient air are poorly understood. Therefore, in this work, the effect of aerosol ions is modeled by a single component $A^+$ with the effective ion mobility $\mu_a = 2.3 \times 10^{-3}$ cm$^2$ V$^{-1}$ s$^{-1}$ and the rate coefficient $k_a = 1.5 \times 10^{-6}$ cm$^3$ s$^{-1}$ for the conversion of light ions into aerosol ions; i.e., we assume $S = -k_a n_{il} n_{ia}$ in Eq. (9) for the density $n_{il}$ of light ions and $S = k_a n_{il} n_{ia}$ in Eq. (9) for the density $n_{ia}$ of aerosol ions. A similar kinetic model was used previously in [4, 5] to simulate the formation of the space charge layer above the ground.

## 4. ALGORITHM OF THE SIMULATION MODEL

A simulation was carried out for two types of grounded electrodes; these are a grounded rod with a hemispherical tip and a grounded hemisphere that is at a height $h$ above the ground. The electric field from a charged hemisphere decreases more strongly with distance than that from a rod electrode.

The wave front of the charge, which is injected into the gap by a stressed electrode, does not remain geometrically similar to the electrode surface during the front propagation. Therefore, in a strict sense, the simulation of a corona discharge near the suggested electrode must be a two-dimensional one. However, any two-dimensional computational model is very time-consuming when a corona discharge is considered in a gap many tens of meters in length. From estimates, we obtain the number $N \sim 100$ of nodes in the one-dimensional computational domain, and $N \sim 10^4$ in the two-dimensional domain.

A computational time step has to be shorter or equal to the time of ion drift along the minimum computational space step

$$\Delta t \leq \frac{\Delta x_{\min}}{w},$$

where $w$ is the ion drift velocity. In the immediate vicinity of the stressed electrode, where $w = \mu E_i$, the mobility of light ions is $\mu \approx 1.5 \times 10^{-4}$ m$^2$ V$^{-1}$ s$^{-1}$, and $E_i \approx$ 3 MV/m, we have $\Delta t \approx 2 \times 10^{-6}$ s under normal condi-

tions. Hence, in order to simulate a corona discharge for $t \sim 1$–$10$ s, it is necessary to cycle a computational loop of $N_t = t/\Delta t \sim 2 \times (10^6$–$10^7)$ time steps, each for every space mesh and ion species considered in the used kinetic model.

There is little sense in performing this time-consuming calculation for those rough input parameters that can be used at present to describe thunderstorm activity (for instance, the evolution in time of the undisturbed electric field in the cloud–ground gap). Our model of corona discharge uses the only simplifying assumption; it is assumed that the space charge layers created near the hemispherical electrode surface hold a hemispherical shape when expanding from the electrode. This would be precisely true when the vector of the electric field strength **E** and the radius vector $r$ drawn from the center of the hemisphere have the same direction and when the absolute value of the electric field depends only on the absolute value of the radius vector. The considered condition is adequately satisfied at $r \ll h$; some violation of this condition away from the electrode is of little importance.

The considered assumption significantly simplifies the calculation by reducing the problem to one-dimensional one. Now, to obtain the average propagation velocity of the hemispherical charge layer, we need only to calculate an electric field at some point of this layer (preferably on a vertical axis). It is also important that, in this case, there is no need to numerically solve Poisson's equation. The electric field at any point of the gap may be imagined as a superposition of the electric fields created by the charge of the grounded electrode (including the induced charges), by the space charge layers in the gap, and by the image of these charges in the earth. Analytical formulas can be suggested to calculate every component of the field (see the Appendix).

The calculation of the induced discharge on a grounded electrode (especially on a rod electrode) is not a simple matter. Estimates show that an efficient tool for solving this problem is the method of equivalent charges [17]. We assume a linear dependence of the charge per unit length of the rod on the distance $z$ from the earth surface ($z = h$): $\tau(z) = \alpha_\tau z$. It is also assumed that the charge of the rod tip $q_t$, being a point charge, is located in the center of the rod tip. A test calculation shows that an error in an electric field introduced by these assumptions under the considered conditions does not exceed 2–3% in comparison with a fully consistent calculation demanding a tens of times longer computational time. To calculate the tip charge $q_t$ and the proportionality factor $\alpha_\tau$ in the expression for $\tau(z)$, at every calculation step we need to solve the system of equations, which gives the potential on the rod tip (a zero potential in our case) and at some different point, e.g., in the middle of the rod at $z = h/2$ (see the Appendix). After obtaining the induced charge, we calculate the electric field on the boundaries of the layers of space charge in the gap, the velocity of the boundaries
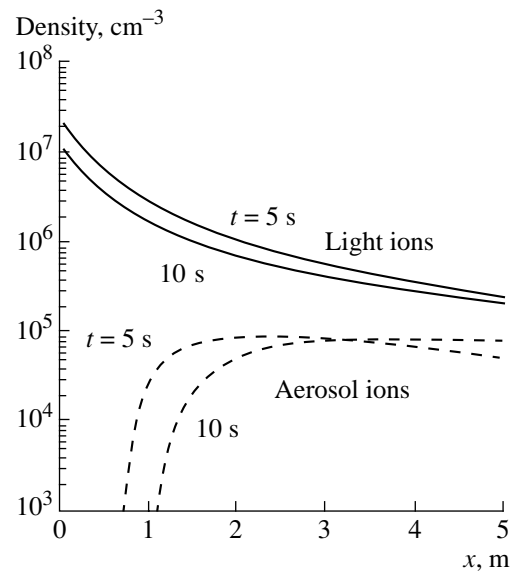


**Fig. 1.** Space distribution of light and aerosol ions over the grounded rod with a height of $h = 50$ m and radius of $r_0 = 5$ cm. The external electric field increases linearly from the magnitude corresponding to the ignition threshold to the maximum value of $E_{0\,max} = 100$ V/cm for $t_f = 5$ s and then does not change.

(separately for light and aerosol ions), and a new electric charge that is inserted into the gap from the stressed electrode at the next computational step (see the Appendix). Simultaneously, we correct the ion composition, which changes in time in accordance with the accepted kinetic model.

The described algorithm is a stable one for up to a few minutes for the measured rise rates of the atmospheric electric field.

## 5. RESULTS OF NUMERICAL SIMULATIONS

### 5.1. Effect of Ion Composition

Numerically, we studied the effect of aerosol ions on the characteristics of a corona discharge in the atmospheric electric field. The undisturbed density of aerosol neutral particles was assumed to be $n_a = 10^5$ cm$^{-3}$, which is typical for urban regions. Figure 1 shows the distribution of the densities of light and aerosol ions with height at $t = 5$ and $10$ s (time is counted from the instant of corona ignition). The calculation was carried out for a grounded rod electrode with a height of $h = 50$ m and radius of $r_0 = 5$ cm. A corona discharge was ignited at the electric field $E_i = 34.5$ kV cm$^{-1}$ near the rod tip. This was obtained when the external thundercloud electric field rose up to $E_{0c} = 53.5$ V cm$^{-1}$. We assume that the external field rises linearly up to a value of $E_{0\,max} = 100$ V/cm for 5 s after corona ignition and then is constant.
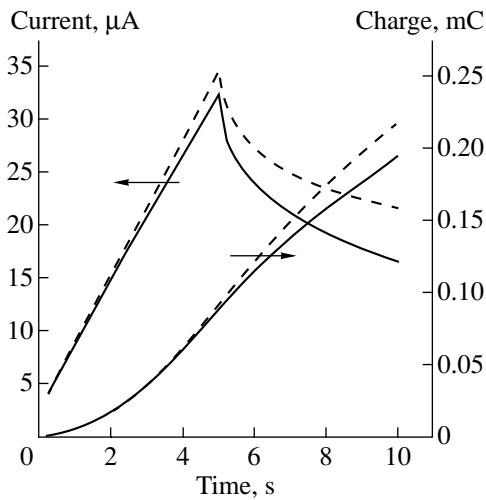
**Fig. 2.** Evolution in time of the discharge current and injected charge when aerosol ions are taken into account (solid curves) or neglected (dashed curves). The curves correspond to the same conditions as those in Fig. 1.
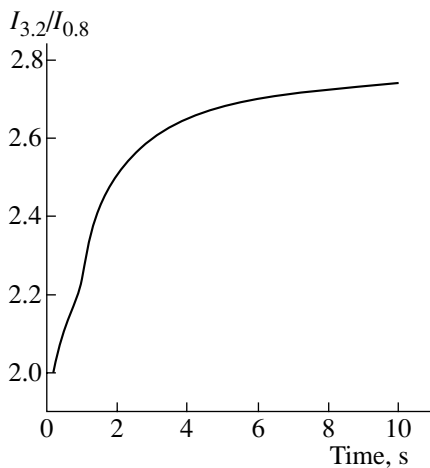


**Fig. 3.** Ratio of the calculated discharge currents at the ion mobilities $\mu = 3.2$ and $0.8$ cm$^2$ V$^{-1}$ s$^{-1}$. The curve corresponds to a grounded rod with $h = 50$ m and $r_0 = 5$ cm. The external electric field increases linearly from the magnitude corresponding to the ignition threshold to the maximum value of $E_{0\,max} = 100$ V/cm for $t_f = 1$ s and then does not change.

It can be seen that the density of aerosol ions is much less than the density of light ions. It is evident that the density of aerosol ions cannot exceed the density of neutral aerosols, which is equal to $10^5$ cm$^{-3}$, whereas the maximum density of light ions is around $10^7$ cm$^{-3}$. In addition, the effect of the removal of aerosol particles from the region near the rod tip is obtained. Owing to the upward drift of aerosol ions, the length of the aerosol-particle-free region exceeds 1 m at $t = 10$ s.
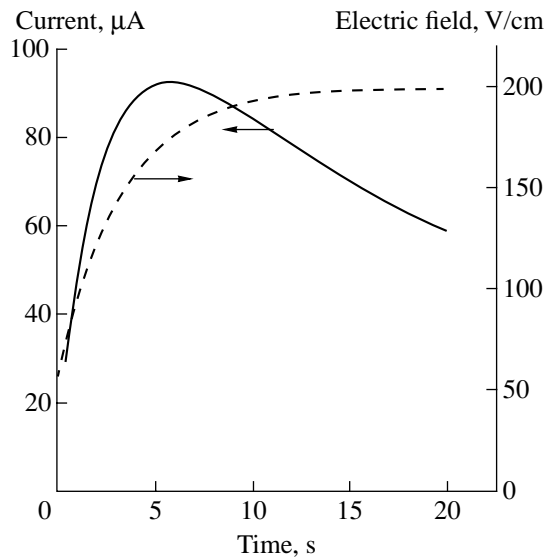
Figure 2 shows the evolution in time of the discharge current $i(t)$ through the electrode and of the space charge $q(t)$. The calculations were carried out by considering (solid curves) and neglecting (dashed curves) aerosol ions. Taking into account aerosol ions only changes the peak value of the current by 8% and the value of the injected charge at $t = 10$ s by 11%. This is due to the removal of aerosol particles from the region near the stressed electrode and due to the low density of neutral aerosols. From this result, it follows that under the considered conditions the effect of aerosol ions can be neglected. However, this is valid only for a short period of time. Our calculation showed that aerosol ions become important when the corona occurs for tens of seconds. In this case, the radius of the injected space charge is tens of meters and the density of aerosol ions and that of light ions are of the same order of magnitude. Taking into account aerosol ions decelerates an increase in time of the discharge current; this changes the discharge current by about 25% at $t = 30$ s and by 100% at $t = 60$ s.

Numerical calculations were also used to verify the slight dependence of the current of transient corona discharge on the ion mobility ($i \sim \mu^{1/2}$), which follows from the simplified analytical approach. Figure 3 shows a relative change in the discharge current at a fourfold increase in the ion mobility (we varied $\mu$ from 0.8 to 3.2 cm$^2$ V$^{-1}$ s$^{-1}$). The discrepancy between the calculation and the analytical approach is only within 10% at $t < 1$ s. Thereafter, when the external electric field is time independent, the ratio of the currents corresponding to $\mu = 3.2$ and $0.8$ cm$^2$ V$^{-1}$ s$^{-1}$ increases, but no higher than $I_{3.2}/I_{0.8} = 2.7$ (Fig. 3). However, the linear dependence of the discharge current on the ion mobility which follows from the Townsend formula for a steady regime is not obtained in a transient corona discharge.

### 5.2. Dependence of the Discharge Current on the Thundercloud Electric Field

Figure 2 gives some information about the relation between the discharge current and the external electric field. The current increases with increasing thundercloud electric field and decreases immediately after the field stabilization. The curve $i(t)$ shows a bend for a linearly rising external electric field $E_0(t)$. Analytical formula (8) gives approximately a linear time-dependence of the current of transient corona discharge for the linearly rising voltage impulse $U = A_U t$ at $U \gg U_c$. Figure 2 shows the same for the discharge current through the grounded rod electrode at the linearly rising external electric field $E_0 = E_{0c} + A_E t$, where $E_{0c}$ is the undisturbed electric field of thundercloud and $A_E = (E_{0\,max} - E_{0c})/t_f$ is the rate of the field rise up to the maximum value $E_{0\,max}$. A linearly proportional relationship between the current of a transient discharge and linearly rising thundercloud electric field is obtained over a wide range of parameters.
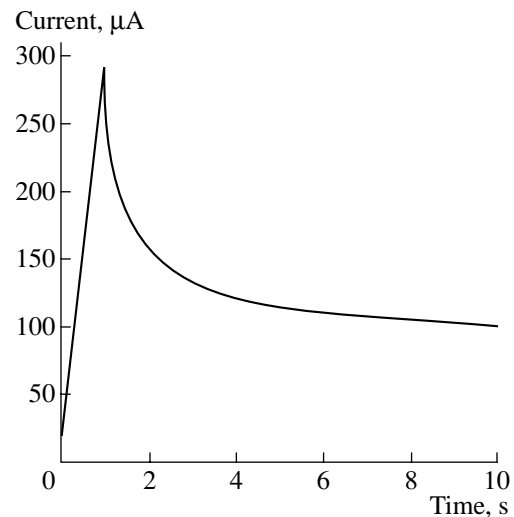
**Fig. 4.** Evolution in time of the discharge current and the exponentially rising external electric field. The curves correspond to the same electrode as that in Fig. 1.



**Fig. 5.** Evolution in time of the discharge current for the case when the external electric field increases linearly from the magnitude corresponding to the ignition threshold to the maximum value of $E_{0\,max} = 200$ V/cm for $t_f = 1$ s and then does not change. The electrode parameters are the same as in Fig. 1.

When the value of $E_0$ rises with a decreasing rate, the current of a transient corona discharge recovers from the rise earlier than the electric field does, as follows from formula (8). This is supported by Fig. 4, which shows the results of the calculation for the exponentially rising thundercloud electric field $E_0(t) = E_{0c} + (E_{0\,max} - E_{0c})(1 - e^{-\beta t})$.

At a constant thundercloud electric field, the discharge current and the rate of its change decrease with time. Figure 5 shows that, in the time interval from 1 to 9 s, the current decreases from 290 to 100 μA in agreement with the analytical approach, which gives $i \sim t^{1/2}$ [see formula (7)].

Figure 6 compares the evolution in time of the discharge current at the fixed value of $E_{0\,max} = 200$ V cm$^{-1}$ and different values of the rise time. The calculation carried out for a rod electrode with a height of 50 m and radius of 5 cm shows that, at $E_{0\,max} = 200$ V/cm, the peak current decreases from 290 to 120 μA as the value of $t_f$ increases from 1 to 10 s. A decrease in the current at a fixed instant of time with increasing $t_f$ is more pronounced. Thus, for $t = 1$ s, the corona current is 290 μA for the shortest front, and it is only 15 μA for the longest front. These results qualitatively agree with formula (7) which shows that the peak discharge current is proportional to $t_f^{-1/2}$ when the voltage rises linearly to the amplitude value, whereas the current at a fixed instant is proportional to $t_f^{-3/2}$ because

$$U(t) = U_c + (U_{max} - U_c)t/t_f.$$

The effect of the maximum thundercloud electric field on the discharge current is also pronounced. This follows from Table 1, which shows the results of the calculation for a rod electrode with a radius of 1 cm and height of 30 m. Under the considered conditions, the corona discharge was ignited in the external field $E_{0c} \approx$
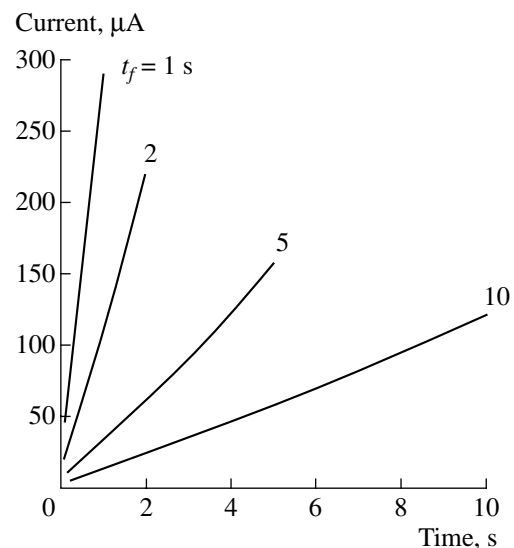


**Fig. 6.** Evolution in time of the discharge current for the case when the external electric field increases linearly from the magnitude corresponding to the ignition threshold to the maximum value of $E_{0\,max} = 200$ V/cm for different rise times $t_f$. The electrode parameters are the same as in Fig. 1.

The effect of the maximum thundercloud electric field on the discharge current

| $E_{0\,max}$, V/cm | 200 | 140 | 80 | 53 | 40.6 |
|---|---|---|---|---|---|
| $E_{0\,max} - E_{0c}$, V/cm | 177.1 | 117.1 | 57.1 | 30 | 17.7 |
| $i_{max}$, μA | 163 | 86.4 | 29.4 | 12.1 | 6.0 |
| $\left(\dfrac{E_{0\,max} - E_{0c}}{200 - E_{0c}}\right)^{3/2}$ | 1.0 | 0.536 | 0.181 | 0.0697 | 0.0316 |
| $i_{max}/i_{max}\,(E_{0\,max} = 200)$ | 1.0 | 0.530 | 0.180 | 0.0742 | 0.0368 |

23 V cm$^{-1}$, which increased linearly from $E_{0c}$ to the peak value $E_{0\,max}$ over 1 s.

The discrepancy between the calculation of the maximum discharge current and formula (7), according to which the maximum discharge current is proportional to $(E_{0\,max} - E_{0c})^{3/2}$, is within only 20%. Thus, the simplified analytical approach gives not only qualitative relationships between the external field and corona discharge current in the transient regime, but can make quantitative estimates as well.

### 5.3. Effect of the Dimensions and Geometry of the Stressed Electrode

The intensity of a corona discharge increases with increasing height $h$ of the stressed electrode and decreasing its radius $r_0$. The first parameter affects the effective voltage $U_0 = E_0 h$ of the external electric field, whereas the latter parameter affects the ignition field $E_{0c}$ and, consequently, the ignition voltage $U_c = E_{0c} h$.
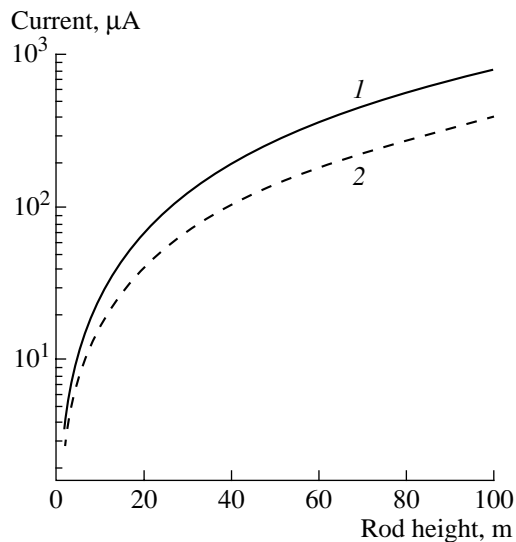


**Fig. 7.** Discharge current as a function of the rod height $h$ at $h/r_0 = 1000$ for $t = $ (*1*) 1 and (*2*) 2 s. The external electric field increases linearly from the magnitude corresponding to the ignition threshold to the maximum value of $E_{0\,max} = 200$ V/cm for $t_f = 1$ s and then does not change.

There is no geometrical similarity in the results of the calculation of discharge current at different dimensions of the stressed electrode.

Figure 7 shows that, at a fixed value of $h/r_0$ and a fixed external electric field, the discharge current increases with increasing the electrode height; the current increases from 3.5 to 810 μA as the height of the grounded electrode increases from 2 to 100 m at $h/r_0 = 1000$, $E_{0\,max} = 200$ V/cm, and $t_f = 1$ s. Such a strong dependence $i(h)$ for geometrically similar electrodes is caused by a weak effect of the rod radius on the current; a variation in the rod radius affects the current only indirectly through a change in the value of the ignition field $E_i$. According to Peek's formula, the ignition field depends only slightly on the rod radius in the practically interesting range ($r_0 > 1$ cm) [9].

It is of interest to compare the characteristics of a transient corona discharge near a rod electrode and those near a hemispherical electrode of the same dimensions because the electrode geometry affects the nonuniformity of the electric field distribution in the gap. Figure 8 shows that, under the same conditions, the discharge current for a hemispherical electrode is distinctly higher than that for a rod electrode. At $t_f = 5$ s, we have a twofold difference in the values of the maximum discharge current and space charge. The higher discharge current in the case of a hemisphere electrode is explained by a twofold increase in the ignition field $E_{0c}$ (all other things being the same) and by a more nonuniform distribution of the external electric field in comparison with the case of a rod electrode.

In order to study these factors separately, the corona discharge near a rod electrode was simulated under the assumption that the discharge is ignited at the external electric field $E_{0c}$, which corresponds to the ignition of a discharge near a solitary hemispherical electrode. In practice, this can be obtained through a decrease in the rod radius (from 10 cm to 4.9 cm) or through a change in the local geometry of the rod tip (for instance, by the mounting of short needles that rises the electric field). A local heating of the thin air layer in the immediate vicinity of the electrode can also be used because the threshold field $E_i$ and, consequently, $E_{0c}$ are approximately proportional to the gas number density which decreases with isobaric heating. By using the different ways of decreasing the value of $E_{0c}$ down to that corre-

sponding to a hemispherical electrode, the calculations gave the same result: the current from the rod increases, but it is 35–40% lower than that obtained for a solitary hemispherical electrode. This discrepancy is due to a more nonuniform distribution of the external electric field in the case of a hemispherical electrode.

A solitary hemispherical electrode is an abstraction. A similar effect can be obtained by using a hemisphere with the radius $r_0$, which is much greater than the radius of its carrying rod $r_{rod}$. However, in this case, it would be difficult to directly use such an electrode at $r_0 \sim 1$ m because too high a voltage would be required for initiating a corona. The problem can be solved if the ignition electric field $E_{0c}$ would be decreased by the mounting of sharp needles on the hemisphere surface. In this case, a corona discharge is initiated in a higher electric field near the needle tips. At a relatively uniform distribution of the needles over the hemisphere surface, the characteristics of the well developed corona discharge will be close to those obtained for a smooth electrode at the corresponding decrease in the value of the threshold field. This engineering solution was proposed and successively realized previously in [18].
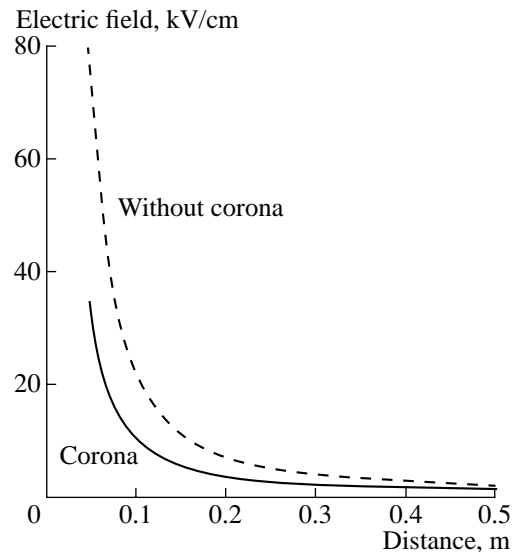
### 5.4. Distribution of the Electric Field in the Gap and near the Ground

It is known from the theory of quasi-steady corona discharge that the distribution of the electric field in a gap is smoothed under the action of the space charge. The electric field in the immediate vicinity of a stressed electrode equals $E_i$ and does not change when the external electric field $E_0$ increases. The space charge "moves" the region of a high electric field into the gap. The scale of this region is controlled by the total space charge, which is around a few mC and is a few orders of magnitude less than the charge of a thundercloud. Therefore, the dimension of the region in which the injected space charge disturbs the electric field is of the same order of magnitude as the height of a stressed electrode and is much shorter than the cloud–ground gap.

Figure 9 shows the space distribution of the electric field near the electrode. According to the boundary condition, the electric field equals $E_i$ (34.5 kV/cm in the case under consideration) near the electrode surface. In the absence of a corona, this field would be 80 kV/cm due to the electric charge induced by an external electric field of 200 V/cm on a grounded rod with a height of 30 m and radius of 5 cm. At $t = 20$ s, the injected space charge was 0.8 mC and the front of the space charge was at a distance of 85 m from the rod tip. The injection of the charge smoothed the distribution of the total electric field in the electrode region in which the total field was equal to the field in the absence of a corona already at a distance of 1 m from the rod tip. The total electric field increased with the distance from the
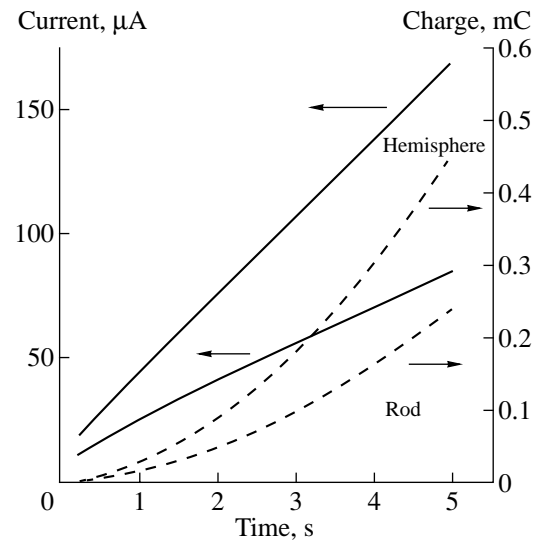
**Fig. 8.** Evolution in time of the discharge current and the electric charge injected by a grounded rod electrode ($h = 100$ m, $r_0 = 10$ cm) and a hemispherical electrode at the same values of $h$ and $r_0$. The external electric field increases linearly from the magnitude corresponding to the ignition threshold to the maximum value of $E_{0\,max} = 100$ V/cm for $t_f = 5$ s.

**Fig. 9.** Space distribution of the electric field over a rod electrode ($h = 30$ m, $r_0 = 5$ cm) in the absence of a corona and at $t = 5$ s after corona ignition. The external electric field increases linearly from the magnitude corresponding to the ignition threshold to the maximum value of $E_{0\,max} = 200$ V/cm for 5 s.

tip, and, at the front of the space charge, it was 1.5 times higher than the external electric field $E_0$.

In order to consider the effect of the injected space charge on the electric field at the ground level, the cal-
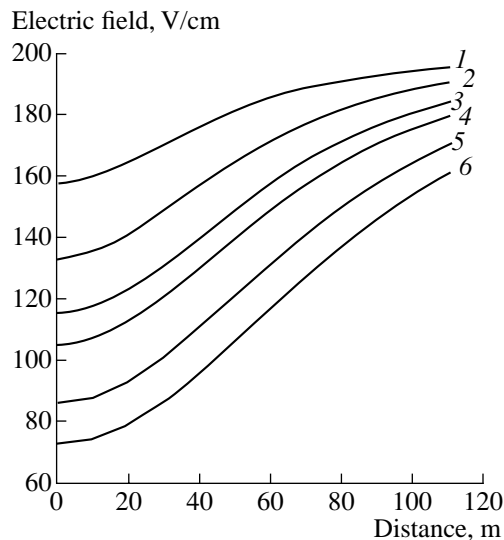
Electric field, V/cm



**Fig. 10.** Electric field at the ground level as a function of the distance to the axis of a grounded hemispherical electrode ($h = 50$ m, $r_0 = 1$ m) for $t = $ (*1*) 5, (*2*) 10, (*3*) 20, (*4*) 30, (*5*) 65, and (*6*) 120 s. The external electric field increases linearly from the magnitude corresponding to the ignition threshold to the maximum valu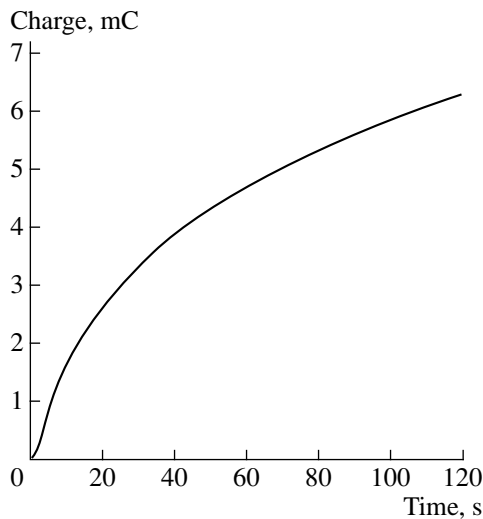e of $E_{0\,max} = 200$ V/cm for $t_f = 5$ s and then does not change. The discharge is ignited at $E_i = 1.47$ kV/cm near the electrode surface.

Charge, mC



**Fig. 11.** Evolution in time of the injected electric charge. The curves correspond to the same parameters as in Fig. 10.

culation was carried out for a solitary hemisphere. In this case, we eliminated the shielding effect for a conductive rod and studied the effect of the space charge in the pure state. It was assumed that the discharge was ignited in an external electric field of ~30 V/cm near a grounded hemisphere with a radius of 1 m due to an increase in the electric field on local sharp elements.

Clearly, this model fails to describe the distribution of the electric field on a scale comparable in length with the sharp elements. It is not important because the maximum size of the sharp elements is at least one order of magnitude smaller than the hemisphere radius.

Figure 10 shows that the region in which an electric field is decreased is comparable in length with the height (50 m in the case under consideration) of the mounting of the hemisphere. The shielding effect becomes more pronounced as the injected space charge increases. Figure 11 shows that most of the charge is injected into the gap upon stabilization of the external electric field over a period of around a minute in spite of decreasing discharge current. Over this period of time, the electric field in the center of an ion cloud is halved. Over the second minute, this field decreases by only 20%; i.e., the saturation is observed. A similar decrease in electric field will be obtained also for ground-level objects placed in the neighborhood of the stressed electrode.

It should be remembered that the calculation simulates the injection of a space charge into the gap under the assumption that the ion transport is controlled only by the drift in the atmospheric electric field. Our simulation shows that the greater part of the space charge is located in the region in which the total electric field is much lower than 1 kV/cm; i.e., a typical ion drift velocity no higher than several m/s. This is comparable to the velocity of a moderate wind which can lead to a long lateral displacement of the charged cloud and to a great change in the shielding effect for a given region on the earth surface. The developed model does not consider the influence of wind ion transport on the characteristics of a corona discharge.

We studied only the positive polarity of the stressed electrode. However, the transport properties of negative ions in ambient air are similar to those of positive ions. Therefore, the characteristics of a corona discharge near a stressed electrode in the electric field of a thundercloud are expected to be similar to those which were obtained in this work for a positive discharge.

## 6. CONCLUSION

Our numerical simulations and a simplified analytical treatment of a positive transient corona discharge near the tip of a high solitary grounded object in the electric field of thundercloud give the following results:

At a short duration of a corona ($t < 10$ s), the effect of aerosol ions is negligible and the density of light ions injected by the corona into the gap is a few orders of magnitude greater than the background ion density. However, the effect of aerosol ions is important when the discharge lasts for minutes.

The simulations demonstrate a weak dependence ($i \sim \mu^{0.5}$ instead of $i \sim \mu$ for a steady corona) of the discharge current on the ion mobility and an approximately linear time dependence of the current for the lin-

early rising voltage impulse. At a constant thundercloud electric field, the discharge current decreases with time. The peak discharge current is inversely proportional to $t_f^{0.5}$ (where $t_f$ is the rise time of the external field) at a fixed peak value of the thundercloud electric field; at a fixed instant of time, the current is inversely proportional to $t_f^{1.5}$. The peak value of the discharge current is proportional to $(E_{0\,max} - E_{0c})^{1.5}$ (instead of $E_{0\,max}(E_{0\,max} - E_{0c})$ for a steady corona), where $E_{0c}$ is the threshold thundercloud electric field at which the corona is initiated.

The intensity of a corona discharge increases with increasing height $h$ and decreasing radius $r_0$ of the stressed electrode. The height parameter affects the effective voltage $U_0 = E_0 h$ of the external electric field, whereas the radius affects the ignition field $E_{0c}$ and, consequently, the ignition voltage $U_c = E_{0c} h$. Under the same conditions, the discharge current for a hemispherical electrode is markedly higher than that for a rod electrode. This is explained by an increase in the value of $E_{0c}$ and by a more nonuniform distribution of the external electric field in the case of a hemispherical electrode.

The dimension of the region in which the injected space charge disturbs an electric field is of the same order of magnitude as the height of a stressed electrode. The injection of the charge smoothes the space distribution of the total electric field; as a result, the total electric field is lower near the electrode and higher at a distance of 1 m. At a distance of tens of meters from the rod tip, this field is 50% higher than the external electric field.

## APPENDIX

The following expressions are used in the calculations.

The point electric charge $q_t$ located at height $h$ above the ground creates at the $z$-axis the electric field

$$E_q(z) = \frac{q_t}{4\pi\varepsilon_0}\left(\frac{1}{z^2} - \frac{1}{(2h+z)^2}\right), \qquad (A.1)$$

where the $z$-axis is pointing upward from the charge.

The electric charge distributed along a rod creates at its axis the electric field

$$E_\alpha(z) = \frac{\alpha_\tau}{4\pi\varepsilon_0}\left[\frac{2h(h+z)}{2hz+z^2} - \ln\left(\frac{2h}{z}+1\right)\right], \qquad (A.2)$$

where $\tau(z) = a_\tau z$ is the rod charge per unit length and $h \gg r_0$.

A thin solitary uniformly charged hemisphere with a radius $R$ and charge $Q$ creates at the $z$-axis the electric field

$$E(z) = \frac{Q}{4\pi\varepsilon_0 z^2}\left(1 + \frac{R}{\sqrt{R^2 + z^2}}\right) \qquad (A.3)$$

$$\text{at} \quad (z > R),$$

$$E(z) = \frac{Q}{4\pi\varepsilon_0 z^2}\left(\frac{R}{\sqrt{R^2 + z^2}} - 1\right) \qquad (A.4)$$

$$\text{at} \quad (z < R),$$

where the $z$-axis is pointing upward from the hemisphere center.

The total potential (zero potential in our case) of the tip of a grounded rod, which is determined by the tip charge $q_t$, the distributed surface charge $\tau(z) = \alpha_\tau z$, the corona space charge $U_s$, and the thundercloud electric field ($U_0(h) = hE_0$), can be written as

$$\frac{\alpha_\tau h}{4\pi\varepsilon_0}\left[\left(1 + \frac{r_0}{h}\right)\ln\frac{2h}{r_0} - 2\right] + \frac{q_t}{4\pi\varepsilon_0}\left(\frac{1}{r_0} - \frac{1}{2h+r_0}\right) \quad (A.5)$$
$$+ U_s(h + r_0) + U_0(h + r_0) = 0.$$

A similar equation for the point in the middle of the grounded rod is written as

$$\frac{\alpha_\tau h}{4\pi\varepsilon_0}\left[\ln\frac{\sqrt{3 \cdot h}}{r_0} - 1\right] + \frac{q_t}{4\pi\varepsilon_0}\left(\frac{4}{3h}\right) \quad (A.6)$$
$$+ U_s(h/2) + U_0(h/2) = 0.$$

A thin, uniformly charged hemispherical layer with an average radius $R$ creates at the $z$-axis the potential

$$U_s(z) = \frac{Q}{4\pi\varepsilon_0}\left(\frac{z}{R} - 1 + \sqrt{1 + \frac{z^2}{R^2}}\right), \qquad (A.7)$$

where the $z$-axis is pointing upward from the hemisphere center and $Q$ is the total charge of the layer.

The equation for the new space charge $\Delta Q_1$ injected into the gap in the computational time step $\Delta t$ is written as

$$-\frac{\Delta Q_1}{4\pi\varepsilon_0}D + \frac{q_t}{4\pi\varepsilon_0}\left(\frac{1}{r_0^2} - \frac{1}{(2h+r_0)^2}\right)$$
$$+ \frac{\alpha_\tau}{4\pi\varepsilon_0}\left[\frac{2h(h+r_0)}{2hr_0+r_0^2} - \ln\left(\frac{2h}{r_0}+1\right)\right] + E_s(r_0) = E_c, \quad (A.8)$$

where

$$D = \frac{1}{r_0^2} + \frac{1}{(2h + r_0)^2} - \frac{R_1}{r_0^2\sqrt{r_0^2 + R_1^2}}$$
$$- \frac{R_1}{(2h + r_0)^2\sqrt{R_1^2 + (2h + r_0)^2}},$$

(A.9)

$R_1$ is the average radius of the first computational charged layer adjacent to the electrode, $E_s(r_0)$ is the total electric field created by all the computational space charge layers except for the first one, and $E_c$ is the field of corona ignition. In order to obtain the values of $\Delta Q_1$, $\alpha_\tau$, and $q_t$ at the current computational step, it is necessary to solve equations (A5), (A6), and (A8).

## REFERENCES

1. F. D'Alessandro and G. Berger, J. Phys. D **32**, 2785 (1999).
2. N. L. Aleksandrov, E. M. Bazelyan, R. B. Carpenter, *et al.*, J. Phys. D **34**, 3256 (2001).
3. M. A. Uman, *Lightning Discharge* (Academic, New York, 1987).
4. S. Chauzy and P. Raizonville, J. Geophys. Res. **87**, 3143 (1982).
5. S. Chauzy and C. Rennela, J. Geophys. Res. **90**, 6051 (1985).
6. N. V. Bogdanova, B. G. Pevchev, and S. W. Polewoy, in *Proceedings of the 4th International Conference on Gas Discharges, London, 1976*, p. 237.
7. V. I. Popkov, *Corona Discharge and Extra-High-Voltage Lines* (Nauka, Moscow, 1990).
8. L. B. Loeb, *Electrical Coronas* (University of California Press, Los Angeles, 1965).
9. Yu. P. Raizer, *Gas Discharge Physics* (Nauka, Moscow, 1992; Springer-Verlag, Berlin, 1991).
10. É. M. Bazelyan, Élektrichestvo, No. 6, 60 (1990).
11. É. M. Bazelyan and Yu. P. Raizer, Usp. Fiz. Nauk **170**, 753 (2000).
12. Ya. I. Sal'm, in *Plasma Chemistry*, Ed. by B. M. Smirnov (Énergoatomizdat, Moscow, 1993), Vol. 17, p. 194.
13. M. L. Huertas and J. Fontan, Atmos. Environ. **9**, 1018 (1975).
14. A. Luts and J. Salm, Uch. Zap. Tartu. Gos. Univ. **824**, 60 (1988).
15. A. Luts and J. Salm, J. Geophys. Res. **99**, 10781 (1994).
16. E. A. Mason and E. W. McDaniel, *Transport Properties of Ions in Gases* (Wiley, New York, 1985).
17. E. S. Kolechitskiĭ, *Computation of Electric Fields of High-Voltage Equipments* (Énergoatomizdat, Moscow, 1983).
18. R. B. Carpenter, Jr. and M. M. Drabkin, in *Proceedings of the 25th International Conference on Lightning Protection, Rhodes, Greece, 2000*, p. 380.

*Translated by the authors*

## LOW-TEMPERATURE
## PLASMA

# Electron Temperature in Nitrogen Afterglow: Dependence of Theoretical Results on the Adopted Set of Cross Sections and on the Type of Molecular Distribution over Vibrational Levels

### N. A. Dyatko, I. V. Kochetov, and A. P. Napartovich

*Troitsk Institute for Innovation and Fusion Research, State Scientific Center of the Russian Federation,*
*Troitsk, Moscow oblast, 142190 Russia*
Received May 23, 2002

**Abstract**—The electron energy distribution function in nitrogen afterglow is simulated using different available sets of cross sections for electron scattering by vibrationally excited molecules. The calculations are performed for two types of molecular distribution over vibrational levels, namely, for the Boltzmann and Treanor–Gordiets distributions. It is shown that the calculated values of the electron temperature in nitrogen afterglow depend strongly on the set of cross sections used and on the type of molecular distribution over vibrational levels. The validity of comparison between theoretical and experimental results is discussed. © *2002 MAIK "Nauka/Interperiodica"*.

## 1. INTRODUCTION

There is a large number of theoretical and experimental studies of the electron energy distribution function (EEDF) in the nitrogen afterglow plasma [1–12]. A characteristic feature of the EEDF formation in this plasma is that the electrons are primarily heated via superelastic collisions with vibrationally excited molecules. As a result, the EEDF is strongly related to the degree of vibrational excitation of nitrogen. The degree of vibrational excitation is usually characterized by the vibrational temperature $T_v$, assuming that the population of the lower vibrational levels is close to the Boltzmann distribution. As to the electron energy spectrum, it can be characterized by the effective temperature $T_e = 2/3 u_m$, where $u_m$ is the average electron energy. At present, there is no complete understanding of the relation between $T_v$ and $T_e$ in nitrogen afterglow.

Detailed probe measurements of the EEDF in the nitrogen afterglow plasma of a repetitive discharge were carried out in [4, 5]. In this case, the time delay between the end of the pulse and the measurements was substantially longer than the EEDF relaxation time and shorter than the characteristic time of variations in the quasi-steady distribution of nitrogen molecules over vibrational levels. It was shown that the EEDF was characterized by the presence of two Maxwellian components (at $u < 1$ eV and $1.6 < u < 3.6$ eV) with different local temperatures. The temperature of the low-energy ($u < 1$ eV) EEDF component ($T_e \approx 1100$ K) was nearly equal to the effective electron temperature. The authors of [4, 5] believe that the local temperature in the energy range 1.6–3.6 eV is equal to the vibrational temperature

of nitrogen molecules, because the excitation and deexcitation cross sections for vibrational levels are maximum in this energy range and the EEDF is primarily formed due to these processes. The vibrational temperature estimated in this way was found to be $T_v \approx 3000$ K $> T_e$.

Subsequent measurements [6] showed that $T_e$ depends on the discharge current: the higher the current, the higher the electron temperature in the afterglow. At the highest current (in the current range under study), the steady-state value of $T_e$ was close to $T_v$. At the same time, the vibrational temperature estimated from the EEDF in the energy range 1.6–3.6 eV was equal to $T_v \approx 2900$ K and only slightly depended on the discharge current. The EEDF was also measured in the decaying plasmas of pulsed RF discharges in pure nitrogen and $N_2$/He mixtures [7]. In that paper, very high values of the electron temperature were reported: $T_e \approx 4500$–8000 K, which is higher than the vibrational temperature $T_v \approx 3100$–4200 K. In this case, the vibrational temperature was estimated independently of the EEDF measurements, assuming the molecular distribution over vibrational levels to be close to the Boltzmann distribution. We also note the paper [9], in which the electron temperature was measured in an Ar/$N_2$ afterglow plasma and the vibrational temperature was estimated independently of the measured EEDF. It was found that, at a certain instant after the end of the discharge pulse, the electron temperature decreased abruptly from $T_e \sim T_v \approx 4000$ K to $T_e \approx 1000$ K, whereas the vibrational temperature changed only slightly.

Numerical calculations of the Boltzmann equation for the EEDF also yield different results. Thus, the authors of [2, 3] arrived at the conclusion that, at moderate vibrational temperatures ($T_v \leq 3500$ K), the electron temperature in nitrogen afterglow is approximately equal to the vibrational temperature ($T_e \approx T_v$). In this case, the molecular distribution over vibrational levels was calculated by solving a set of differential equations for the level populations, whereas $T_v$ was estimated from the relative population of the first vibrational level. In contrast, in [8], it was found that $T_e \approx 1100$ K for $T_v = 3000$ K, which agrees well with the experimental results of [5]. We note, however, that this result was obtained by assuming the Boltzmann distribution of molecules over vibrational levels and by choosing a specific set of cross sections for the electron scattering by vibrationally excited N$_2$ molecules. In [9, 10], under the same assumptions, it was shown that, when electron–electron ($e$–$e$) collisions are taken into account, the calculated electron temperature depends strongly on the electron density (the degree of ionization). At low degrees of ionization, $T_e$ is substantially lower than $T_v$ and slightly depends on the electron density, whereas at high degrees of ionization, $T_e$ is close to $T_v$. Moreover, in a certain range of the vibrational temperature and the degree of ionization, the Boltzmann equation for the EEDF in the discharge afterglow in an Ar/N$_2$ mixture [9] and pure N$_2$ [10, 11] can have two stable solutions with very different values of $T_e$.

The results of numerical calculations depend on the adopted set of cross sections for electron scattering by nitrogen molecules. There is no generally accepted set of cross sections in the literature, and different authors use different sets. For example, so far, there have been different opinions about the normalization of the cross sections for the excitation of vibrational levels of nitrogen molecules from the ground state. However, the most uncertain cross sections are those for the transitions between vibrational levels. Note that these transitions play an important role in the EEDF formation in the afterglow plasma. There is also an arbitrariness in choosing the type of distribution of nitrogen molecules over vibrational levels when simulating a specific experiment. Experiments usually allows one to estimate only a certain average vibrational temperature (see, e.g., [9]) characterizing the populations of the lower vibrational states. Simulations of vibrational kinetics also fail to provide reliable results. The problem is that, in simulations (under conditions typical of the EEDF measurements), the quenching of vibrational excitation on the discharge chamber wall must be taken into account, whereas the corresponding accommodation coefficients are known only roughly.

In this paper, we examine how the calculated values of the electron temperature in nitrogen afterglow depend on the adopted set of cross sections for the electron scattering by vibrationally excited nitrogen molecules and on the type of nitrogen molecular distribution over vibrational states.

## 2. NUMERICAL MODEL

The problem was investigated by numerically solving the following steady-state Boltzmann equation for the EEDF:

$$I_{e-M} + I_{in} + (SUP)_v + (SUP)_e + I_{e-e} = 0. \tag{1}$$

Here, the terms on the left-hand side are the collision integrals for the elastic and inelastic collisions, superelastic vibrational collisions, superelastic electron collisions, and $e$–$e$ collisions, respectively. A detailed description of all the terms in Eq. (1) is given in [8]. Note that, under the given conditions, we can use the steady-state Boltzmann equation because the electron thermalization time is substantially shorter than the characteristic times during which the plasma parameters (such as the population of vibrational levels and the plasma density) vary. Equation (1) was solved by the iteration method (see [8] for details).

Calculations were performed for a gas temperature of $T = 300$ K and pressure of 0.5 torr. These conditions are typical of experimental studies of the EEDF in nitrogen afterglow [6]. The population of all the electron levels (except for $A^3\Sigma_u^+$) was assumed to be zero. The particle density at the $A^3\Sigma_u^+$ level was set at $1.6 \times 10^{11}$ cm$^{-3}$ (i.e., the degree of excitation was $10^{-5}$, which corresponded to the conditions of [5, 6]). The electron density $n_e$ was specified as an independent parameter.

## 3. CHOICE OF CROSS SECTIONS

The transport cross section and the excitation cross sections for the rotational and electronic levels of nitrogen molecules were taken the same as in [8], in which the principle for the choice of these cross sections is described in detail.

As for the cross sections for the excitation of vibrational levels from the ground state,

$$\mathrm{N_2}(X^1\Sigma_g^+, v = 0) + e \longrightarrow \mathrm{N_2}(X^1\Sigma_g^+, v = i) + e, \\ i = 1, \ldots, 8, \tag{2}$$
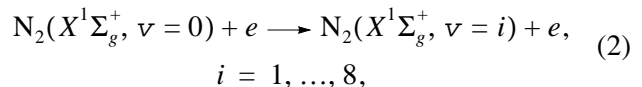
in all our previous studies [8–10], we used the same set of cross sections (see [8] for details), which was based on the experimental data presented in [13]. In particular, in [13], the near-threshold excitation cross sections for three lower levels were measured in detail. The resonant component of the cross sections was normalized according to [14]. This normalization allowed us to obtain a good agreement between the calculated and experimental dependences of the electron drift velocity on the reduced electric field in both pure nitrogen (see [8]) and nitrogen–argon mixtures [14, 15].

We note that the energy dependence of the cross sections for the excitation of vibrational levels from the ground state is fairly well known. At the same time, different authors use different normalizations for these cross sections. Thus, many authors use the cross sections for electron scattering by nitrogen molecules from the well-known set of Phelps and Pitchford [16]. The normalization factor for the cross sections from the set of [16] is 1.4 times higher than that for the cross sections used by us. For this reason, in the present paper, processes (2) were described by using two versions of the cross sections: our traditional set (symbolized by the letter $D$) and a set (symbolized by the letter $P$) in which our cross sections are increased by a factor of 1.4.

The interaction of electrons with vibrationally excited nitrogen molecules was described by the processes

$$N_2(X^1\Sigma_g^+, v = i) + e \longrightarrow N_2(X^1\Sigma_g^+, v = j) + e; \quad (3)$$
$$i = 1, ..., 7; \quad i < j \le 8.$$
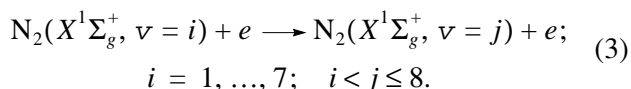
Since there is a lack of experimental data on the cross sections for these processes in the literature, the electron kinetics in nitrogen was simulated by using the calculated cross sections. The problem is additionally complicated by the fact that, in order to solve the Boltzmann equation, it is necessary to have the full matrix of cross sections (3), whereas many theoretical papers give information on the cross sections only for individual transitions. In this paper, we use the following available sets of cross sections for processes (3):

(I) A set from [17] calculated by a semiempirical method by Mihajlov and Pivovar [18]. In that paper, the cross sections for processes (3) were calculated by using the cross sections for the excitation of vibrational levels from the ground state that were taken from the set of Phelps and Pitchford. Therefore, in order to use the cross sections of [17] simultaneously with set $D$, the normalization factor should be decreased by 1.4 times.

(II) A set in which the cross section $Q^{i \to j}(u)$ for the transition from the $i$th vibrational level to the $j$th level is taken to be the cross section for the transition from the ground state to the $(j–i)$th level with a corresponding change $d_{ij}$ in the threshold,

$$Q^{i \to j}(u) = Q^{0 \to j-i}(u + d_{ij}); \quad i = 1, ..., 7;$$
$$i < j \le 8.$$

Set II is organized in such a way that the normalizing factor for the cross sections changes automatically when the normalization of cross sections (2) changes. This set was used in [8].

(III) A set used by Capitelli *et al.* (University of Bari, Italy). This set is based on the cross sections calculated in [19] by using the so-called "boomerang method." In [19], the cross section for the transition $v = 1 \longrightarrow v = 0$ was calculated; thus, by using the prin-

ciple of detailed balance, we can calculate the cross section for the direct process. An analysis shows that the cross section for the direct transition $v = 0 \longrightarrow v = 1$ is close to a similar cross section from the set of Phelps and Pitchford. Thus, we may suppose that the normalization of cross sections from set III agrees with the normalization of cross sections $P$. Accordingly, when using simultaneously with set $D$, the cross sections of set III were decreased by a factor of 1.4.

(IV) A set from [20], where the cross sections were calculated by Chen's method [21]. The normalization factor for the cross sections was chosen such that the cross section for the transition $v = 0 \longrightarrow v = 1$ calculated by similar formulas agreed with the cross section used ($P$ or $D$).

Below, the combination of the cross sections used in calculations will be denoted by a letter and a Roman numeral (e.g., $D$I, $P$III, and so on), keeping in mind that the normalization factors in the cross sections for processes (2) and (3) are brought into accordance.

Figure 1a shows the cross sections for the excitation of three lower vibrational levels from the ground state (set $P$), and Figs. 1b–1d show the cross sections for transitions between some vibrational levels (the values of the cross sections agree with set $P$). In order to not overload the figures, the cross sections from set II are omitted in Figs. 1b–1d; the values of these cross sections can be judged from Fig. 1a (see the description of set II). As follows from Fig. 1, the cross sections from different sets differ in their values and energy dependences. In particular, we note a substantial difference in the behavior of the cross sections at low energies. The cross sections for superelastic collisions were calculated from the principle of detailed balance. Accordingly, a similar difference will also exist for the cross sections for superelastic collisions.

## 4. CHOICE OF THE TYPE OF NITROGEN MOLECULAR DISTRIBUTION OVER VIBRATIONAL LEVELS
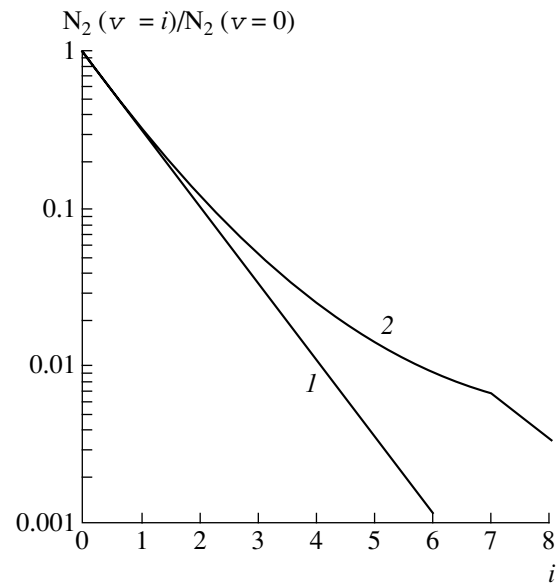
As was mentioned above, different authors use different types of molecular distribution over vibrational levels. In the simplest version, the distribution is assumed to be a Boltzmann distribution with a given vibrational temperature. In other papers, this distribution is calculated by numerically solving a set of differential equations. Under conditions typical of the EEDF measurements (e.g., in [6], the tube radius was 1.7 cm and the pressure was 0.5 torr), it is necessary to take into account the quenching of vibrational excitation on the tube wall when calculating the vibrational distribution. Accordingly, the results of calculations depend on the accommodation coefficient used.

Since this study was not aimed at describing a specific experiment, we did not calculate the vibrational distributions under given experimental conditions and used two conventional distributions, namely, the Boltz-
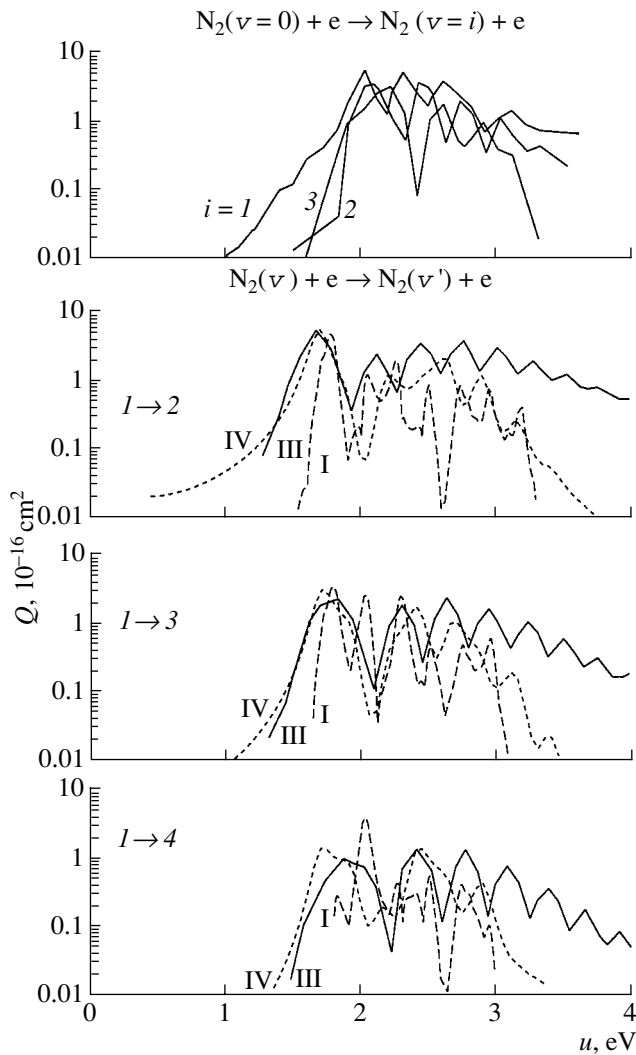
**Fig. 1.** Cross sections for transitions between some vibrational levels of $N_2$ molecules. Numerals denote the numbers of sets from which the cross sections are taken (see the text). The normalization of all the cross sections corresponds to set *P*.



**Fig. 2.** Model distributions of nitrogen molecules over vibrational levels: (*1*) Boltzmann distribution with $T_v = 3000$ K and (*2*) Treanor–Gordiets distribution with $T_{01} = 3000$ K and $T = 300$ K.

mann distribution with the temperature $T_v = 3000$ K and the so-called Treanor–Gordiets distribution [22]. The latter distribution is convenient because it is unambiguously determined by the gas temperature and the local vibrational temperature of the first vibrational level, $T_{01}$. We note that the measured populations of the vibrational levels of nitrogen in He/$N_2$ mixtures [23] are well described by this distribution. In calculations, we used a Treanor–Gordiets distribution for $T_{01} = 3000$ K and $T = 300$ K; i.e., $T_{01}$ was chosen such that the local vibrational temperature of the first vibrational level coincided with the vibrational temperature of the Boltzmann distribution. Figure 2 illustrates both of the distributions used. It can be seen from the figure that the relative population of the vibrational levels $v = 3–8$ for

the Trinor–Gordiets distribution is substantially higher than that for the Boltzmann distribution.

## 5. RESULTS AND DISCUSSION

Figure 3 shows the calculated EEDFs in nitrogen afterglow for $n_e = 2 \times 10^{10}$ cm$^{-3}$ and the Boltzmann distribution over vibrational levels. It can be seen from Fig. 3 that the EEDFs calculated with different sets of cross sections have the same local temperature (approximately equal to the vibrational temperature) in the energy range $1 < u < 2.5$ eV and different local temperatures at $u < 1$ eV. Further, for ease of comparison, the EEDF will be characterized by the effective electron temperature $T_e$, which is approximately equal to the temperature of the low-energy Maxwellian component of the EEDF. We note that the local maximum of the EEDF at $u \approx 5$ eV is due to superelastic collisions with electronically excited molecules.

Figure 4 shows the calculated dependences of $T_e$ on the electron density for the Boltzmann distribution over vibrational levels. The curves were calculated by using different combinations of the sets of cross sections. Let us consider in detail the results of calculations with cross sections *P* (Fig. 4a). It can be seen from the figure that the values of $T_e$ obtained for different sets differ markedly at low electron densities ($n_e \approx 10^9$ cm$^{-3}$). The highest value of $T_e$ (close to $T_v$) is obtained for set IV. This fact is, apparently, a consequence of the energy dependence of the corresponding cross sections (in particular, the high values of these cross sections near the threshold). For other sets of cross sections, the calcu-
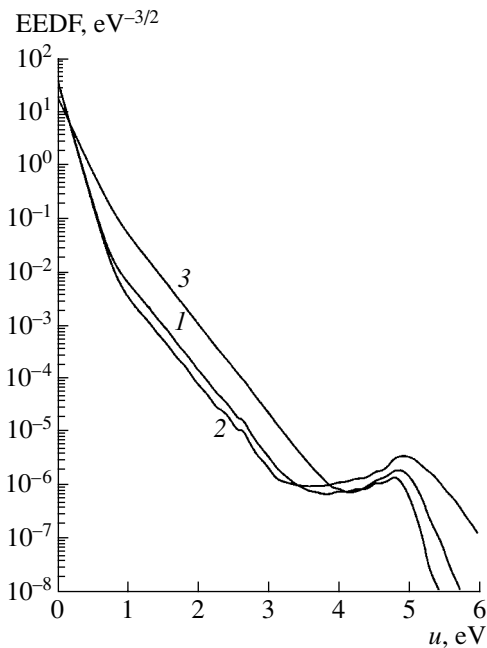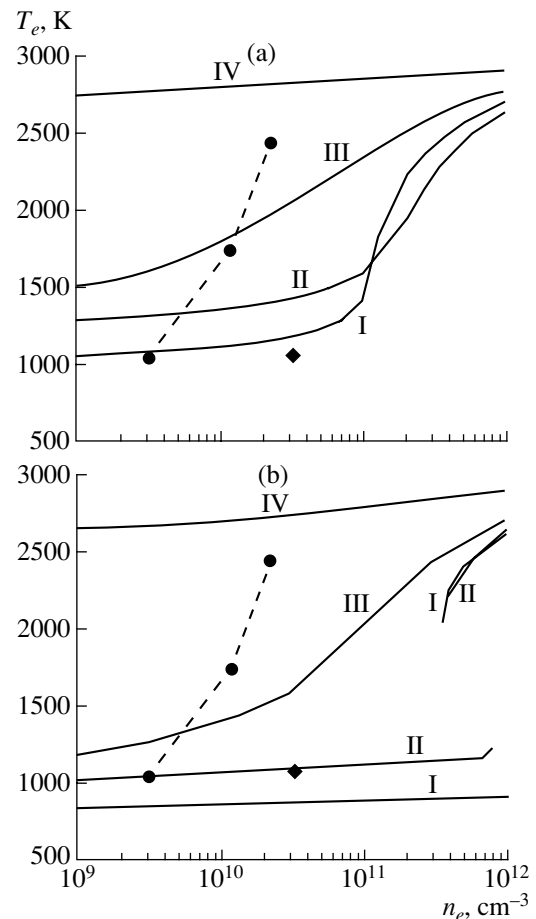
**Fig. 3.** Calculated EEDFs in nitrogen afterglow with a Boltzmann distribution of molecules over vibrational levels ($T_v = 3000$ K) and $n_e = 2 \times 10^{10}$ cm$^{-3}$ for sets (*1*) $P$I, (*2*) $D$II, and (*3*) $P$III.



**Fig. 4.** Calculated electron temperature in nitrogen afterglow with a Boltzmann distribution of molecules over vibrational levels ($T_v = 3000$ K) as a function of the electron density for sets (a) $P$ and (b) $D$. The Roman numerals by the curves correspond to the numbers of the used sets of cross sections for processes (3). The circles show the experimental data of [6], and the rhombuses show the experimental data of [5]. The experiment of [5] was carried out at $p = 0.3$ torr. The values of $n_e$ presented in the figure are recalculated to the degree of ionization used in [5].

lated values of $T_e$ are much lower than the vibrational temperature.

The electron temperature increases with increasing $n_e$. This fact can be explained as follows. The electrons in nitrogen afterglow are heated due to superelastic collisions with vibrationally excited molecules. At low values of $n_e$, the EEDF in this plasma consists of two Maxwellian components with different local temperatures: $T_e < T_v$ for $u = 1$ eV and $T_e^* \approx T_v$ for $1 < u < 3$ eV (Fig. 3). Electron–electron collisions result in the mixing of these two components. At high $n_e$ values, this leads to the thermalization of the EEDF throughout the entire energy range under study; in this case, the temperature of this Maxwellian EEDF should be close to the vibrational temperature in order to be in equilibrium with the heat source. We note that, at $T_e \approx T_v$, the electron energy loss by elastic collisions and by the excitation of rotational levels is small as compared to the energy spent on the excitation of vibrational levels. It can be seen from Fig. 4a that, as the electron density increases, $T_e$ increases and approaches $T_v$ in different ways for different sets of cross sections. Thus, for set III, $T_e$ increases smoothly, whereas for set I and, especially, set II, the electron temperature increases more abruptly as the electron density approaches a level of $n_e \approx 10^{11}$ cm$^{-3}$.

With the use of cross sections $D$ (Fig. 4b), the values of $T_e$ calculated for low electron densities somewhat decrease. The behavior of the $T_e(n_e)$ dependences for

sets III and IV is qualitatively the same as in Fig. 4a, whereas it is essentially different for sets I and II. For both sets I and II, at electron densities of $n_e \approx 4 \times 10^{11}$–$10^{12}$ cm$^{-3}$, the Boltzmann equation has two stable solutions with different electron temperatures.

The possibility of this effect (the EEDF bistability) has already been studied theoretically for afterglow plasmas in nitrogen [10, 11] and Ar/N$_2$ mixtures [9]. Hence, we do not dwell on a detailed description of this effect. We note, however, that it is $e$–$e$ collisions (along with the specific energy dependences of the cross sections used) that ensure the nonlinearity of the Boltzmann equation (the property required for the appearance of two stable solutions).

Figure 4 also shows the experimental data of [5, 6]. It can be seen that the results of different experiments

EEDF, eV$^{-3/2}$
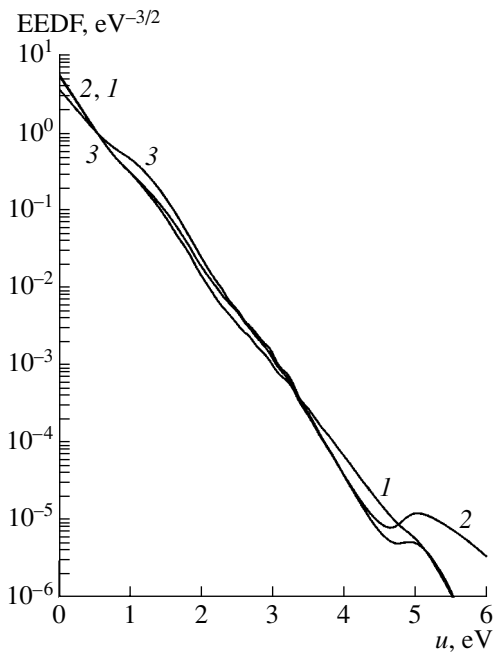
**Fig. 5.** Calculated EEDFs in nitrogen afterglow with a Treanor–Gordiets distribution of molecules over vibrational levels ($T_{01} = 3000$ K) and $n_e = 2 \times 10^{10}$ cm$^{-3}$ for sets (*1*) *P*I, (*2*) *D*II, and (*3*) *P*III.

$T_e$, K
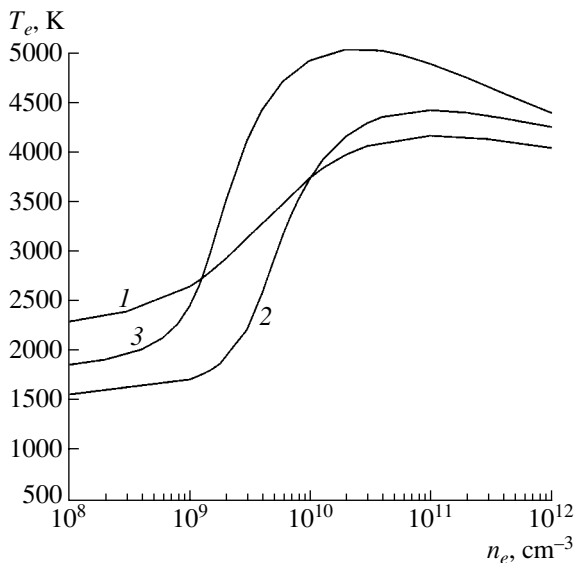
**Fig. 6.** Calculated electron temperature in nitrogen afterglow with a Treanor–Gordiets distribution of molecules over vibrational levels ($T_{01} = 3000$ K) as a function of the electron density for sets (*1*) *P*I, (*2*) *D*II, and (*3*) *P*III.

are somewhat contradictory. When the calculated data are compared with the results of [5], the best fit is obtained with set *D*II. It is this set that was proposed in [8] to achieve agreement with the experimental data of [5]. The minimum value $T_e$ from the data of [6] also lies

well on curve II. We note that none of the calculated curves describe the experimental dependence $T_e(n_e)$ [6] as a whole.

However, the experimental data of [6], with which we make a comparison, raise some doubts. In particular, for all of the investigated regimes (discharge currents), the vibrational temperature estimated from the EEDF in the energy range $1.6 < u < 3.6$ eV appears to be nearly the same. Actually, under the condition of a repetitive discharge [6], the degree of vibrational excitation should depend on the time-averaged energy deposition into vibrational levels. Estimates show that the average energy depositions at the minimum and maximum currents (corresponding to the minimum and maximum values of $T_e$ in Fig. 4) differ by a factor of 5. Because of this difference, the degrees of vibrational excitation should also be different. In addition, it is unlikely that the molecular distribution over vibrational levels under the experimental conditions is a purely Boltzmann distribution.

Figures 5 and 6 show the results of calculations performed with the use of a Treanor–Gordiets vibrational distribution (Fig. 2). Figure 5 shows the EEDFs calculated for three sets of cross sections. As follows from the figure, the average local temperature of the EEDF in the energy range $1.6 < u < 3.6$ eV is ≈4000 K, which is noticeably higher than the local vibrational temperature of the first vibrational level, $T_{01} = 3000$ K. In other words, the local temperature of the EEDF in this energy range is an average characteristic of the degree of vibrational excitation.

Figure 6 shows the dependences $T_e(n_e)$ calculated for three sets of cross sections. It can be seen from the figure that the values of $T_e$ at low electron densities are considerably higher than in the case of a Boltzmann distribution over vibrational levels (see the corresponding curves in Fig. 4). As $n_e$ increases, the electron temperature tends to the value $T_e \approx 4000$ K. We note that $T_e$ does not increase monotonically, but passes through a maximum, whose value (depending on the set of cross sections used) can substantially exceed the limiting value. Note that the limiting value coincides with the local temperature of the EEDF in the energy range $1.6 < u < 3.6$ eV (Fig. 5). A comparison of Figs. 4 and 6 shows that, for a Treanor–Gordiets distribution, the transition from low to high $T_e$ values occurs at substantially lower electron densities. In addition, we do not observe the bistability of the EEDF (at least for $T_{01} = 3000$ K) in this case.

The above analysis shows that the calculated values of the electron temperature in nitrogen afterglow depend strongly on the set of cross sections for electron scattering by vibrationally excited molecules, as well as on the type of molecular distribution over vibrational levels. At present, there is no reliable method to determine which of these sets of cross sections is the most realistic. In principle, to verify the cross sections, we

can compare the calculations with experimental results from the EEDF measurements in the afterglow plasma. However, in this case, it is necessary to experimentally measure not only the EEDF, but also the distribution over vibrational levels, which may be used in calculations (we note that it should be detailed measurements, rather than estimates of the vibrational temperature of the lower level).

We also note that, under typical experimental conditions (see, e.g., [6]), the radius of the discharge tube is comparable with the characteristic length over which the EEDF is established. It may turn out that, under these conditions, the effects of the EEDF nonlocality and the polarization electric field caused by ambipolar diffusion should be taken into account for a correct theoretical modeling of the EEDF.

## 6. CONCLUSION

The cross sections for electron scattering by vibrationally excited nitrogen molecules used by different authors substantially differ in both the value and the energy dependence. We have shown that the calculations of the electron temperature in nitrogen afterglow with the use of these different sets of cross sections yield very different results. We have also shown that the calculated electron temperature depends on the type of molecular distribution over vibrational levels. Hence, it is hardly possible to correctly compare the calculated results with the experimental data because, in experiments on determining the EEDF in nitrogen afterglow, detailed measurements of the molecular distribution over vibrational levels have not yet been performed.

## ACKNOWLEDGMENTS

## REFERENCES

1. M. Capitelli, C. Gorse, and A. Ricard, *Nonequilibrium Oscillatory Kinetics*, Ed. by M. Capitelli (Springer-Verlag, New York, 1986; Mir, Moscow, 1989).
2. C. Gorse, M. Capitelli, and A. Ricard, J. Chem. Phys. **82**, 1900 (1985).
3. C. Gorse, M. Cacciatore, M. Capitelli, *et al.*, Chem. Phys. **119**, 63 (1988).
4. N. A. Gorbunov, N. B. Kolokolov, and A. A. Kudryavtsev, Zh. Tekh. Fiz. **58**, 1817 (1988) [Sov. Phys. Tech. Phys. **33**, 1104 (1988)].
5. N. A. Gorbunov, N. B. Kolokolov, and A. A. Kudryavtsev, Zh. Tekh. Fiz. **61** (6), 52 (1991) [Sov. Phys. Tech. Phys. **36**, 616 (1991)].
6. A. A. Kudryavtsev and A. I. Ledyankin, Phys. Scr. **53**, 597 (1996).
7. G. Dilecce and S. Benedictis, Plasma Sources Sci. Technol. **2**, 119 (1993).
8. N. A. Dyatko, I. V. Kochetov, and A. P. Napartovich, Fiz. Plazmy **18**, 888 (1992) [Sov. J. Plasma Phys. **18**, 462 (1992)].
9. N. A. Dyatko, Yu. Z. Ionikh, N. B. Kolokolov, *et al.*, J. Phys. D **33**, 2010 (2000).
10. N. A. Dyatko and A. P. Napartovich, in *Proceedings of the 20th School on Physics of Ionized Gases, Belgrade, 2000*, Contrib. Papers, p. 115.
11. N. A. Gorbunov, N. B. Kolokolov, and F. E. Latyshev, Fiz. Plazmy **27**, 1143 (2001) [Plasma Phys. Rep. **27**, 1079 (2001)].
12. V. Guerra, P. A. Sa, and J. Loureiro, Phys. Rev. E **63**, 046404 (2001).
13. M. Allan, J. Phys. B **18**, 4511 (1985).
14. N. L. Aleksandrov, I. V. Kochetov, and A. P. Napartovich, Khim. Vys. Energ. **20**, 291 (1986).
15. G. N. Haddad, Aust. J. Phys. **37**, 487 (1984).
16. A. V. Phelps and L. C. Pitchford, JILA Information Center Report, No. 26 (Boulder, 1985).
17. A. A. Mihajlov, V. D. Stojanović, and Z. Lj. Petrović, J. Phys. D **32**, 2620 (1999).
18. A. A. Mihajlov and V. A. Pivovar, Zh. Tekh. Fiz. **45**, 1063 (1975) [Sov. Phys. Tech. Phys. **20**, 668 (1975)].
19. L. Dube and A. Herzenberg, Phys. Rev. A **20**, 194 (1979).
20. N. L. Aleksandrov, A. M. Konchakov, and E. E. Son, Fiz. Plazmy **4**, 1182 (1978) [Sov. J. Plasma Phys. **4**, 663 (1978)].
21. J. C. Y. Chen, J. Chem. Phys. **40**, 3513 (1964).
22. B. Gordiets and S. Zhdanok, *Nonequilibrium Oscillator Kinetics*, Ed. by M. Kapitelli (Springer-Verlag, New York, 1986; Mir, Moscow, 1989).
23. S. Benedictis, G. Dilecce, and M. Simek, J. Phys. B **27**, 615 (1994).

*Translated by N. F. Larionova*

=== **OBITUARY** ===

# In Memory of Semen Samoĭlovich Moiseev
# (November 23, 1929–June 5, 2002)

Professor Semen Samoĭlovich Moiseev, a well-known theoretical physicist; a prominent Russian scientist in the fields of plasma physics, theory of turbulence, and processes of self-organization in nonequilibrium media; and a principal researcher at the Institute of Space Research of the Russian Academy of Sciences died in his 73rd year on June 5, 2002, after an extended illness.

S.S. Moiseev was born on November 23, 1929. After graduating in 1952 with honors from Kharkov State University (KSU), he worked as a teacher in Slavyansk and Poltava. However, his inquisitive intellect craved new knowledge. Therefore, in 1960, he moved to Novosibirsk, where he began to work in the field of controlled fusion research at the Institute of Nuclear Physics of the Siberian Division of the USSR Academy of Sciences. There, he obtained pioneering results, which were reported at the largest international conferences and were the basis for his candidate's and doctoral theses. Among those results, it is worth noting the solution of the problem of anomalous Bohm diffusion in fusion devices, the studies on low-frequency instabilities in inhomogeneous plasmas and transformation of electromagnetic waves in nonsteady and inhomogeneous plasmas, and the development of principles of novel plasma diagnostics based on the generation of higher harmonics in plasma resonance layers.

It should be noted that the versatile scientific activity of Moiseev resulted in the development of a number of important directions in plasma physics, hydrodynamics, and nuclear energetics. His works, which were always in the vanguard of scientific research, gained worldwide recognition in the scientific community.

In 1968, Moiseev moved to the Kharkov Institute for Physics and Technology (KIPT). There, he further developed his earlier studies on plasma stability and plasma heating as applied to beam–plasma systems and proposed new, original ideas in other fields of plasma physics, among them, a model of the nonlocal transfer of electromagnetic signals in inhomogeneous plasmas (the effect of kinetic transparency of wave barriers), new mechanisms for the generation of electromagnetic radiation associated with the wave conversion in the presence of plasma density gradients, the focusing and channeling of radiation in a plasma, and the resonant-cone effect in the excitation of electromagnetic waves by small-size sources. He also developed new approaches to the theory of strong hydrodynamic turbulence and to the formation of nonequilibrium power-law distributions of charged particles in collisional media. The results of these studies were published in Reviews of Plasma Physics and Usp. Fiz. Nauk (Sov. Phys. Uspekhi). For these results, which were very important for practical applications, Moiseev received a series of inventor's certificates. For works on the kinetic transparency of wave barriers in a plasma, Moiseev and his colleagues were awarded the 1979 Ukrainian SSR State Prize in Science and Technology.

In 1980, Moiseev began to work in Moscow at the Institute of Space Research of the USSR Academy of Sciences. There, he developed new approaches toward increasing the efficiency of absorption of high-power laser radiation in an inhomogeneous plasma via the channeling and self-focusing of laser beams. The results of his long-term studies on the mechanisms for the generation of electromagnetic radiation in a plasma were published in the monograph *Nonequilibrium and Resonant Processes in Plasma Radiophysics* (Nauka, Moscow, 1982), written together with his colleagues. For his research in plasma physics, Moiseev was awarded the 1987 USSR State Prize in Science and Technology.

Simultaneously, he worked in the field of hydrodynamics. An important result of these investigations was the discovery of a helical mechanism for the generation of large-scale tropical vortices. This made it possible to develop a new approach to the important problems of

forecasting hurricanes, typhoons, and extratropical cyclones and monitoring cyclogenesis zones. Based on these theoretical results, two expeditions to the Pacific Ocean were organized to carry out in situ measurements in the zones of intensive cyclogenesis. The theory developed at the Institute of Space Research allowed Moiseev to elaborate a system of physical precursors and indicators of tropical cyclones. These studies laid the theoretical foundations of the contemporary methods for forecasting large-scale crisis processes in the atmosphere, such as typhoons and extratropical cyclones. The experimental data from the expeditions showed that these indicators may be abnormal fluctuations of the background atmospheric parameters, such as infrasonic activity, the dynamics of fractal parameters, and the helicity of atmospheric turbulence. Later, he and his pupils investigated this field of research in more detail: they analyzed the formation of non-Kolmogorov turbulent spectra, examined the structural properties of hydrodynamic turbulence and the mechanisms for helicity generation, and studied the influence of turbulence helicity on the particle and energy transport. In essence, he founded a new line of investigation—the helical dynamics of nonlinear media. The results of his studies in the fields of plasma physics and hydrodynamics were published in the monographs *Nonlinear Instabilities in Plasmas and Hydrodynamics* (IOP, Bristol, 1999), written together with V.N. Oraevsky and V.G. Pungin, and *Turbulence and Structures. Chaos, Fluctuations, and Helical Self-Organization in Nature and the Laboratory* (Academic, New York, 1999), written together with H. Branover, A. Eidelman, and E. Golbraikh.

Along with these studies, Moiseev, together with his colleagues from KIPT and KSU, prolonged investigations of nonequilibrium power-law particle distributions in solid-state plasmas and developed the principles of their applications for direct and more efficient nuclear-to-electric energy conversion. In particular, based on theoretical and experimental results, they proposed a new secondary-emission radioisotope current source, which has obvious advantages (with respect to the efficiency, lifetime, environmental safety, etc.) in comparison with available nuclear batteries. The creation of a prototype of such a battery will stimulate the development of prospective future technologies of fabricating multilayer thin-metal-film structures.

In recent years, Moiseev investigated very interesting chiral effects, which play an important role, e.g., in producing new materials with unusual electrodynamic characteristics. These studies are related to another promising area of investigation—the electrodynamics of bianisotropic media.

For his major contribution to science and the training of qualified specialists, Moiseev was awarded the title of an Honored Scientist of the Russian Federation.

Due to Moiseev's talent for intuiting new, promising directions in physics, his works stimulated a number of new lines of investigations, which have been further developed by his pupils and colleagues. Many of his results were confirmed experimentally and gained worldwide recognition. Although Moiseev was a theorist, he always tried to initiate the experimental testing of the results obtained.

His style of work, kindness, sociability, respect for the scientific opponent's opinion, and striking spiritual power deeply impressed those around him. Under his supervision, many of his pupils have defended doctoral theses, achieved great success, and gained wide recognition in the scientific community. Now, they constitute Moiseev's scientific school, continuing the studies initiated by him and developing his ideas.

Moiseev spent a great deal of time and energy on the development of international collaboration. He worked at various renowned science centers, such as the MHD Research Center of Ben-Gurion University (Israel) and the Nieuwegein Institute of Plasma Physics (Netherlands). For a long time, Moiseev convened one of the sections of the General Assemblies of the European Geophysical Society; he was a member of the organizing committees of several large international conferences.

The memory of Semen Samoĭlovich Moiseev, a scientist caught up in his work; a skillful organizer; an exclusively reliable person; and a modest, friendly, kind, and cheerful man with a sense of humor will always remain in the hearts of his friends, colleagues, and pupils.

*B. Alterkop, V.M. Balebanov, M. Bornatici,*
*V.N. Budnikov, N.S. Buchel'nikova, V.A. Buts,*
*G. Vekshtein, A.A. Vodyanitskiĭ, E.D. Volkov,*
*V.I. Volosov, A.A. Galeev, A.V. Gaponov-Grekhov,*
*V.B. Gil'denburg, V.E. Golant, G.S. Golitsyn,*
*S.N. Gordienko, M.B. Gokhberg, I.G. Granberg,*
*E.Z. Gusakov, G.I. Dimov, A.M. Dykhne,*
*G.M. Zaslavskiĭ, V.E. Zakharov, L.M. Zelenyĭ,*
*A.M. Egorov, N.S. Erokhin, V.V. Zheleznyakov,*
*V.I. Karas', I.V. Karas', H. Kikuchi,*
*A.S. Kingsep, R.A. Kovrazhkin, E.Ya. Kogan,*
*S.I. Kononenko, V.M. Kontorovich,*
*V. Krasnosel'skikh, É.P. Kruglyakov,*
*E.A. Kuznetsov, N.P. Laverov, V.I. Lapshin,*
*A.G. Litvak, J.G. Lominadze, G.Z. Machabeli,*
*I.N. Meshkov, M.A. Miller, A.B. Mikhaĭlovskiĭ,*
*V.I. Moroz, A.I. Morozov, V.I. Muratov,*
*L.A. Nazarenko, A.V. Nikolaev, I.N. Onishchenko,*
*V.N. Oraevskiĭ, O.S. Pavlichenko, A.D. Pataraya,*
*E.N. Pelinovskiĭ, M.I. Petelin, A.D. Piliya,*
*I.V. Pryanikov, A.K. Richter, A.A. Rukhadze,*
*D.D. Ryutov, R.Z. Sagdeev, V.P. Silin,*
*A.N. Skrinskiĭ, K.N. Stepanov, R.A. Syunyaev,*
*V.I. Talanov, V.Yu. Trakhtengerts, Ya.B. Faĭnberg,*
*G.M. Fraĭman, A.M. Fridman, U. Frish,*
*V.S. Tsypin, B.V. Chirikov, O.G. Chkhetiani,*
*V.D. Shafranov, V.D. Shapiro,*
*A.B. Shvartsburg, and D. Schertzer*